Order Number 9325167

Ultrafast spectroscopy in conjugated organic and biological materials

Yan, Ming, Ph.D.

City University of New York, 1993

U·M·I
300 N. Zeeb Rd.
Ann Arbor, MI 48106

ULTRAFAST SPECTROSCOPY IN CONJUGATED ORGANIC AND BIOLOGICAL MATERIALS

by

MING YAN

A dissertation submitted to the Graduate Faculty in Engineering in partial fulfillment of the requirement for the degree of Doctor of Philosophy, The City University of New York.

• 1993 •

This manuscript has been read and accepted for the Graduate Faculty in Enginering in satisfaction of the dissertation requirement for the degree of Doctor in Philosophy.

4/27/93
Date:

Chairman of the Examining Committee:
Dr. Robert. R. Alfano, Distinguished Professor of Science and Engineering, Departments of Physics and Electrical Engineering, The City College of The City University of New York.

4/27/93
Date:

Executive Officer
Professor Gerard Lowen

Dr. Lewis Rothberg,	Member of Technical Staff, AT & T Bell Laboratories, Murray Hill, NJ 07974.
Dr. Roger Dorsinville,	Professor, Department of Electrical Engineering, The City College of The City University of New York.
Dr. Ping Pei Ho.	Professor, Department of Electrical Engineering, The City College of The City University of New York.
Dr. Samir Ahmed.	Professor, Department of Electrical Engineering, The City College of The City University of New York.

Supervisory Committee

The City University of New York

Abstract

ULTRAFAST SPECTROSCOPY IN CONJUGATED ORGANIC AND BIOLOGICAL MATERIALS

by

Ming Yan

Adviser: Professor Robert R. Alfano

The dynamics of two kinds of conjugated materials, the visual pigment rhodopsin and the organic polymer poly(*p*-phenylene vinylene), have been studied utilizing femtosecond spectroscopy.

The 11-*cis* to all-*trans* torsional isomerization of the retinal chromophore in rhodopsin for both protonated and deuterated aqueous environments have been studied by time-resolved absorption measurements at room temperature. The kinetic results are well modeled by rate equations based on the scheme which involves the isomerization along the torsional coordinate of the 11-*cis* bond of the retinal chromophore. A metastable intermediate 90 degree twisted state is formed within 200 fs on the excited state surface by rotation around the C_{11}-C_{12} double bond, and it takes 3 ps to form the fully isomerized all-*trans* photoproduct known as bathorhodopsin and to repopulate the ground state rhodopsin. These results agree well with the semiempirical energy level and molecular dynamics calculations. The observed dynamics are insensitive to deuteration of the exchangeable protons which suggest that proton translocation is unimportant at physiological temperatures.

The conjugated polymer, Poly(p-phenylene vinylene) (PPV) in a stretch oriented film, has been studied using polarized time-resolved absorption with subpicosecond resolution and transient luminescence measurements. Excitations are generated by photoexcitation near the band edge (500nm-540nm) with a 200 fs pulse and the resulting spectral changes are probed with a white light pulse. Lattice stabilized (singlet) self-trapped excitons are formed within 200 fs which are observed by measuring the stimulated gain in their emission band which decay at 10 ps. The agreement of the photoinduced exciton gain spectrum (<1ps), the transient luminescence spectrum (10 ps) and the steady state luminescence spectrum suggest that the singlet excitons are not further trapped after 200fs of their formation time. Excitation wavelength dependence measurements suggest that the polarization anisotropy effect is due to the different dipole-allowed absorptions for different polarized excitation. Raman gain is observed at 1170 cm^{-1} and 1560 cm^{-1} when the pump and probe pulses overlap in time, and are distinguished from stimulated exciton gain by tuning the excitation wavelength. The induced absorption is characterized by a fast decay (~1ps), a slow decay (~100ps) and a long-lived absorption process, which correspond to the decay time of free excitons and polaron pairs, respectively. The polaron pairs are formed within 800 fs and decay non-exponentially. Polaron pairs initially decay in about 100 ps to form (singlet) self-trapped excitons which contributes to the long tail of luminescence. A model for the relaxation kinetics in PPV is proposed. The intra- and inter- chain photoexcitations which involve different energy level transitions are discussed.

In Memory of
my grandmothers
Min-zhen Wang and Fu-Kang You
who passed away during the time that I was working on this degree

Acknowledgment

I wish to thank Prof. Robert Alfano for introducing me to the ultrafast laser field, and his deep and broad understanding in this field has given me a most exciting and interesting education while working on my thesis. I trully thank him for stressing depth into these problems and his critical and firm opinions lead to improvement of this thesis. I also thank Dr. Lewis Rothberg, with whom I have worked closely for the past two years, for his patient guidance and insight. Without his kindly help, this thesis could not have been completed. I also thank Prof. Robert Callender, Prof. Roger Dorsinville and Prof. Ping-Pei Ho for their expert help in vision, conjugated polymers and lasers, respectively. I thank Dr. Nate Ockman for his stimulating comments and conversations, and his kindness correcting this thesis. Thanks to Mr. Wubao Wang and Hsieh-Shin Chao for their technical expertise in teaching me laser techniques. Thanks to Dr. Daney Manor, Miss Gezhi Weng, Mr. Liwen Wang and Dr. R.H. Hsieh for their expert advise on rhodopsin and conjugated polymers and in their preparations of the samples used in this thesis. I wish to thank the IUSL where all my experiments were performed and to thank all my friends there for their assistance.

This work is dedicated with respect and love to my parents, An-ling Yan and Yu-ping Sun. Without their support, this thesis would not be completed. I am particularly indebted to my mother for her sacrifice in taking care of my two-month-old daughter so that I can complete the writing of this thesis. This thesis is also dedicated to my wife Rong Xiao and my daughter Jennifer Yan.

Table of Contents

List of Tables

List of Figures

Chapter 2

Chapter 8

Chapter 1 Introduction

1.1) Organic and Biological Molecular Electronics

The tremendously increasing volume of information processing and communication is continuously challenging modern technology. Faster operation rates and smaller volumes for high capacity storage are the goals in our expanding information-based societies. Today, most of the materials used for devices are metals and semiconductors. But, in almost all cases, the best performing and most reliable systems are in living organisms[1.1], such as the photochemistry in the visual system, photosynthesis in the plant and neural networks in the brain. Large efforts have been made to use biological molecules and organic materials in electronic devices, the so-called molecular electronics devices. For example, bacteriorhodopsin, a chromophore similar to the visual pigment, which is used in spatial light modulators, a highly efficient molecular 3-D optical memory[1.2] and an artificial photoreceptor array[1.3]; Molecular crystals have been made into the world smallest memory storage devices; Organic polymers have been extensively used in electro-optical devices[1.4], such as light modulation, optical switching, photoconduction, schottky structure[1.5], p-n junction[1.6] and MIS[1.7] devices. Doping in conjugated polymers has achieved a conductivity up to 10^4 $(\Omega cm)^{-1}$, Therefore, doped conjugated polymers as organic conductors have been used in many applications. The unlimited possibilities of organic synthesis, controllability, flexibility and injection or doping of charge carriers in such organic polymers give these materials a promising future in device applications.

Molecular electronics is an emerging field that lies at the interface of chemical physics, biophysics, electrical engineering, and solid state science. It involves the encoding, manipulation, and retrieval of information at a

macromolecule level as opposed to current techniques[1.2]. This field not only represents efforts in the miniaturization of computer circuitry, but it also provides promising new methodologies for high speed signal processing, optical data storage, and content-addressable memory devices using the unique nature the biological and organic materials.

The retinal in the visual pigment and the polymer backbone are essentially one dimensional with highly conjugated electronic distributions. In such systems, optical excitation (also electronic injection) always results in the distortions of the delocalized electronic distributions, and results in molecular structure changes. The photoisomerization in the visual molecule results in the significant shifting of electronic absorption. The rearrangements of polymer lattice structures results in localized electronic distributions to form localized excitations which, in turn, shift the absorption to below the energy gap. These photochromic properties in such low-dimensional organic systems are quite different from 3-D materials, such as semiconductor, and are particularly interesting in many memory storage device applications.[1.2]

Poly(p-phenylene vinylene) (PPV), an organic polymer discussed in this thesis, have had particularly interesting applications in electroluminescence devices[1.8] and xerographic applications. Significant electron-injected luminescence from PPV films was reported [1.8] with a quantum yield of a few percentage, therefore, the development of low-cost large-area light-emitting diodes (LED) have become possible. Good optical quality films of PPV can be conveniently prepared via a soluble precursor polymer [1.9] with very low concentrations of charge and spin defects. The synthesis also makes it possible to control the optical absorption gap by substitution of sides group in the PPV family. Although potential technological opportunities have been provided by these organic materials, they are also interesting for fundamental research, such as

low dimensional system studies. The dynamics study is important for understanding the basic properties of organic materials both for applications and fundamental studies. The generation of ultrafast laser pulses make it possible for temporal spectroscopic studies in such organic materials in the time range of 10^{-10} to 10^{-15} second.[1.1] Energy transfer, rotational and vibrational relaxation, structure rearrangements, photo disassociation and many ultrafast events involved in molecular dynamics have been opened for investigation.

1.2) Thesis Statement

The objective of this research is to study the dynamics of conjugated organic materials utilizing femtosecond spectroscopy. Two kinds of organic materials, visual pigment rhodopsin and conjugated polymer(PPV), have been studied in this thesis They both involve structural rearrangements after photoexcitation in which the arrangement of carbon nuclei is distorted by the excited electronic cloud and their conformations are transformed to a high energy state. The primary visual process involves molecular structural isomerization. The absorbed photon energy is stored in the chemical energy of the conformationally changed molecular structures. In conjugated polymer (PPV), the molecular lattice structure is distorted after photoexcitation due to the strong electron-phonon interaction. The absorbed energy is stored in the gap state excitations which involve the fundamental transformation of the lattice structure into the form of various excitations, such as solitons, polarons and excitons. The changes of molecular structure in both materials are studied on the sub-picosecond time scale, by measuring the absorption spectrum changes. The oriented sample enables us to study its unique one-dimensional properties in terms of absorption and luminescence by excitation polarization, intensity and wavelength dependence studies. This thesis task is to use femtosecond transient spectroscopic

measurements to study the initial structural change of the rhodopsin molecule occuring in the primary process of vision, and the photoexcited primary state of excitations in oriented PPV films.

1.3) Organization of Thesis

This thesis is organized into nine chapters.

In chapter 2, the techniques of ultrafast laser spectroscopy are described. A brief review of the techniques used in ultrafast laser spectroscopy are given with details of femtosecond laser generation, amplification, pulse compression (dispersion compensation) and continuum generation and amplification. I also describe the ultrafast spectroscopic measurement methods which include pulse duration measurements, transient absorption and luminescence measurements. The data acquisition procedures are also provided.

In chapter 3, I review the basic background of the visual pigments in rhodopsin and bacteriorhodopsin, in terms of their structures, bleach sequences and the primary photochemistry process.

In chapter 4, a detailed description of the previous experimental results in the primary process of vision are given. I describe the Raman measurements which yields structural information of rhodopsin and its photoproducts, the results of transient absorption, luminescence and transient Raman measurements in the picosecond region, and the related models of the primary visual process.

In chapter 5, the research on the primary process of vision are presented. I report the results of transient absorption measurements with subpicosecond resolution. A conventional *cis-trans* isomerization model is used to explain our experimental results, and two intermediates formed prior to the formation of bathorhodopsin are discussed and compared with the recent result of femtosecond absorption measurements. Various models of the primary process of

vision are presented, compared and discussed.

In chapter 6, I review the background of conjugated polymers in terms of structures and basic excitations which include the concept of the "lattice dressed" soliton, polarons and excitons.

In chapter 7, previous research on the charged and neutral excitations in conjugated polymers in terms of their absorption, luminescence and Raman scattering are provided. The carrier dynamics in the degenerate and non-degenerate ground state polymer are discussed in relation to the understanding of carrier dynamics in PPV. The detailed previous experimental results in PPV are discussed.

In chapter 8, the experimental research on stretch oriented PPV films are provided. I report on the results of the time-resolved absorption and luminescence measurements in oriented PPV films. The experimental results of excitation polarization dependence and excitation wavelength dependence are used to explain the dynamics of the excitons, Raman gain and charged excitations in the subpicosecond time domain. Based on the experimental results, a formulated model is established to describe the relaxation kinetics in PPV and "intra- and inter-chain transition" and the decay mechanism for singlet exciton luminescence. In the last section, I describe the model for the relaxation dynamics of excitations in the picosecond region and discuss possible application utilizing the experimental results.

In chapter 9, I present my overall remarks of my work on organic and biological material utilizing ultrafast spectroscopy, and discuss possible future experiments.

CHAPTER 2 ULTRAFAST LASER SPECTROSCOPY

2.1) Introduction

Laser spectroscopic techniques have been used to study a broad range of phenomena for many years. The cw laser spectroscopy has made it possible to realize high-precision and ultrasensitive spectral measurements.[2.1] The advent of picosecond and femtosecond pulsed lasers has given impetus to extensive development of techniques with high timporal resolution. The indirect methods which attempt to measure dynamics in the frequency domain often will not substitute for direct measurements in the time domain. The elementary physical processes that precede the formation of long-lived intermediates species, such as vibrational energy exchange, rotational motion, structural rearrangement and electronic relaxation,[2.1-2.4] are too rapid to study with flash photolysis at microsecond time resolution. The newly developed femtosecond laser[2.5-2.7] opened up a further eight orders of magnitude in time resolution (from 1μs to about 10 fs) and brought all of these elementary processes within experimental reach. Femtosecond pulses have been amplified to gigawatt powers and frequency broadened to extend over the entire visible spectrum and beyond while retaining femtosecond pulse duration. Thus, ultrafast laser spectroscopy has offered exciting possibilities for accurate studies in both ultrashort temporal and broad spectral range on previously unresolved process in biology, chemistry and physics.

This chapter describes the experimental methods used in this thesis. The first section will describe the principles and methods to generate ultrashort laser pulses. The detailed description of a tunable wavelength femtosecond absorption spectrometer is provided, including a description of CPM laser oscillator, amplification system, pulse compressor, supercontinuum generation and

amplification system. This laser system schematically shown in figure 2.1 produces a tunable pump pulse wavelength from 500nm-850nm with a few microjoule energy and is capable of probing in the broad wavelength range from 400nm-1200nm. The second section of thism chapter is the ultrashort laser measurement techniques applicable to this thesis. The details of measuring transient absorption spectra using an OMA and dynamics using single shot normalization are provided.

2.2) Subpicosecond Pulse Generation

A. General Principle

Organic dyes provide a nearly ideal medium for generating ultrashort optical pulses. Dye lasers are widely used in research and applications because of their broad tunability and stability. The vibration- and rotation-broadened electronic energy levels in organic dyes result in gain over a wide range of frequencies. [2.1, 2.6-2.7] Typically an organic dye laser can be tuned over 10-30 nm. Since the gain spectrum is broad, a large range of frequency components can be coherently summed to produce short, tunable pulses. This coherent summation of frequency components is called mode-locking. Mode-locking[2.8-2.9] is the basic principle of generation of ultrashort pulses and its principle is demonstrated as follows. Consider N oscillating modes within the lasing profile locked together and with equal amplitudes. The total amplitude is:

$$E(t) = \sum_{-(N-1)/2}^{(N-1)/2} e^{i(\omega_0+n\omega)t} = e^{i\omega_0 t}\frac{\sin(N\omega\tau/2)}{\sin(\omega\tau/2)} \qquad (2.1)$$

where E is the optical field, ω_0 is the center frequency and ω is the separation of lasing modes $\omega=\pi c/L$, L is the laser cavity length. The laser intensity I(t) is proportional to $E(t)E^*(t)$. Thus

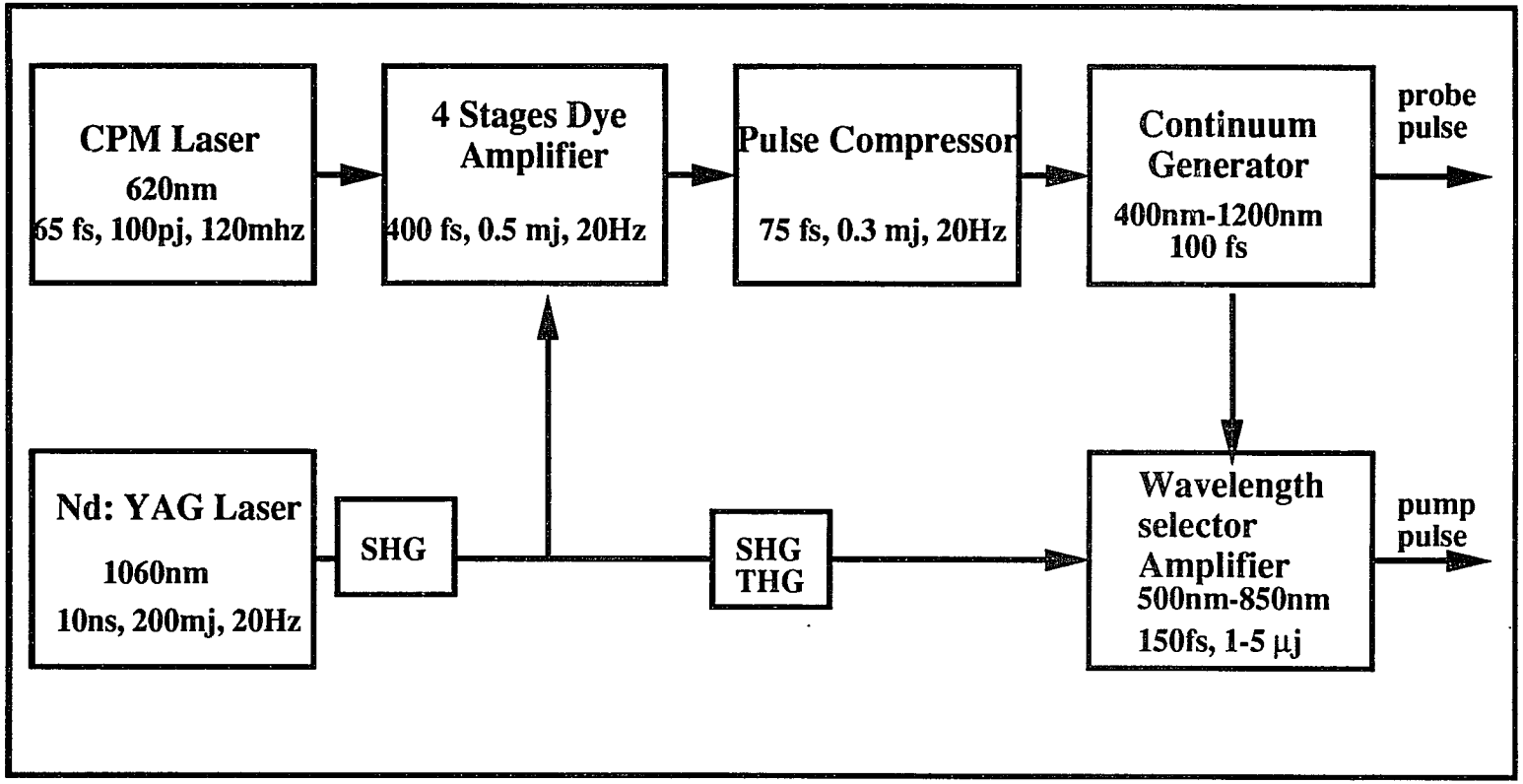

Fig.2.1 Block diagram for generation of a femtosecond tunable excitation wavelength (500nm-850nm) and continuum probe (400nm-1400nm) laser source based on a CPM laser for spectroscopic purpose.

$$I(t) = \frac{\sin^2(N\omega\tau/2)}{\sin^2(\omega\tau/2)} = N^2 \frac{\mathrm{sinc}^2(N\omega\tau/2)}{\mathrm{sinc}^2(\omega\tau/2)} \qquad (2.2)$$

The peak laser intensity is N^2 times the amplitude of a single mode, and laser width $t=2\pi/\omega N$. The number of oscillating modes can be determined from the width of the lasing spectrum $\Delta\omega$ as $N\sim\Delta\omega/\omega$. Using this relation, the pulse width is

$$\Delta t = 2\pi/\Delta\omega = 1/\Delta\nu \qquad (2.3)$$

Thus the minimum duration of mode-locked pulses depends inversely on the gain linewidth of the laser. By considering a Gaussian profile of mode amplitude, one can obtain the uncertainty relation

$$\Delta\nu\Delta\tau>=0.441 \qquad (2.4)$$

If the lasing linewidth is 10nm at 620nm, the pulse width $\Delta\tau$ is about 56.5 fs, which is called a transform limit pulse width.

Practically, mode locking is achieved by modulating the loss (or the gain) of the laser with a period equal to the cavity round trip time T. The passive mode-locking method is used in generating subpicosecond pulses of a CPM dye laser. In this thesis, passive mode locking is achieved by inserting a second dye (saturable absorber) in the cavity, the saturable absorber modulates the loss of light in the cavity and it acts in concert with the gain medium to produce a short pulse.

B. Colliding-pulse Mode Locking (CPM) Dye Laser

Colliding pulse mode locking is a form of passive mode locking technique demonstrated by Fork et al.[2.5-2.6] Figure 2.2 depicts the ring cavity configuration of CPM laser. The laser system is optically pumped by 2-3 watts of continuous power at wavelength of 514.5 nm from a commercial argon laser (Spectra-physics Model 171). The CPM laser oscillator consists of 7 mirrors, 2 jet streams and four prisms as shown in figure 2.2. Three mirrors (including the

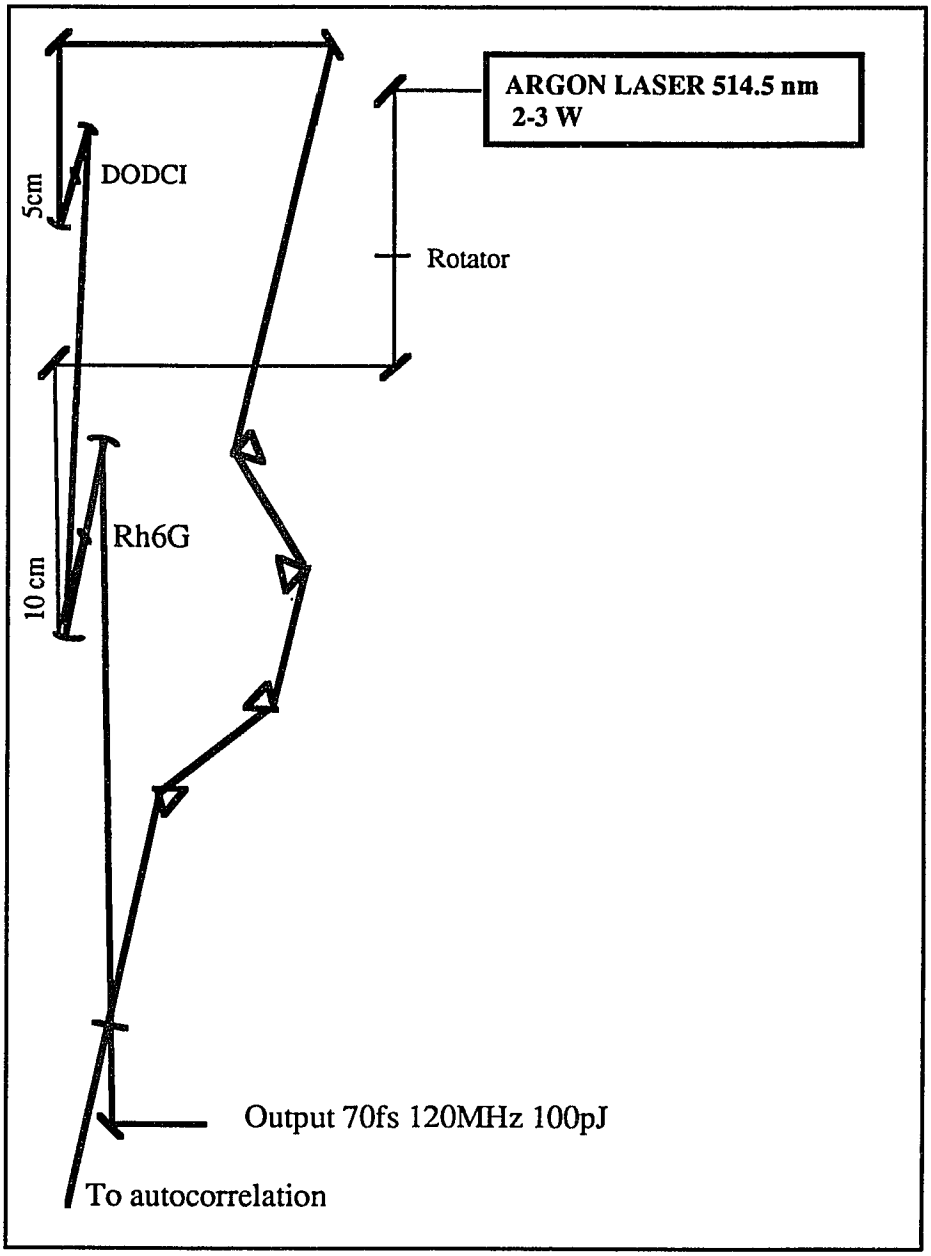

Fig.2.2 Schematic diagram of CPM laser cavity

output coupler) are flat and used to close the ring. The other four cavity mirrors, two 10 cm radius for the laser medium and two 5 cm for the saturable absorber, are used to focus the beam at the dye jet streams. The dye gain medium used in the CPM laser is rhodamine 6G at concentration of about 1.5×10^{-3} molar in a free-flowing thin stream of ethylene glycol produced by a 300μm nozzle. A second free-flowing saturable absorber dye (DODCI) flow through a 100μm nozzle positioned at a quarter of cavity length away. The DODCI is at concentration of 10^{-4} molar in an ethylene glycol solution. The laser mode is focused more tightly in the absorber stream than in the gain stream to enhance the non-linearity of the saturable absorber for better stability.

The novel feature of colliding pulse mode locking are the two counterpropagating pulses which are synchronized to precisely overlap in the saturable absorber.[2.5-2.6] The colliding-pulse ring laser is schematically shown in figure 2.3, where the absorber and gain media are separated by one quarter of cavity round trip distance. The two counterpropagating pulses in this ring laser always meet in the saturable absorber because the intracavity loss is sharply reduced for that condition. This sharp reduction in intracavity loss occurs because the interference of the two overlapping pulses creates a transient standing wave pattern in the saturable absorber and reduces the energy required to saturate the absorber.[2.5, 2.9-2.10] These two pulses saturate the absorber while only one saturates the gain at a given time, this effect increase the stability of mode-locked laser[2.5,2.8,2.10-2.11]. The quarter cavity length between the position of the gain and absorber media ensures that clockwise and counterclockwise circulating pulses see the same gain, since the continuously pumped gain dye has the same time to recover following each pulse. This has the effect of reducing the formation of additional pulses in the cavity. The ring cavity eliminates the need to precisely position the saturable absorber stream as required

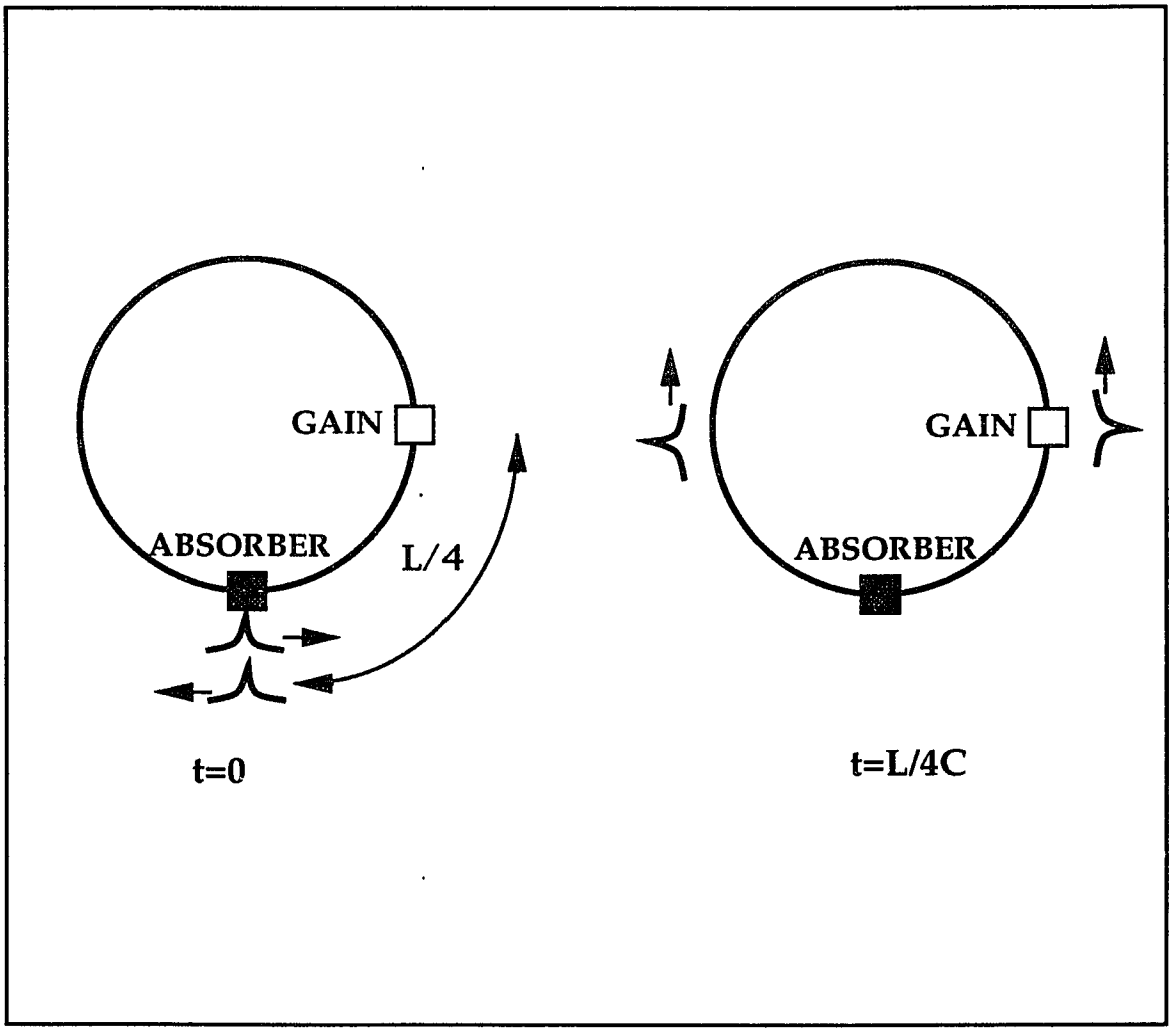

Fig.2.3 Schematic diagram of Colliding-pulse ring laser. The spacing between the gain and absorber is the quater of circumference of the cavity.

in a linear geometry.

The fundamental constraints of a CPM laser has been found to be the bandwidth of the gain and absorber media and the group velocity dispersion in the optical cavity.[2.5,2.6] Careful selection of 19 1/4-wave layer dielectric coated mirrors minimizes the intracavity group velocity dispersion which would broaden the pulsewidth. The group velocity dispersion caused by self-phase modulation(SPM)[2.14-2.15] in the absorber jet is compensated by inserting 4 Quartz prisms in the laser cavity. The negative dispersion provided by the prism set can be adjusted simply by moving a prism along a normal to the prism base. More details about prism compression are given in the following pulse compression section. With the compensation of the dispersion in the cavity by the prism set, the output pulsewidth is improved from 100fs to 56fs which is close to the transform limit of the 12nm laser bandwidth. Optical pulses generated by CPM laser have energies of 100 pJ at repetition rate of 120Mhz. The central wavelength is 624 nm and FWHM bandwidth is about 12 nm. A typical autocorrelation trace from CPM laser is measured by its SHG at 310nm and shown in figure 2.4. The FWHM of the autocorrelation signal is about 100fs which yields a pulse width of 65 fs assuming a $sech^2$ pulse shape.

C. Pulse Amplification

The energy of the CPM laser from the oscillator is insufficient for many spectroscopic applications. To obtain higher energies, optically pumped organic dyes have been used to amplify the femtosecond laser pulse to several gigawatts. [2.15] A Q-switched Nd-YAG laser (Quanta-Ray DCR-2) is synchronized and used to amplify the CPM laser pulse as depicted in figure 2.5. Ten ns pulses at the second harmonic wavelength (530 nm) from a Q-switched Nd-YAG laser with 20 Hz repetition rate are used to excite a four stage dye amplifier. The second

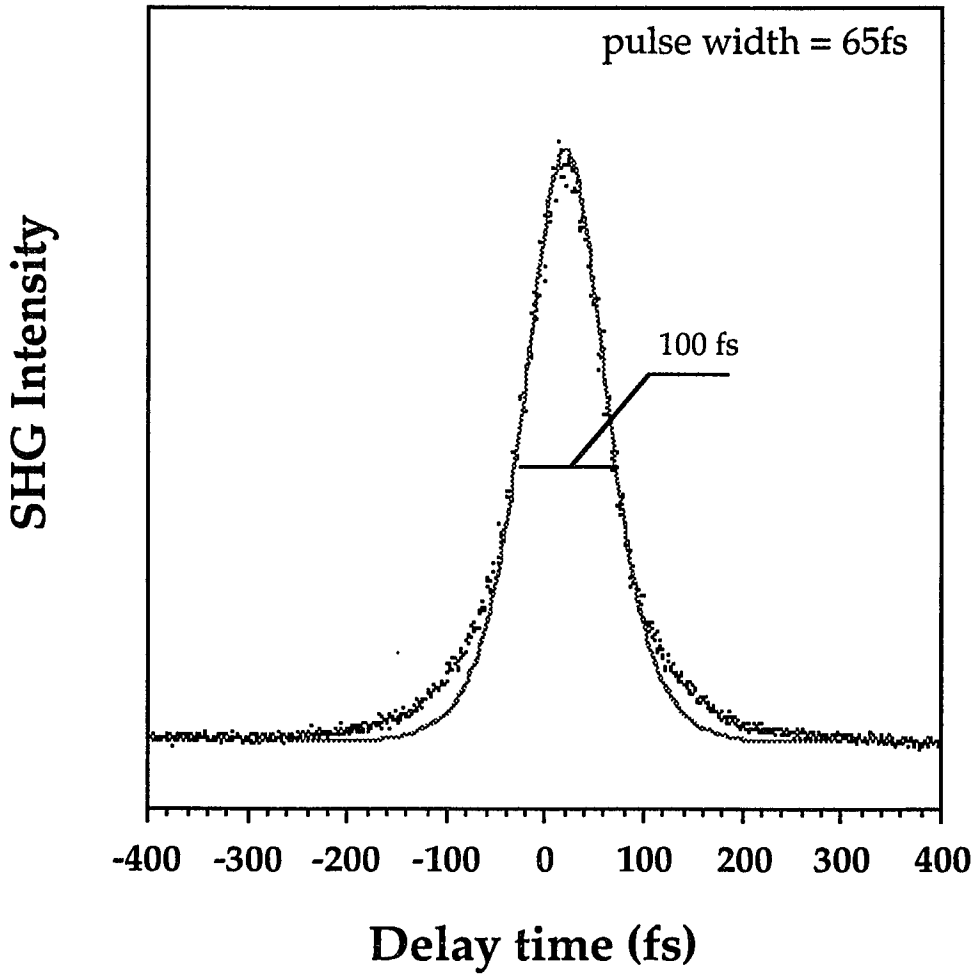

Fig. 2.4 Autocorrelation trace of CPM laser oscillator by measureing SHG signal. The pulse width is about 65 fs assuming $sech^2$ pulse profile.

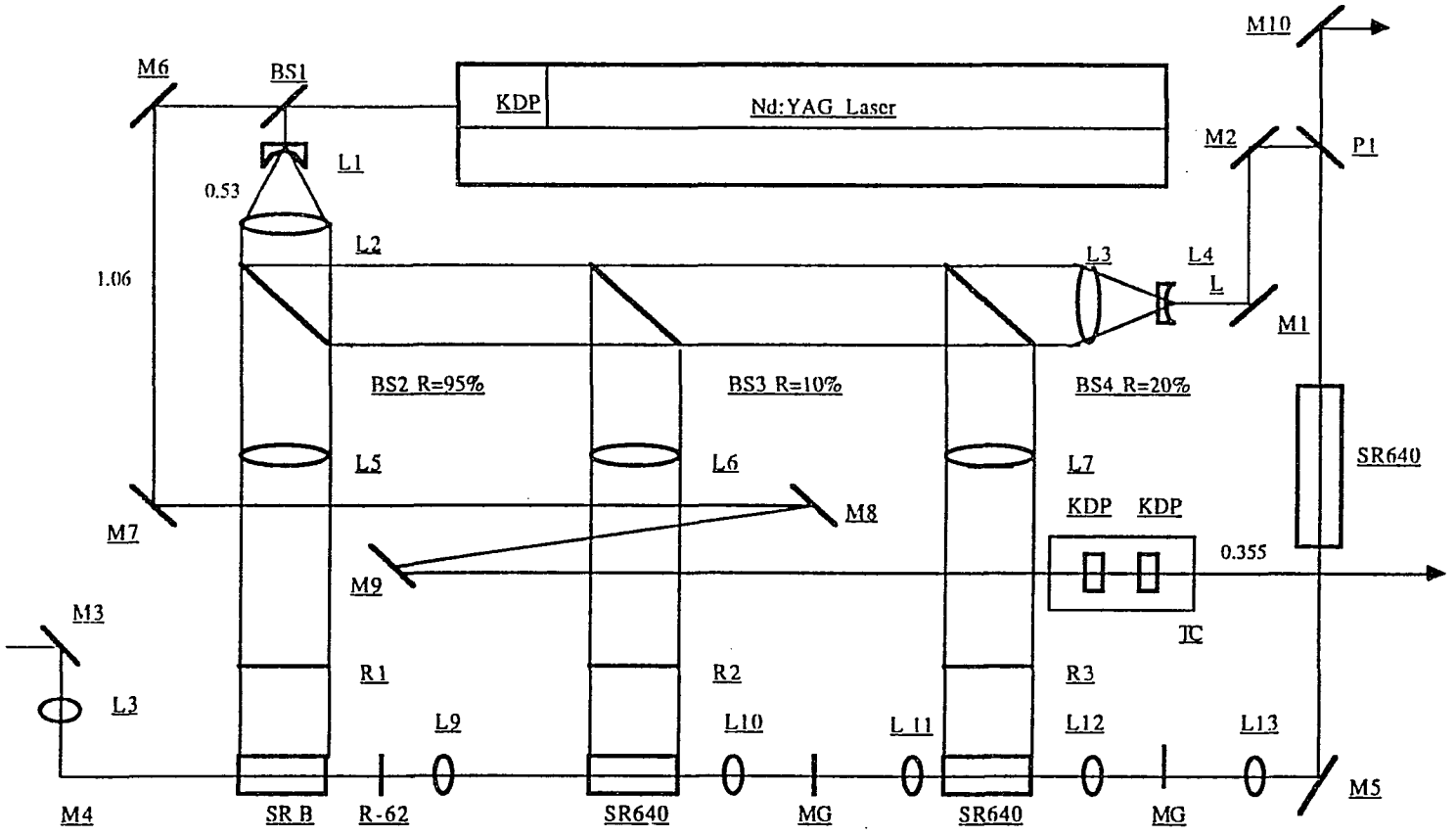

Fig.2.5 Schematic diagram of dye laser amplifier system. The frequency doubling of 20Hz Nd:YAG laser is used to pump this four stages dye amplifier.

harmonic energy of 250 mJ pulse is divided into four pump beams as fractions of 5%, 10%, 17% and 68% to pump the four stages. The first three stages were pumped transversely and the fourth was pumped longitudinally. The optical length for first three stage is 3.5 cm and 7.5 cm for fourth stage. Kiton red in water was used in the first stage, and Sulforhodamine 640 in water was used in the other stages. Kiton red has a low absorption at the seed pulse wavelength of 620nm which minimizes absorption loss at the high concentration used in the first stage. The peak net gain of sulforhodamine 640 closely approximates our amplified pulse wavelength 619 nm, also sulforhodamine 640 is used to limit distortion due to wavelength dependent gain.[2.6,2.15] A spatial filter (small pin hole) and two thin jets of saturable absorber (Malachite Green in ethylene glycol) were inserted between adjacent stages of the dye amplifier to suppress the amplified spontaneous emission and to control preferential amplification of the pulse leading edge[2.15]. The amplification gain of the four stages are 200, 150, 25 and 4, respectively, the total gain is about $3x10^6$. Thus, 100 pJ pulses from the CPM laser are amplified to about 0.3 mJ. The constraints on amplifying the dye laser to higher energy are rapid depletion of gain by amplified spontaneous emission and short spontaneous emission time of dyes (1ns).

One of the major concerns in amplifying femtosecond pulses is the pulse distortion. The temporal broadening by group velocity dispersion (GVD) in the dye solvent and amplifier optics is significant in femtosecond pulse. The time delay τ_d due to group velocity dispersion between two wavelength with difference $\Delta\lambda$ is

$$\tau_d = \frac{\lambda L}{c}\frac{d^2n}{d\lambda^2}\Delta\lambda \qquad (2.5)$$

Here L is the medium length, n is the index of refraction and λ is the optical wavelength. Short pulse width corresponds to broad bandwidth, thus group velocity dispersion is larger in short pulses. In our four stage amplifier, the pulse

from the CPM laser is broaden from 65 fs to 500 fs due to the group velocity dispersion in dye solution (30cm) and optical components. The temporal broadening by group velocity dispersion is mostly linear frequency sweep therefore can be compensated by optical elements with negative dispersion which is described in the next section. Nonlinear broadening, however, also occurs in the dye solvents and can combine with group velocity dispersion to yield irreversible temporal broadening. For example, nonlinear frequency generation, wavelength dependent gain, saturable absorption and saturable gain can not be easily avoided. Such nonlinear broadening is minimized by selecting pump energy and appropriate dyes in each stages.[2.15]

The synchronization of Nd:YAG laser and CPM laser is accomplished by a gated low jitter pulse generator which is schematically shown in figure 2.6. Part of the CPM laser pulse train is detected by a fast photodiode and amplified by a wide band amplifier. The output from the amplifier is used to trigger a synchronous series of clock pulses. These are used with a prepulse from the Q-switch of the Nd:YAG laser to generate a synchronized trigger of the Nd:YAG's Pocket's cell. A variable delay line (0.25ns resolution) is used to delay the firing time of the Nd:YAG laser to optimize amplification by overlapping the Nd:YAG laser and CPM laser pulses.

D. Pulse Compression

The pulse broadening through four stage amplification results in phase (or frequency) modulation. The dominant pulse broadening is mostly due to GVD which is a positive monotonic frequency sweep (linear chirp). The lower frequencies lead higher frequencies in the pulse duration in a normal dispersion medium such as dye solution and optical glass. The pulse phase shift depends on the frequency and can be developed in a power series of $(\omega-\omega_0)$[2.8,2.16-2.17].

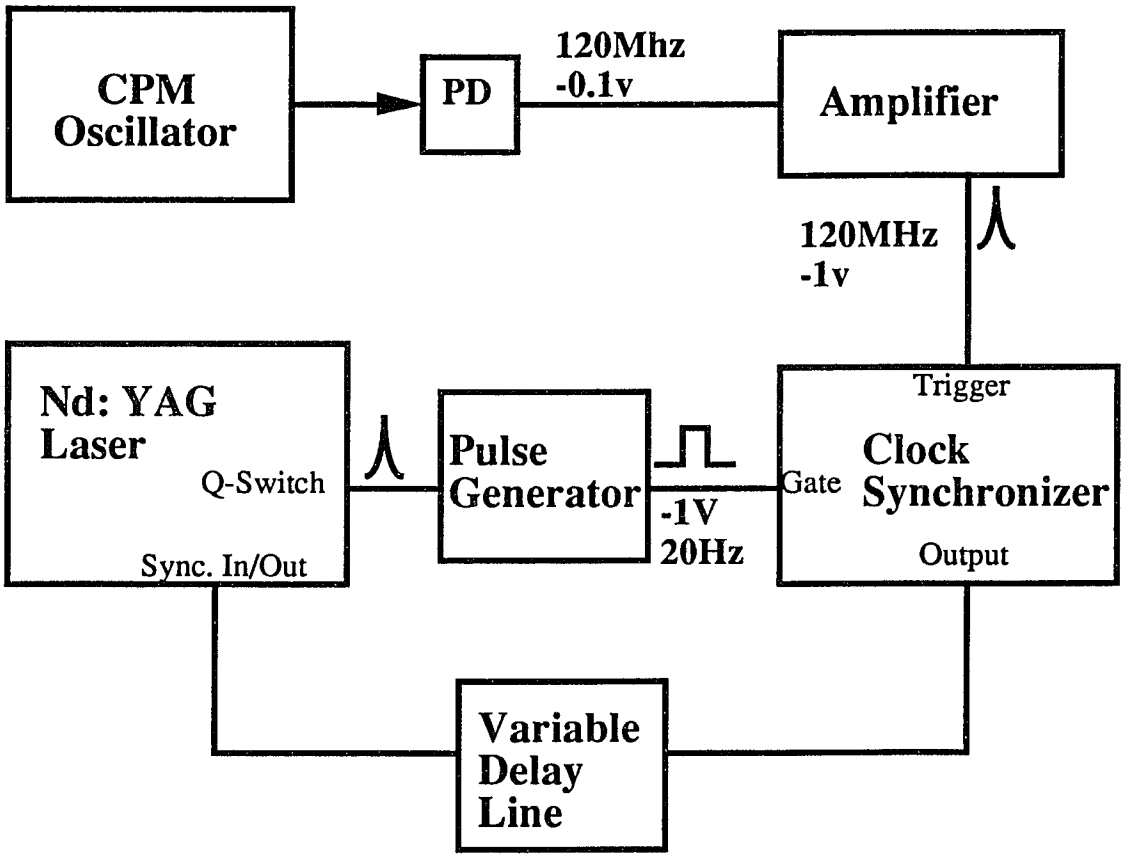

Fig.2.6 Synchronization diagram for CPM laser and Nd:YAG laser

Using only the first three terms we write

$$\phi(\omega) = \phi(\omega_0) + (\omega - \omega_0)\phi'(\omega_0) + \frac{1}{2}(\omega - \omega_0)^2 \phi''(\omega_0) \qquad (2.6)$$

where $\phi'(\omega_0)= (d\phi/d\omega)_L$, $\phi''(\omega_0)= (d^2\phi/d\omega^2)_L$, and L is the length of the medium. Considering Gaussian beam propagation, the group velocity dispersion ϕ'' increases the output pulse width τ_{out} by a factor[2.8,2.16]

$$\tau_{out} = \tau_0 * [1 + (4\ln 2\ \phi''/\tau_0^2)^2]^{1/2} \qquad (2.7)$$

where τ_0 is the chirp free pulsewidth or the transform limited pulsewidth. We recall the expression (2.5) for the GVD introduced by a length l of a transparent medium:

$$\phi_M'' = (\lambda_0^3/2\pi c^2) n_0'' L \qquad (2.8)$$

where λ_0 is the central wavelength and $n_0''= (d^2n/d\lambda^2)_{\lambda_0}$. Thus, we list the GVD ϕ_M'' for the four amplifier stage as follows

Medium	GVD Formula	length l(mm)	$\phi''_M(fs^2)$
lens (BK7)	I"=70.14l	56.6 ± 4.0	3944 ± 280
dye solution	I"=54.92l	180 ± 5	9885 ± 275
glass (S_iO_2)	I"=51.19l	8 ± 2	820 ± 154

Tab.2.1 The amount of GVD ϕ''_M introduced by the four amplifier stage.

The total GVD ϕ_M'' is about 1.5×10^4 fs^2. Using eqn.2.7 and the CPM laser pulse width τ_0=70 fs, we calculated τ_{out}=580 fs which agrees with the amplified pulse width, therefore, the temporal broadening is mostly introduced by GVD. It is interesting to note that when the GVD is large ($\phi''/\tau_0^2>1$) the output pulsewidth is inversely proportional to the input pulsewidth, i.e. when $\phi''/\tau_0^2>1$, the eqn.2.7 can be simplified as

$$\tau_{out} = \tau_0 * [1 + (4\ln 2\ \phi''/\tau_0^2)^2]^{1/2} = \tau_0 * (4\ln 2\ \phi''/\tau_0^2) = 4\ln 2\ \phi''/\tau_0 \qquad (2.9)$$

This is because the bandwidth inversely changes as the transform limit pulse

width. Therefore the GVD is significantly affected in the short pulse generation, amplification and propagation.

The linear chirp, ϕ", can be compensated by negative group-velocity dispersion devices such as a prism and grating set[2.16-2.19]. A pulse compensator using four prisms of high-index denseflint glass SF10 is depicted in figure 2.7, where the higher frequency travel through less pathlength than the lower frequencies. Therefore, this prism set provides negative dispersion which is proportional to the distance between the apex of the two prism, S, as in figure 2.7. Salin at al [2.16] has calculated the dispersion by this prism set as follow:

$$\phi_P'' = \frac{4\lambda^3}{\pi c^2}\{-Sn^2 + \frac{L}{\sqrt{3}}[\frac{nn''}{1+n^2} + n^2(1-\frac{1}{n^2(1+n^2)})]\} \qquad (2.10)$$

where n is the index of refraction of SF10 glass, and l is the total pathlength in the four prisms. The dispersion of the prism set contains two terms. The first one is proportional to S provides negative GVD, and the second one depends on the amount of pathlength in the prism glass (L) and contributes positive dispersion. Note, the dispersion of a high index prism is five times that of regular glass. By adjusting the dispersion of the prism set ϕ_P" , the positive dispersion ϕ_M" introduced by the amplifier can be compensated, $\phi''_{total}=\phi_P''+\phi_M'' \Rightarrow 0$. The pulse width after compensation vs the distance of two prism S is plotted in figure 2.8(a) with different amount of dispersion ϕ_M" and τ_0 is a constant, and in Figure 2.8(b) with different τ_0 and dispersion ϕ_M" is a constant. These calculations show that the output pulse width is sensitive to the distance (S) of the prisms when the transform limited pulse width gets short. In the experiment, we found that the output pulse width is sensitive to the incident angle to the prism. Brewster angle prisms (about 60^o in 620nm for SF10 glass) were used to compress the amplified pulses from 450fs to 75 fs which is close to the transform limit of the 10 nm bandwidth of the amplified pulses but lose about 40% of their intensity. The

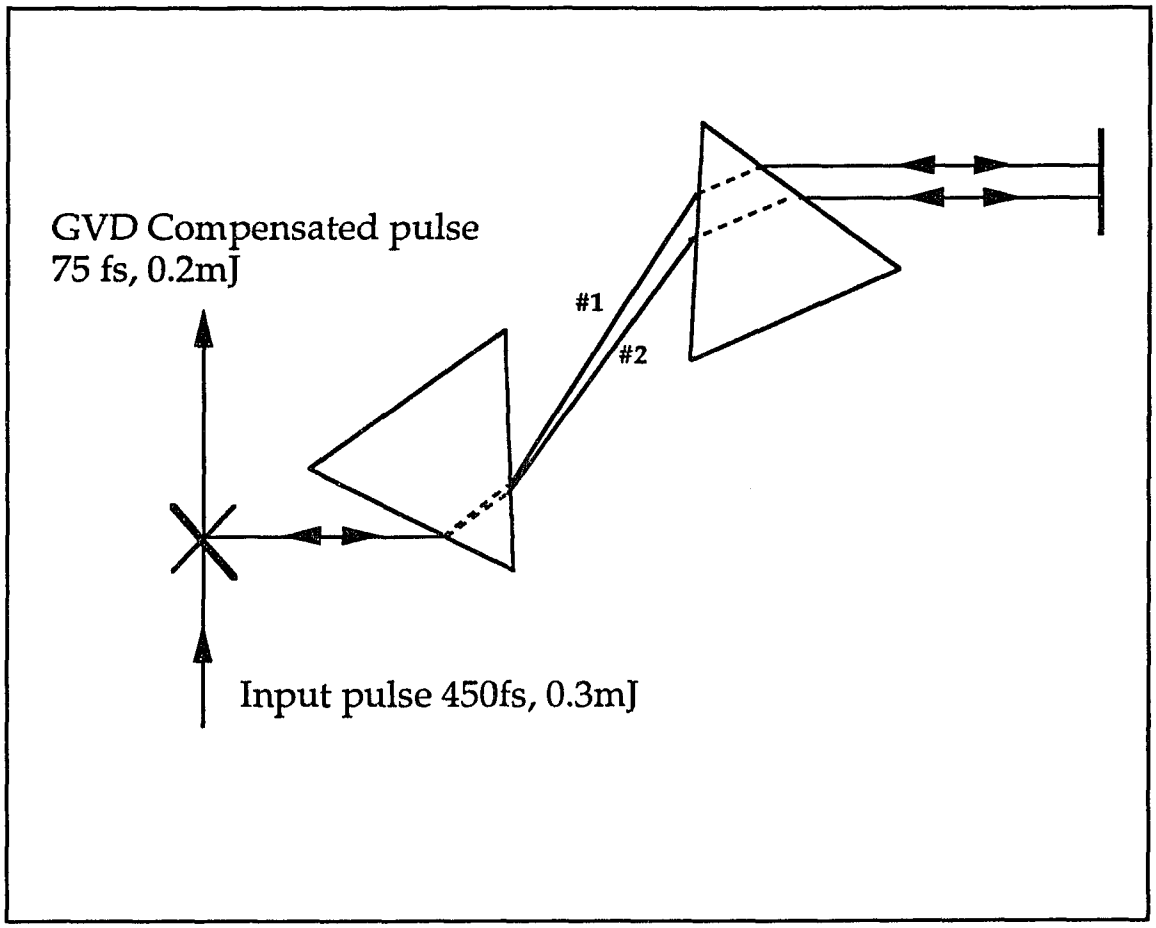

Fig. 2.7 Pulse compression (compensation) use prism set as a negative GVD device in which the redder part light trave longer pathlength (#1) and bluer part in #2. Double path through two prisms is used instead of four prisms.

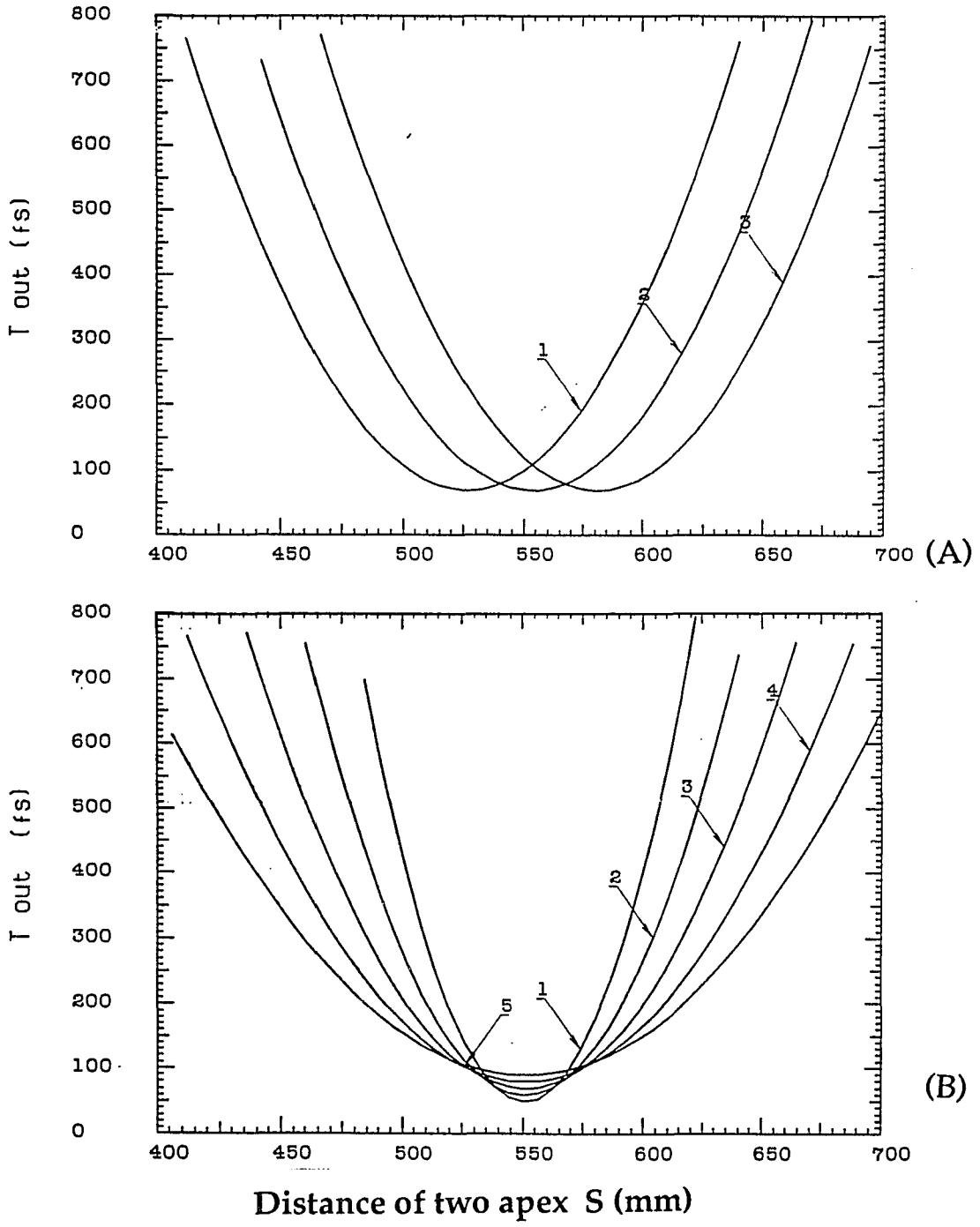

Fig. 2.8 The calculation of the output pulse width with distance between the apex of two prisms in pulse compression (GVD compensation) using prism set. In (a): the transform limit pulse width τ_0=70 fs, and the amount of dispersion introduced by amplifier is varied (1) 15810 (2) 17140 (3) 18470 fs^2. In (b): the amount of dispersion is 17140 fs^2 and τ_0 is (1) 50 (2) 60 (3) 70 (3) 80 (5)90 fs.

autocorrelation of the amplified CPM pulses is measured by their SHG at 310 nm as plotted in figure 2.9. To compensate the dispersion to the transform limited pulse width, higher order dispersion must be considered. The combination of a set of prisms and gratings has demonstrated to compensate the higher order GVD [2.18].

E. Supercontinuum generation and amplification

The compressed amplified femtosecond pulses provides an intense (0.1-0.2 mJ) and short (<100fs) laser pulse. However, the wavelength in the CPM laser is limited around 620 nm because the gain bandwidth of the dye medium. Spectroscopic measurements requires a spectrally broad short pulse to measure the transient spectrum. Alfano and Shapiro [2.13] have discovered that a white-light continuum is generated by focusing a short pulse into a transparent medium and maintains the short pulse width. This white-light generation due to self phase modulation (SPM) is explained as follows. An intense short pulse distorts the electronic distribution in a medium and hence induce a refractive index change. The phase of the light's electrical field in the medium[2.14] can be written as:

$$\phi = \omega t + (n_0 + n_2 E^2(t)) \frac{z\omega}{c} \qquad (2.11)$$

This intensity dependence modulates the instantaneous phase of the pulse and thus the frequency distribution is altered. The phase modulation leads to a frequency modulation

$$\Delta\omega = -\frac{d\phi}{dt} = -\frac{n_2 z\omega}{c} \frac{dE^2(t)}{dt} \qquad (2.12)$$

Therefore, both redder and bluer frequencies than the input frequency are generated. The redder components (lower in frequency, $\Delta\omega<0$) arise from the leading edge of the incident pulse ($\frac{dE^2(t)}{dt}>0$) and bluer components from the

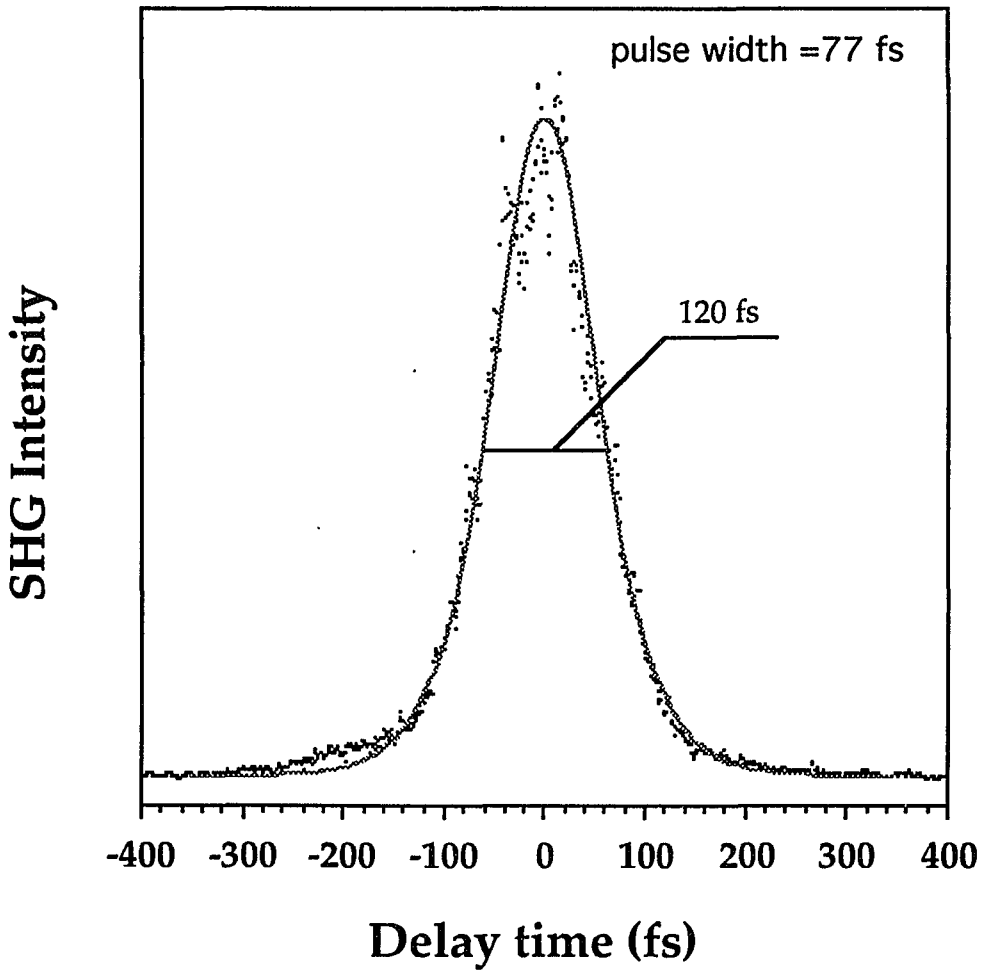

Fig. 2.9 Autocorrelation trace of amplified CPM laser (dispersion compensated) by measuring SHG signal. The pulse width is about 77 fs assuming sech pulse profile. The solid line is the $\mathrm{sech}^2(t/\tau)$ fitting where τ=70 fs

trailing edge. Frequency shifts of order, $\Delta\omega_{max}=\frac{\omega n_2 Iz}{c\tau}$, are obtainable, and $\Delta\omega_{max}$ is inversely proportional to the laser pulse width, τ. In this thesis, the amplified 100fs pulse is focused by a 6 cm focal lens into a 1 mm ethylene glycol jet stream or a 1cm water cell to generate a white supercontinuum (400nm-1200nm) for different measurement purposes. The 1 cm cell can generate intense detectable broad spectral bandwidth which can extent in wavelength to 1.4 μm since the broad bandwidth of the continuum is proportional to the medium length z within the confocal region. The conversion efficiency of the continuum is very high, approximately, a 80 nJ pulse at 500nm with 10nm band width is generated by about a 100μJ pulse at 620 nm. The white continuum light is collected by a 4 cm focal lens and collimated into a 6 mm spot size beam. The white-light continuum pulse is also highly chirped since the SPM and GVD brings the redder components to the leading edge of the pulse. The group velocity dispersion is very large due to the broad wavelength bandwidth, approximately 0.3 ps dispersion results from traveling through 1cm glass for 100nm wavelength difference. The dispersion of our continuum light is measured using the cross-correlation (frequency mixing) method (see experimental method section). The sum frequency of the excitation wavelength (e.g. 500nm) with the white continuum light in a 100 μm KDP is measured in the uv, The uv signal is selected by a spectrometer and detected by a uv sensitive photomultilier. The continuum frequency ω_C can be obtained by

$$\omega_C = \omega_E + \omega_{UV} \qquad (2.13)$$

where ω_E is the frequency of excitation pulse and ω_{UV} is the measured sum frequency uv pulse. Figure 2.10 shows the zero time of the cross-correlation signal at different wavelength which is the same as the dispersion of the continuum light produced from a 1mm jet stream. Because of the phase matching

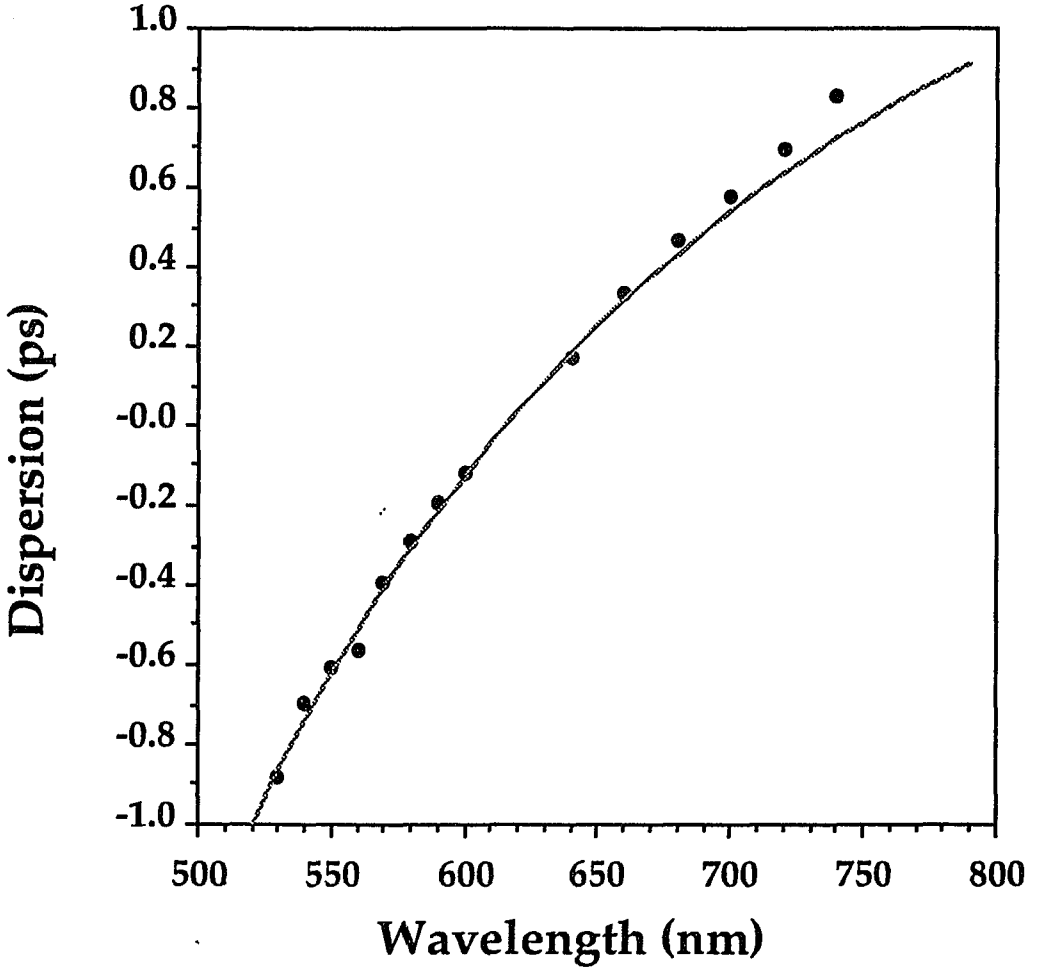

Fig.2.10 The dispersion curve of continuum light generated by a 1mm ethylene glycol and measured by the zero time of cross-correlation signal, see text. The solid fitting is the calculation of GVD in 2.4 cm BK7 galss. (The index of refraction data is taken from Schott Glass)

in the KDP (The orientation of KDP can not be tuned in this dispersion time measurement), we can measure the continuum wavelength from 500-800nm at one fixed KDP angle. The dispersion data depicted in figure 2.10 is fitted with GVD in glass, it shows the GVD is the dominating channel in the dispersion of the continuum light. The correction of the continuum dispersion is important for obtaining correct dynamics for less than 0.2 ps. A prism set can be used to compensate for the dispersion and make a "chirp free" white light continuum within a limited wavelength range[2.20].

In the experiments on rhodopsin and PPV, it was also necessary to generate a pump pulse above their absorption edges (~2.4 eV). To do this the white-light continuum is passed through a 10nm interference filter to obtain the specific wavelength experimentally required, and amplified using optical pumping of dyes as described in the previous section. A 1-cm pathlength dye cell is pumped transversely by the 10 ns third harmonic of a Nd-YAG laser at 353nm with about 10 mJ energy to amplify the selected continuum light. The pulses at 500nm are amplified to a few microjoule in a 1-cm cell flowing Coumarin 500 dye at a concentration of $5x10^{-4}$ molar in a Methanol solution. The dye cell is pumped by the third harmonic from the Nd:YAG laser at 353nm and about 10 mJ in energy. The gain in this one stage amplifier is about 200. Other dyes such as LDS have been used to amplify 700, 750, 800nm to the same order of energy as 500nm. It is worth noting that different wavelengths can be amplified using the same dye within its 30-60nm emission band width. We have amplified 500, 510, 520, 530 and 540nm to a few microjoles per pulse using Coumarin 500 dye and simply changing a narrow band filter. This tunable excitation wavelength (over 60 nm) is particularly useful for near band edge photoexcitation wavelength dependence studies.

2.3) Ultrafast Measurement Methods

There are various ultrafast measurement method for transient measurements. In this section, the ultrafast techniques within the scope of this thesis are described.

A. Autocorrelation and Cross-correlation Measurements

Autocorrelation and cross-correlation[2.21,2.22] are the standard techniques to measure ultrashort laser pulse duration. These are basically interferometric arrangements as depicted in figure 2.11. In autocorrelation, two pulses (620nm) split from one pulse are focused by a 5 cm focal lens into a nonlinear crystal, a 100μ KDP, to generate second harmonic detected by a uv sensitive photomultiplier. Since the uv (310nm) signal in the phase matched direction for absorbing a photon in each beam can only be detected during temporal overlap, the second harmonic signal obtained by varying the delay of one pulse is the pulse autocorrelation. By deconvolution, one can obtain an approximate pulse duration. Assuming a squared hyperbolic secant $sech^2$ pulse profile, the pulse width is the autocorrelation trace width divided by 1.55. If the two pulses have different wavelength, the sum frequency is generated in the nonlinear crystal instead of the second harmonic. The uv signal measured at the sum frequency is the two pulse cross-correlation. As mentioned above, the pulse duration of the white-light continuum is measured using sum frequency with one fixed wavelength. A spectrometer is placed before the uv sensitive photomultiplier to detect the light at the sum frequency from the KDP crystal. By delaying the fixed frequency pulse and changing the spectrometer wavelength, the cross-correlation of the fixed frequency with the whole continuum wavelength is obtained. With the KDP crystal phase matching angle fixed, the

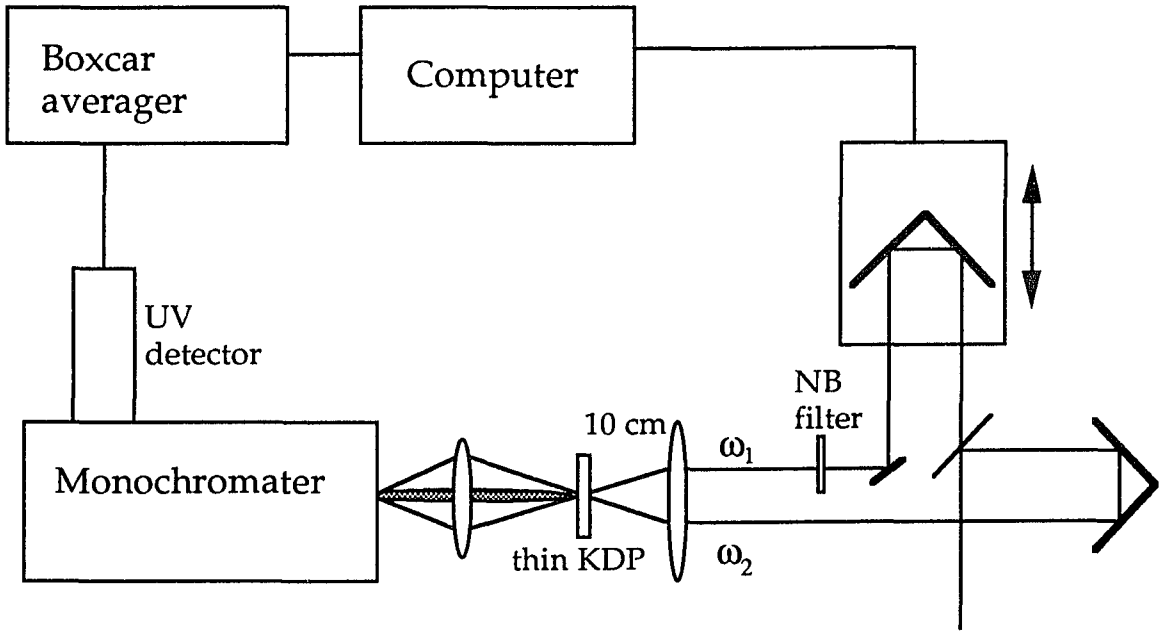

Fig.2.11 Pulse duration measurement use correlation method. If $\omega_1=\omega_2$, the SHG obtained from KDP is called autocorrelation and if $\omega_1 \neq \omega_2$ the sum frequcy $\omega_s = \omega_1+\omega_2$ is the cross-correlation.

zero time (relative dispersion) of the continuum light is measured in the wavelength range from 500nm to 800nm. The dispersion of the whole continuum light can be measured by several such wavelength range.

B. Pump-probe Measurements (Time resolved absorption)

The pump-probe technique is a basic method to do transient absorption spectroscopy. The sample is excited by an intense pulse and subsequently probed by a weak pulse as the material relaxes to its original state or moves through some photochemical reaction. The absorption change measured by a weak probe pulse at intensity $I_b(\lambda,t)$ is given by:

$$\Delta\alpha(\lambda,t) = \int_{-\infty}^{\infty} I_b(\lambda,t')\Delta\alpha'(\lambda,t-t')dt' = I_b(\lambda,t)\otimes\Delta\alpha'(\lambda,t) \qquad (2.14)$$

where $\Delta\alpha'(\lambda,t)$ is the impulse response of the molecular absorption change. The pump-probe setup is depicted in figure 2.12, where the beam at 500nm is used as a pump pulse and the continuum between 400nm-1200nm as probe. The probe and reference pulses were taken from the continuum pulses about 4% each via a small angled wedge. The remaining of the continuum pulses was pas through a 500nm nerrow band filter and further amplified to 1 μJ in a 1-cm cell of flowing coumarin-500 dye in methanol. The pump and probe pulses were focused by a 8 or 15 cm achromatic lens into the sample. The polarization of either pump and probe pulses could be rotated by a half wavelength plate. Since the pulses are linearly polarized, a configuration of rotator and polarizer can also be used in intensity dependence measurements by rotating the half wave-plate with a fixed polarizer. By changing the narrow band filter, pump pulses between 480nm and 540nm could be generated to tune the photoexcitation wavelength and keep the pulse energy at about 1 μJ.

The time delay between the pump and the probe pulses was accomplished

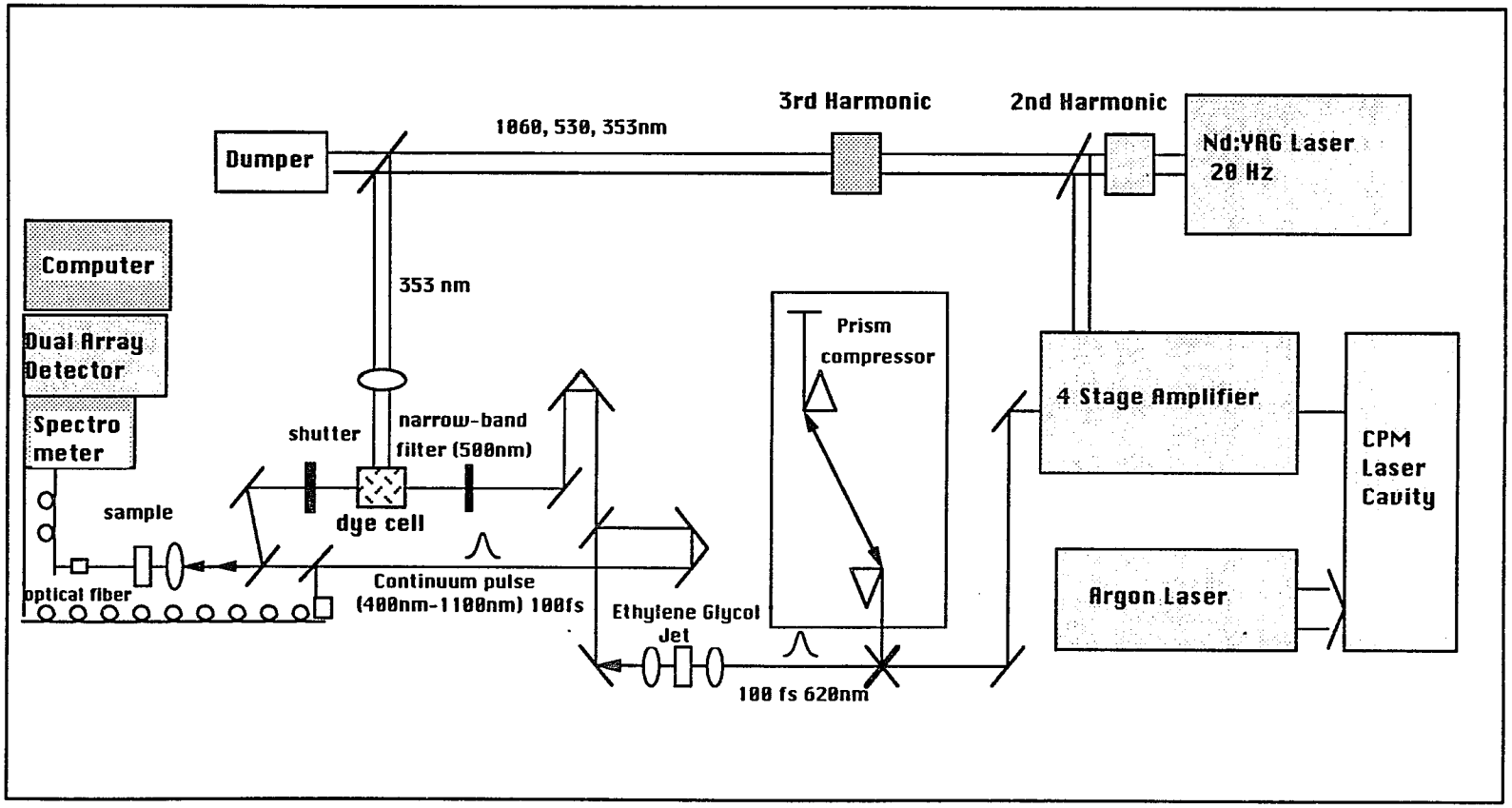

Fig.2.12 A pump-probe transient absorption setup based on a CPM laser system. The excitation wavelength can tune from 500nm to 850nm with 1-4 μJ energy and white light probe. The temporal resolution is about 250fs-300fs.

by varying the pathlength of the pump pulse with a translation stage that was controlled by computer as depicted in figure 2.13. The kinetics of the absorption changes can be followed by moving the delay stage across the time domain of interest. The white light probe and reference pulses were focused into two optical fiber bundles whose output were imaged onto separate diode arrays at the output of the spectrograph (SPEX or Jarrell-Ash). The transmitted spectra $I_t(\lambda,t)$ and reference spectra $I_r(\lambda,t)$ at each delay point t were averaged for about 400 laser shots. The normalized transmission $T(\lambda,t)$ is the ratio $I_t(\lambda,t)/I_r(\lambda,t)$. The transmission change $\Delta T/T$ +1 is the ratio of $T(\lambda,t)$ to the transmission $T(\lambda)$ when the pump beam is blocked. The background transmission $T(\lambda)$ was measured at each delay time and transmission changes of the sample with noise levels less than 0.5% could be measured. The data acquisition procedure is provided in figure 2.13. The change in the optical density is obtained as:

$$\Delta OD(\lambda,t) = - \log [T(\lambda,t)/T(\lambda)] \qquad (2.15)$$

The time resolution of the transient absorption technique is limited only by the duration of the laser pulse (=< 0.2ps).

For wavelengths between 800nm-1200nm which are out of the detection range of the diode array detector, a similar acquisition procedure were performed. Instead of fiber and diode array detector, a photomultiplier and monochromater were used to detect transmission changes a single wavelength at a time. The transmitted and reference signals were both sent to a boxcar integrator at the same time and a computer monitored the quotient to reduce the laser pulse amplitude fluctuation by single pulse normalization at 20 Hz. The laser fluctuation is reduced by setting a window on the reference signal. Only pulses with signal within 20% of the mean values of the reference intensity were used and a signal to noise ratio of unity obtained for 0.5% effects. The error of the experimental data is obtained by calculating the standard error of $\Delta T/T$ at a delay

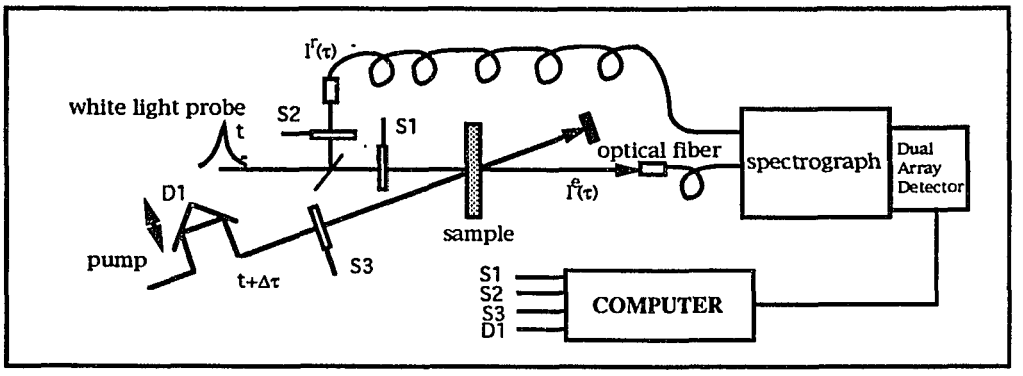

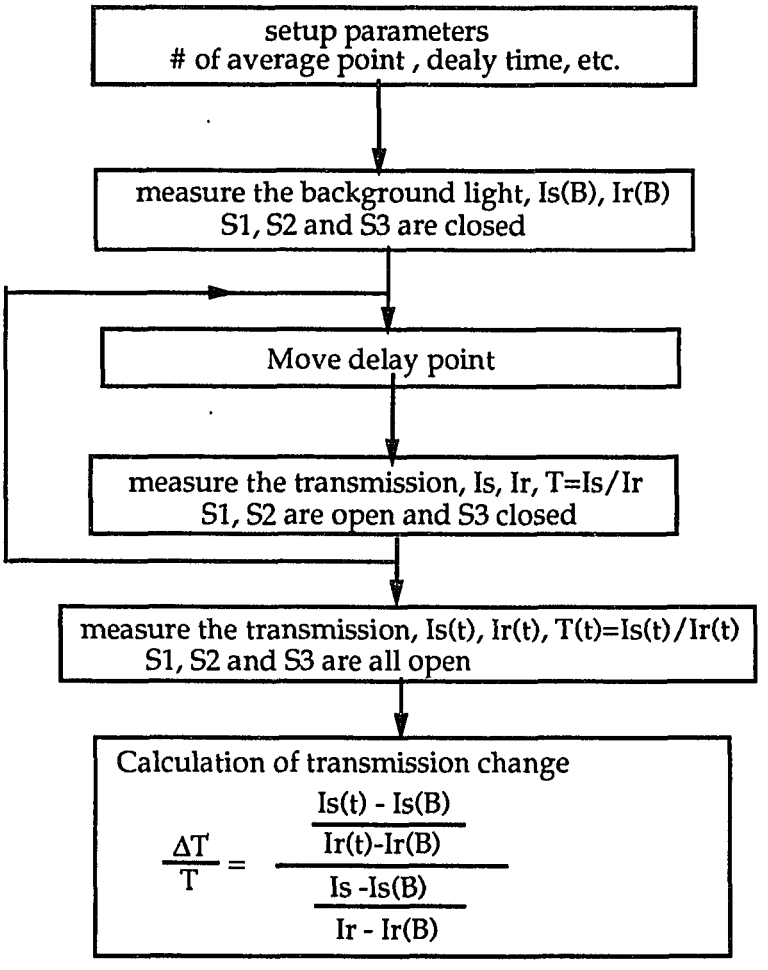

Fig. 2.13 shematic diagram of setup for transient absorption measurement using an OMA and the procedure of acquisition

point.

The time resolution of the apparatus was determined independently from the cross correlation trace from a thin KDP nonlinear crystal. The cross correlation trace is about 200-250 fs in FWHM in all the wavelength range we probed. The probe pulse is highly chirped due to the self-phase modulation, the zero time for each probe wavelength were also determined by cross-correlation (Fig.2.10) and corrected the zero delay time for different wavelength by the computer.

The pump-probe measurement were also performed at high repetition rate (540 Hz) with asynchronously pumped dye laser system with a similar configuration shown in figure 2.14. The 540Hz high repetition rate can take advantage of a lock-in amplifier to directly measure the transmission change (ΔT) of the probe beam upon chopping the excitation beam. A boxcar is used at the same time to measure the transmission (T) of the probe. Therefore, the transmission change ΔT and the transmission T can be obtained at the same time. This laser system can measure the $\Delta T/T$ to 0.1%.

C. Time Resolved Luminescence Measurement (Streak Camera)

The ultrafast streak camera is one of the most versatile instruments used today in picosecond luminescence spectroscopy[2.1,2.21-23]. It can measure pulse temporal profiles directly with excellent time resolution (1-10ps) on a single shot and it is straightforward to integrate into remarkably simple experimental configurations. In the streak camera tube, a light pulse is incident on a slit (typically 50 μm) and produces an image of the slit on the photocathode of the streak image tube. Photoelectrons leave the photocathode and are rapidly accelerated towards the phosphor. A voltage ramp is applied across the deflection plates causing the leading electrons in the burst to strike the phosphor

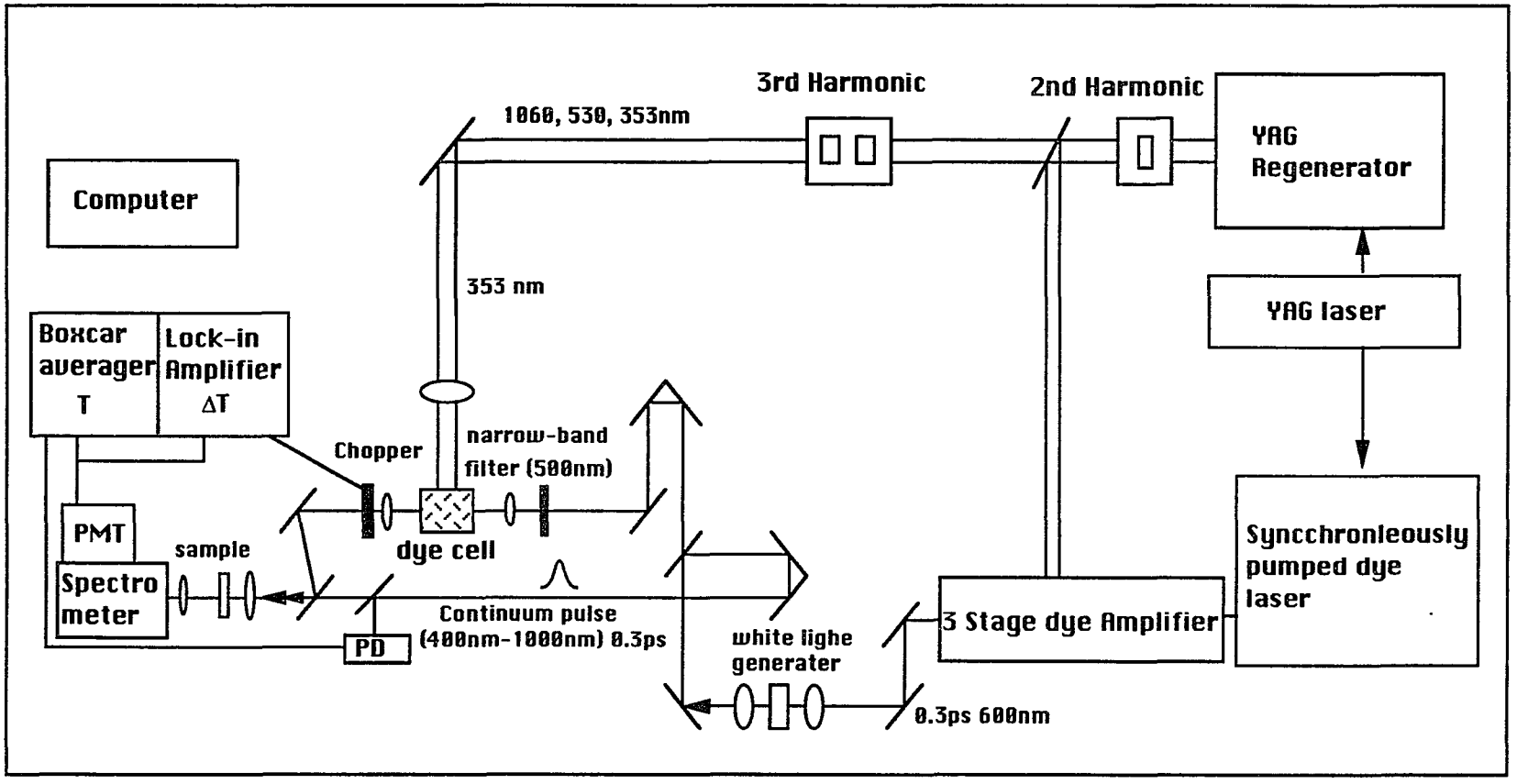

Fig.2.14 A pump-probe transient absorption setup based on a synchroneously pumped dye laser system at 540 Hz repetition rate. The boxcar averager is used to measure the transmission (T) while a lock-in amplifier to measure the differential transmission upon th epump (ΔT).

at a different position from the trailing electrons. By measuring the image shape on the phosphor and calibration of the voltage ramp rate ("streak speed"), the pulse shape and duration are determined. In practice, because of space charge effects in the image tube, an image intensifier is required to enhance the phosphor image before detection. The streak image is detected using a video system, such as an optical multichannel analyzer, to record and digitize the streak image. A streak camera can be coupled with a spectrograph and a two-dimensional array in order to provide both the temporal and spatial characteristics of the fluorescence.

Figure 2.15 shows the configuration of the streak camera used in this thesis, which can measure the temporal profiles of fluorescence at two polarizations simultaneously. The excitation pulses at 500nm from the amplified CPM laser at 20Hz are split by an angled wedge. 4% of each pulses is used as a pre-pulse and about 90% of each pulse is focused by a 10cm focal lens into the sample. The luminescence is collected and collimated by a 15 cm focal lens. The collimated luminescence and pre-pulse refracted by a 1-2μ thin glass are sent to a Wollaston crystal and split into two orthogonally polarized beams. Each of the orthogonally polarized beam is focused into two separate spot on the entrance slit of a synchroscan streak camera. The streak image of these two orthogonally polarized luminescence are detected by two window of a OMA detector. The streak camera is triggered by a signal derived from the CPM laser pulses at a repetition rate of 120 MHz. The streak image averages about 10-20 shots on the detector. The wavelength of the luminescence is selected by a narrow band interference filter and the excitation polarization dependence can be measured by rotating a half-wave plate.

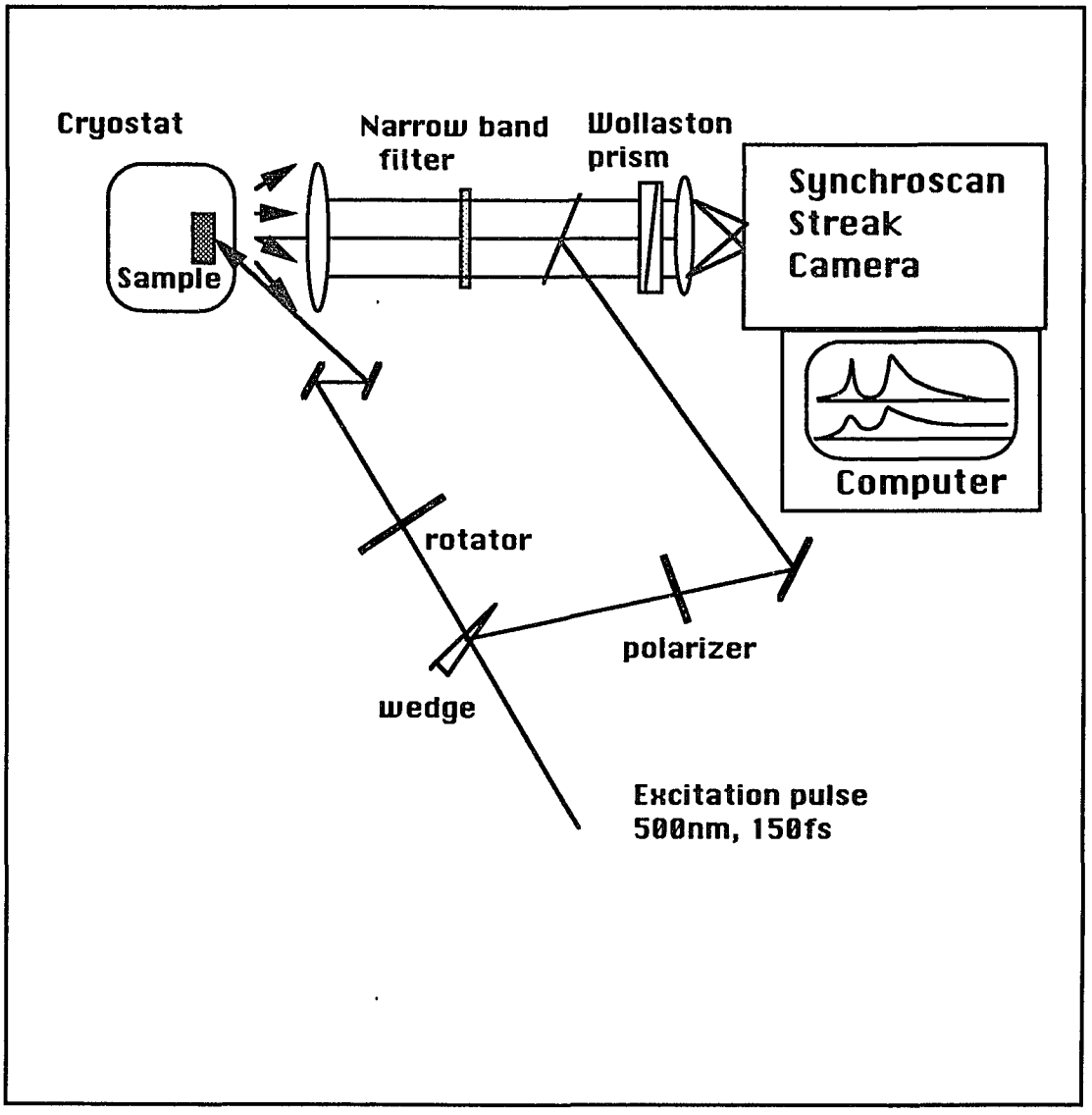

Fig.2.15 Time resolved luminescence measurement using a synchroscan streak camera. The two orthogonal polarized luminescence are split by a wollaston crystal and measured at same time. The polarization of prepulse is set 45 degree to the these two orthogonal polarization.

Chapter 3 Background of the Primary Event of Vision

3.1) Introduction

In this chapter, I will describe the structure and the function of photoreceptor cells and visual pigments rhodopsin. The sequence of visual process and primary process of vision will be reviewed.

3.2) Structure of Visual Pigments

The pigment responsible for vision is rhodopsin. It is located in the rods and cones in the retina. Humans have four different kinds of rhodopsin in their retinas.[3.1] Three of them are located on the cones and absorb at blue, green and red wavelength and are responsible for color vision. The fourth, in the rods, enables the eyes to see a low level of light. Rods and cones form synapses with bipolar cells, which in turn interact with other nerve cells in the retina. The electrical signals generated by the photoreceptor are processed by an intricate array of nerve cells within the retina and then transmitted to the brain by the fibers of the optic nerve. Cattle rhodopsin located in rods in the retina is studied in this thesis.

The molecular basis of this exquisitely sensitive visual pigment is schematically shown in figure 3.1. Rods have slender, elongated structures which have dimension of a diameter of 1 μm and a length of 40 μm.[3.2] The major functions of a rod cell are highly compartmentalized. The outer segment of the rod is specialized for photoreception. It contains a stack of about 1000 discs, which are closed, flattened sacs about 160 Å thick. These membranous structures are densely packed with the photoreceptor molecules rhodopsin. The disc membranes are separate from the plasma membrane of the outer segment. The inner segment generates ATP at a very rapid rate and is highly active in

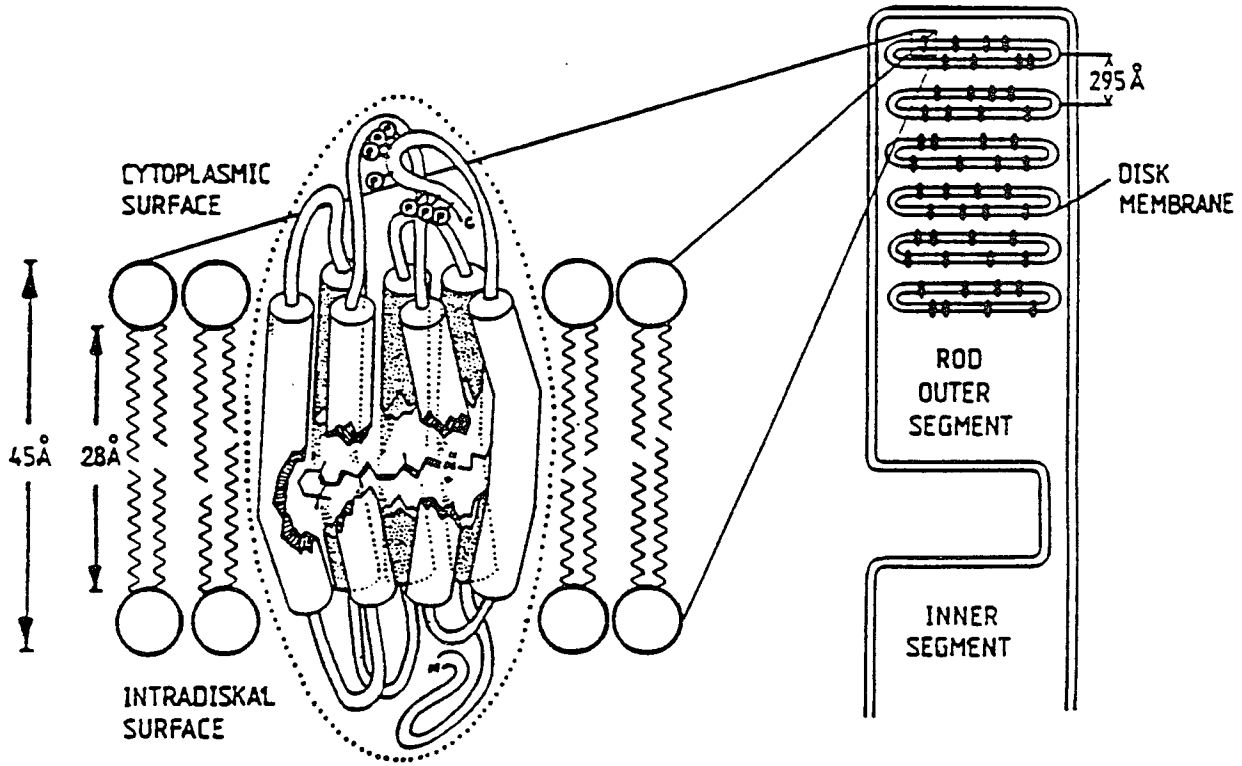

Fig. 3.1 The structure of the rod photoreceptor cells which consist disc membrane. The inset shows the helical transmembrane protein segments represented by cylinders located in the lipid bilayer, retinal lies in the middle of the bilayers and inside of the protein. This drawing is based on similar representations by A. Lewis et al. *Physics Today* Jan. 1988.

synthesizing proteins [3.2-3.3]. The rhodopsin is in the lipid bilayer of a disc membrane as shown in the inset of figure 3.1. It is an integral membrane protein containing seven transmembrane helices[3.2-3.4]. Rhodopsin contain a chromophore 11-*cis* retinal and a protein generally called opsin. Retinal (a vitamin A derivative) is bonded to proteins by a protonated Schiff base linkage. This 11-*cis*-retinal chromophore lies in a pocket of the protein, near the center of the bilayer membrane, with its long axis nearly parallel to the plane of the membrane.

3.3) The Sequence of the Visual Process

In 1958, George Wald and his coworkers showed that light isomerize the 11-cis-retinal group of rhodopsin to all-trans-retinal by synthesis of rhodopsin with a all-trans vitamin A, the precursor of the rhodopsin chromophore, and opsin, the protein of rhodopsin, and enzymes[3.5-6]. Now, there is a large body of evidence suggesting that this isomerization process forms an all-trans photoproduct called bathorhodopsin[3.7-8]. This isomerization alters the geometry of retinal, see figure 3.2. The Schiff-base linkage of retinal moves approximately 5 Å in relation to the ring portion of the chromophore[3.3,3.8-3.10]. In essence, a photon energy has been converted into the atomic motion. Bathorhodopsin is thermally unstable at room temperature, both retinal and the protein continuously change their conformations. The sequence of the events which follows the light absorption by rhodopsin leads to the release of retinal from the protein.[3.3,3.11-12] This bleaching sequence is shown in figure 3.3. The intermediates in the bleaching sequence were first identified by their low temperature absorption spectrum. As the temperature rises after photoexcitation of rhodopsin at low temperature, a series of intermediates were identified by their shifted absorption spectrum, beginning with the red shifted species bathorhodopsin which is identified at 77K.[3.11-12] Each intermediate is stable

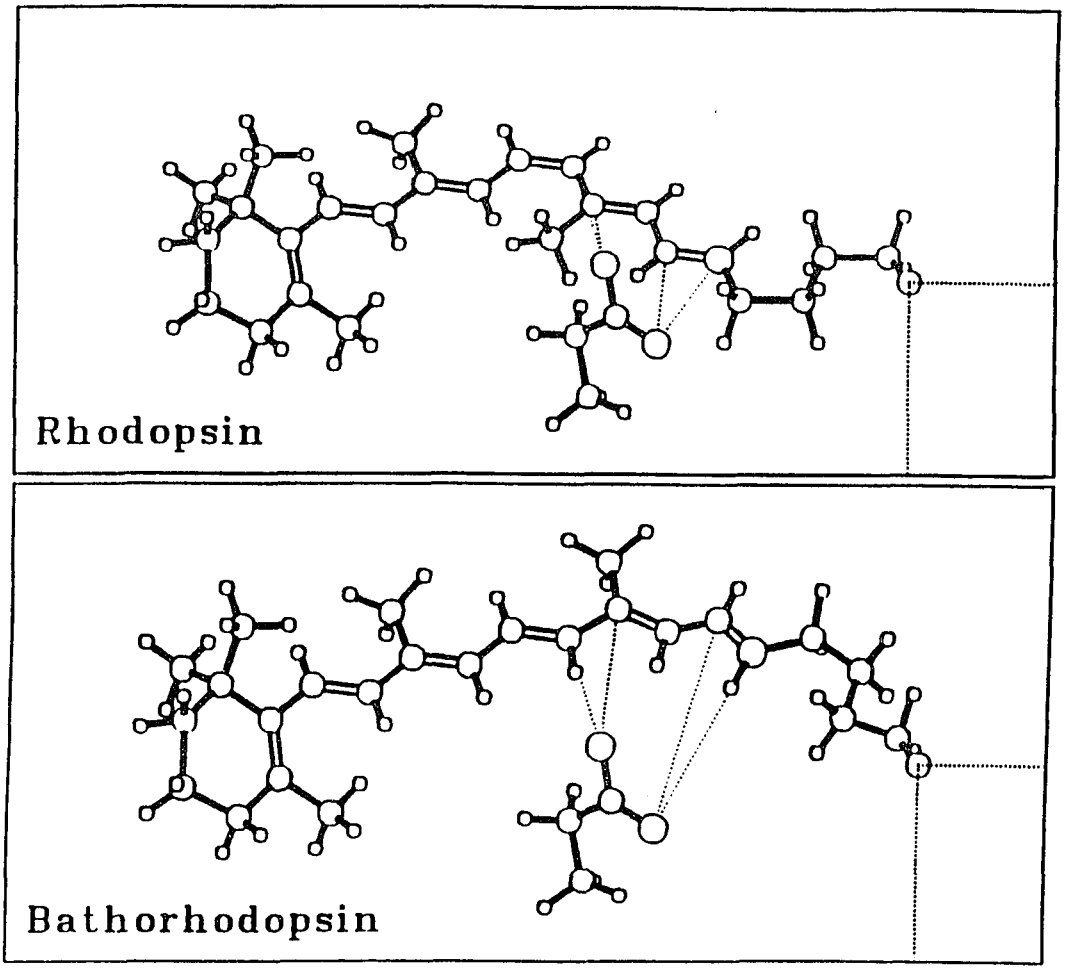

Fig.3.2 The model of the binding site of rhodopsin (top) and the primary photochemical event that generates bathorhodopsin (bottom) (from J.R. Tallent et al. *J. Am. Chem. Soc.* **114**, 1581 (1992))

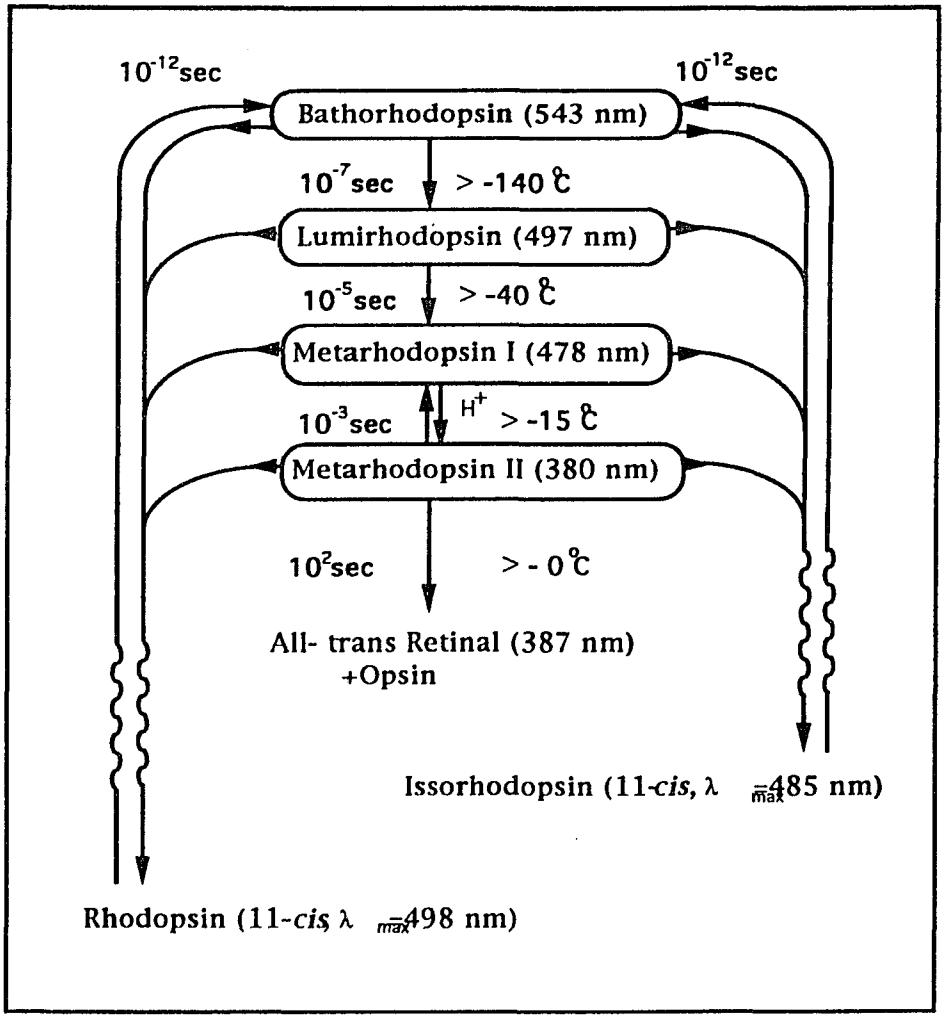

Fig. 3.3 Bleaching sequence of cattle rhodopsin. Photoreactions are denoted by wavy lines and thermal reaction by straight lines.

below a transition temperature.[3.11] The Schiff-base linkage (indicated in figure 3.2) becomes deprotonated in the transition from metarhodopsin I to II, which takes about a millisecond at 300K.[3.3] Metarhodopsin II, also called as photoexcited rhodopsin (R^*), triggers a series of enzymatic reactions that ultimately hyperpolarize the plasma membrane of the rod cell in the retina to generate a nerve impulse.[3.1] The sequence ends in about a minute with the detachment of the chromophore from the protein to yield an opsin and an all-trans-retinal, the retinal diffuses away from the protein because it does not fit into the binding site for the all-trans isomer. The all-trans-retinal is isomerized in the dark to 11-*cis*-retinal on the behalf of enzymes, which associates with opsin to regenerate rhodopsin.[3.1] As a consequence, a single photon generates a nerve impulse which hyperpolarized membranes close to 1mV.[3.1]. The trigger for these sequential conformational changes that leads to the visual excitation which involves the photochemistry of *cis-trans* isomerization of the chromophore. This is the primary events in visual excitation and the main focus of this thesis. Many experimental evidence[3.12] shows that the primary process of vision occurs at a picosecond time scale, therefore, picosecond transient measurements must be applied to understand this first step of the visual process.

Another light-sensitive protein was discovered in the purple membrane protein of baceterium *Halobacterium Halobium*[3.3,3.11-12]. These purple membranes contain retinal and constitute a protein remarkably similar to rhodopsin, called bacteriorhodopsin (bR).[3.13-14] As rhodopsin, the photochemistry of bacteriorhodopsin results in isomerization. The intermediates in the bacteriorhodopsin photocycle, like those in the rhodopsin sequence, have been studied by low-temperature spectrophotometry. In many respects the sequence of intermediates in bacteriorhodopsin has proved to be parallel to the sequence in rhodopsin. A red-shifted photoproduct K is formed at low

temperature, and decays to other, spectrally distinct, species as the sample is warmed. The photocycle of bacteriorhodopsin[3.12] is shown in figure 3.4. Unlike the rhodopsin sequence, however, bacteriorhodopsin photochemistry is a cycle, and does not result in the expulsion of the chromophore from the protein.[3.13-14] The understanding of the isomerization in bacteriorhodopsin would be beneficial to the study of the primary processes in visual pigments.

3.4) The Primary Events of Vision

In the primary process of vision, light is only involved in the first stage of vision, for the transition from 11-*cis* rhodopsin to all-trans bathorhodopsin. The conversion of optical to chemical energy is remarkably efficient, about two third of the absorbed light is converted to chemical energy[3.10-12]. This energy storage (35 kcal per mole) by isomerization of the chromophore as explained by Honig et al.[3.7] is due to the changed interaction of the protein with retinal; The isomerization produced by twisting the retinal C_{11}-C_{12} double bond breaks the ionic bond between the protonated schiff base and a counter ion located in the protein and stores energy by charge separation, see figure 3.2. How this conformational change occurs (from 11-*cis* to all-*trans* retinal) and how fast this isomerization is completed is addressed in this thesis. Picosecond and femtosecond transient experiments are expected to be lead to the understanding of this ultrafast isomerization process in terms of studying its electronic and vibrational properties by absorption and scattering.

The conjugated polyunsturated chain of 11-cis-retinal gives rhodopsin the ability to absorb light over a broad region of the visible spectrum with a peak at 500 nm, which nicely matches the solar output. The absorption coefficient of rhodopsin at 500nm is about 40,000 cm^{-1} M^{-1}.[3.1,3.11] The integrated absorption strength in the visible band is very large among the organic

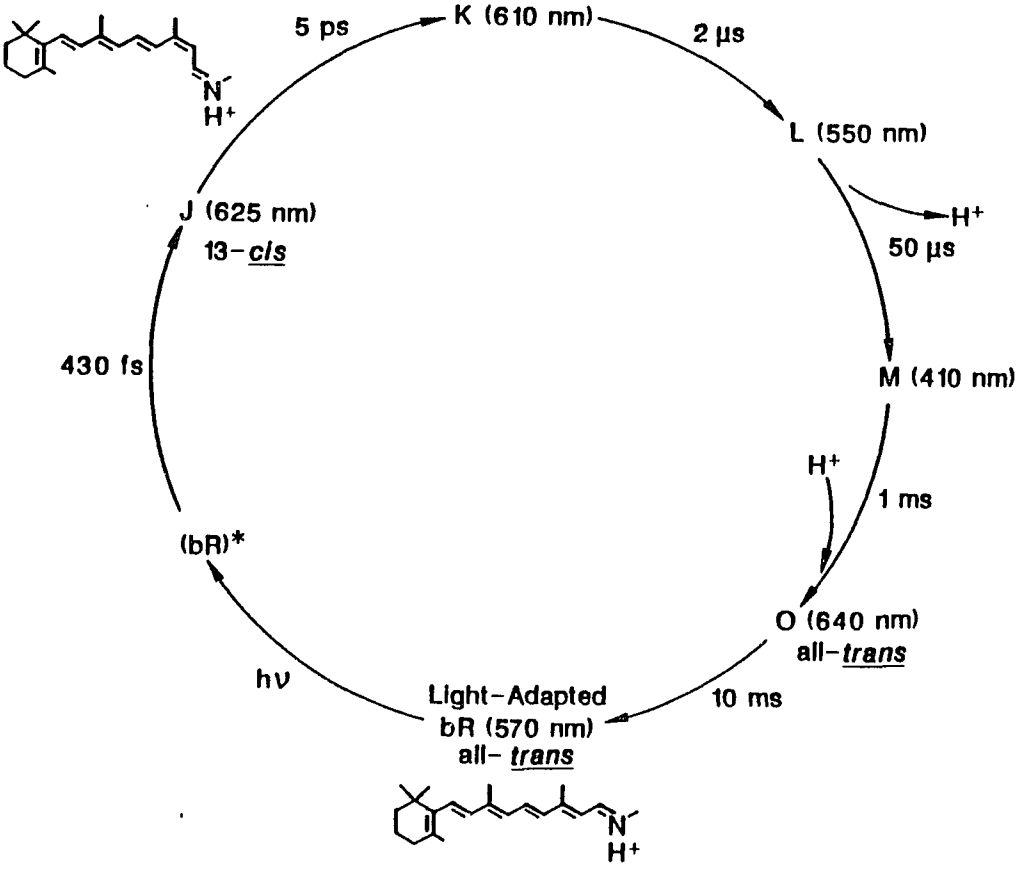

Fig.3.4 The Photocycle of light-adapted bacteriorhodopsin (bR). K is the primary photoproduct and J is its intermediate. (From R.M. Hochstrasser and C.K. Johnson in *Ultrafast Laser Pulses* ed. by Kaiser p.398)

compounds. The different absorption maxima of rhodopsin in comparison with retinal in solution (380nm) is caused by interactions between the proteins and the chromophore. It is believed[3.1] that the protein affects the absorption by changing the degree of delocalization of the π electron system of the chromophore. The interaction of the protein and the chromophore creates a specie that has the absorption maximum anywhere from 450-620 nm, depending on the origin of the protein.

Chapter 4 Models and Previous Experiments in the primary visual process

4.1) Introduction

In this chapter, I will summarize the previous experimental results on the primary process of vision, including the results of resonance Raman spectroscopy, transient absorption and luminescence spectroscopy. The theoretical models, proton translocation, and *cis-trans* isomerization, will also be discussed.

4.2) Resonance Raman Spectroscopy

Resonance Raman spectroscopy has played a major role in identifying intermediates in the rhodopsin sequence and bacteriorhodopsin cycles, and has produced the most detailed structural information yet available for rhodopsin and its visual intermediates. Experiments[4.1-4.2] have provided strong evidence of a twisted all-*trans* conformation of retinal in bathorhodopsin. The resonance Raman measurements [4.3-4] have identified rhodopsin and isorhodopsin (an artificial pigment) as 11-*cis* and 9-*cis* conformations, respectively. Both rhodopsin and isorhodopsin are converted photochemically to bathorhodopsin by photoexcitation, this supports the fact that the conformation of bathorhodopsin is all-*trans*. The conformational evidence, as well as resonance Raman evidence that the schiff base of retinal is protonated in both rhodopsin and bathorhodopsin[4.5-4.6], has been invoked in models of the primary process of vision which incorporate isomerization of a protonated retinal Schiff base. The resonance Raman excitation profile has been used to measure the excited-state structure and isomerization dynamics of the retinal chromophore in rhodopsin.[4.7] By analyzing the low-frequency torsional modes, the excited-state wavepacket is found to be moving rapidly (~35 fs) and permanently away from the Frank-Condon geometry along skeletal stretching and torsional

coordinates.

Time-resolved resonance Raman measurement is a more direct study of the intermediates as a function of time after photoexcitation. Various experiments have been performed in bacteriorhodopsin. In early stage of picosecond, it has been concluded [4.8-10] that the chromophore in the J state is highly twisted and thermally excited but it cools and conformationally relaxes to a more planar 13-*cis* chromophore within 3 ps to form the K state. The time-resolved resonance Raman measurement of the visual pigment rhodopsin [4.11] shows that the all-trans species (bathorhodopsin) is formed within laser resolution of 30 ps. The understanding of bacteriorhodopsin in picosecond time scale may give us a comparison picture to visual pigment rhodopsin.

4.3) Picosecond Transient Absorption

The absorption maximum of 11-cis rhodopsin (λ_{max}=500 nm for bovine rhodopsin) changes substantially after isomerization to bathorhodopsin (λ_{max}=543 nm) which is stabilized at 77K as shown in figure 4.1. The kinetics of isomerization can therefore be easily studied by transient absorption spectroscopy. A pump laser pulse is used to initiate the photoreaction while a delayed weak probe pulse detects the absorption change as described in the previous chapter.

The first picosecond measurements were performed by Busch et al.,[4.12] who found that the photoinduced absorption increases in the absorption region of bathorhodopsin at 561 nm which appears less than 6 ps after photoexcitation at 532 nm at room temperature. This measurement has been repeated by many other groups under different conditions and in different samples.[4.13-15] Green at al[4.13] have found that the photoinduced absorption has a risetime, $\tau_{1/2}$, of 3 ps which is assigned as the formation time of bathorhodopsin. Similar picosecond

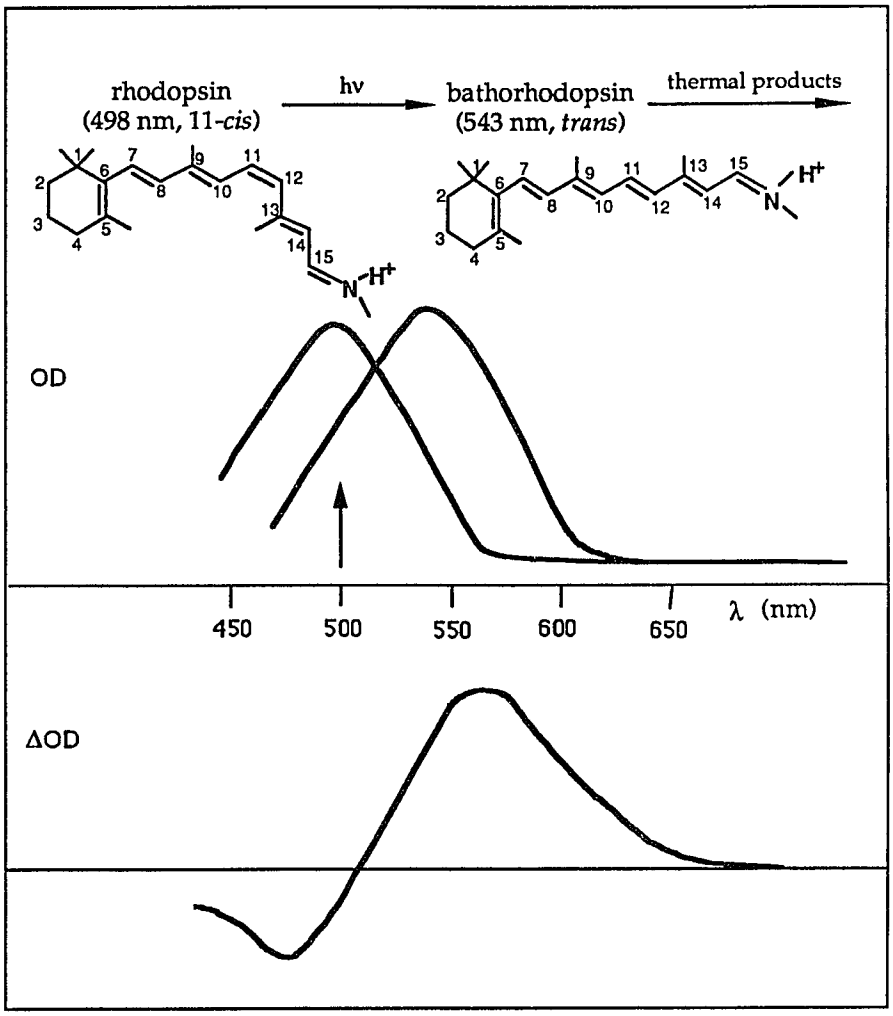

Fig.4.1 Schematic diagram of absorption spectrum of *11-cis* rhodopsin to *all-trans* bathorhodopsin and difference absrption spectra of rhodopsin and bathothodopsin. The excitation wavelength is indicated.

kinetics, which lead to the formation of batho intermediate, were obtained in experiments with isorhodopsin (9-*cis* rhodopsin).[4.16] The observation that bathorhodopsin appears within 3 ps after excitation for both rhodopsin and isorhodopsin strengthened the hypothesis of a primary photoisomerization mechanism based on a common batho intermediate.

The difference spectra of rhodopsin during excitation within a 7 ps pulse resolution and after 100 ps were measured in the 450nm-750nm range by Monger et al[4.14] at room temperature. Both spectra were found to have an induced absorption band with a maximum at 570nm and a bleach band with a maximum at 485 nm. The isobestic point is found at 510 nm. This difference spectra observation confirmed the bathorhodopsin formation within 3 ps by Green [4.13] et al.

Kobayashi et al [4.17] have observed a considerable bleaching at about 480 nm during excitation with a 6 ps green pulse, which relaxes with two step τ_1=15$\pm$5 ps and τ_2=50$\pm$30 ps. They also found a red absorbing (600-630nm) species, which they called hypsorhodopsin, occurred during the excitation prior to the formation of bathorhodopsin and concluded the reaction scheme is as follows:

$$\text{Rhodopsin} \xrightarrow[h\nu]{} S_1 \xrightarrow[15\pm5\text{ps}]{} \text{Hypsorhodopsin} \xrightarrow[50\pm20\text{ps}]{} \text{Bathorhodopsin} \qquad (4.1)$$

where S_1 is the excited state of 11-cis rhodopsin and absorbs further in the red spectral region than bathorhodopsin.[4.17]

Shichida et al [4.18,4.19] also have studied this red absorbed species which formation precedes bathorhodopsin by measuring the difference spectra using 25 ps excitation pulses. They found that the 15-ps spectrum (within the excitation pulse) was shifted by 10nm into the red spectral region as compared with the 100-ps spectrum. The latter spectrum agrees with the spectra of bathorhodopsin

measured at low-temperature. They called this red shifted intermediate photorhodopsin and conclude their scheme as follows

$$\text{Rhodopsin} \xrightarrow[<25\,\text{ps}]{} \text{Photorhodopsin} \xrightarrow[40\,\text{ps}]{} \text{Bathorhodopsin} \qquad (4.2)$$

The absorption spectrum of photorhodopsin and bathorhodopsin are obtained from the experimental measurement and shown in figure 4.2. The magnitude of oscillator strength of photorhodopsin was found between rhodopsin and bathorhodopsin. These results[4.19] suggest that photorhodopsin is an all-trans chromophore at the C_{11}-C_{12} bond with nearby single bonds highly distorted.

Many transient absorption experiments [4.20-24] have been performed to study the ground and excited state dynamics in bacteriorhodopsin. These experiments indicate the formation of a precursor to K, called J, which is believed to be a ground state species with a 13-*cis* retinal structure. The excited state dynamics has shown that the motion out of the initially populated Frank-Condon region proceeds in 200 fs, and reaches a relaxed state at the minimum of the S_1 potential surface which decays in 500 fs to the ground state J. The dynamics scheme is summarized as follows.

$$\text{bR(all-trans)} \xrightarrow[h\nu]{} \text{bR}^*\text{(F-C)} \xrightarrow[200\text{fs}]{} \text{bR}^*(90^\circ) \xrightarrow[500\text{fs}]{} \text{J} \xrightarrow[5\text{ps}]{} \text{K} \qquad (4.3)$$

where bR^*(F-C) represents the Franck-Condon (vertical) excited state, $bR^*(90^\circ)$ represents the excited state at minimum of the S_1 protential surface near the rotation angle 90° around C_{13}=C_{14} torsional bond. K is the primary photoproduct of bR which is analog to bathorhodopsin.

4.4) Excited state dynamics/ Evidence for isomerization as the primary process

The fluorescence of bovine 11-*cis* rhodopsin measured by a streak camera

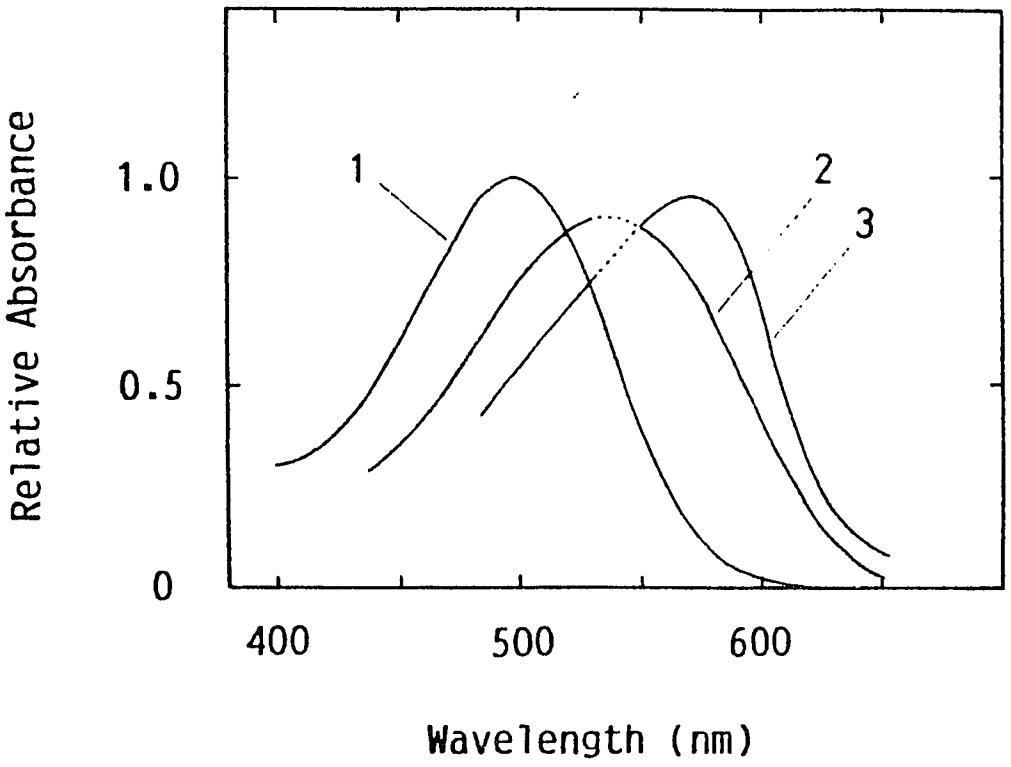

Fig.4.2 Absolute absorption spectra of cattle rhodopsin (1), bathorhodopsin (2) and photorhodopsin (3) at room temperature measured by Shichida et al. (Biophys. J. 456 (1987))

shows that the lifetime of the fluorescence is less than the resolution time of 12 ps [4.25-26] in the wavelength range of 550-660 nm. The quantum yield of fluorescence was estimated to be $(1.2\pm0.5)\times10^{-5}$. On the basis of quantum yield and the radiative lifetime of 11-*cis* rhodopsin of 5 ns, the lifetime of the excited state was estimated to be about 0.1 ps. When the sample is cooled down to liquid helium temperature, the lifetime of the fluorescence remains less than 12 ps and the quantum yield is practically unchanged (6.5×10^{-6}).[4.27] A similar value of the quantum yield of fluorescence at 5K was obtained for the deuterated sample. The fluorescence emission properties of a rhodopsin analog Rh7 where the C_{11}-C_{12} double bond is rotationally blocked was studied.[4.28] Much slower fluorescence kinetics and larger quantum yields are obtained for analogy Rh7. This suggests that the fast fluorescence and small quantum yield in rhodopsin is due to the efficient isomerization occurred around the C_{11}-C_{12} double bond of retinal, and it also agrees with measurements shown that the dynamics in the excited state is very rapid.

4.5) Deuteration and Temperature Effect

It has been shown that the Schiff base hydrogen would be replaced by deuterium[4.29] in the deuterated rhodopsin. Photoinduced absorption in deuterated samples of rhodopsin has been studied by Rentzepis and co-workers.[4.30] They concluded that at low temperature (4K-40K) an initial transient which is assigned to the first excited state (S_1) of rhodopsin decays to form bathorhodopsin. The decay kinetics of the initial transient species are slowed when the temperature decreases to 4K, suggesting that the formation of bathorhodopsin is slowed at low temperature. The formation of the long-lived species (bathorhodopsin) is slower in the deuterated samples than rhodopsin, and this difference can be observed up to 40 K. There, bathorhodopsin in the

undeuterated rhodopsin is formed in less than 6 ps, while bathorhodopsin from deuterated rhodopsin is formed in 17 ps. At 4K, this fast formation of bathorhodopsin is slowed down to 257 ps for the deuterated sample and 36 ps for the undeuterated rhodopsin. Over the temperature range they measured, the isotope effect on the rate k_H/k_D was found approximately as 7. The dependence of the rate of formation of bathorhodopsin upon temperature is plotted in figure 4.3. The data for both rhodopsin and deuterated rhodopsin show non-Arrhenius behavior. At very low temperatures the rate of formation of bathorhodopsin is nearly independent of temperature and has a finite value as the temperature approaches 0K rather than vanishing as predicted for a normal Arrhenius temperature dependence.

4.6) Proton translocation model

The large isotope effect and non-Arrhenius behavior were taken as the evidence for quantum mechanical tunneling of a proton along the protonated Schiff base hydrogen bond during the photoexcitation process leading to the formation of bathorhodopsin. Since the deuterated Schiff base would be expected to have no effect on a *cis-trans* isomerization process, Peters et al have re-examined the isomerization model and suggested models for the proton translocation leading to the formation of bathorhodopsin. These models,[4.30] as depicted in figure 4.4, show that such translocation may proceed by either (A) a single proton translocation to the Schiff base nitrogen producing a carbonium ion, or by (B) a concerted double hydrogen transfer leading to a retro-retinal structure. Using these model as a guide for proton tunneling, one can calculate the energy barrier for the formation of bathorhodopsin. An expression can be used for the rate of tunneling (k):

$$k = \nu_0 \exp\left(-\frac{\pi^2 a k}{h}\sqrt{2mE_a}\right) \qquad (4.4)$$

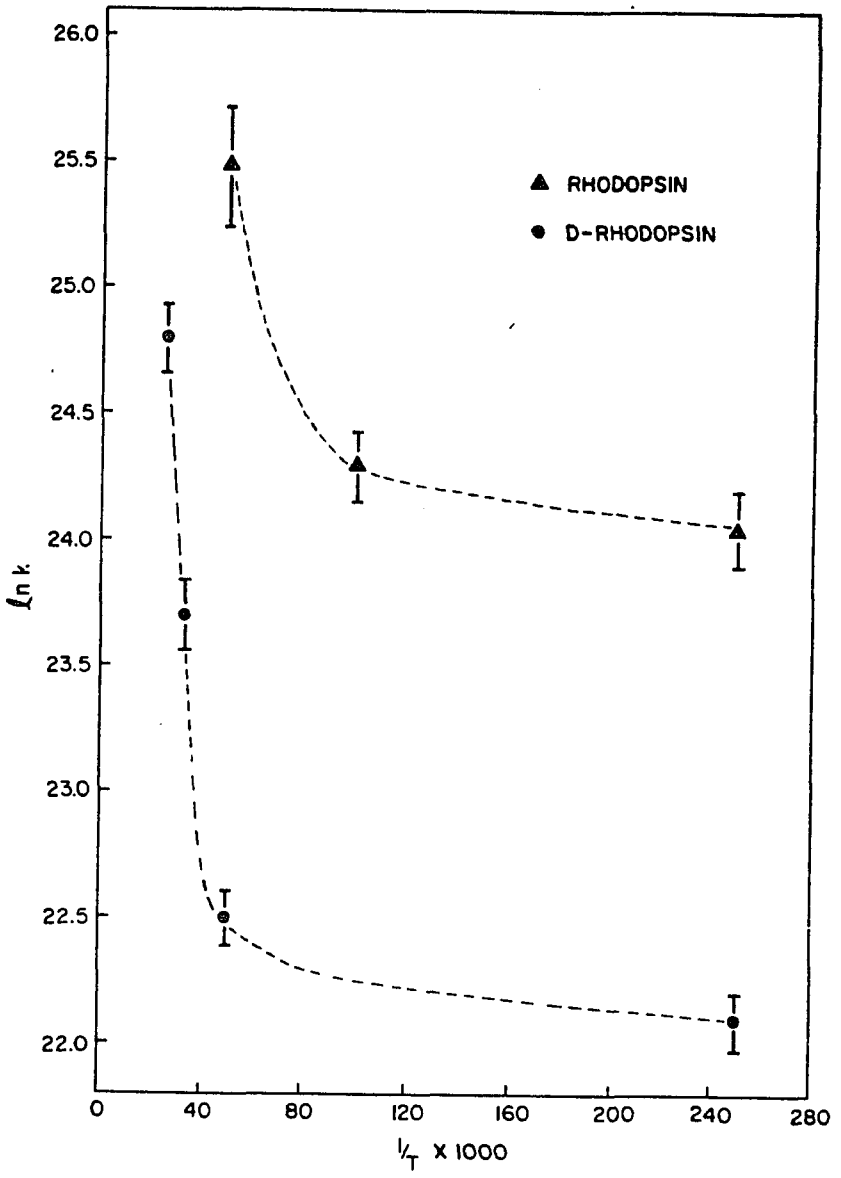

Fig. 4.3 An Arrhenius plot of ln*k* for the formation of preluminrhodopsin (bathorhodopsin) verus 1/T (K)x10^3 , the value ln*k*=25.84 corresponds to a lifetime of 6 ps.

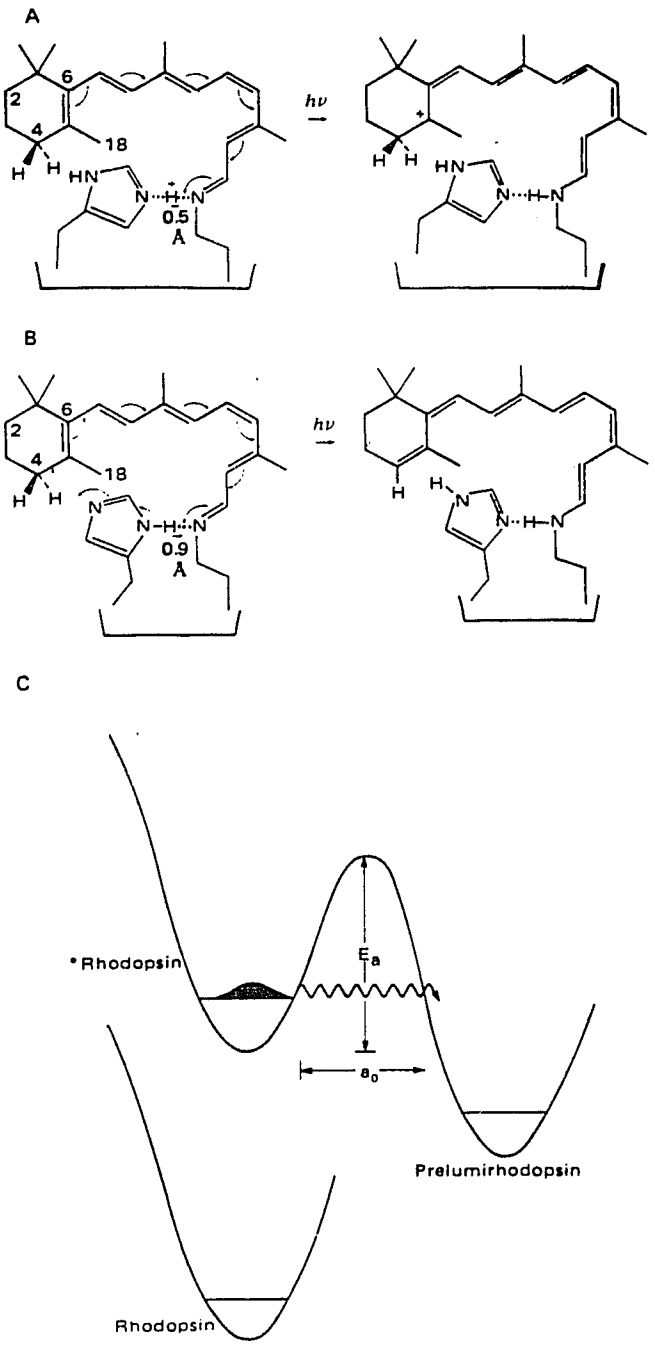

Fig. 4.4 Models for proton translocation to form prelumirhodopsin (bathorhodopsin). (Model A) Single proton translocation with carbonium ion formation. (Model B) Concerted double proton translocation with retro-retinal formation. (C) The energy barrier Ea for proton tunneling calculated as 4.5 kcal/mol and 1.4 kcal/mol for a0=0.5A and 0.9A in model A and B, respectively. (From Peters et al. Proc. Natl. Acad. Sci. USA **74** , 3119 (1977))

The barrier E_a is found to be 1.4 kcal /mol for a proton translocation distance of 0.9 Å at 4K. It also has been discussed that the translocation of a hydrogen towards the Schiff base nitrogen would result in red shift of the absorption.[4.30] The proton translocation model can predict that deuteration of the Schiff base should result in a marked isotope effect.

Obviously, the proton translocation model suggested by Peters et al contradicts the evidence of isomerization. Honig et al [3.7] have argued that rhodopsin repopulate from the common excited state for formation of bathorhodopsin. Since the rhodopsin ground state is repopulated in less than 6 ps, the temperature dependent decay rate observed by Peter et al could not correspond to the decay of excited state (S_1). Thus, they assign this temperature-dependent and deuterium-dependent process to a ground intermediate state decay kinetics rather than the decay of excited state (S_1) proposed by Peters et al. They have postulated that the formation of bathorhodopsin involves two steps. The first step involves the isomerization of the chromophore, on a barrierless excited-state potential surface, to form a ground state intermediate which is called batho', this first step is completed in less than 6 ps at all temperature. The second step, deuterium-dependent process, involves a ground state relaxation of the protein induced by the isomerization and may take from less 6 ps to 36 ps, depending on temperature. The sequence of primary event proposed by Honig et al is as follows.

$$\text{Rhodopsin} \xrightarrow[h\nu]{} \text{Rhodopsin*}\ (S1) \xrightarrow[<6ps]{} \text{Batho'} \xrightarrow[6\text{-}36ps]{} \text{Bathorhodopsin} \qquad (4.5)$$

It still remains a question as to whether tunneling occurs at the chromophore at physiological temperature. A deuteration dependent measurement in subpicosecond time scale can clarify this point.

4.7) Theoretical Models and Simulations

Birge et al [3.3, 3.8-10] have performed theoretical studies of the primary process of vision using a semiempirical molecular dynamics formalism. The ground state and excited state surfaces connecting rhodopsin and bathorhodopsin along the C_{11}-C_{12} torsional angle reaction path were partially mapped based on a revised model of the protein binding site with a counter ion interacting with the C_{13} to C_{15} region of the chromophore. The ground state surface was generated by using MNDO/AM1 procedures and the excited surface was generated by INDO-PSDCI procedures including both single and double configuration interaction. The first excited state exhibits a barrierless reaction path for C_{11}-C_{12} diherdral torsion with a local minimum (activated complex) centered at $\phi_{11,12}=90^\circ$ as shown in figure 4.5(a). Semiempirical molecular dynamics procedures are used to simulate the forward and reverse photochemistry. The activated complex is reached in about 375 fs following excitation. The simulation of rhodopsin to bathorhodopsin photoconversion is presented in figure 4.5(b). The quantum yield (ϕ) for isomerization and the product formation time (τ) are calculated based on the semiclassical coupling models. Best results are obtained by including both dynamic and phased nonadiabatic coupling: $\phi_{R\text{-}B}$ =0.690; $\tau_{R\text{-}B}$ =1.360 ps; $\phi_{B\text{-}R}$ =0.521; $\tau_{B\text{-}R}$ =1.628 ps. Similarly, the S_1 excited state absorption spectrum is calculated as function of time following excitation of rhodopsin as depicted in figure 4.6. The key feature of the early time spectra (0-325fs) is the presence of a strong absorption centered between 540-580nm, which is surprisingly similar in oscillator strength and energy to the absorption band of bathorhodopsin. This feature broadens and decreases in intensity once the molecule enters the activated complex. A longer wavelength band at ~780nm appears after ~375 fs which is diagnostic of C_{11}-C_{12} dihedral angles in the region $80^\circ<\phi_{11,12}<100^\circ$.

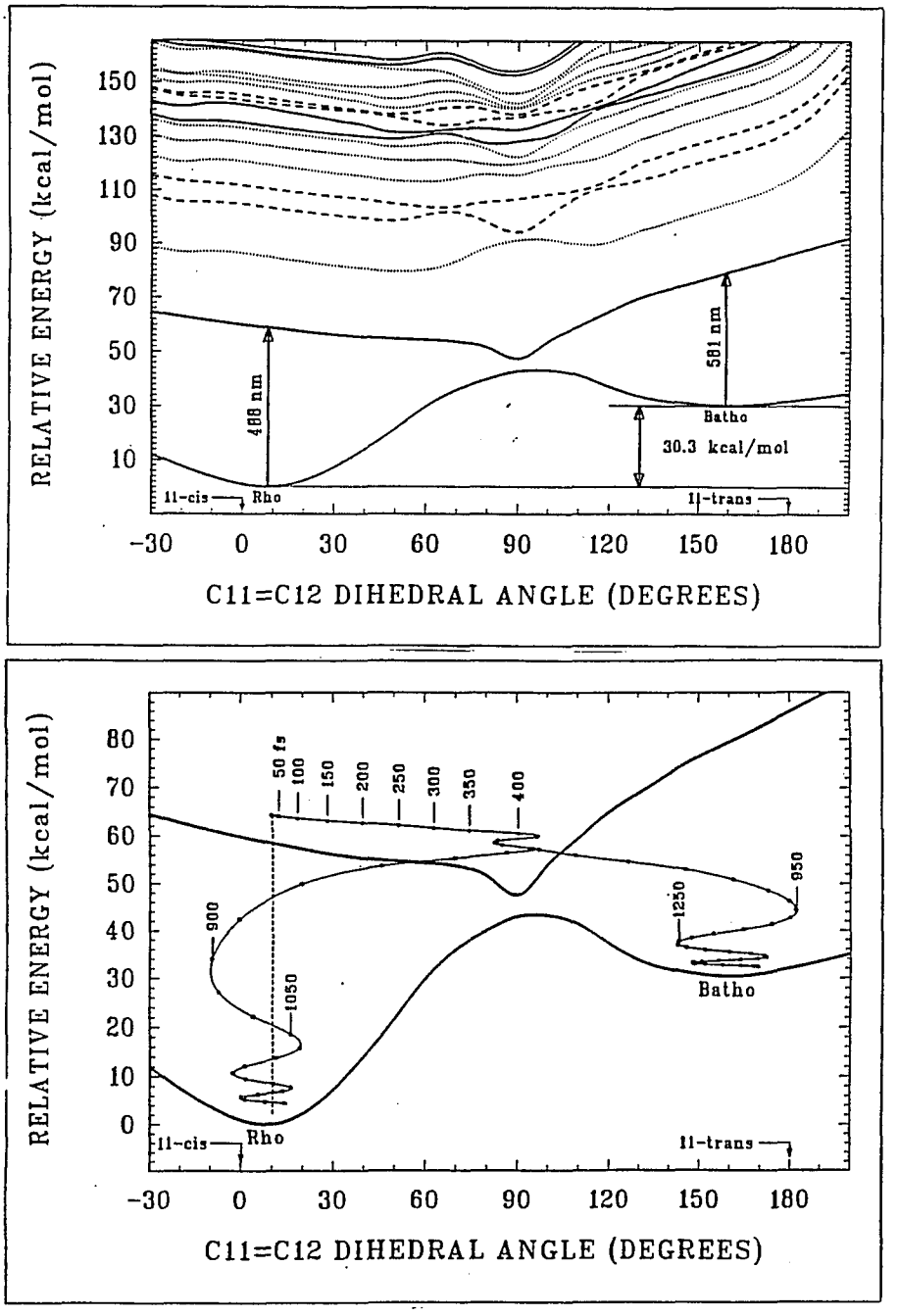

Fig. 4.5 (Top) Ground and lowest seventeen excited singlet state potential surfaces as a function of the C_{11}=C_{12} dihedral angle. The dotted line (.....) represents the oscillator strengths of S_n<-S_1 less than 0.1, and dashed line (- - -) for oscillator strengths greater than 0.1. (Bottom) The molecular dynamics of the rhodopsin (Rho) -> bathorhodopsin (Batho) photochemical transformation based on the adiabatic ground and first excited singlet state potential energy surfaces shown in top. (from J.R. Tallent et al. J. Am. Chem. Soc. **114**, 1581(1992))

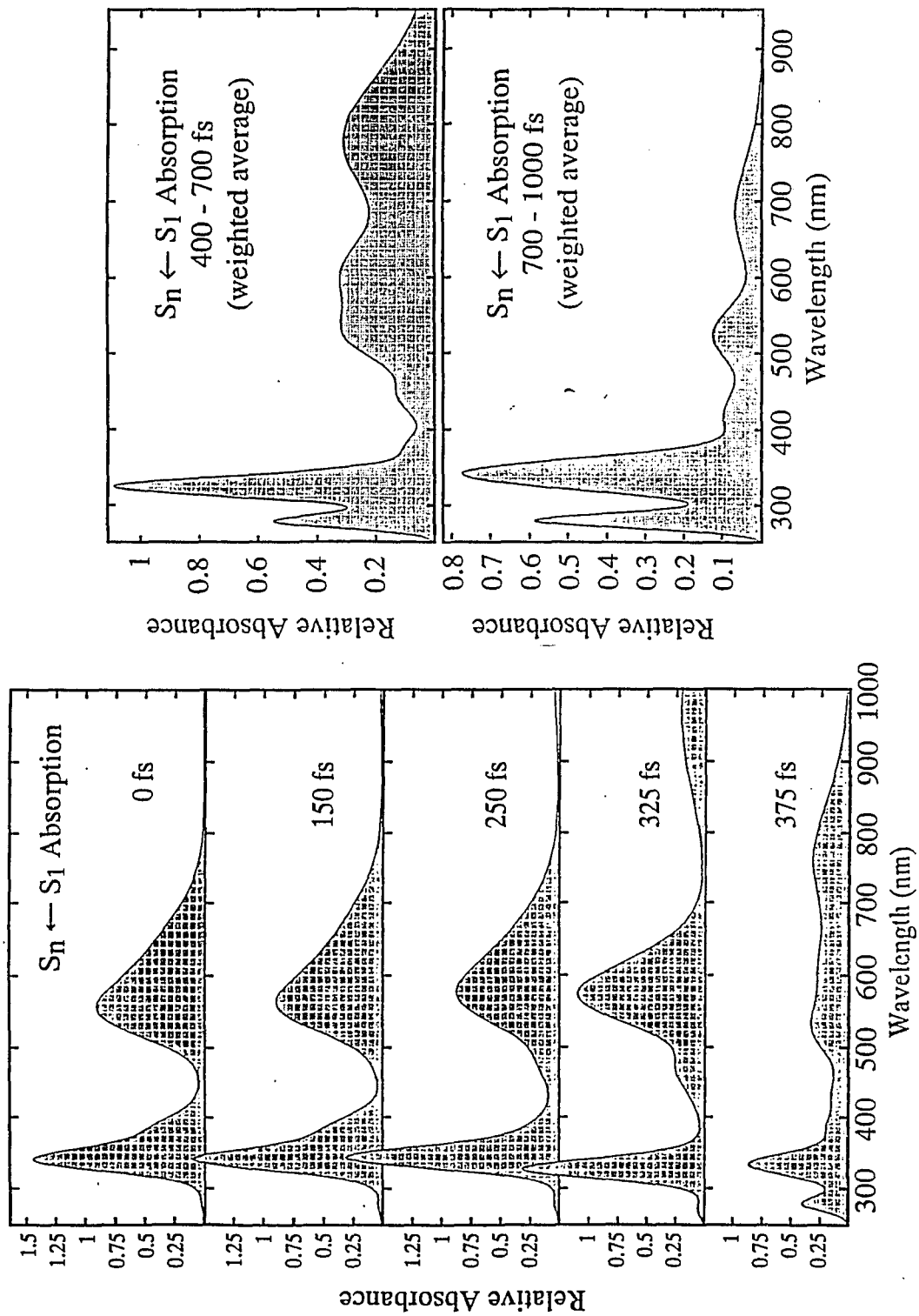

Fig.4.6 The simulation of Sn<- S1 absorption spectra of rhodopsin as a function of time following excitation into the first excited singlet state. (from J.R. Tallent et al. J. Am Chem. Soc. **114**, 1581 (1992))

Another molecular dynamics simulation is the so called "bicycle-pedal" model for isomerization which was developed by Warshel et al.[4.31-32] The isomerization of "bicycle-pedal" model involves several bond coordinates rather than the isomerization along C_{11}-C_{12} single bond proposed by Birge et al. A similar dynamic scheme is still proposed. The molecule first changes its conformation by moving downhill on the potential surface of the excited state and then crosses to the ground state once the C_{11}-C_{12} torsional angle is approximately 90°. In the ground state, the molecule becomes trapped in a strained all-trans form. Warshel at al have calculated the isomerization time to be about 200 fs. This faster isomerization time theoretically may be due to the rotation of several bonds of the chromophore which is constrained at the end of the molecule so that it must move in a "bicycle-pedal" motion.

4.8) Most recent transient absorption measurement

Recently, in parallel but later with the work done in this thesis, Schoenlein et al[4.33] have performed femtosecond absorption measurement on bovine rhodopsin using a 35 fs excitation laser pulse at 500nm and a 10 fs probe pulse at wavelength 450-580nm. Their difference absorption spectrum is plotted in figure 4.7. They assigned the increase in absorption between 490 and 540 nm to the excited-state (S_1-S_n) transition, the initial appearance of photoproduct is indicated by the differential absorption observed between 540-580 nm. Between 33 fs and 200 fs, the photoproduct absorption increases, and the initial rhodopsin bleach between 470 and 540nm becomes evident. Based on the fact that photoproduct absorption at 570nm remains unchanged after 200 fs, the time needed to complete of the isomerization process is concluded to be 200 fs. The blue shift of the isobestic point (from 540 to 515 nm) and the decrease of bleach at that wavelength region is explained as due to vibrational cooling of both the

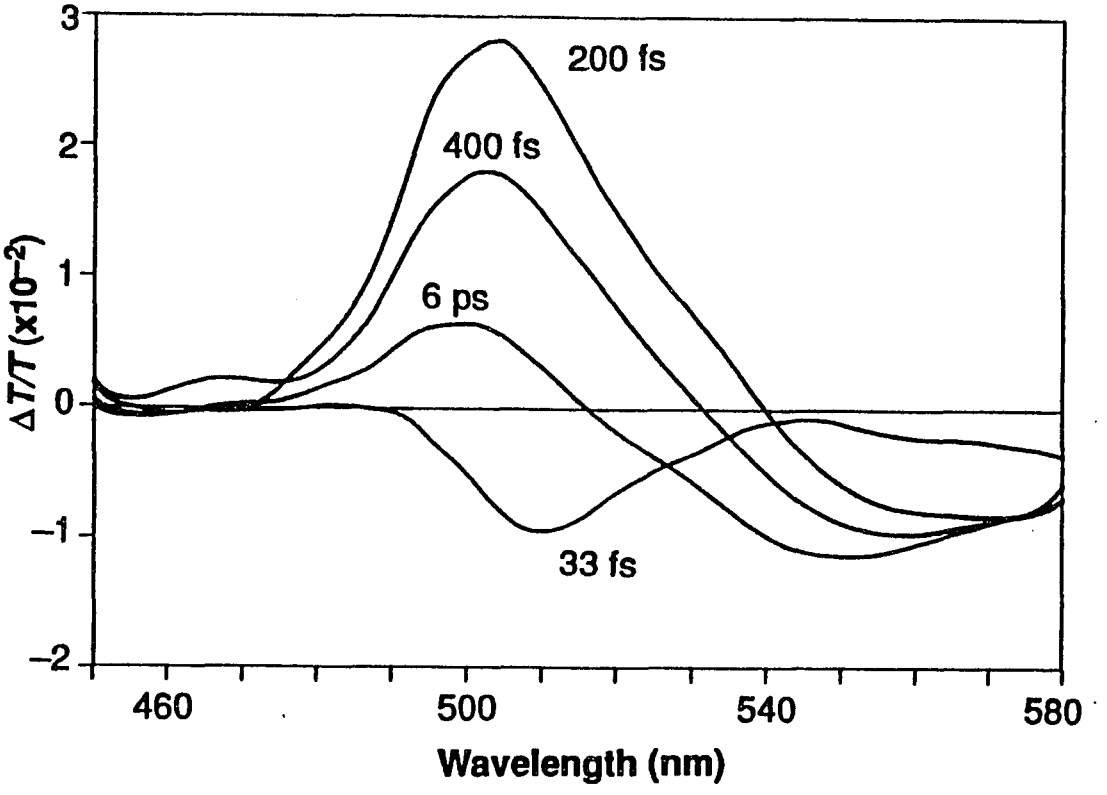

Fig.4.7 Difference spectra measurents of 11-cis rhodopsin at 11-cis rhodopsin at various delays following a 35-fs pump pulse at 500nm. (Data taken form Schoenlein et al. Science **254**, 412 (1991))

rhodopsin and photoproduct ground state, as well as to conformational relaxation. They assumed that the initial photoproduct is the intermediate, photorhodopsin, identified by Shichida et al and concluded the conformation change of rhodopsin is accomplished within 200 fs which is shown in figure 4.8. Oscillatory behavior is observed in time resolved measurements, which indicates that non-stationary vibrational states are excited by short pulses, the authors found the vibrational frequency of these oscillations (~ 135 cm^{-1}) consistent with the low-frequency torsional modes of rhodopsin. The authors claim that 200 fs is faster than typical vibrational dephasing and relaxation times and suggest the photochemistry occurs from a vibrational coherent system. No model fitting of their data was presented to date. Authors claim that their results contradicts the traditional picture of photochemistry which assumes vibrational relaxation in the excited state followed by partitioning to photoproduct and to reactant. They suggest that isomerization follows a nonadiabatic potential surface (shown in dotted line in figure 4.8) which results from the strong coupling between the rhodopsin excited state and the ground state of all-*trans* products. Therefore, authors has setup a new paradigm to explain the photochemistry in the primary process of vision. In this thesis, I will discuss the results of this femtosecond absorption measurements and explain their results based on our conventional 11-*cis* to all-*trans* isomerision scheme. I also will try to explore whether this new scheme is necessary or not to explain the visual photochemistry.

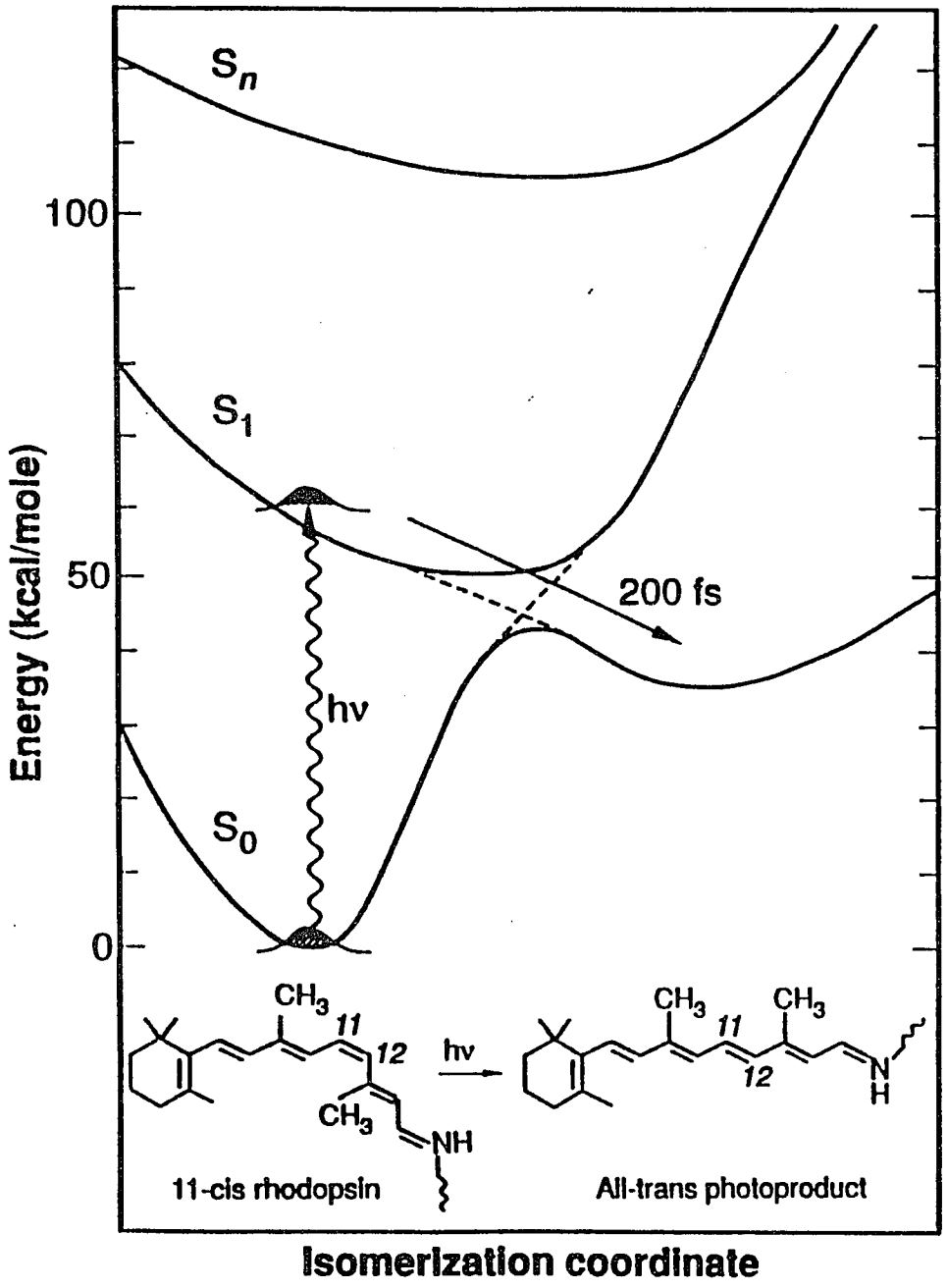

Fig.4.8 Schematic ground-state and excited-state potential energy surfaces for the 11-cis to 11-trans isomerization in rhodopsin. The reaction path of the photoisomerization is indicated by the nonadiabatic potential surfaces (dotted lines) (from R.W. Schoenlein et al. *Science* **254**, 412(1991))

Chapter 5 Research on primary events of vision

5.1) Introduction

Picosecond measurements have successfully measured many properties of the primary event of vision, but there are still mysteries to be explored. The following gives a summary of experimental background. Bathorhodopsin formation time was measured as an exponential rising constant of 3 ps using a 6 ps laser pulse. The red shifted precursor to bathorhodopsin, called photorhodopsin, was assumed to have formed within the laser resolution[4.18], and it is still a mystery what happens at earlier times (< 6 ps). The excitation intensity dependence, temperature-dependent and deuterium-dependent formation of bathorhodopsin need further clarification. The model proposed by Honig et al. need further experimental evidence of the existence of a batho' state at all temperature. The nature of intermediates which formation precedes bathorhodopsin, such as photorhodopsin [4.18], batho'[3.7] and hypsorhodopsin[5.1], are still unresolved in early picosecond time scale. Therefore a measurement with better time resolution is definitely needed to clarify the primary photochemistry of visual processes.

The recent generation of subpicosecond blue-green ultrafast optical pulses has made sensitive transient measurements on visual pigment possible. We performed experimental studies on the early photochemistry of rhodopsin in both protonated and deuterated aqueous environments at 295 K using the pump-probe technique which is described in previous chapters. Two laser systems were used in this experiment. One is the time resolved femtosecond absorption apparatus based on an amplified CPM laser which is shown in figure 2.12. the pump pulse at 500nm photoexcite the rhodopsin sample at 20 Hz repetition rate and a weak probe white-light pulse monitors the resulting

absorption change with 200fs resolution. An optical multichannel analyzer with dual diode array and photodiode were used to measure the transient absorption spectrum and absorption change at certain wavelength, respectively, as described in chapter 2. A 540 Hz high repetition laser system, shown in figure 2.14, allowed us to measure with sufficient accuracy of low absorption change (0.1%) onduced by photoexcitation of the rhodopsin with a low intensity excitation laser with a resolution of about 1 ps. The kinetic profiles of data collected with either system were similar. The rhodopsin samples, both deuteried and undeuterated, were placed in an ice-chilled reservoir and circulated through a 2mm-pathlength cuvette by a peristaltic pump. The flow rate was such that after each laser pulse the absorbing sample was completely replenished. Pump and probe pulse were colinearly focused into the sample.

The question of whether bathorhodopsin is the first intermediate of the photoreaction and its speed are addressed in this thesis using femtosecond laser spectroscopy. The deuteration effect is studied at room temperature to understand the tunneling process at primary visual process.

5.2) Time resolved transient absorption kinetics

Figure 5.1 illustrates the change in absorption at 620 nm after excitation at 500 nm. The photoinduced absorption is formed within the laser resolution (~300 fs) after photoexcitation. The induced absorption clearly indicates two exponential decay constants, a rapidly (~200 fs) decaying transient, and a slower (3 ps) decay to a long-lived species which is not substantially changed between 10 ps and 100 ps. The induced decrease in transmission at long times is about 6% for an excitation fluence F of 5×10^{15} photons/cm^2. This corresponds to a probability σF of 0.8 that a given molecule at the front of the sample cell is photoexcited where σ is the known rhodopsin absorption cross-section at 500

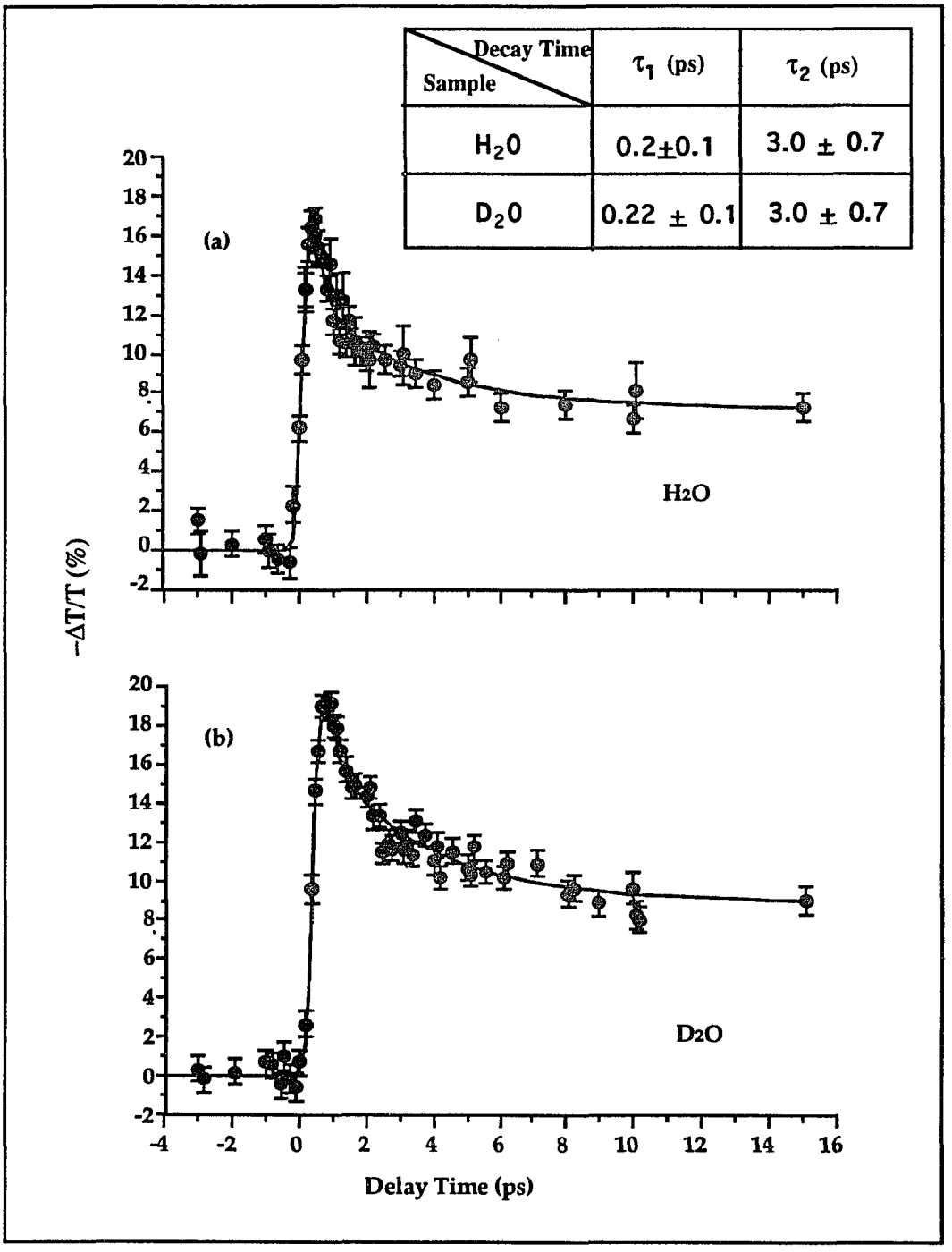

Fig. 5.1 (a). Absorption change at 620 nm induced by a 500 nm pump pulse as a function of pump probe delay time. The time resolution is approximately 300 fs. The points are the data and the solid line is the calculated fit discussed in the text. (b) is the same as (a) except that the samples were deuterated. The inset table list the decay time constants of the fitting curves.

nm. The signal at the maximum in transient absorption is strictly linear in pump fluence for incident power levels of up to $1x10^{16}$ photons/cm^2. The photoinduced absorption at 620nm with flux of $2x10^{15}$ photos/cm^2 is shown in figure 5.2. The shape of the dynamics is nearly indistinguishable over this power range. The shape of the curve is also indistinguishable, within our signal to noise, using probe wavelengths from 590-620 nm. The spectral feature of induced absorption at 100 ps delay time which peaks near 570 nm, is essentially similar to the bathorhodopsin-rhodopsin absorption difference spectrum[4.29].

From these measurements we concluded the photoisomerization is fully completed within 10 ps and have identified the 10 ps to 100ps spectrum as the isomerized bathorhodopsin species. The solid line in figure 5.1 is a kinetic fit of the two exponential decay kinetic model to the data. The two exponential decay kinetics suggest at least two intermediates must be excited prior to the formation of bathorhodopsin. Figure 5.1(B) shows the same experiment as figure 3.12a except the sample is suspended in D_2O. No difference in the kinetic profile between figure 5.1a and 5.1b is observed within our signal to noise. The same was true over the entire 550-620 wavelength range. Therefore, deuteration does not affect the dynamics observed at physiological temperature.

The intensity dependence of the photoinduced absorption at 620nm is plotted in figure 5.3. The photoinduced absorption at 0 ps and 10 ps after excitation shows a linear pump intensity dependence up to the excitation flux of 10^{16} photon/cm^2. The photoinduced absorption at 0 ps is always larger than at 10 ps delay time in the entire excitation flux range ($5x10^{14}$ - 10^{16} photon/cm^2). This also shows that the intermediate is excited in the entire excitation intensity.

Figure 5.4 illustrates the absorption change at 590nm when pumped at 500nm using the 540 Hz high repetition laser system. The induced absorption has similar features as those for the 620nm probe using the CPM laser system.

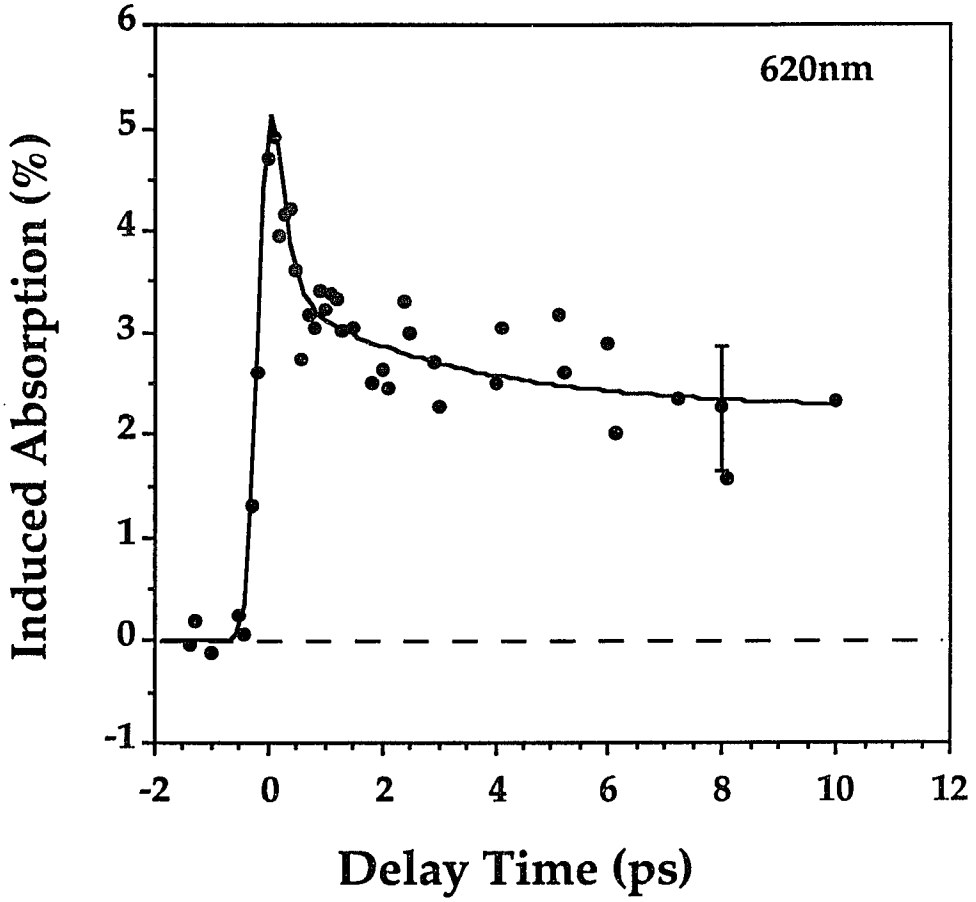

Fig. 5.2 Absorption change at 620 nm induced by a 500 nm pump pulse as a function of pump probe delay time. The time resolution is approximately 300 fs. The points are the data and the solid line is the calculated fit discussed in the text. The excitation flux is 2×10^{15} photon/cm^2

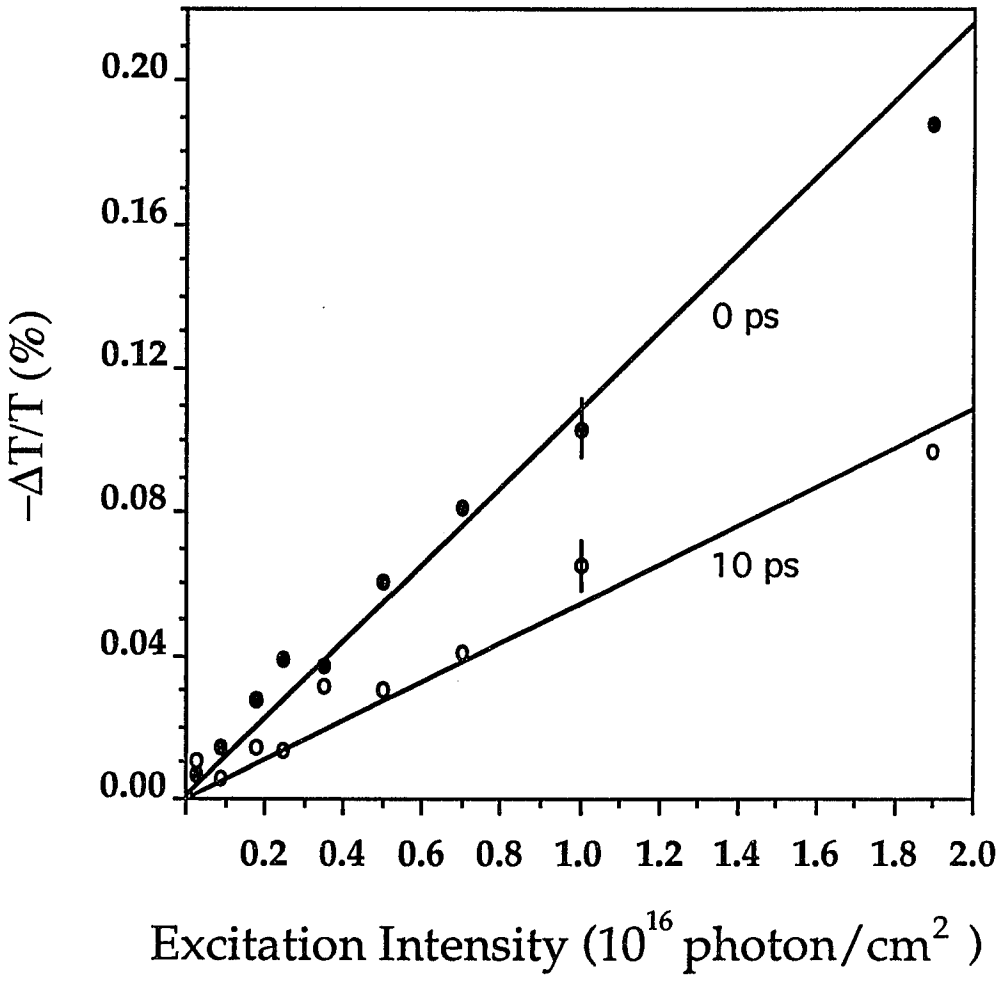

Fig.5.3 Linear intensity dependence of photoinduced absorption at 0 ps and 10 ps after excitation probed at 620nm.

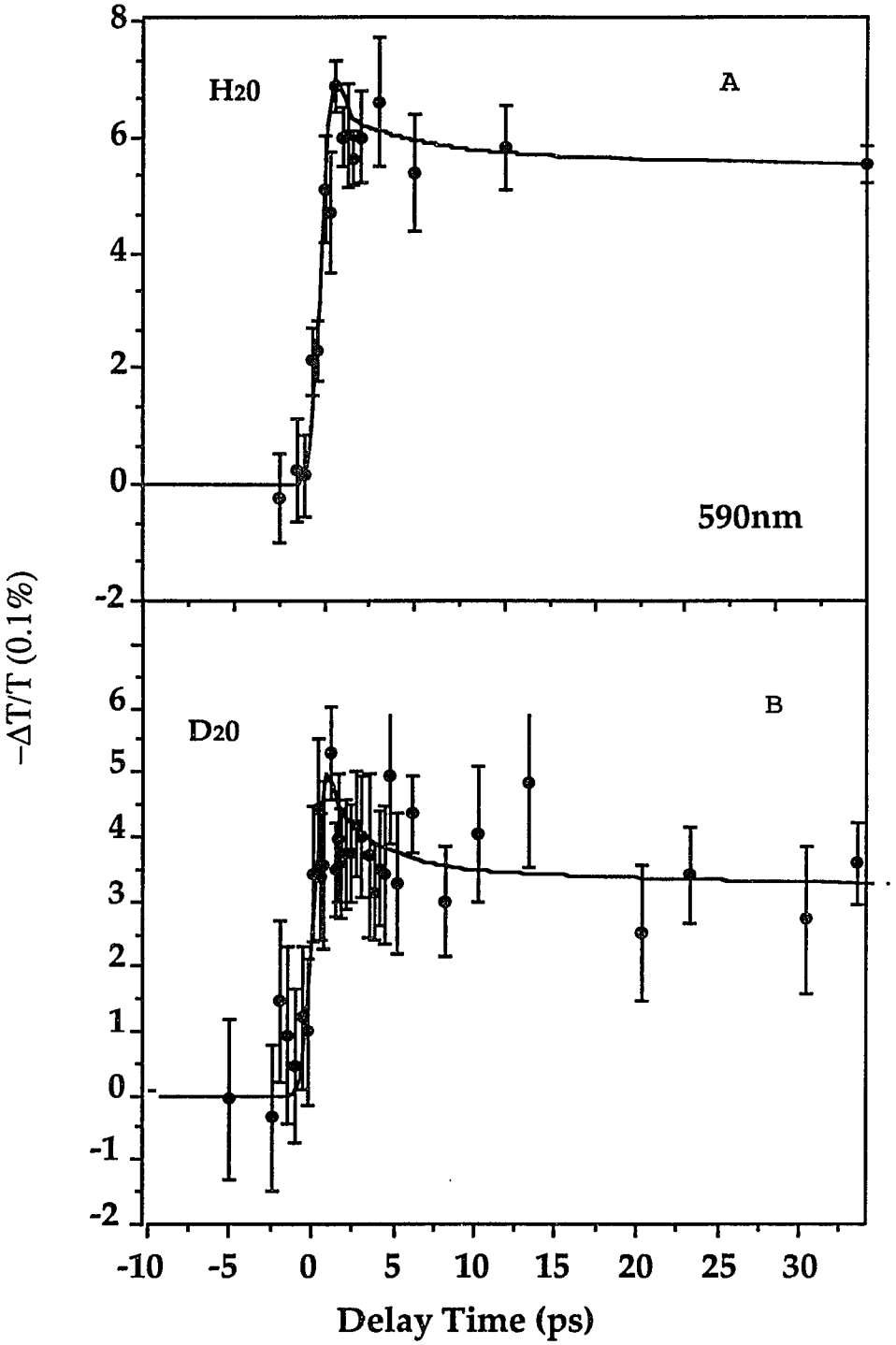

Fig.5.4 (A) Absorption change at 590nm induced by a 500nm pump pulse as a function of pump probe delay time. (B) The same as in A except the sample were deuterated. This data were taken using 540 Hz laser system.

The induced absorption at long times is about 0.5% for an excitation fluence F of $5x10^{14}$ photons/cm^2. The decay kinetics observed at 620nm is consistently observed in this wavelength. Time-resolved absorption probed at 550nm is shown in figure 5.5(C) which differs with the decay kinetics at 590nm and 620nm. This results from the overlapping absorption band of intermediates and rhodopsin, it also indicates that the absorption of intermediates is the same as the absorption of long-lived bathorhodopsin at this wavelength.

The bleaching of absorption is observed at wavelength of 520 nm and 525 nm as shown in figure 5.5(A) and 5.5(B). An unresolved increase in transmission (bleaching) is observed which recovers with a 3.0 ps time constant at 520nm and 525 nm. There is no transmission change after the recovery of the bleaching at 520nm which indicates that 525 nm is the isobestic point between rhodopsin and bathorhodopsin. Thus, absorption changes resulting from rhodopsin depletion are balanced by bathorhodopsin formation. Therefore, an intermediate or unrelaxed bathorhodopsin species must be present for 3 ps. The initial absorption prior to bleaching are observed at 520nm and 525 nm due to the rhodopsin excited state absorption.

It is obvious that time-resolved kinetics can not be fitted by a single exponential rising for the formation of bathorhodopsin using a fitting procedure previously used by Monger et al[4.13-14]. The data is satisfactorily fitted by a double exponential decays, implying two transient species exist between rhodopsin and bathorhodopsin. A least squares fit to the data yields kinetic lifetimes of 200 ± 100 fs and 3.0 ± 0.7 ps for these two decay constants. As discussed below, we assign these species as the excited "Franck-Condon state" and a 90° twisted isomerization intermediate. After photoexcitation, the excited rhodopsin molecule relaxes from it ground state nuclear configuration, which we called Frank-Condon state, along the barrierless first excited singlet potential

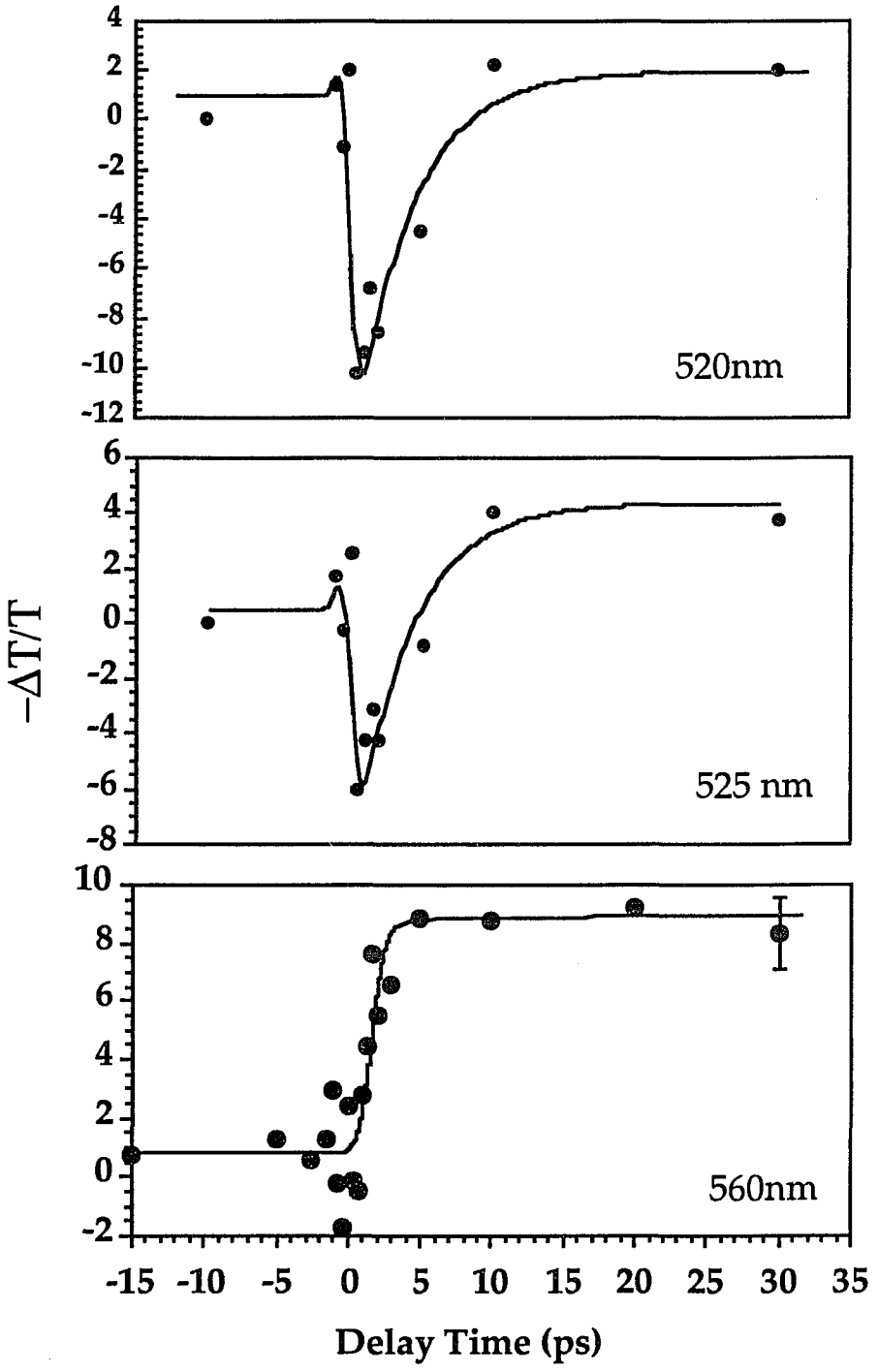

Fig.5.5 Time-resolved photoinduced absorption change at 520nm, 525nm and 560nm as a function of delay time excitation by a 500nm pump pulse. Solid line are fit described in text.

surface of C_{11}-C_{12} torsional angle, as shown in figure 4.5. It twists into a local minimum of a twisted metastable state centered at $\phi_{11\text{-}12}$=90°, which is called 90° twisted state. It then crosses to the ground state photoproduct, bathorhodopsin, or back to repopulate the ground state rhodopsin.

5.3) Time resolved differential absorption spectrum

To complement the isomerization kinetics, the differential absorption spectral measurements over the entire photoinduced absorption wavelength range form 530 to 680 nm are plotted in figure 5.6, These measurements were done with a spectrograph and a dual diode array detector. At the early time (-0.3 to -0.1 ps, note, zero here may not exactly be absolute zero) after excitation, an increase in absorption appears in the wavelength range from 570nm-680nm, which may results from the Franck-Codon state (excited rhodopsin state). Between 0 ps to 0.5 ps, the photoinduced absorption increase and blue shifts until it reaches about λ_{max}=585 nm. We believe this reflects the excited molecule twisting to its 90° twisted configuration, and takes about 200 fs. After 0.5 ps after excitation, the absorption maximum shifts down in wavelength and the magnitude of the photoinduced absorption decreases for about 3 ps. The photoinduced absorption almost stays the same after 5 ps and matches the known bathorhodopsin spectrum indicating that the isomerization is complete on this time scale. This differential absorption spectrum agrees with the kinetic measurement, The initial decay (~200fs) corresponds to the initial blue shift (650nm shift to 585 nm). The slower decay component (3 ps) corresponds to a further blue shift (from 585nm to 575 nm). Therefore, the initial absorption from excited rhodopsin (Franck-Condon region) absorbs more red than the 90° twisted intermediate (3ps species), which also absorbs more red than the long-lived bathorhodopisn. The induced absorption as a function of delay time is

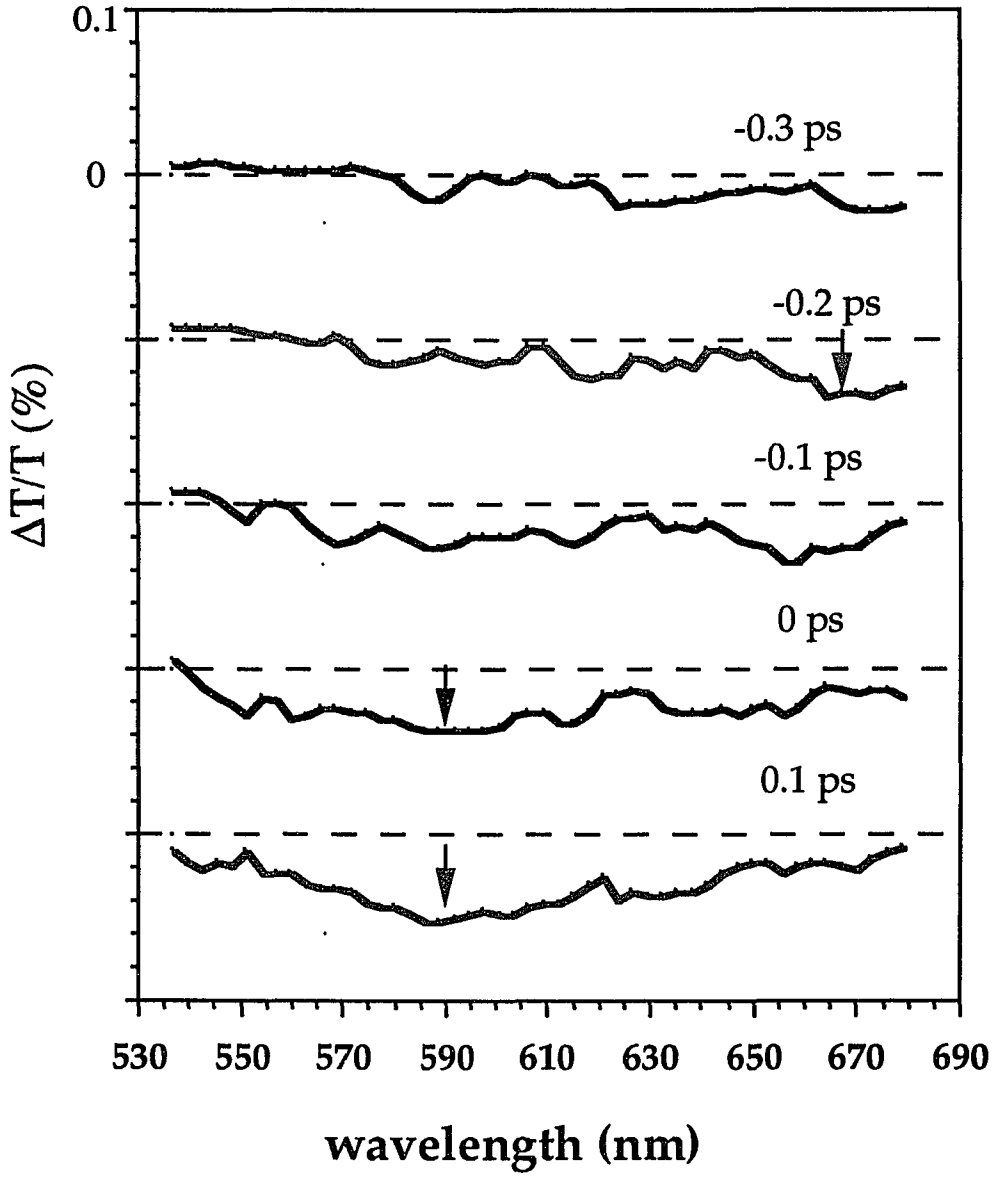

Fig.5.6(A) Differential absorption spectra of rhodopsin at different pump-probe delay time (from -0.3 ps to 0.1 ps) after photoexcitation at 500nm.

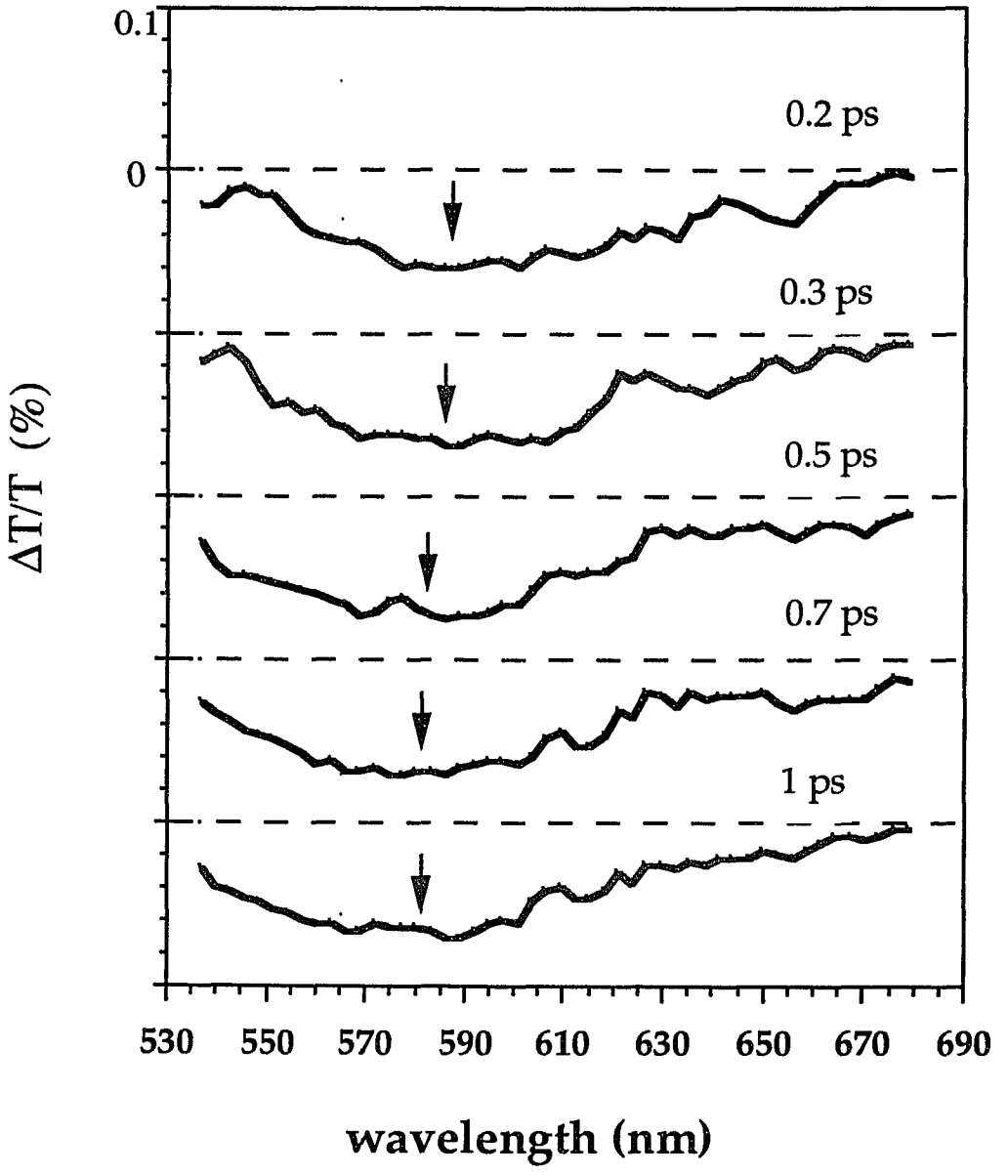

Fig.5.6(B) Differential absorption spectra of rhodopsin at different pump-probe delay time (from 0.2 ps to 1 ps) after photoexcitation at 500nm.

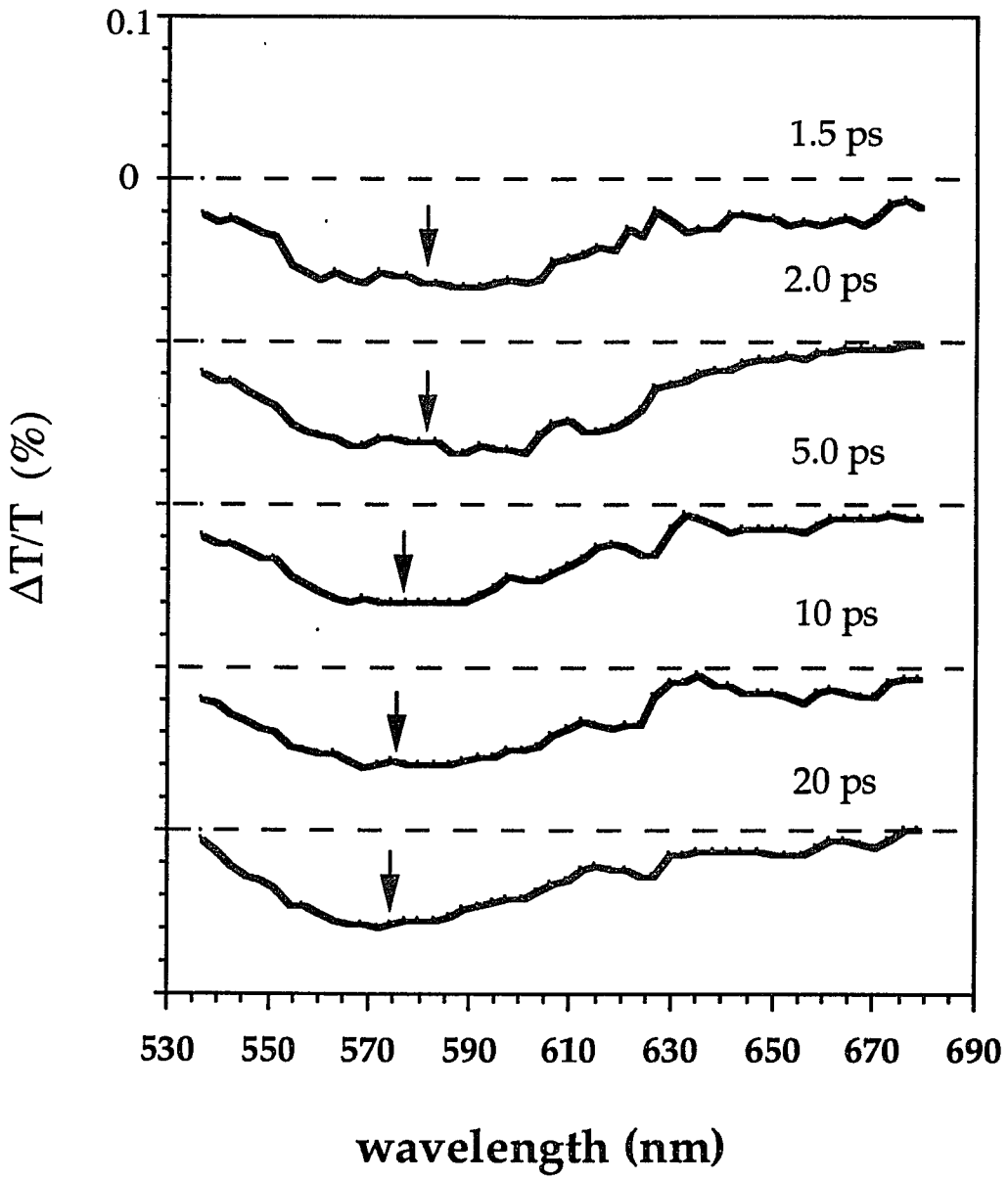

Fig.5.6(C) Differential absorption spectra of rhodopsin at different pump-probe delay time (from 2 ps to 20 ps) after photoexcitation at 500nm.

extracted from the differential absorption spectrum in figure 5.6 and plotted in figure 5.7. The kinetics is same as we discussed above, one may realize that the induced absorption has different kinetics in 540nm and 600nm. The induced absorption keeps a constant after its 200 fs formation time (our instrument resolution) in 540nm. But, the induced absorption decays at probing wavelength of 600nm. This is because the absorption band overlapping between intermediates state and final bathorhodopsin state. We will discuss this absorption spectrum of intermediates later in this text.

5.4) Analysis and Modeling

Time-resolved measurements can be modeled satisfactoryly using two intermediates; the Franck-Condon and 90° twisted state, as discussed above and shown in figure 5.8. The observed photoinduced kinetics can be explained by the absorption of these two intermediates, the relatively long-lived bathorhodopsin isomer and the bleaching of the ground state of rhodopsin. We assume the Frank-Condon state is formed instantaneously after the ground state rhodopsin absorbs a photon and that its spectrum is unique over its 200 fs lifetime. Measurements of the fluorescence quantum yield from this species and theoretical calculations suggest that rotation out of the Frank-Condon region is in the order of a hundred femtoseconds[4.7,4.28], this is in good agreement with the observed 200 fs lifetime of the Franck-Condon transient species. The metastable intermediate 90° twisted state is formed with a time constant τ_1 by following the excited state potential surface, and takes a time constant τ_2 to cross over to the ground state potential surface to form bathorhodopsin with a yield of η or regenerate rhodopsin with a yield of $1-\eta$. The populations of rhodopsin, $N_r(t)$, excited Frank-Condon state, $N_{fc}(t)$, excited 90° twisted state, $N_{90}(t)$ and bathorhodopsin state, $N_b(t)$ are then described by the following rate equations:

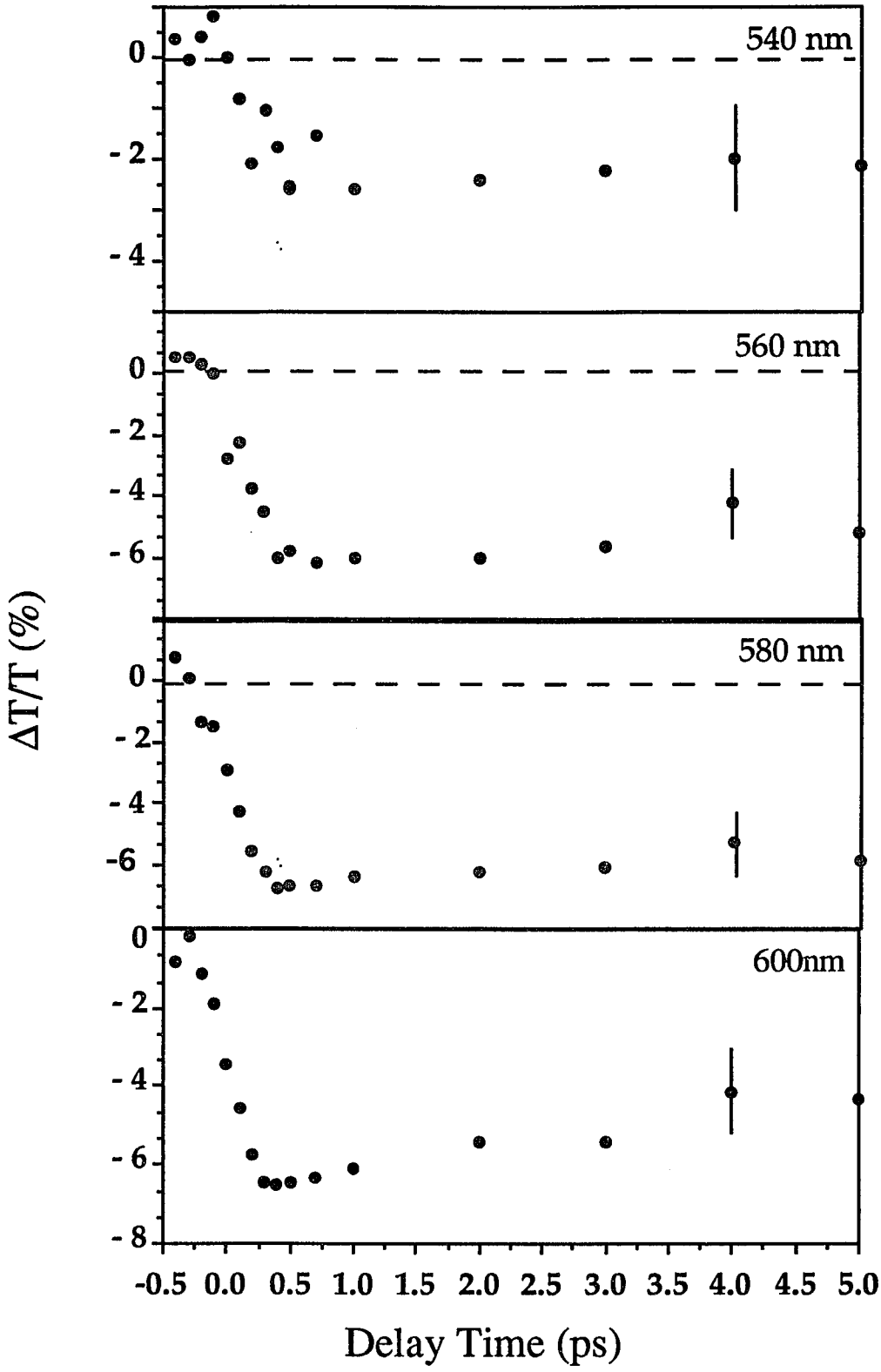

Fig.5.7 Photoinduced absorption at 540, 560, 580 and 600nm as a function of delay time excited by 500 nm.

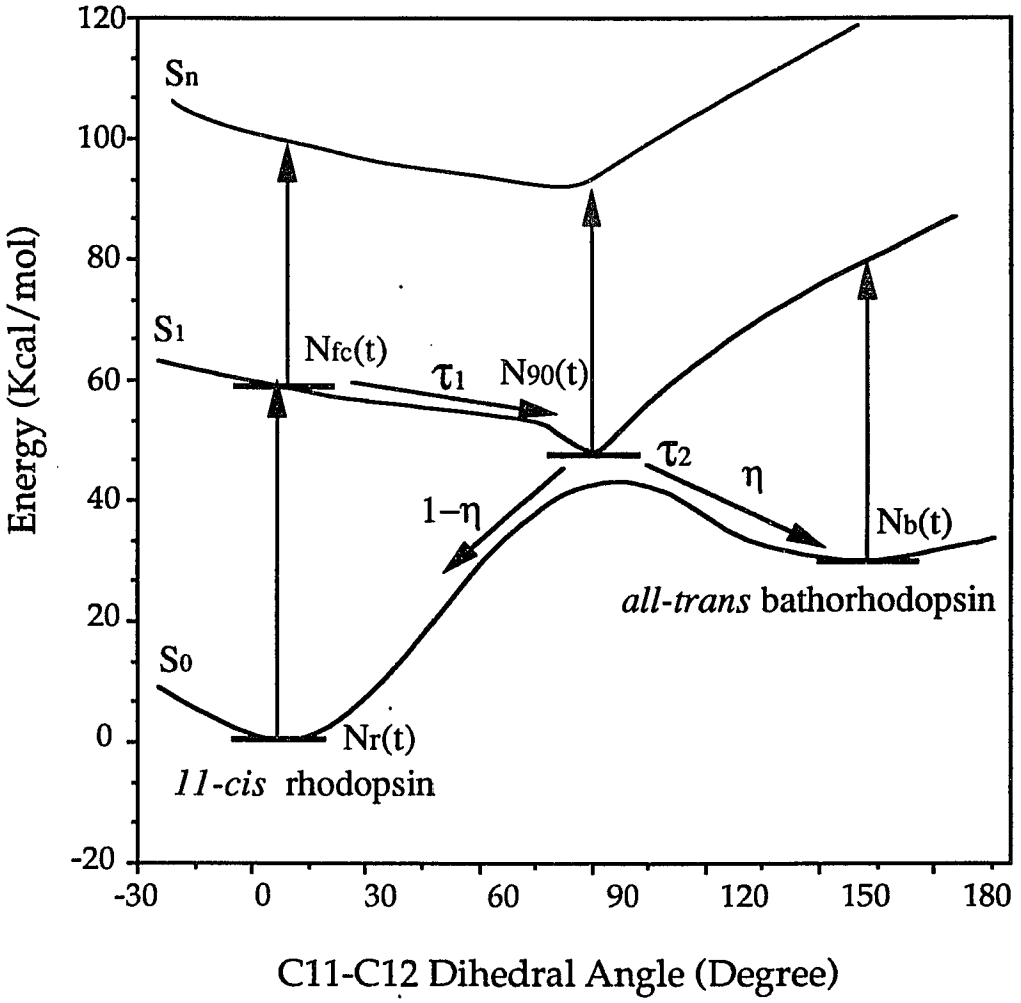

Fig. 5.8 The simplified model (I) of the dynamics along potential surface for the C_{11}=C_{12} dihedral angle. Two intermediates, Rh*(FC) and Rh*(90), are indicated in the figure to represent the metastable states.

$$\frac{\partial N_r(t)}{\partial t} = (1-\eta)\frac{N_{90}(t)}{\tau_2} - \alpha I_p(t)N_r(t)$$
$$\frac{\partial N_{fc}(t)}{\partial t} = -\frac{N_{fc}(t)}{\tau_1} + \alpha I_p(t)N_r(t) \qquad (5.1)$$
$$\frac{\partial N_{90}(t)}{\partial t} = \frac{N_{fc}(t)}{\tau_1} - \frac{N_{90}(t)}{\tau_2}$$
$$\frac{\partial N_b(t)}{\partial t} = \eta\frac{N_{90}(t)}{\tau_2}$$

where $I_P(t)$ is the pump pulse intensity, and η is the quantum yield for rhodopsin to bathorhodopsin conversion .

The total absorption change is described by:

$$\Delta A(\lambda,t)=\sigma_{90}(\lambda)N^*_{90}(t)+\sigma_{batho}(\lambda)N^*_b(t)+\sigma_{fc}(\lambda)N^*_{fc}(t)+\sigma_r(\lambda)(N^*_r(t)-N^*_r(-\infty)) \qquad (5.2)$$

where $\sigma_{90}(\lambda)$, $\sigma_{fc}(\lambda)$, $\sigma_{batho}(\lambda)$ and $\sigma_r(\lambda)$ are the absorption cross-sections of the 90° twisted, Franck-Condon, bathorhodopsin and rhodopsin species, respectively. λ is the probe wavelength. $N^*(t)$ is the convolution of N(t) with the probe pulse $I_b(t)$. $N^*_i(t) = \int N_i(t')I_b(t-t')dt' = N_i(t)\otimes I_b(t)$

$$N^*_i(t) = \int N_i(t')I_b(t-t')dt' = N_i(t)\otimes I_b(t) \qquad (5.3)$$

The kinetic equations 5.1 for four individual populations, $N_{fc}(t)$, $N_{90}(t)$, $N_b(t)$ and $N_r(t)$, are solved analytically using a Gaussian representation of pump and probe pulses, and substitute into eqn.5.2 and 5.3 to obtain the total absorption change $\Delta A(t)$. For detailed calculations see Appendix I. The solution for the total absorption change $\Delta A(t)$ is a two exponential decay convoluted with the pump-probe laser cross-correlation function P(t) as shown in the following:

$$\Delta A(\lambda,t) = (a_1(\lambda)e^{-t/\tau_1} + a_2(\lambda)e^{-t/\tau_2} + a_3(\lambda)) \otimes P(t) \qquad (5.4)$$

where:

$$a_1(\lambda) = \sigma^*_{fc} - \frac{\tau_2}{\tau_2-\tau_1}\sigma^*_{90} + \frac{\eta\tau_1}{\tau_2-\tau_1}\sigma^*_b$$
$$a_2(\lambda) = \frac{\tau_2}{\tau_2-\tau_1}(\sigma^*_{90} - \eta\sigma^*_b) \qquad (5.5)$$

$$a_3(\lambda) = \eta\sigma^*_b$$

where $\sigma^*_i(\lambda)$ is the difference absorption cross-section between i species and rhodopsin, i.e. $\sigma^*_i(\lambda) = \sigma_i(\lambda) - \sigma_r(\lambda)$ here i stands fc and 90° and b for Franck-Condon, 90° twisted and batho respectively.

The photoinduced absorption in different wavelength are fitted using eqn.5.4 to obtain two lifetimes, τ_1 and τ_2, and three amplitude constants, a_1, a_2 and a_3. The fitting results, a_1, a_2 and a_3 can be used to solve using eqn.5.5 for the difference absorption cross sections of the intermediates σ^*_{90} and σ^*_b which are shown in figure 5.9. The photoinduced absorption spectrum of the intermediate, 90° state, is red shifted to that of bathorhodopsin and the amplitude of its maximum is smaller than the maximum of bathorhodopsin.

5.5) Discussion

The kinetics can be well rationalized in terms of rhodopsin to bathorhodopsin isomerization. The Franck-Condon state and the twisted 90° state are two precursors to bathorhodopsin. The dynamic scheme includes these two precursors Rh*(FC) and Rh*(90°) which are described using conventional 11-cis to all-trans isomerization reaction coordinate is given in the following:

$$\text{Rh}^*(11\text{-}cis) \xrightarrow{h\nu} \text{Rh}^*(\text{FC}) \xrightarrow{\tau=200\text{fs}} \text{Rh}^*(90°) \xrightarrow{\tau=3\text{ps}} \text{Batho}(trans) \qquad (5.6)$$

The kinetics measured here agree remarkably well with molecular dynamic simulations of the primary photochemical event in rhodopsin by Birge and his coworkers[3.3,3.8-10]. In these calculations the 90° state is formed in ~400 fs and bathorhodopsin in ~3 ps. The 90° state is calculated to show several significant absorption bands, from Rh*(90°) to several higher excited states, distributed throughout the visible range[3.10]. Our observation of the difference

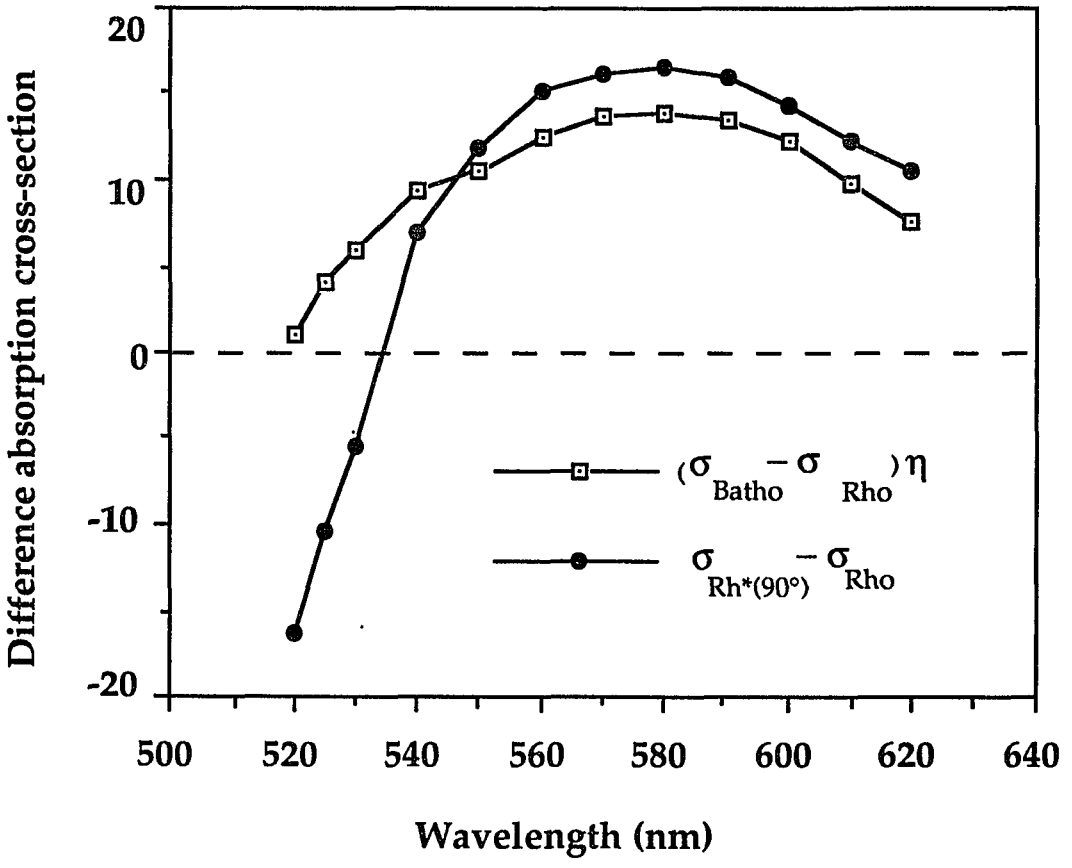

Fig.5.9. The difference absorption cross-section of bathorhodopsin and its kinetic precursor, identified as Rh*(90), minus that of rhodopsin as calculated from our kinetic fits to data. η is the fraction of bathorhodopsin formed from photoexcited species, i.e. quantum yields.

absorption cross-section for Rh*(90°) centered near 580 nm is in reasonable agreement with this.

Similar transient absorption experiments by Schoenlein et al.,[4.33] are interpreted in terms of complete photoisomerization of retinal chromophore in visual pigments occuring in approximately 200 fs. Clearly, the differential absorption spectrum obtained by this thesis and Schoenlein et al. shows that the photoinduced absorption is not stabilized 200 fs after photoexcitation. The stabilized photoinduced absorption, which is maximum at 570nm and distinct as bathorhodopsin, is formed in two step, a fast (~200fs) formation of one metastable species with absorption maximum at 585nm followed by a slow (~3 ps) evolution to a bluer absorption spectrum characteristic of the long-lived bathorhodopsin state.

Due to similar oscillator strength of the metastable state and bathorhodopsin in the wavelength range of 550-570nm, one may not be suprised that the photoinduced absorption does not change after formation of the metastable intermediate at these wavelengths. We use our model shown in figure 5.8 to fit the kinetics data obtained by Schoenlein et al[4.33] with the fitting procedures described above. The fits are very good and depicted in figure.5.10. Obviously, the results of Schoenlein et al can be well described by our two intermediate species model and the absorption cross-sections of intermediates from these fits are depicted in figure 5.11 and agree well with those obtained in this thesis.

Due to the short time resolution they applied, the absorption cross-section of the Franck-Condon state σ_{FC} can be extracted and is red shifted from the cross-section of bathorhodopsin and the 90° twisted state and agrees with the observation of a red shifted Franck-Condon state. Due to their use of discrete probe wavelengths, the shifting of intermediate species to bathorhodopsin is not

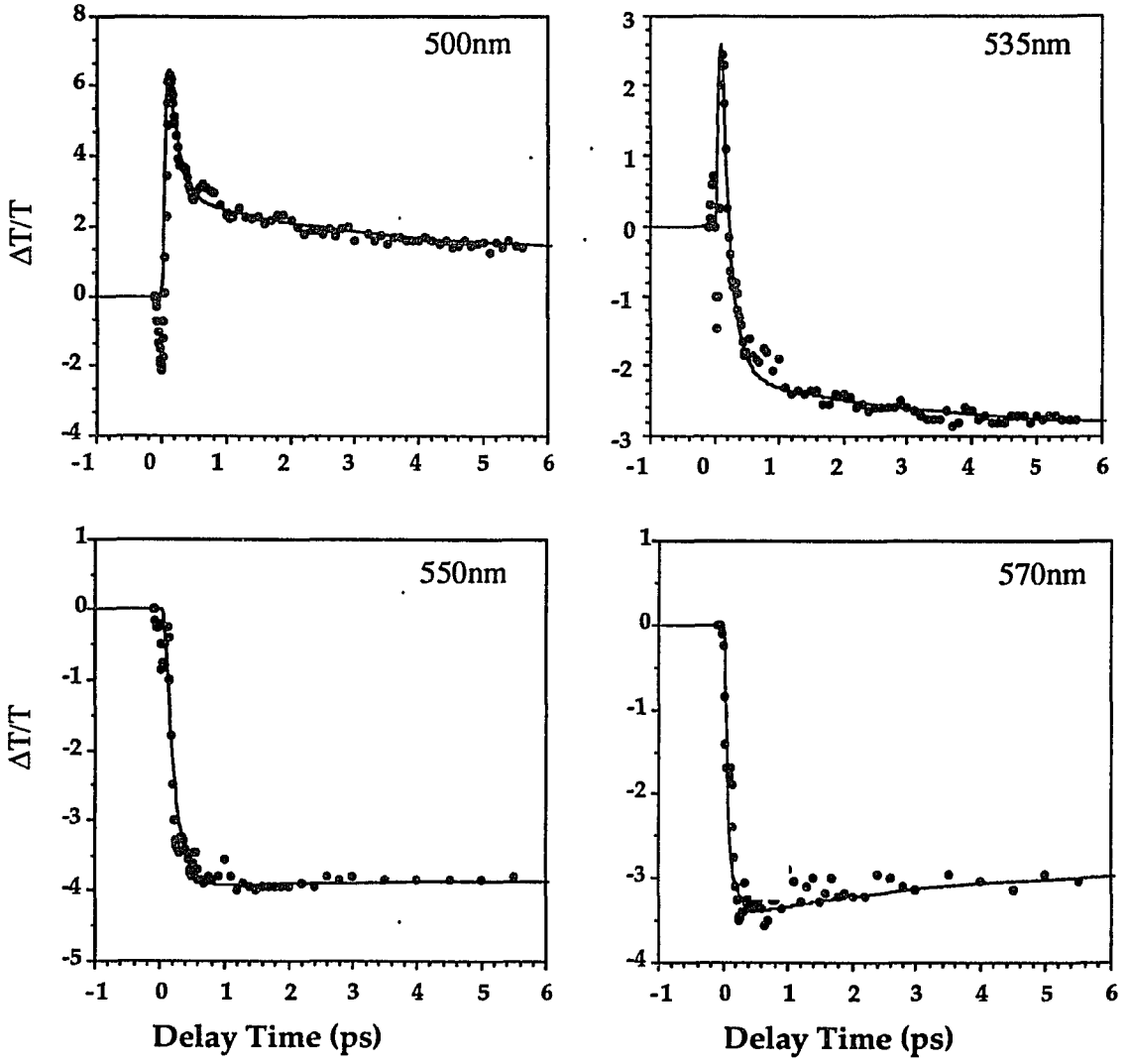

Fig.5.10 The fits the experimental data by Schoenlein using the model of a twisted 90 degree state which described in the text. The dots are the experimental data (from R.W. Schoenlein et al. *Science* **254**, 219 1991) and line are the fits described in the text.

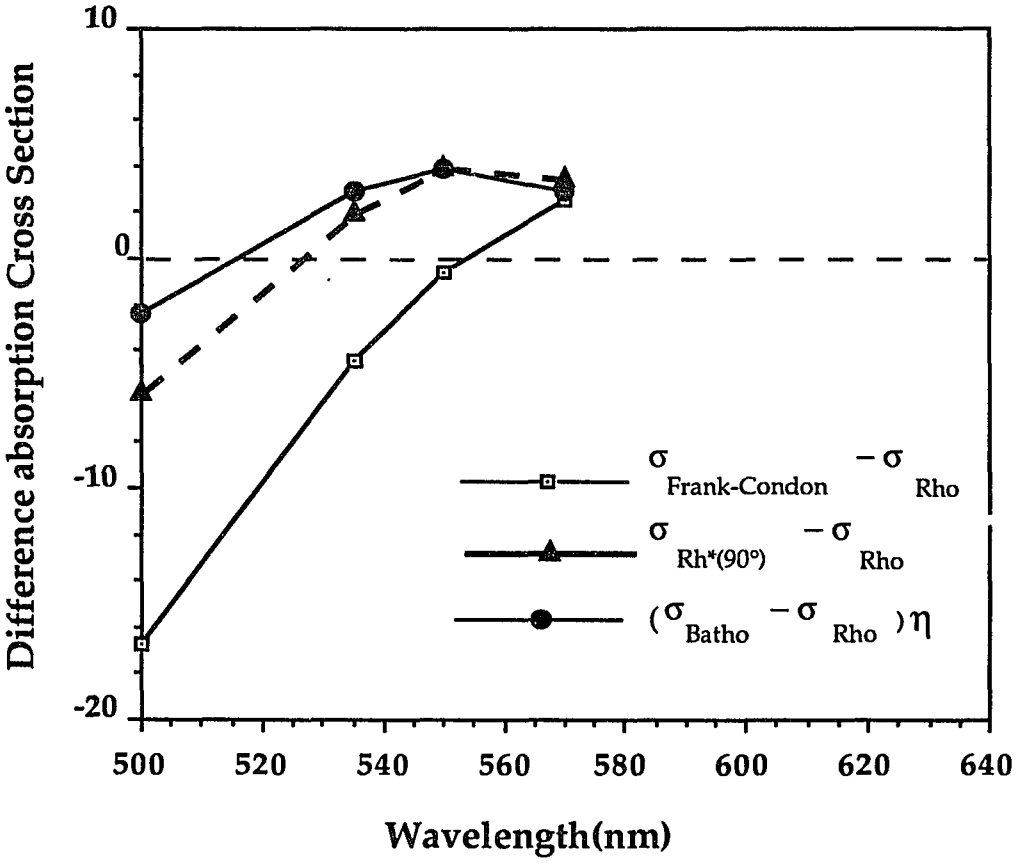

Fig.5.11. The difference absorption cross-section of bathorhodopsin its kinetic precursor Rh*(90) and Franck-Condon state Rh*(FC), minus that of rhodopsin as calculated from our kinetic fits to data obtained by Schoenlein et al. η is the quantum yield to form bathorhodopsin formed from photoexcited species. The horizontal axis is used in such a way so that one can compare this figure with Fig.5.9.

very clear, but our fit to their data extracts the same absorption cross-sections in figure 5.11. We therefore see no need for a new model to explain rhodopsin photochemistry.

Femtosecond absorption and picosecond resonance Raman measurements in bacteriorhodopsin shows that the excited bacteriorhodopsin decays from its Franck-Condon state in about 100-200 fs[4.20-4.24] to the lowest energy state located in the S_1 excited state which is a half twisted state. This excited state dynamics in bactriorhodosin is similar to our scheme proposed in rhodopisn and invokes with the scheme that isomerization is completed within 200 fs proposed by Schoenlein et al.[4.33] In Bacteriorhodopsin, the half twisted state decays to a ground state, J, which most resarchers consider as a 13-cis form[3.2,4.8,4.24] in 500 fs and then take about 5 ps to form the 13-cis retinal K state.

We will further discuss whether the metastable species is an excited state twisted at 90° or a ground pre-bathorhodopsin state in rhodopsin. As was pointed out earlier, such metastable pre-batho state has been discuss by many authors, such as the batho' state by Honig[3.7] and photorhodopsin by Shichida[4.18]. We therefore summarize the kinetic scheme, here called model II, as follows:

$$\underset{}{\text{Rh(11-}\textit{cis}\text{)}} \xrightarrow[h\nu]{} \underset{}{\text{Rh}^*(S_1)} \xrightarrow[200\text{fs}]{} \underset{}{\text{batho'(photorhodopsin)}} \xrightarrow[3\text{ ps}]{} \underset{}{\text{batho(all-}\textit{trans}\text{)}} \qquad (5.7)$$

the ground state batho' (or photorhodopsin) is formed from the excited rhodopsin in 200 fs. This dynamic schematic is depicted in figure 5.12. Photorhodopsin has been suggested as an all-trans chromophore at the C_{11}-C_{12} bond with nearby single bonds highly distorted [4.18]. According to Honig et al this fast isomerization is not temperature or deuterium dependent. The second step is the formation of bathorhodopsin, which involves proton translocation according to Honig et al [3.7]. The measurement of Peters et al [4.30] suggested this proton

translocation process is temperature and deuterium dependent. According to our measurement (figure 5.1) deuteration of rhodopsin has no effect on the dynamics. Therefore, there is no deuteration effect on the isomerization dynamics at 295 K which is different than in the case of low temperature measurement.[4.30] This is consistent with the first twisted 90° metastable model that the simple isomerization reaction described above will be unaffected since the viscosity and dielectric properties of the solvent and chromophore environment are nearly identical in H_2O and D_2O. Low temperature experiments with sub-picosecond resolution should further clarify this point.

The maximum absorption cross-section of the 90° state is smaller than that of relaxed bathorhodopsin, but larger than that of rhodopsin. This agrees with the model of a 90° twisted state because the more planar all-trans bathorhodopsin has the larger oscillate strength. Based on the pre-batho ground state model, only a fraction η of the excited rhodopsin molecules is converted into the pre-batho intermediate state, as shown in figure 5.12. Similar rate equations as eqn.3.2 can be written. (see Appendix I) We found that changing eqn 3.2 is equivalent to substituting $\sigma_{b'}$ to $\eta\sigma_{90}$ (see proof in Appendix I). According to this model the absorption cross-section of the 200 fs pre-batho intermediate would be larger than the relaxed all-trans bathorhodopsin. This contradicts the fact that the all-trans configuration chromophore in batho has a larger absorption cross-section than any partial unrelaxed or twisted state.

Further, the photorhodopsin or batho' proposed in model II is formed from the common excited state as is the recovery of ground state rhodopsin. The recovery of the ground state shows two decay kinetics, 200 fs and 8 ps, while the formation of photorhodopsin is only within 200 fs. Therefore, the 8 ps bleach recovery is inconsistent with the complete isomerization in 200fs.

Further more, the recent femtosecond time-resolved absorption

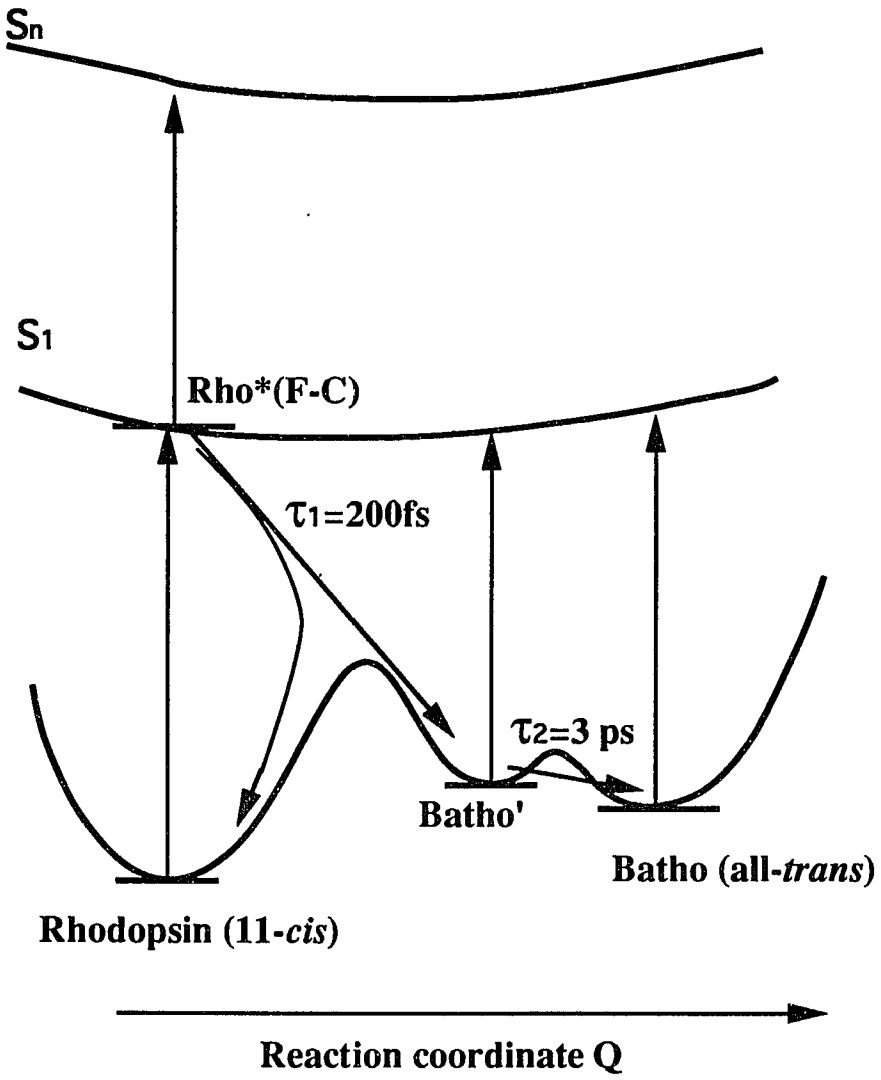

Fig.5.12 Schematic potential surface for cis-trans isomerization model (II) described in the text. A metastable state which formed within 200 fs after photoexcitation is treated as a pre-batho ground state, called batho', which relaxes into fully isomerized batho in 3 ps.

measurements in octopus rhodopsin by Kobayashi's group [5.2] observed similar kinetics of photoinduced absorption. The photoinduced gain in the wavelength range (860-920nm) was measuremed with a lifetime about 2 ps and 4 ps for protonated and deuterated octopus rhodopsin, respectively. In our point of view, this gain observation supports that the excited state species has a lifetime of about 2-4 ps, which agrees with our model that the half twisted intermediate state is an excited state species. The further experiment looking for the stimulated emission of bovine rhodopsin might help to distinguish weather the intermediate state is an excited state or a pre-batho state. Our work fail to observe gain in cattle rhodopsin in the wavelength range from 700nm to 1000 nm.

As a summary, it is inadequate to consider the 200fs intermediate state as a pre-batho ground state or to assume that the isomerization is complete within 200fs. We believe that the experimental data indicate that the intermediate state formed within 200 fs is a twisted 90° excited state.

5.6) Conclusion and application

We have presented experimental evidence for the initial step in vision. The kinetic can be well rationalized in terms of rhodopsin to bathorhodopsin isomerization. The potential surfaces along the 11-*cis* (rhodopsin) to 11-*trans* (bathorhodopsin) reaction coordinate have been theoretically characterized [3.3,3.8-10] and are depicted schematically in figure 5.13. The formation of bathorhodopsin starts by exciting rhodopsin to the vertically excited Frank-Condon species, $Rh^*(FC)$. The Franck-Condon state relaxes to a 90° twisted around 11-double bond of retinal which takes 200fs. The twisted state is electronically excited and decays in 3 ps to either complete isomerization or recovery of rhodopsin. The dynamics of the primary photochemistry of vision are well described by figure 5.13 via the potential surface for cis-trans isomerization.

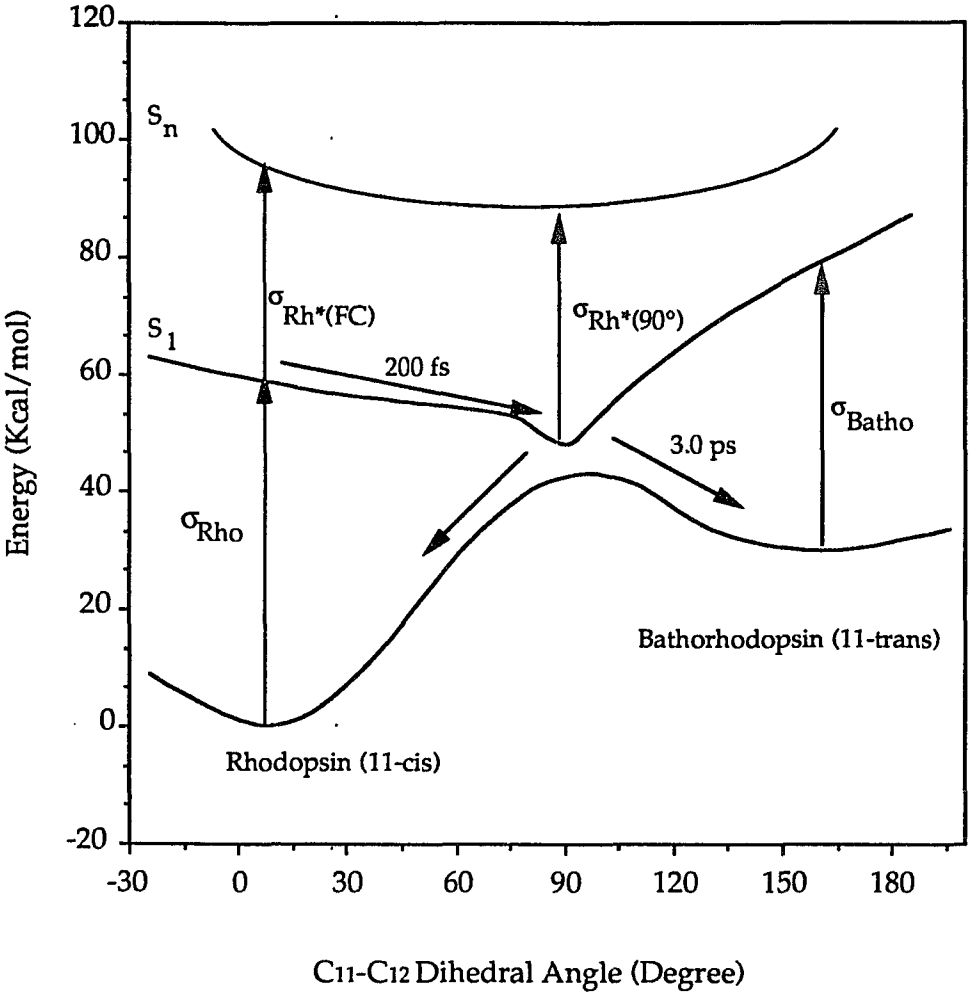

Fig.5.13 The model of first step of vision described by the schematic potential surface for the cis-trans isomerization. A metastable state twisted at 90 degree forms in 200fs and takes in 3 ps to complete the isomerization to form bathorhodopsin and repopulate the ground state of rhodopsin.

The isomerization of the primary visual process has been found remarkably efficient and fast. The process is completed in 3 ps with two third quantum yield for absorption of a photon. This efficiency and speed allow enough energy to be stored in the protein for further transfer to the nerve system. The agreement of the experimental results and the theoretical model calculations may give us some understanding of retinal and protein bonding and interactions.

The isomerization resulting from the absorption spectrum shift may provide an ultrafast optical trigger. The optical pulse acts as a trigger to start the isomerization of the chromophore so that a channel opens to store the photon energy as chemical energy and for further transfer into an electrical signal to map the visual picture to the brain. The ultrafast speed of this energy storage system explains the high efficiency of the visual system. Therefore, in a simple optical switch using rhodopsin a 500nm light can quickly turn on an absorption within transparent wavelength region(600nm-700nm) to switch off a signal at 600nm. The switching time is only limited by the formation time of the metastable state (200 fs).

Chapter 6 Structure and Fundamental Excitations in Conjugated Polymers

6.1) Introduction

In this chapter, I will describe the molecular configuration and various bonding in conjugated polymers. I will discuss the model of one dimensional conjugated polymer which leads to the classification of two kinds of conjugated polymers by their degeneracy in the ground state. The characterization of carriers in conjugated polymers are quite different from the electrons and holes in metals and semiconductors. I will introduce the basic concept of the "lattice dressed" excitations, such as solitons, polarons and excitons, in degenerate ground state and non-degenerate ground state conjugated polymers.

6.2) Structure of Conjugated Polymers

Usual organic polymers are insulators since all of the four carbon valence electrons are tied up in covalent bonds. The atoms in most familiar semiconductors are crystallized in the diamond or zincblende structure and have four nearest neighbors. The carbon atoms in conjugated polymers have only three nearest neighbors. Therefore, the bonding configuration no longer consists of sp^3 hybrids, but contains sp^2 hybrids directed towards the three nearest neighbors, plus one P_z orbital which is perpendicular to the sp^2 hybrids and thus perpendicular to the polymer backbone, which are shown in figure 6.1.[6.1-6.3] The three valence electrons forming sp^2 hybrids are strongly coupled to each other to form a σ bond and contribute to the rigidity of the polymer. The fourth electron occupies the unpaired P_z orbital. There is a small coupling, on the order of 2.5 ev, between the P_z orbitals on neighboring carbon atoms. The band is formed by the coupling between P_z orbital is called the π bond. These π electrons are delocalized principally along the chain and contribute to the electronic

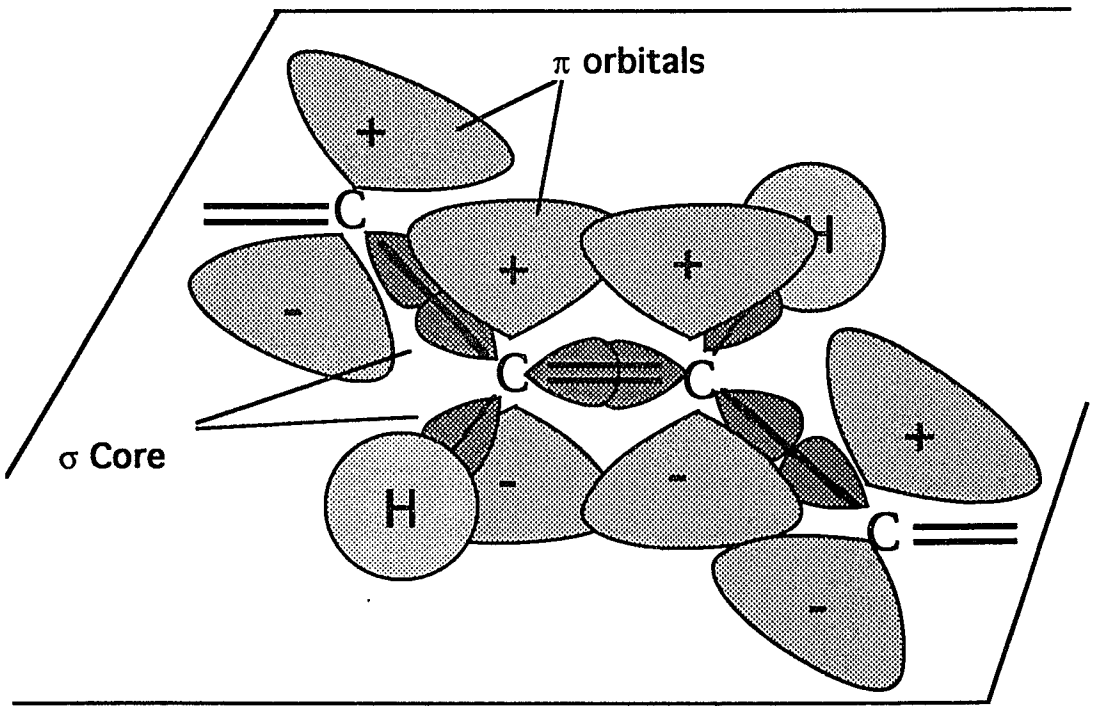

Pz (π) orbital

sp^2 orbital

H hydrogen

C carbon

Figure 6.1 $sp^2(\sigma)$ and Pz (π) orbits of carbon in t-PA

properties studyed here. Therefore, these system are electronically essentially one dimensional[6.1-6.3] and exhibit semiconductor properties which is the topic this thesis focuses on.

The unpaired π electrons are stabilized by dimerization of the lattice structure which leads to the formation of short (double) bonds and long (single) bonds, see Appendix II. The ground state property of the dimerized polymer is described by the Su-Schrieffer-Heeger(SSH)[6.4] model. By considering the electron and phonon coupling, the Hamiltonian of the simplest polymer, polyacetylene, can be written as[6.4]:

$$H=-[t_0+\alpha(u_n-u_{n+1})](C^+_{n+1}C_n+C^+_nC_{n+1})+\frac{K}{2}(u_n-u_{n+1})^2+\frac{M}{2}(\frac{du_n}{dt})^2 \qquad (6.1)$$

where $t_0+\alpha(u_n-u_{n+1})$ is the linear approximation of the transfer integral, C^+_n and C_n are the creation and annihilation operators for a π electron on the nth C atom. For the ground state, $\frac{du_n}{dt} = 0$. The dimerized displacement of atoms form equally spaced lattice point is written as $u_n= (-1)^n u$. By replacing these condition and doing a Fourier transform to diagonalize the Hamiltonian matrix, one obtains the energy change after dimerization as:

$$\Delta U(u) = -\frac{8N}{\pi}[\ln(\frac{2t_0}{\alpha u})-\frac{1}{2}]\frac{\alpha^2u^2}{t_0}+2NKu^2 \qquad (6.2)$$

The plot of ΔU vs the displacement u is shown in figure 6.2(a). Two minimum of $\Delta U(u)$ occur at $u=\pm u_0$ which define the two degenerate lattice structures formed by exchanging the "single" and "double" bond as shown in figure 6.2(a). This kind of polymer is called a degenerate ground state (DGS) polymer. If after exchanging the "single" and "double" bonds (mathematically replace u_0 with $-u_0$), the polymer has no longer the same energy it is called a non-degenerate ground

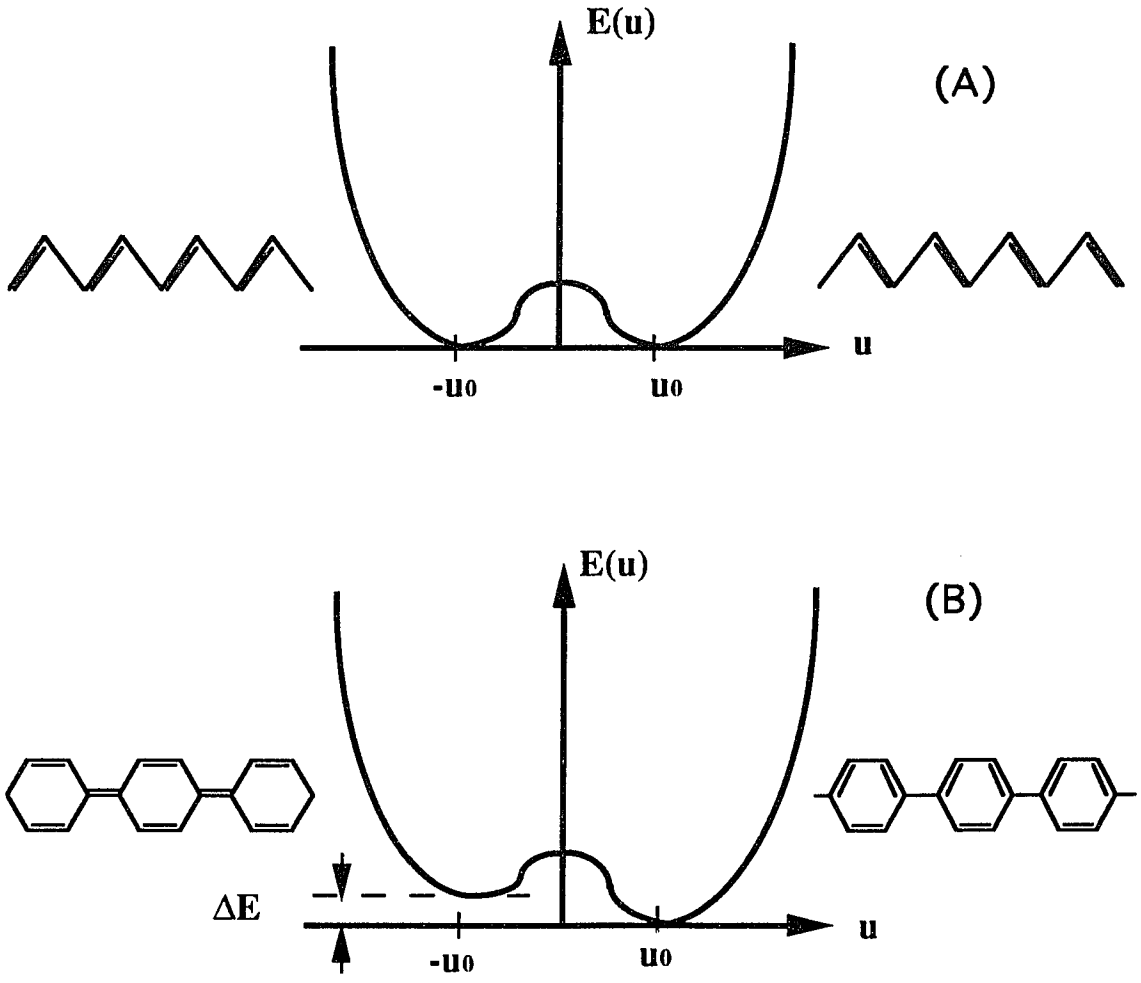

Fig.6.2 The energy diagram of a degenerate (A) and a non-degenerate (B) ground state 1-dimensional polymer. Two minimum energy are corresponding to the two dimerized structures shown at side.

state (NDGS) polymer and the energy of the two ground states differ by ΔE as shown in figure 6.2(b). The corresponding two polymer structures are indicated in figure 6.2(b). The two possible dimerized lattice structures (with zero or a small energy shift) lead to self-localized nonlinear excitations such as solitons and polarons due to the strong electron-phonon coupling after doping or photoexcitation. In a DGS polymer, such as *t*-Polyacetylene (*t*-PA), the value for the dimerized displacement u_0 is about 0.04 Å, it is much less than the typical displacement value of 0.1 Å in organic materials which equals half of the difference between the length of "single" and "double" bond.[6.1-6.3] Therefore, the π electrons in conjugated polymers are delocalized along the chain.

6.3) Fundamental excitations

A. Solitons

In degenerate ground state polymers, such as *t*-polyacetylene, the solitons are the major carriers. A soliton is a quasi-particle defect in the SSH model[6.1-6.3], in which, the carbon lattice is distorted between the chain with two different dimerized structure that exchange the single to double bond as shown in figure 6.3(A). Due to the energy degeneracy in the two dimerized structure, the "defect" can move freely along the chain without requiring excess energy to change bonds in these two phases, so it is called a soliton. The electron distribution of a soliton is localized around the distorted lattice atoms and the associated energy band lies in the middle of the energy gap. A soliton can be either neutral in charge with the spin 1/2, or have a $\pm q$ charge with spin 0. Their energy bands and related optical transition are shown in figure 6.3(B) where the coulomb interaction is neglected. Su et al [6.4] have calculated the lattice displacement distribution of soliton between the segment of two degenerate configurations. By minimizing the adiabatic energy, one obtain the displacement as:

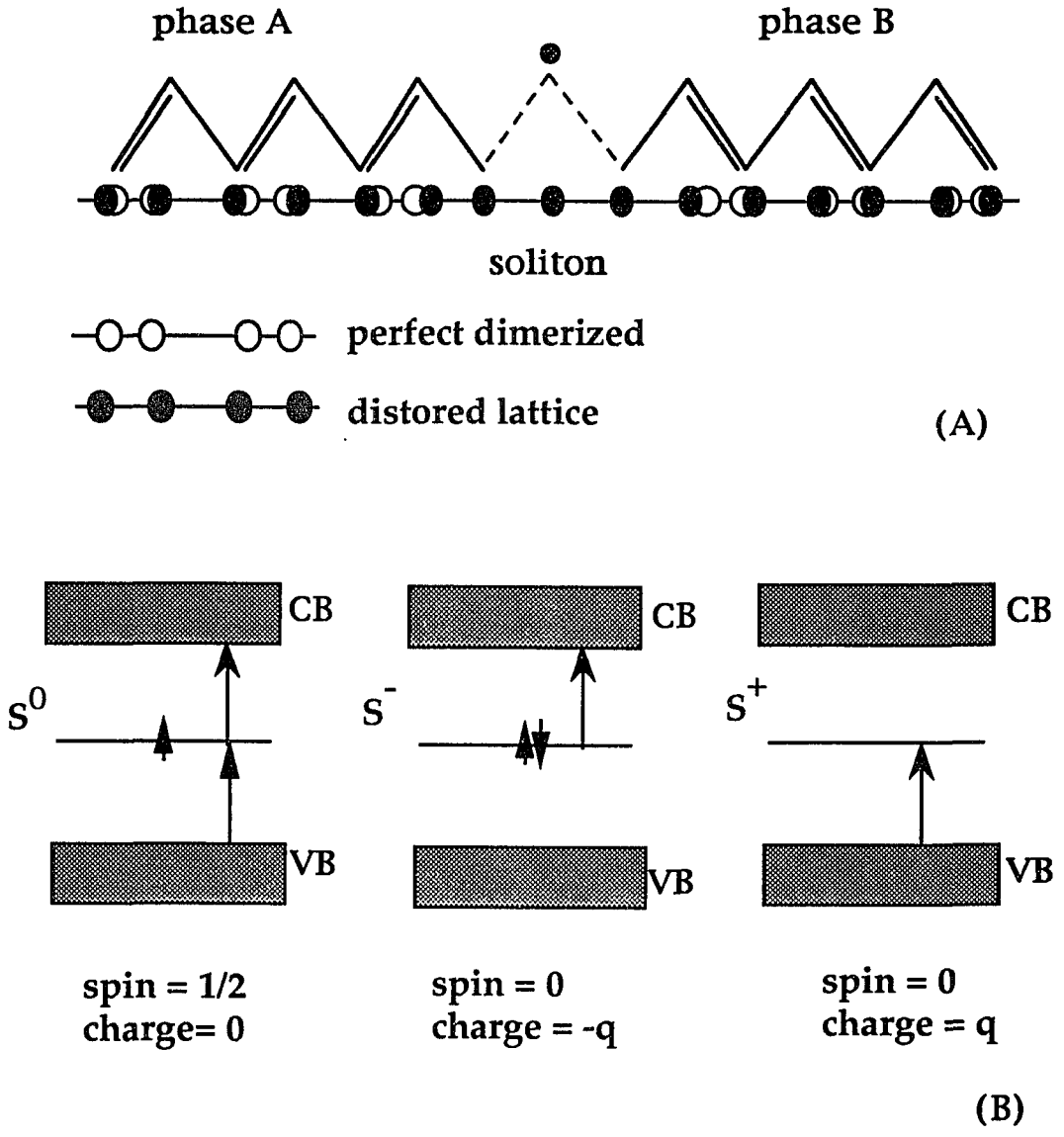

Fig. 6.3 Schematic diagram of lattice structure of a soliton (A) and the energy diagram and optical transitions (B)

$$u = u_0 \tanh[\frac{(x-x_0)a}{d}] \qquad (6.3)$$

where d=~7a for the SSH set of parameters. About 14 atoms are affected to form a soliton. The soliton associated mid-gap state is formed by removing a state from the two valence bands.[6.4-6.6] Since the isolated soliton is a topological defect, only soliton pairs can be generated by photoexcitation. In the NDGS polymers studied in this thesis, a single soliton can not exist since the ground state is not degenerate in energy, therefore, the soliton has to exist in pairs. The soliton pairs can form either single charged polarons, double charged bipolarons or neutral excitons by combination of different charges (or neutral in charge) carried by solitons. A polaron is a pair of a charged and neutral solitons, a bipolaron is a pair of solitons with same charge and an exciton is a pair of soliton with different charge. These are three major excitations in NDGS polymers.

B. Polarons

A single charged polaron is a bounded state of a charged and a neutral soliton pair as shown in figure 6.4. A polaron has either a positive or a negative charge +e with spin 1/2. The displacement of a polaron is given by[6.2,6.7]:

$$u=u_0+ \frac{u_0}{2} [\tanh(\frac{x-x_0}{2l}) - \tanh(\frac{x+x_0}{2l})] \qquad (6.4)$$

where x_0=l/2 ln(1+$\sqrt{2}$) ~ 0.623l ~2a. Therefore, a polaron is the superposition of a soliton and an anti-soliton pair, it can be thought of as a quasi-particle of an electron or hole strongly coupled with a locally distorted lattice on a perfect dimerized polymer chains. This is the same as the conventional description of polarons in solid state physics. A polaron is formed by isolating the charge in different chains by photoexcitation or doping. The structure and optical transitions of polarons is shown in figure 6.4. There are there optical absorption bands involving the transition from gap state to the either valenece band and

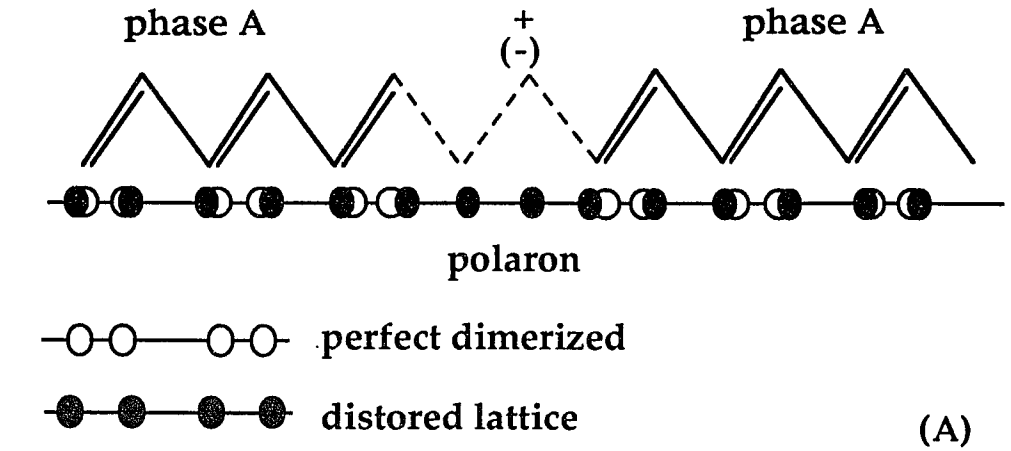

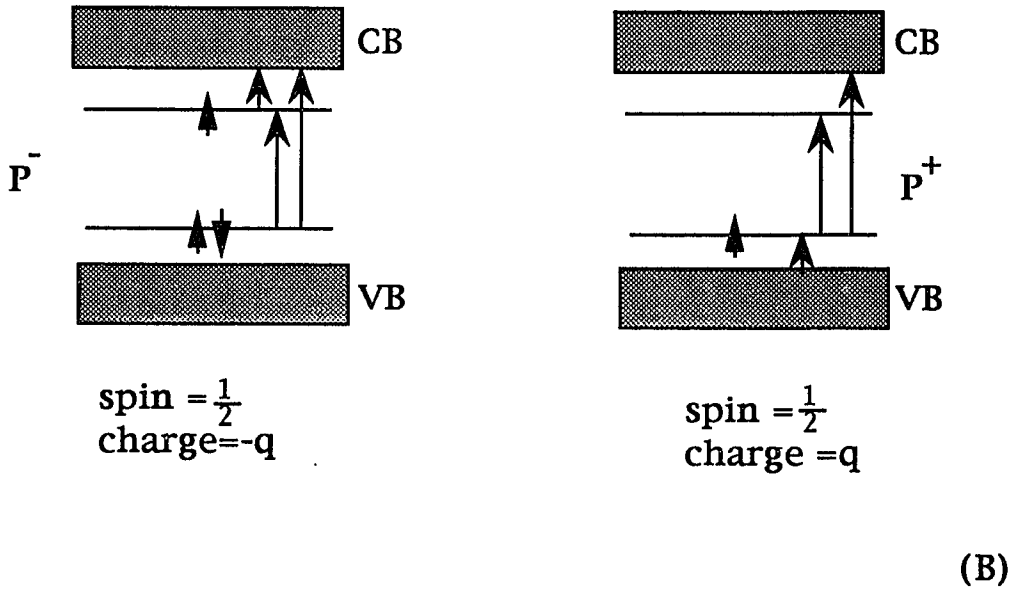

Fig. 6.4 Schematic diagram of lattice structure of a polaron (A) and the energy diagram and optical transitions (B)

conducting band due to the electron occupancy of the gap state.

C. Bipolarons

A double charged bipolaron is a bounded state of two solitons with the same charge as shown in figure 6.5. In a NDGS polymer, the ground state degeneracy is weakly lifted as shown in figure 6.2(B) so that soliton pairs can not separate because of the excess energy required to extend a segment with high energy dimerized structure[6.1-6.3,6.7]. A bipolaron can be thought of as a confined pair of like charged solitons. I will use PPV as an example of a NDGS polymer. In figure 6.5(A) the part of the polymer unit in the dimerized structure (phase A) between the soliton and the antisoliton pair has higher energy, E_a, than the energy E_b in the rest of the polymer (phase B). The excess energy $\Delta E = (E_a - E_b)l$ is proportional to the length l of the polymer in phase A. The polymer wants to lower its energy by reducing the segment length l of its high energy phase A. Therefore, that part of the geometric distortion in the chain is acting like an attractive force, which is balanced by the Coulomb repulsive force between the soliton and anti-soliton which have charges of the same sign. In bipolarons, the gap state is split into two symmetric states[6.7], the energy diagram of the bipolaron, its population and the related optical transitions are shown in figure 6.5(B). One may note that only two optical transitions from gap states to continuum band are allowed in bipolarons rather than the three in polarons due to the different occupancy in the gap states. From this, the polaron and bipolaron can be distinguished by their optical transitions.

The major charge carriers, namely, polarons and bipolarons, in conjugated polymers are "dressed" with lattice distortions which is quite different from electrons and holes in conventional organic and semiconductor materials. the picosecond measurements are expected to lead to an understanding of how these

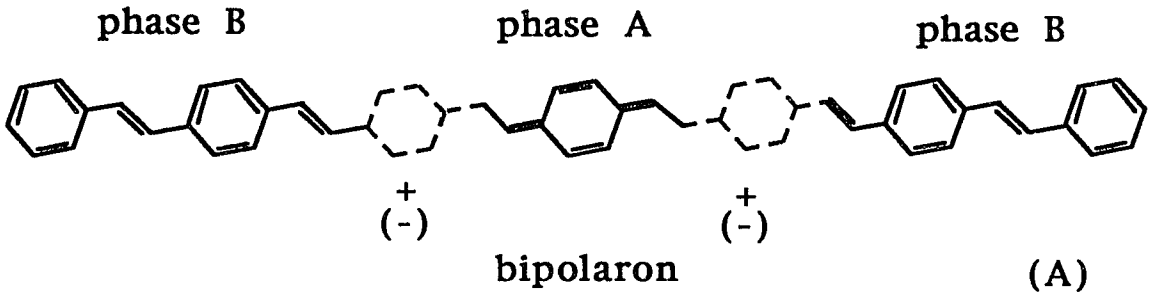

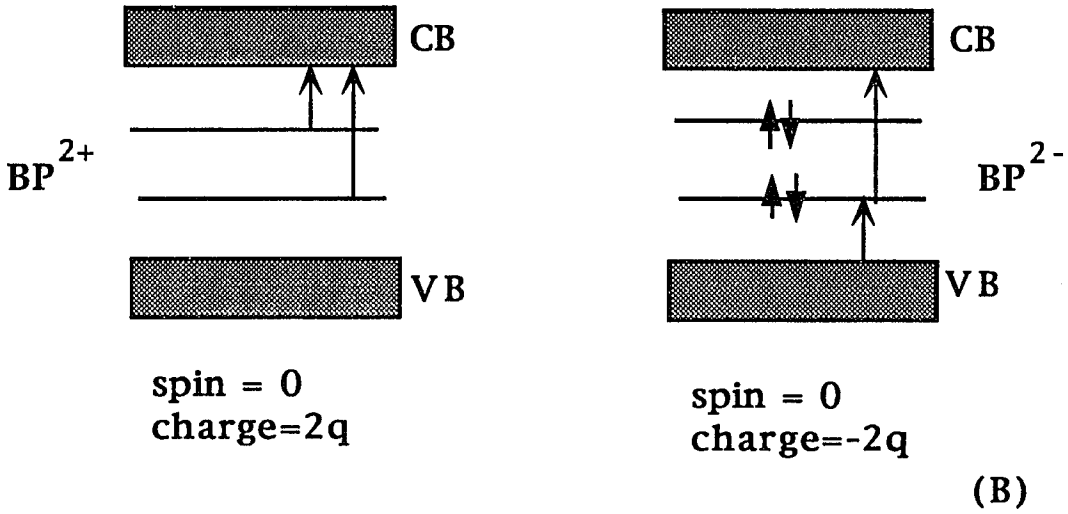

Fig. 6.5 Schematic diagram of lattice structure of a bipolaron (A) and its energy diagram and optical transitions (B)

charged carriers are formed and to study their transport properties from the diffusion of electron-hole pairs created by photoexcitation. The understanding of charged carriers are important for polymer physics and polymer device applications.

D. Excitons

Besides charged carriers in conjugated polymer, such as polarons and bipolarons, neutral excitations are formed by two bound opposite by charged solitons as shown in figure 6.6(A) (or polarons or also free electron and hole). Neutral excitations are generally called excitons. Due to the strong electron-phonon interaction, these excitons are "dressed" with localized phonons. Therefore, an exciton in conjugated polymer is also called a "polaron exciton" [6.8] or a "self-trapped exciton" [6.9]. Excitons can be either spin half for singlet excitons or spin one for triplet excitons. The energy diagram of both excitons and related optical transitions are shown in figure 6.6(B).

Using the same argument as previously used to explain why a bipolaron is a stable quasi-particle, one may show that a singlet exciton is not a stable configuration because the attractive Coulomb force can not be balanced by the partial lattice distortion. The singlet exciton is distinguished by its radiative recombination emission as shown in figure 6.6. which corresponds to the transition from a high energy state to a low half filled energy state.

A triplet exciton, Two bound charge carriers with parallel spin, is expected to be more stable than a singlet exciton since the transition from the triplet manifold to the singlet ground state is forbidden, therefore triplet exciton has a long radiative lifetime about a millisecond.

These elementary excitation discussed in this section will be used to describe the temporal kinetics in PPV.

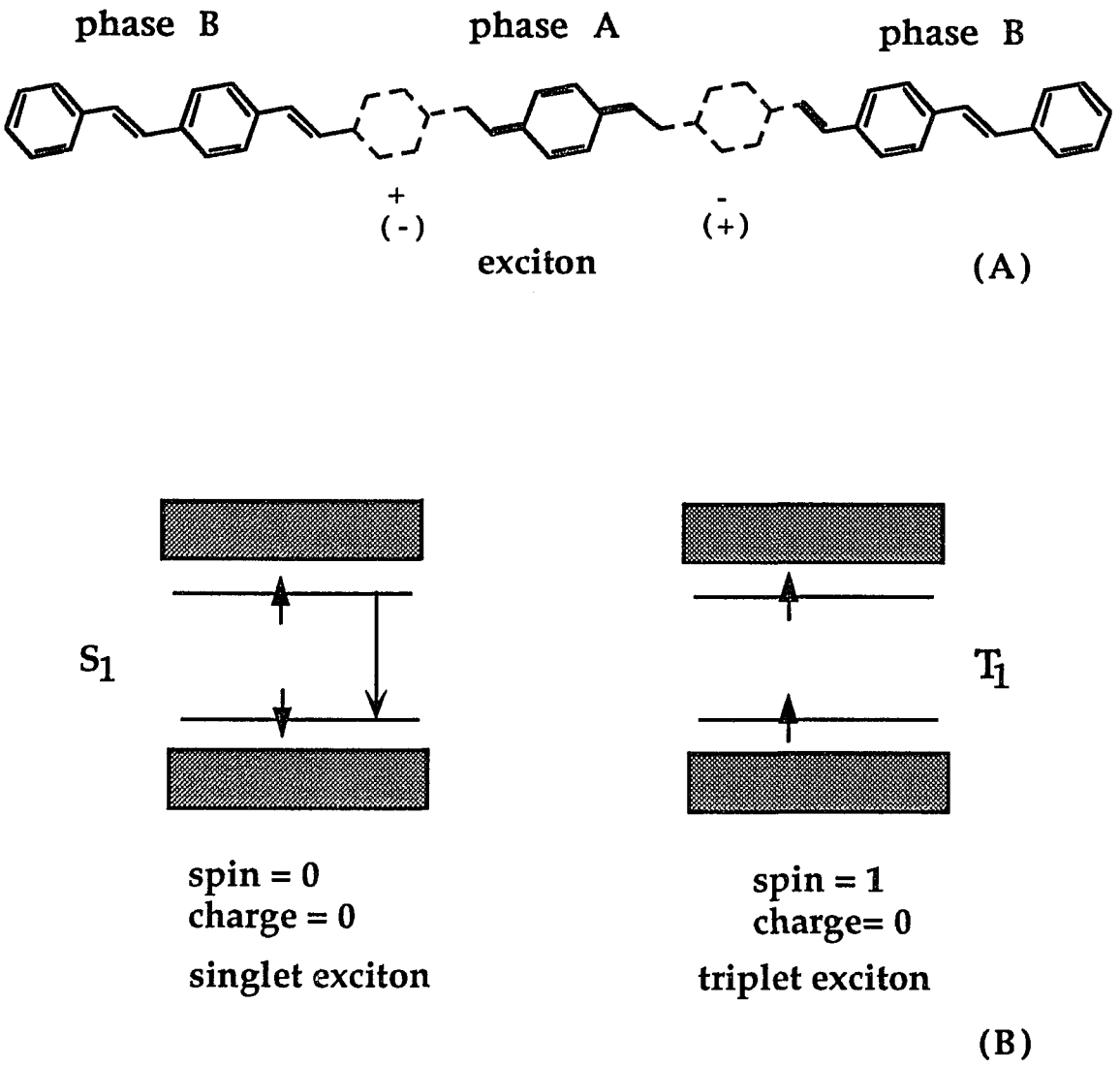

Fig. 6.6 Schematic diagram of lattice structure of a singlet exciton and a triplet exciton (A) and their energy diagram and optical transitions(B)

E. Material - Streatch oriented poly(p-phenylene vinylene) (PPV) films

The molecular structure of PPV and the oriented films are shown in figure 6.7. The polymer structure of PPV consist phenylene rings connected by vinylene groups. Due to rigidity of phenylene groups, PPV polymer has the most stable structure in conjugeted polymers which have been studied.[6.8]. The PPV film stable in high temperature, and has a good mechanic stabilities. The large quantum efficiency of photoluminescence and electron injection luminescence has made this material be interested recently. The LED device and p-n junction device have been developed recently.[1.8] But the mechanism and kinetics of the excitations in PPV films are still unknown.

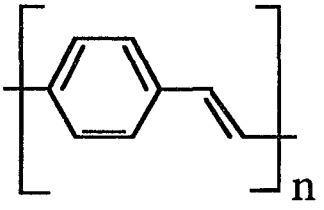

(A)

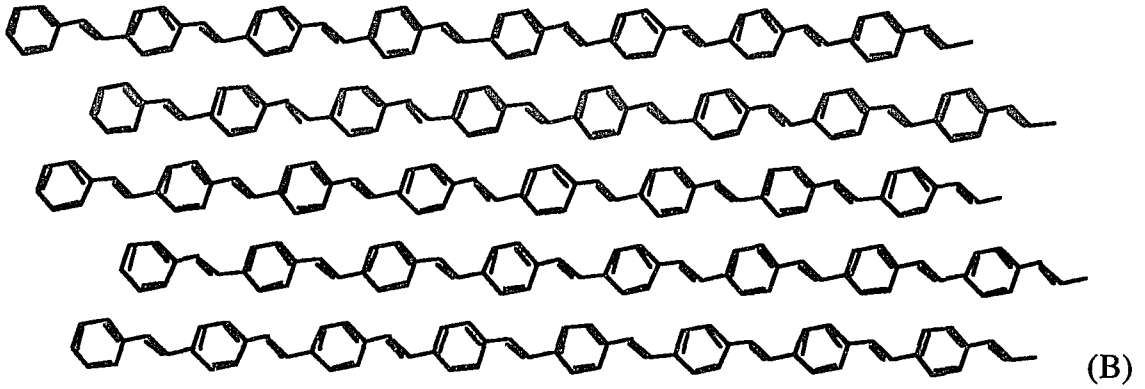

(B)

Fig.6.7 (A) Molecular structure of poly(*p*-phenylene vinylene) (B) the strectch oriented PPV films. The strectch ratio is about 6:1.

The picosecond experiments performed in this thesis are expected to lead to the understanding of the dynamics of excitons in terms of their absorption and luminescence. The singlet and triplet exciton intersystem transition is also of

interest in such electronic and vibrational coupled system. These excitonic and vibrational information will contribute a great deal to the understanding and development of electroluminescence devices[1.8] using PPV films.

Chapter 7 Previous Experiments on Excitations and Carrier Dynamics in PPV films

7.1) Introduction

The elementary excitations in PPV are single charged polarons, double charged bipolarons, and neutral excitons with spin half if they are singlet exciton and spin one if they are triplet excitons. Many experiments have been performed to test the existence of these excitations in conjugated polymer since the synthesis of polyacetylene in 1974 by Schirakawa and colleagues[7.1]. In this section, I will discuss several previous experiments in non-degenerate ground state polymers, in particular, PPV, including Raman, doping induced and photoinduced IRAV absorption, and electronic gap state absorption with their spin characterization. The experimental results and carrier dynamics will be discussed.

7.2) Charged Excitations- polaron and bipolarons in PPV

As described in the previous chapter, the lifting of the ground-state degeneracy leads to confinement of soliton-antisoliton pairs into bipolarons with the lowest confinement energy. One needs a two-step mechanism to form long-lived charged excitations.[6.2] The first step is the photogeneration of electron and hole pairs, some of pairs are expected to relax to form singly charged polarons on separate chains, which will be able to move three-dimensionally through the lattice. The second step is the self-trapping of these charged excitations by coalescence of pairs of like charges to form bipolarons which results in a the much stronger degree of self-localize of the excitations.

There are two important experimental signatures of bipolaron formation. These are:

(A) the formation of localized structural distortions with associated localized vibrational modes (IRAV modes) in the mid-infrared.

(B) the generation of symmetric gap states and associated electronic transitions. The reversed spin-charge relation, i.e. charge storage in a spinless bipolaron.

Each of these features has been verified in experiments carried out on PPV both after doping and during photoexcitation.

A. Infrared-active vibrational modes

Doping experiments in PPV and its derivatives[7.2-3] showed that there are IRAV modes at 1150, 1282, 1314, 1419, 1505 cm^{-1} and additional weaker modes at 553, 837, and 960 cm^{-1}. The existence of the IRAV modes is a definitive evidence of the formation of structural distortions around the charge storage configuration.

Photoinduced IRAV spectra of PPV [7.2, 7.4-6] showed that there are strong stretch modes at 1113, 1275, 1318, 1414 and 1480 cm^{-1} which correspond to the principal Raman lines observed at 1172, 1327, 1409, 1547 and 1586 cm^{-1} in the pure polymer. In addition to the stretch modes corresponding to the backbone vibrations in PPV, weak modes are observed in photoinduced absorption at ~550, ~830 and ~960 cm^{-1} which correspond to the ring vibrations at 555, 837 and 965 cm^{-1} in the pure polymer. This one to one correspondence between the principal IRAV modes observed on photoexcitation and that after doping implies that the same charge storage configuration is involved in both cases, and contributes to the evidence of "bipolaron bands" [7.5]. The experimental results and theoretical calculations of the Raman, doping induced and photoinduced IR absorption spectra [7.5] are shown in figure 7.1.

The infrared-active vibrational modes (IRAV) in PPV are listed below as

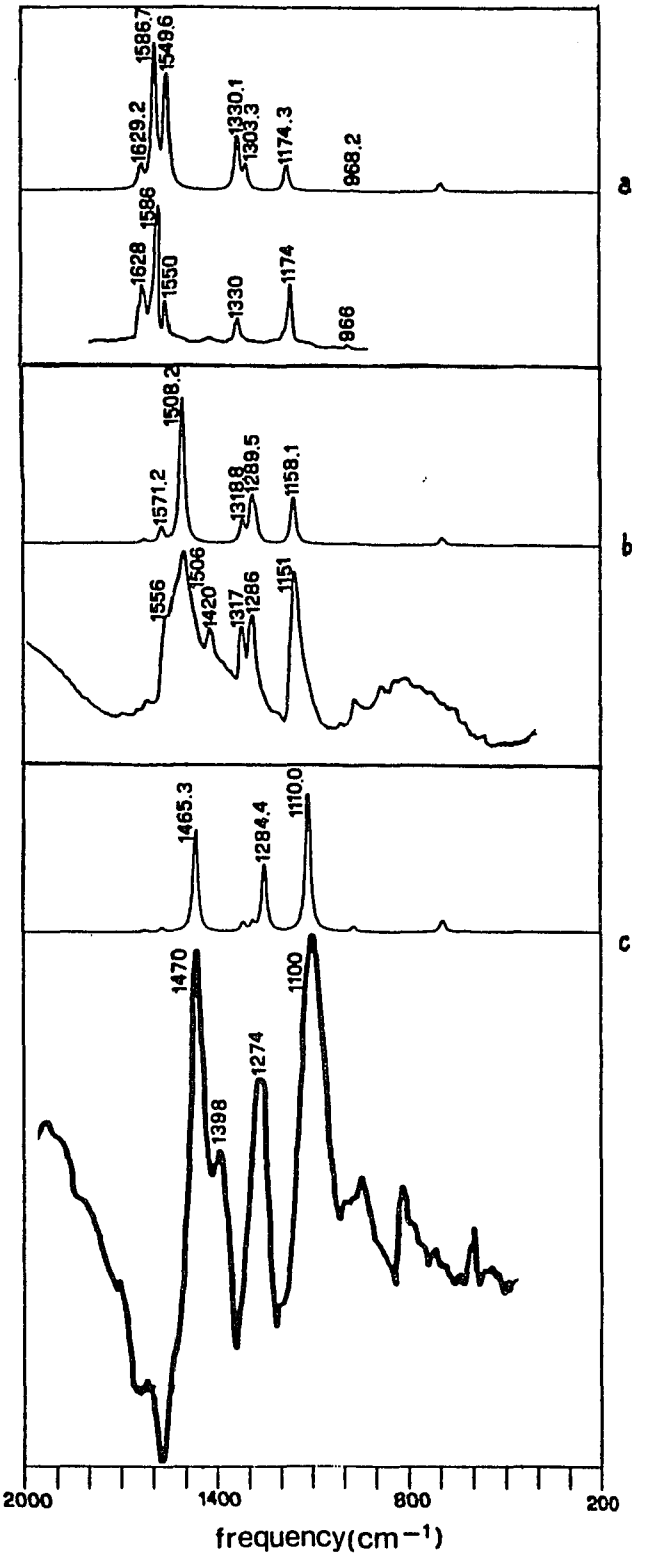

Fig.7.1 Experimental and theoretical calculation spectra of (a) Raman (b) doping induced infrared and (c) photoinduced infrared absorption of PPV. (From B. Tian el al. *J. Chem. Phys.* **95**, 3198 (1991))

Raman modes, doping induced and photoinduced IR modes. The assignment to these modes is also provided.[7.2]

Raman	Doping	Photo	Assignment
555	553	549	p-phenylene ring bend
837	837	820	p-phenylene ring bend
	876	872	in plane quadrant deformation
965	960	947	C-C asymmetric hextant breathing
1100	1003	1003	C-C asymmetric hextant breathing
1172	1150	1113	C-C symmetric hextant stretch
1327	1281	1275	trans-vinylene C-C stretch
1409	1314	1318	C-C symmetric hextant stretch
1547	1419	1414	C-C symmetric semicircle stretch
1586	1505	1480	C-C symmetric quadrant stretch
1628	1619	1621	trans-vinylene C=C stretch

Table 7.1 Raman, doping induced and photoinduced IRAV modes

As shown in Table 7.1, the frequency of the photoinduced IRAV modes is red shifted with respect to the doping-induced modes, which, in turn, are red shifted with respect to the Raman modes. The size of the red shift for any given mode is dependent upon the size of the electron-phonon coupling constant and the pinning strength in the given system.[6.2] The larger red shifted modes in doping-induced IRAV is due to the strong pinning of doping-induced excitations via Coulomb binding of bipolarons to dopant counter ions. It has been found that the red shift of the IRAV modes grows dramatically with increasing side-chain length [7.2] for derivative of PPV. This implies that the pinning strength of bipolarons decreases with increasing side-chain length.

B. Symmetric gap states and the reversed spin-charge relation.

The doping induced gap states transitions in PPV were observed in the IR below the absorption gap edge[1.9, 6.8]. The difference spectra clearly showed two absorption features arising from electronic transitions between the valence band and the two localized gap states upon charge transfer doping and is consistent with charge storage in bipolarons.

The doping induced gap state dependence on the dopant concentration has been discussed in P3MT, a derivative of PT. At low doping concentration regime (<1%), three absorption features were observed and implied polaron formation [7.7-7.8]. When the doping concentration is larger (>4%) the gap absorption becomes two peaks as observed in PT [7.9] indicating bipolaron formation. The magnetic susceptibility χ which measures the spin per charged excitation, decreases as the concentration of doping increases.[7.8]. Electron-spin resonance measurements confirmed that spinless bipolaron is the charge storage configuration in PT and its derivatives. Since charges are initially injected as polarons, bipolarons can only be formed through the combination of polarons. Although the bipolaron configuration has the lowest energy, polarons can be kinetically metastable at dilute concentrations in low molecular-weight samples in which defects and imperfections are sufficiently numerous to restrict polaron mobility and thereby inhibit the bipolaron formation.[7.8] The same doping concentration effect is expected in PPV, but the polaron has a larger chance to survive in the samples with impurities such as PT and its derivatives.

The photoinduced gap absorption spectrum of PPV consists of two asymmetric electronic state[1.9,6.8,7.10]. These two subgap electronic absorption peaks are at 0.6 eV and 1.6 eV. These photoinduced absorption bands derive their strength from states above 2.5 eV where photoinduced bleaching is observed. The IRAV and the photoinduced electronic bands have been verified

originally from the same charged species in PTs[7.11]. The ESR measurements by Wei et al.[7.10] confirm that the photoinduced absorption spectrum corresponds to the spinless bipolaron for the above-band-gap photoexcitation in derivatives of PPV. The electron spin resonance photoinduced gap state absorption is shown in figure 7.2 The asymmetry of the 0.35-eV and the 1.3-eV bands indicates that the transition from (to) the continuum density of states at the band edge are involved, in agreement with predictions for bipolaron transitions. Polarons are not observed in PPV.

The photoinduced absorption spectrum (figure 7.2) is similar to the doping-induced absorption spectrum. The photoexcitation transition energies are shifted [7.11] due to Coulomb repulsion.

$$h\omega_1 + h\omega_2 = E_g - 2U_b \qquad (7.1)$$

where U_b is the difference in Coulomb energy between the initial state of the spatially extended bipolaron (double charge) and the final state (single charge) with fixed lattice coordinates. Since $h\omega_1 + h\omega_2$=1.7 ev and E_g=2.3 eV in DOO-PPV, a derivative of PPV, therefore U_b =~0.3 eV or U_b/E_g = 0.12. This small Coulomb repulsion energy for U_b is consistent with the existence of bipolarons rather than polarons as the dominant charged excitation. For doping-induced bipolarons, the shift of each transition by U_b is compensated by the Coulomb energy (E_b) to the dopant counter ion, So that,

$$(h\omega_1 + h\omega_2)_{doping} = E_g - 2(U_b - E_b) == E_g \qquad (7.2)$$

7.3) Neutral excitations- singlet and triplet exciton

Besides the charged bipolarons in PPV and its derivatives, neutral excitations also exist. The singlet exciton exhibits its properties via geminate recombination luminescence.[1.9,6.8,7.12-13] The luminescence spectrum is associated with the energy levels of the singlet exciton (corresponding to a

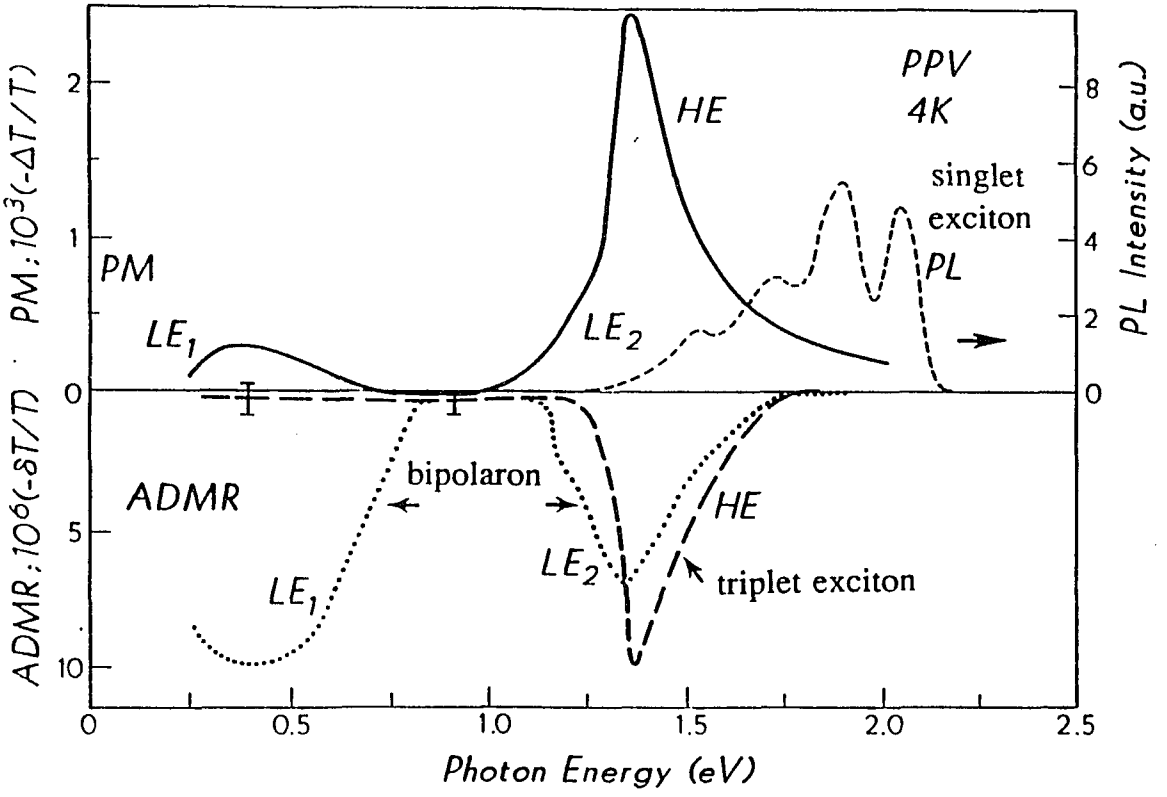

Fig.7.2 The photoinduced absorption spectrum of triplet exciton and bipolaron which is distinguished by their spin identification in ESR measurments by Wei et al. (from Phys. Rev. Lett. **68**, 666(1992))

transition from the upper to the lower gap state close to the π-π^* transition band edge as shown in figure 6.7). Photoluminescence is quite strong with a quantum yield of several percent, and the vibrational structure with an energy spacing of 0.14 eV [7.13] corresponds fairly well to the frequency of the C-C vibrations of the polymer backbone observed in Raman measurements [1.9,7.6]. Time resolved photoluminescence [7.13] with 20 ps time resolution indicates that the decay of photoluminescence exhibits non-exponential behavior. Measurements have shown that the luminescence in stretch-aligned samples is more intense for excitation polarized perpendicular to the polymer chain (E$\perp$C) than for parallel excitation (E//C). They also have shown that the decay rate is faster for parallel excitation (40 ps) than for perpendicular excitation (60 ps) in fully converted PPV samples at 300K. The decay kinetics seems more non-exponential for parallel excitation. Therefore, it was proposed concluded that this anisotropy effect could be result of the nonlinear dependence of the decay rate on photoexcited carrier density. The luminescence data were successfully fitted tto monomolecular and bimolecular recombination involving in both the radiative and non-radiative decay process.

Electroluminescence of PPV was observed by Burroughes et al[1.8] who found the same luminescence spectrum as for photoluminescence which was assigned to the radiative recombination of the singlet exciton (or polaron exciton) formed by photoexcitations. The electro-luminescence is generated by the recombination of electrons and holes injected from opposite sides of the structure. Due to the strong electron-phonon interaction in conjugated polymers, the injected charges are expected to self-localize to form either polaron and bipolaron. Since the bipolaron is strongly self-localized and trapped at a deep gap state, bipolaron seems unlikely to have sufficient energy for radiative decay at photon energies of 2.2 eV. Therefore, the authors suggest that the charge

carriers involved are probably polarons. The combination of polarons to form polaron excitons requires that the polaron gap states move no further into the gap than those of the polaron exciton of 2.2 eV.

The triplet exciton spectrum was measured at 1.36 eV for a derivative of PPV[7.10] which is shown as the HE peak in figure 7.1 and at 1.45 eV in PPV [7.14]. This single photoinduced absorption peak involving the triplet to triplet transition was verified by electron-spin resonance measurements [7.10,7.14]. The triplet exciton has a longer lifetime than the singlet exciton because the transition of the triplet state to the singlet ground state is forbidden. The 1.45-eV triplet-triplet absorption lifetime has been experimentally [7.14] estimated in excess of 60 ms at 80K. The triplet lifetime at 1.45-eV absorption intensity decreases when the temperature increases.[7.14]

7.4) Dynamic schemes

The experimental evidence, together with the theory of the non-interacting model Hamiltonian (SSH model) and the theory of electron coulomb interaction, almost give a complete picture of the photoexcitation dynamics in polyacetylene. The understanding of degenerate ground state polymers, like polyacetylene, can give a comparison picture with NDGS polymers, such as PPV studied in this thesis. The dynamic scheme of polyacetylene summarized by Rothberg et al[7.15-16] is schematically shown in figure 7.3.

After photoexcitation, intrachain electrons and holes quickly form Su-Schrieffer soliton pairs S^+S^-, coupling with the lattice deformation, in about 100 fs. These charged soliton pairs are not stable along the chain and geminately recombine to form neutral solitons in 0.5 ps and further decay to phonons. The interchain electrons and holes form polarons P^+ and P^- since they are isolated in different polymer chains, these charged polarons stay in the chain for hundreds of

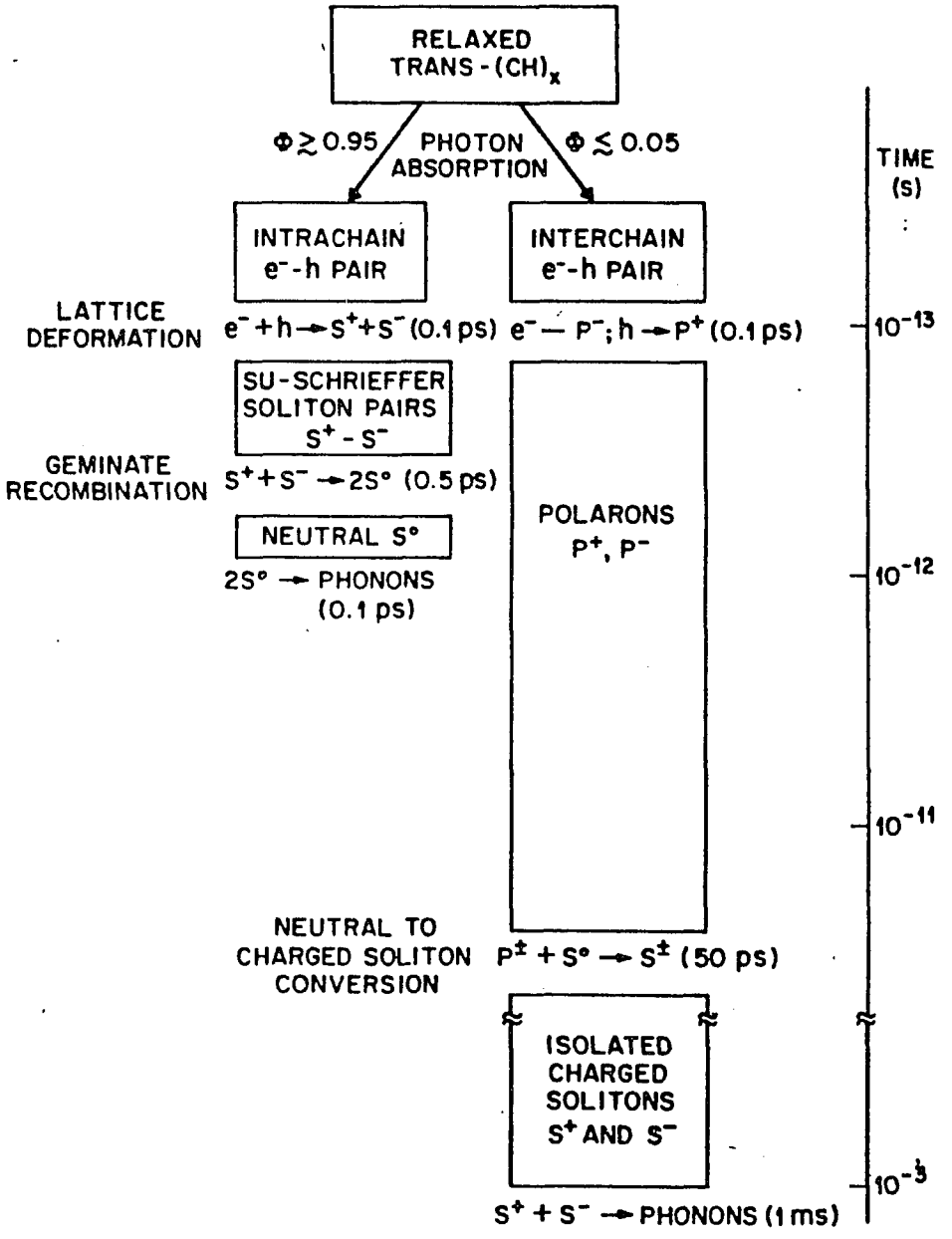

Fig. 7.3 Block diagram summarizing the picture of the photoexcitation dynamics in trans-$(CH)_x$. (from Rothberg et al. in *Phys. Rev. B* **36**, 7529(1987))

picosecond then form charged solitons. Isolated charged solitons geminately recombine to phonons in about a millisecond. These interchain charged polarons and solitons are involved in photoconductivity in polyacetylene.

Carrier dynamics in non-degenerate ground state polymers are not as well understood as polyacetylene. In non-degenerate ground state polymers such as PPV and PT, the soliton pairs can not separate due to the intrinsic confinement of the polymer backbone. The nonlinear excitations are in the form of polarons which include neutral polaron excitons, single charged polarons and double charged bipolarons. Recent photoinduced absorption measurements of PT at 220K by Kanner et al.[7.17] have identified the absorption of the polaron and bipolaron and shows that the lifetime of the polaron is of the order of 10 μs and much longer for bipolarons. Their measurements covered energies from 0.25 to 1.9 eV are shown in figure 7.4. Two gap states at 0.5 eV and 1.35 eV correspond to bipolarons and the HE band at 1.8 eV is associated to a polaron transition. At early nanoseconds after photoexcitation, photoluminescence observed at 1.9 eV has similar dynamics as photoinduced absorption at 1.2 to 2.2 eV. These authors concluded that the dominant photoexcitation in the picoseconds to nanoseconds time ranges are self-trapped (polaron) excitons.

Kobayashi et al.[6.9,7.18] have reached the similar conclusions that major excitations are excitons by performing a series of femtosecond experiments on PT and PDA. The model of relaxation kinetics of exciton proposed by Kobayashi et al. is depicted in figure 7.5. According to this model, the free exciton (FE) are instantaneously created by photoexcitation. The relaxation process of self-trapped excitons (STE) involve three step process following 1 to 4 in figure 7.5. First, it takes about 10-20 fs to form unrelaxed STE from free excitons which is the 1->2 process shown in the adiabatic potential surfaces of exciton in figure 7.5. Second, it takes about 100 fs to emit phonons to form relaxed but

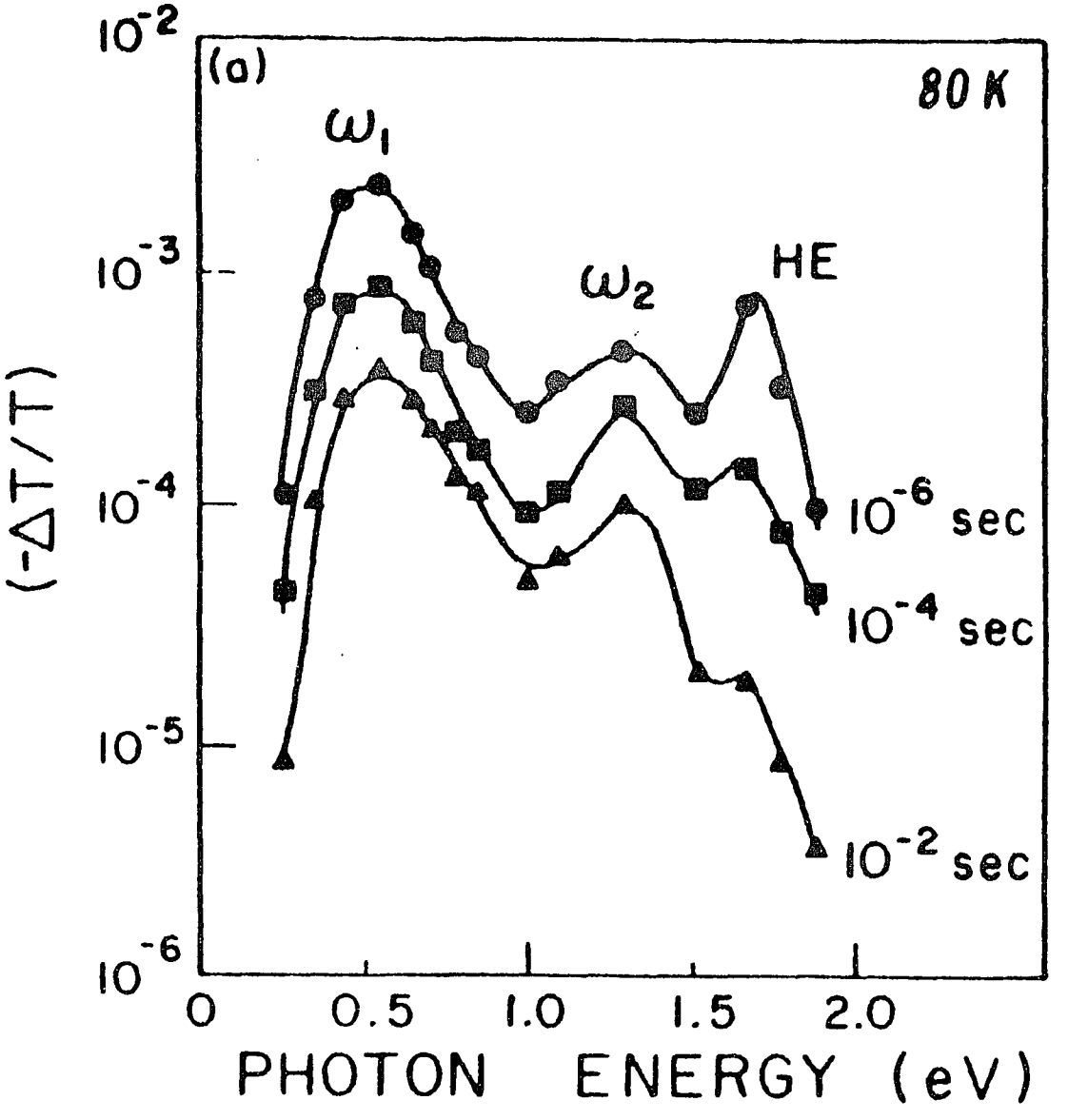

Fig. 7.4 The time resolved photoinduced absorption spectrum from microsecond to 10 millisecond. The ω_1 and ω_2 peaks correspond to bipolarons and the HE peak corresponds to the polaron which are distinguished by their spin identification in ESR measurements by Kenner et al. (from Phys. Rev. Lett. **69**, 538(1992))

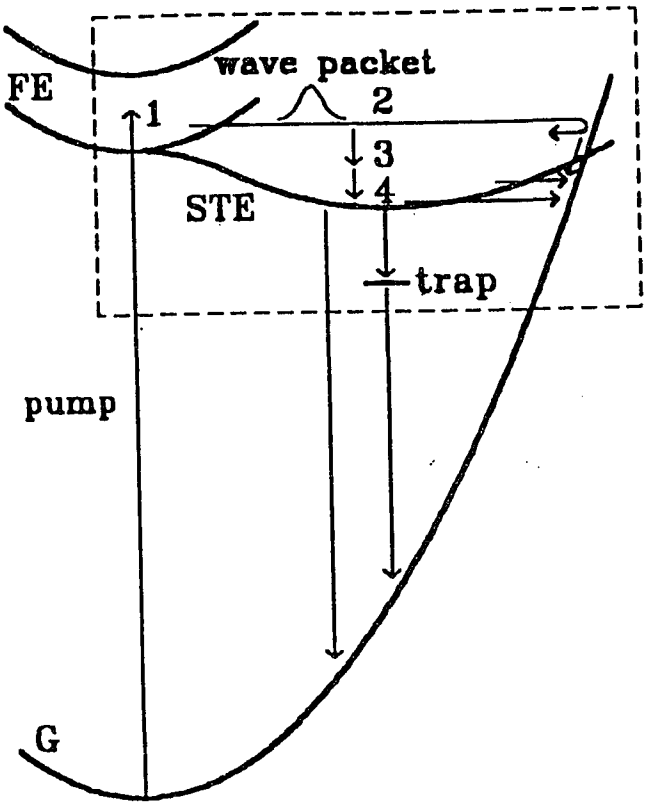

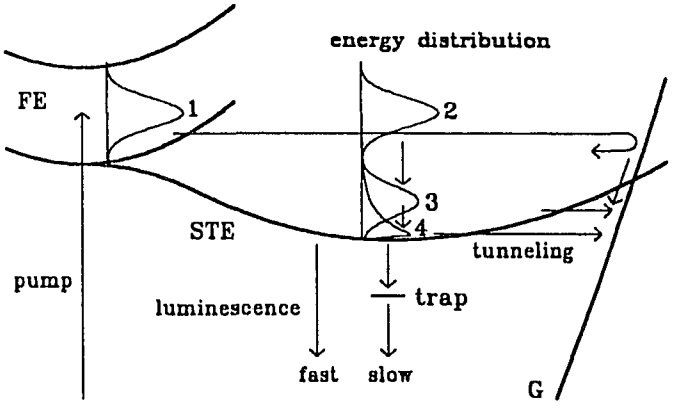

Fig.7.5 Models of relaxation kinetics shown in adiabatic potential surfaces of excitons in PTs. FE: free exciton, STE self-trapped exciton, G: ground state, 1: free exciton, 2: unrelaxed STE, 3: unthermalized (relaxed) STE, 4: thermalized STE. Relaxation process are: 1-2 self-trapping, 2-3 phonon emission, and 3-4 thermalization. (From T. Kobayashi et al. *Appl. Phys.* **B53**, 296 (1991))

unthermalized STE which is the 2->3 process shown in figure 7.5. Third, it takes about 1 ps to thermalize with the lattice to form thermalized STE in the 3->4 process shown in figure 7.5. The decay kinetics of the luminescence observed in PDA has fast and slow components. The life time of the fast component is less than 30 ps. The decay curve of the slow component is fitted by $\exp(-\sqrt{\frac{t}{\tau}})$, the time constant t is about 50 ps at 290 K. The fast decayed luminescence is concluded from the intrinsic radiative recombination of STE to ground state. The slow component is explained by a trapping model that the photoexcited species decay at a trap center after random walk in a one-dimensional chain. This exciton recombination via a recombination center (traps) by random walk diffusion process has been discussed by many authors.[7.12-14,7.18] According to this trapping center model, one may expect quite different luminescence spectra from intrinsic exciton and trapping centers. Therefore, the measurement of luminescence spectra at early picosecond and long delay time is crucial to understand this random walk process. This model will be discussed in my research.

The long-lived (>100ps) induced absorption has been assigned due to polarons in PT and PDA by Kobayashi et al.[7.18] and triplet excitons in PPV by Friend et al. [7.19]. But the origin of these long-lived species and the relation to the (singlet) self-trapped excitons is not discussed. An alternated model to explain the long-lived luminescence rather than the trapping model is that the bounding of free polarons to form singlet self-trapped excitons in a long decay time scale (~100ps) and the later one give the slow component of luminescence. This intrinsic relaxation kinetics of STE and polarons are discussed in the research experiment of this thesis.

Chapter 8 Research on oriented PPV film

8.1) Introduction

In this chapter, I will describe photoinduced absorption and photoluminescence measurements on oriented PPV film. These experimental results are were carried out to understand the photoexcitations dynamics in oriented PPV films in the picosecond time scale. The broad supercontinuum probe light from 400nm to 1300nm covers the absorption of polarons and excitons, which spectra have been well defined in the μs to ms measurements. The dynamics of these excitations are expected to be time resolved with 200fs time resolution. The tunable excitation wavelength near the band edge of PPV at 2.5 eV provides us an opportunity to study the bandedge excitation dynamics and density effects. The stretched oriented samples provide us with a new physical dimension to probe the excitation state and dynamics by polarization dependent absorption and luminescence measurements. A dynamics scheme of oriented PPV films thus is expected to be established as aresults of these investigations.

8.2) Time-resolved photoinduced absorption measurements

In this section, I will describe the results of femtosecond transient absorption measurements on oriented PPV film. These experiments are performed with the excitation polarization parallel and perpendicular to the oriented polymer chain to study anisotropy effects, and with different excitation wavelength (500nm-540nm) to study the excitation wavelength dependence.

A. Excitation polarization dependent absorption spectrum

Figure 8.1(A) depicts the absorption spectra of a stretch oriented PPV film

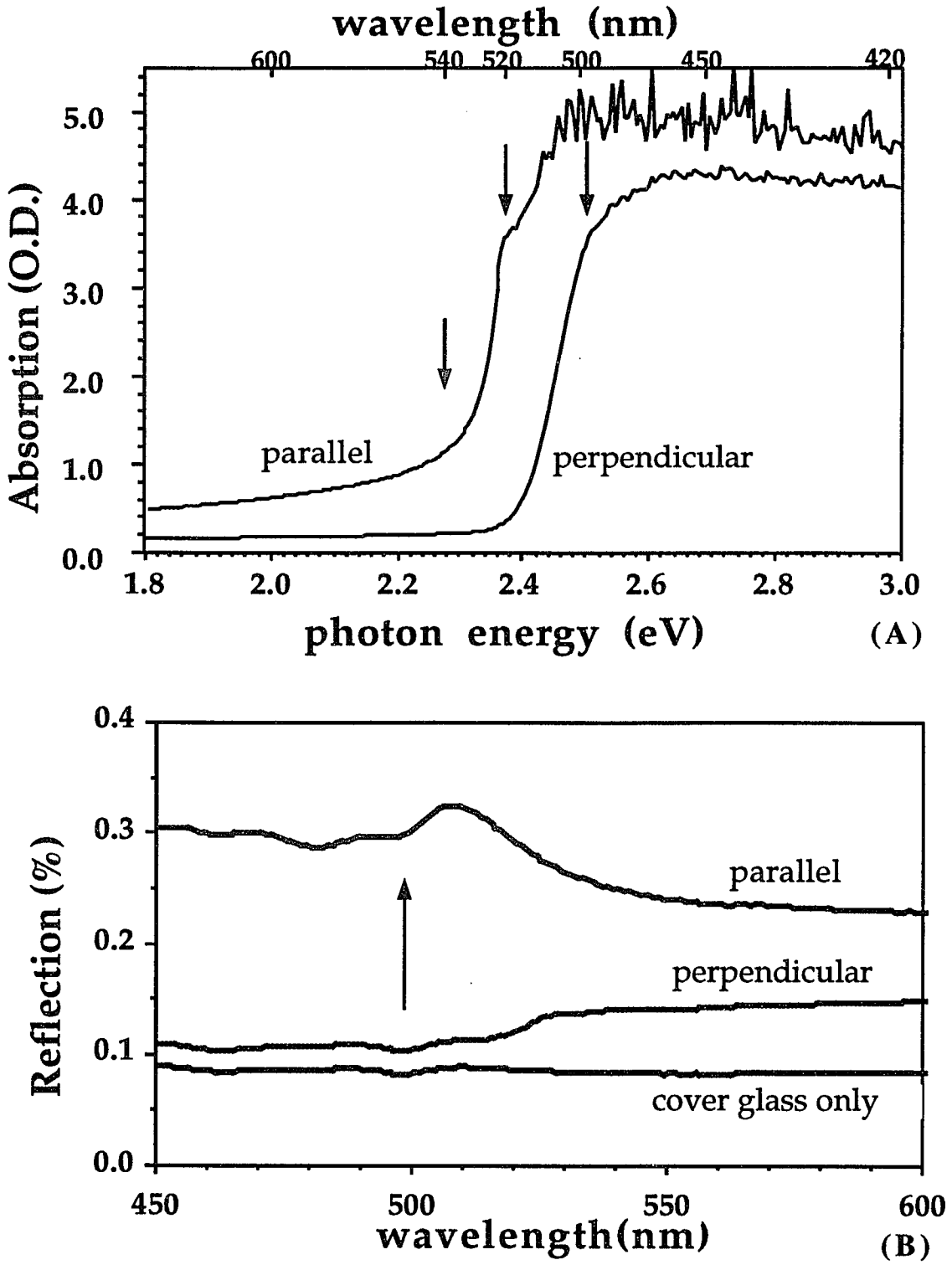

Figure 8.1 Absorption spectrum(A) and reflection spectrum (B) of an oriented PPV film. The polarization of the detected light is set parallel and perpendicular to the polymer chain.

at room temperature. The probe light is polarized parallel (//) and perpendicular ($\perp$) to the oriented direction of the main chain. The absorption is much stronger when the probe light is polarized parallel to the chain because the dipole along the chain has a larger oscillator strength for absorption. The arrows in figure 8.1 indicate the photoexcitation wavelength in transient measurements. The anisotropic reflection spectrum is depicted in figure 8.1(B). One may realize that there is about 33% of light reflected when the excitation is polarized along the chain while only 11% of light is reflected in perpendicular excitation at 500nm. The sample is optically thick for an excitation wavelength shorter than 500 nm when the polarization is perpendicular to the chain and for a wavelength shorter than 530 nm when the polarization is parallel to the chain. Therefore, all the excitation energy is observed, excluding the reflected photons in our femtosecond experiments.

The temporal photoinduced absorption change is measured from 1.0-2.5 ev after photoexcitation at 2.5 ev (500nm), the π-π^* transition band gap indicated in figure 8.1. The temporal photoinduced absorption spectrum depicted in figure 8.2 and figure 8.3 for different delay times (0-200 ps) is plotted from top to bottom starting with the probe pulse preceding the pump pulse. The pump pulse is polarized parallel to the oriented direction of the PPV polymer chain in figure 8.2 and perpendicular to the chain in figure 8.3. Note, the probe pulse is always polarized parallel to the samples oriented direction to obtain a maximum photoinduced absorption signal. In both pump pulse polarizations, a broad photoinduced absorption rapidly appears in the red part of our spectrum (620nm-1100nm) and decays into an isolated single absorption band peaking at 850 nm 200 ps after excitation. In the blue part of the spectrum (500nm-620nm), photoinduced gain is observed in the case of excitation polarized perpendicular to the chain while only photoinduced absorption is observed when the excitation

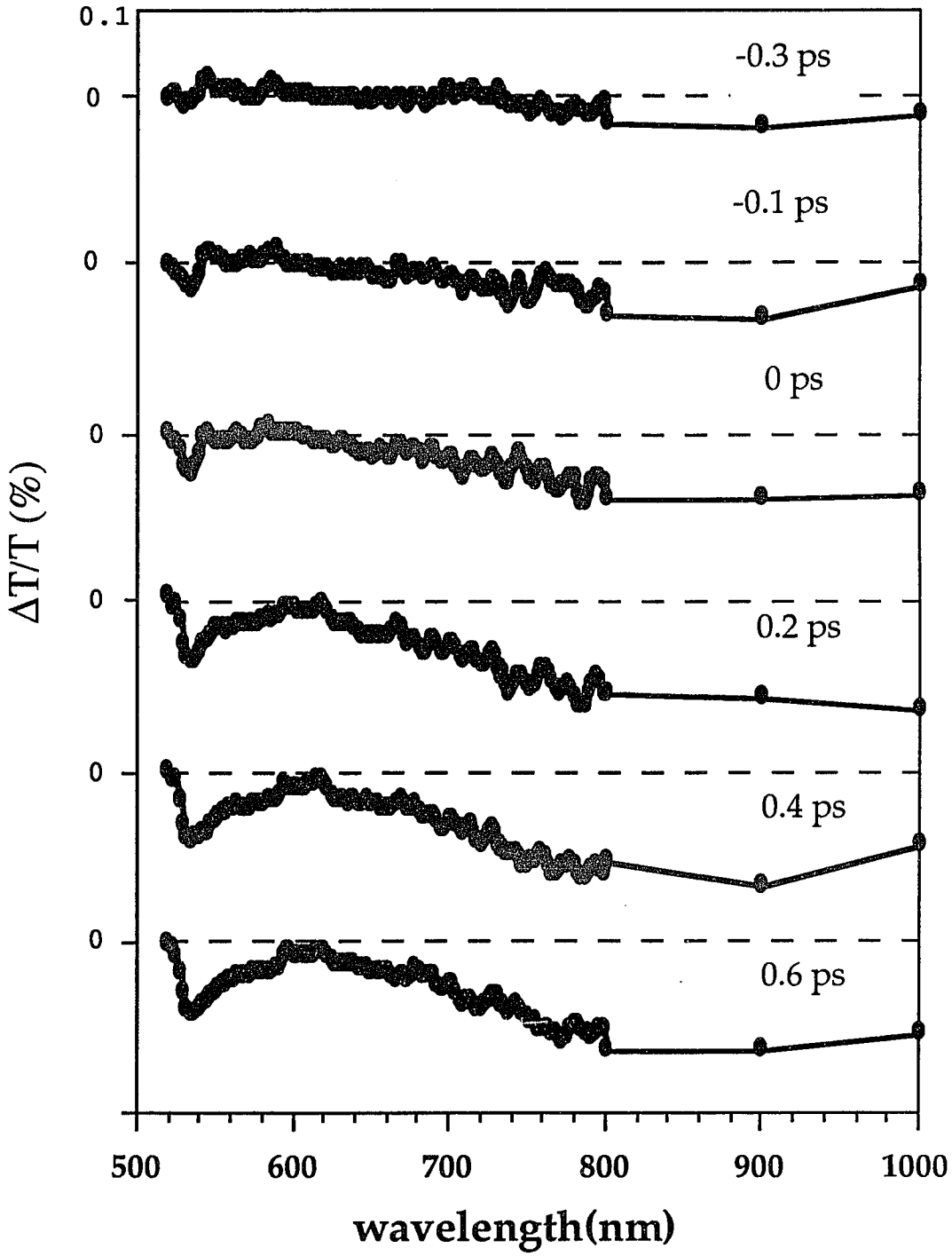

Fig. 8.2(A) Time resolved photoinduced transmission change of an oriented PPV film after photoexcitation at 500nm and polarized parallel to the polymer oriented direction. Delay time is from -0.2 ps to 0.6 ps.

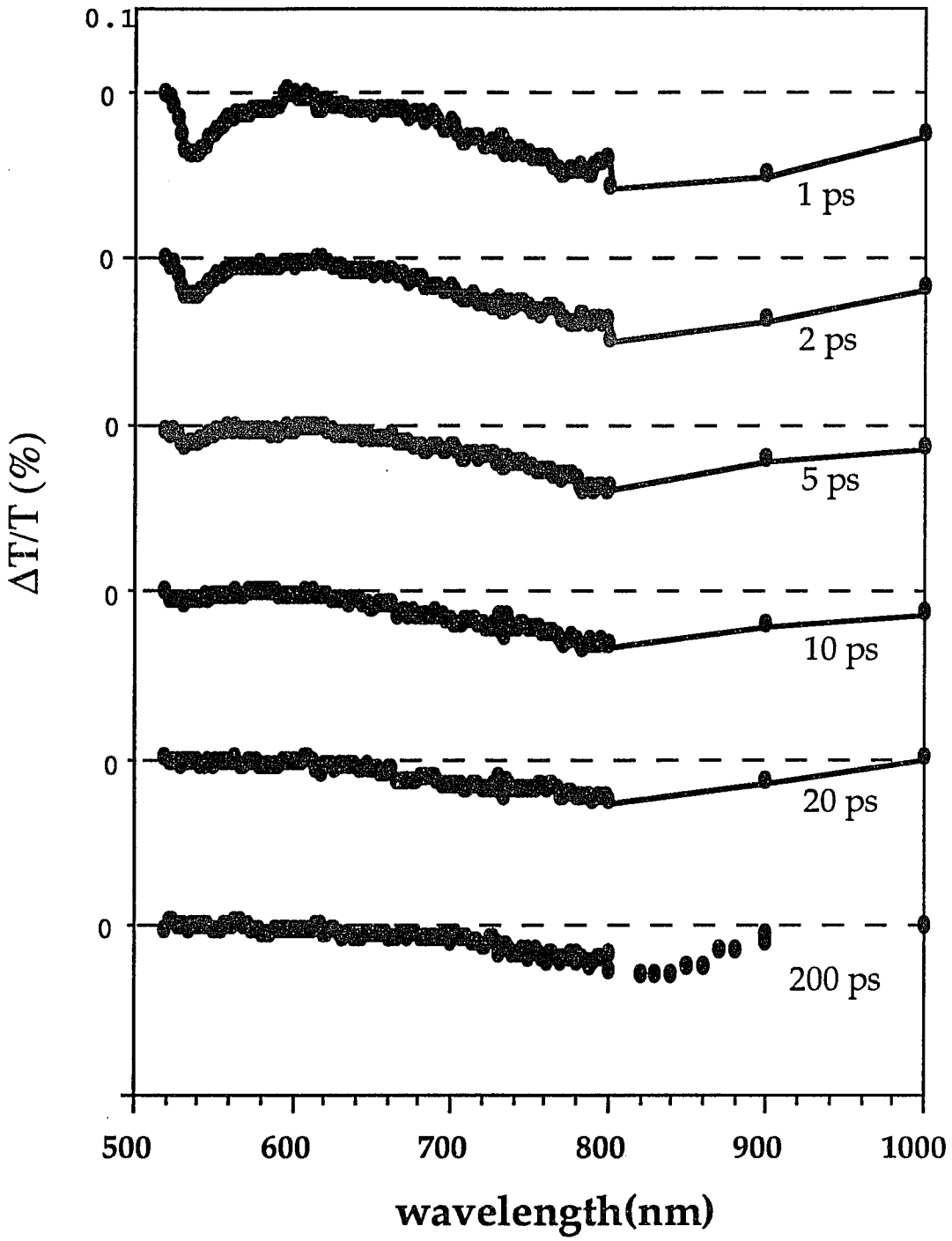

Fig. 8.2(B) Time resolved photoinduced transmission change of an oriented PPV film after photoexcitation at 500nm and polarized parallel to the polymer oriented direction. Delay time is from 1 ps to 200 ps.

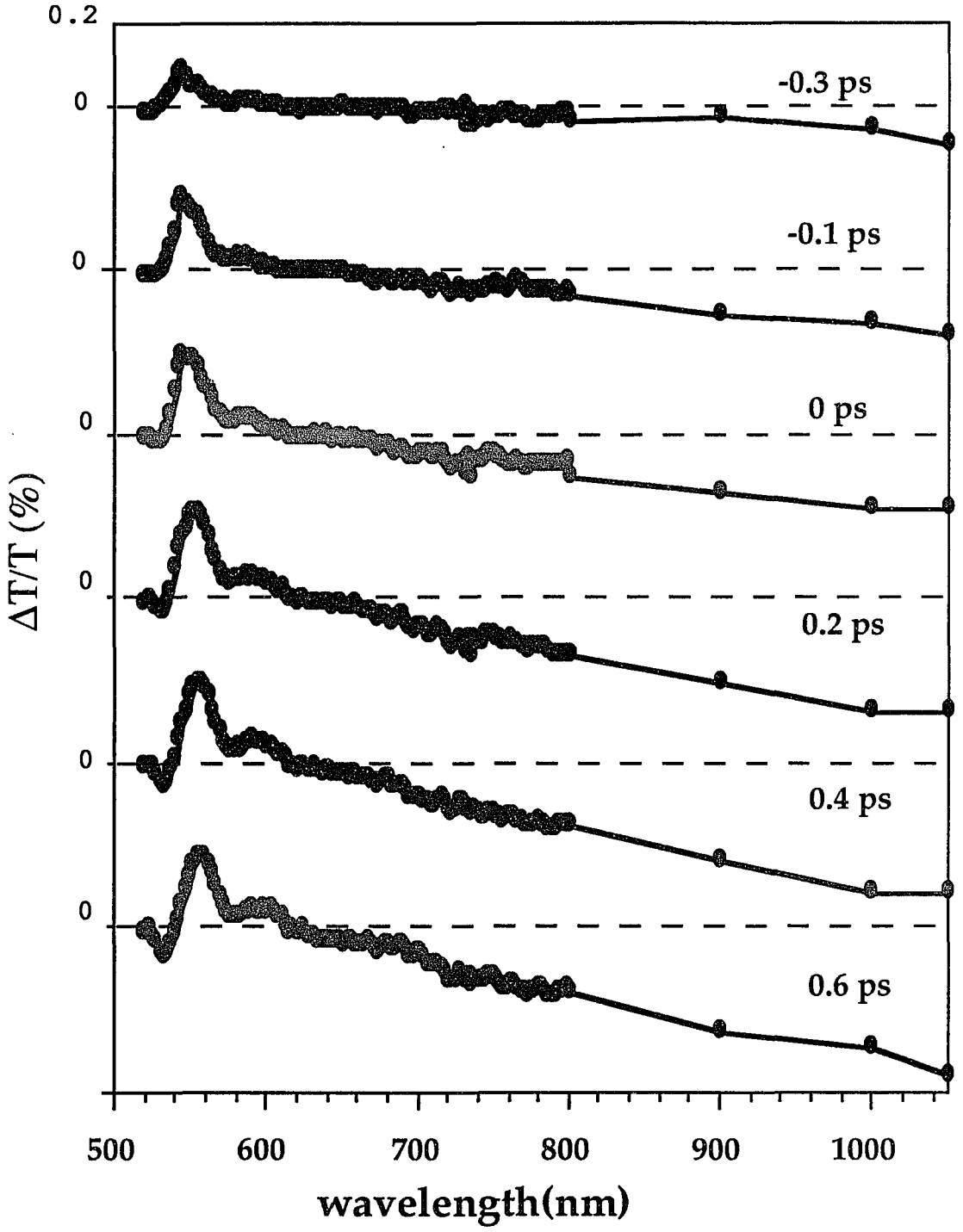

Fig. 8.3(A) Time resolved photoinduced transmission change of an oriented PPV film after photoexcitation at 500nm and polarized perpendicular to the polymer oriented direction. Delay time is from -0.2 ps to 0.6 ps.

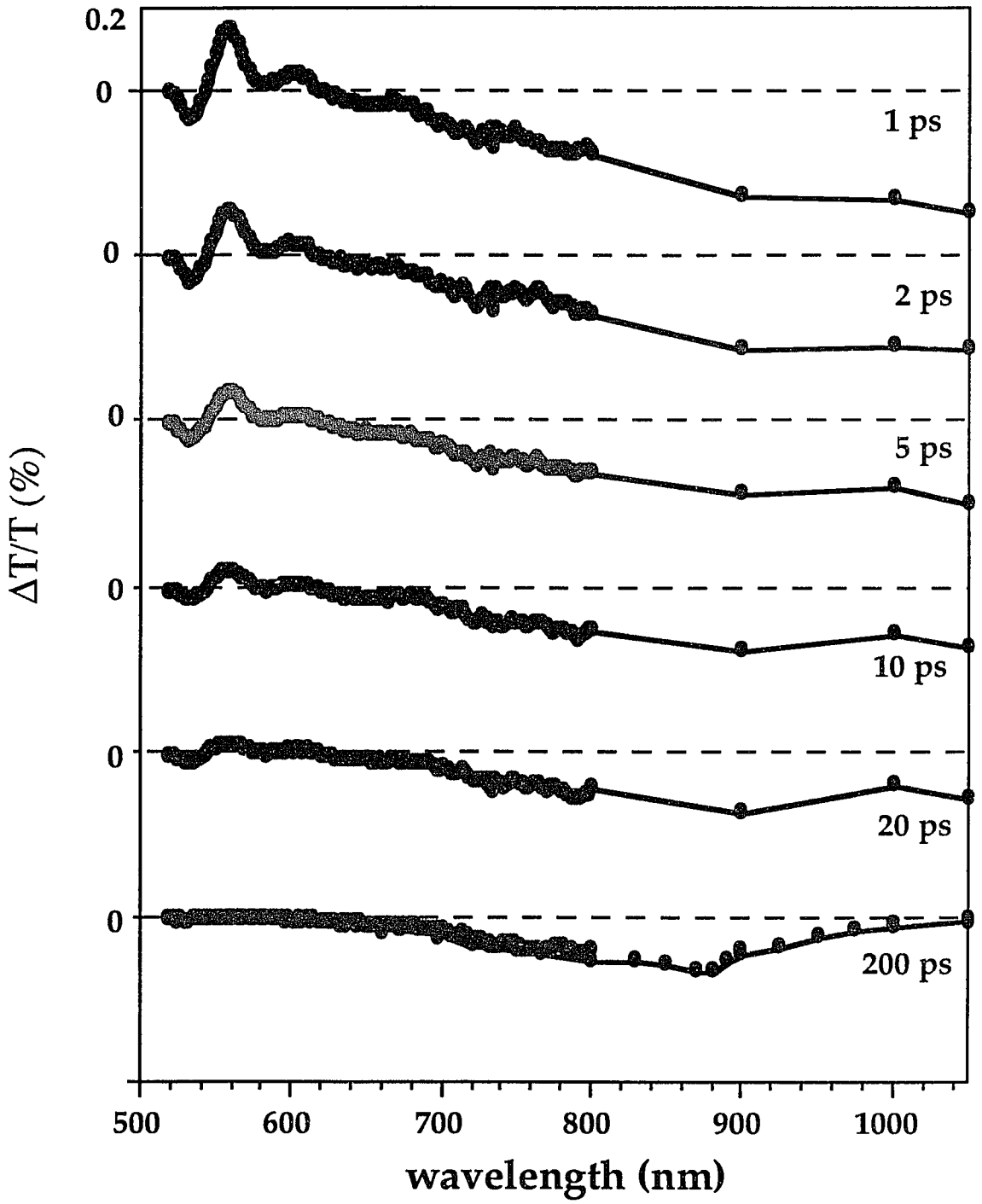

Fig. 8.3(B) Time resolved photoinduced transmission change of an oriented PPV film after photoexcitation at 500nm and polarized perpendicular to the polymer oriented direction. Delay time is from 1 ps to 200 ps.

is polarized parallel to the chain. We will discuss the experimental results in terms of the blue and the red part of the spectrum as specified above.

In the red part of the time-resolved spectrum (650nm-1100nm), photo-induced absorption is characterized by a monotonic increase as the probe wavelength become longer in the early picosecond region (-0.2ps to 1 ps) for both excitation polarizations. Note, since the scale in figure 8.3 is twice as large as the scale in figure 8.2, the photoinduced absorption (PA) change for perpendicular excitation is about twice the intensity of PA for the parallel excitation. For both pump polarizations, all the pump light that is not reflected is absorbed because the sample is optically thick. Even taking the excitation energy loss by reflection into account, the photoinduced absorption is still larger for the perpendicular polarized excitation than for the parallel polarized excitation. Within a 200-ps delay time the photoinduced absorption band to evolves into a single isolated absorption peaking at 850nm (1.45 eV) for both excitation polarizations. We assign this absorption band to polaron pairs. The kinetics of the photoinduced absorption in the red wavelength range (650nm-1100nm) is similar for all wavelengths and for both polarizations.

A typical time-resolved absorption curve for 900 nm is shown in figure 8.4. The experimental curve is fitted to a double exponential convoluted with the laser Gaussian profile as follows:

$$\Delta A(\lambda,t) = (a_1(\lambda)e^{-t/\tau_1} + a_2(\lambda)e^{-t/\tau_2} + a_3(\lambda)) \otimes P(t) \qquad (8.1)$$

where P(t) is the Gaussian profile of the convolution of the pump and probe pulse. The fitting yields a fast 800fs decay component followed by a slow ~100ps decay component. The dynamics in the red wavelength range is similar for all wavelengths and for both excitation polarizations. The fast decay (~800fs) absorption which is broad and monotonically increase with the probe

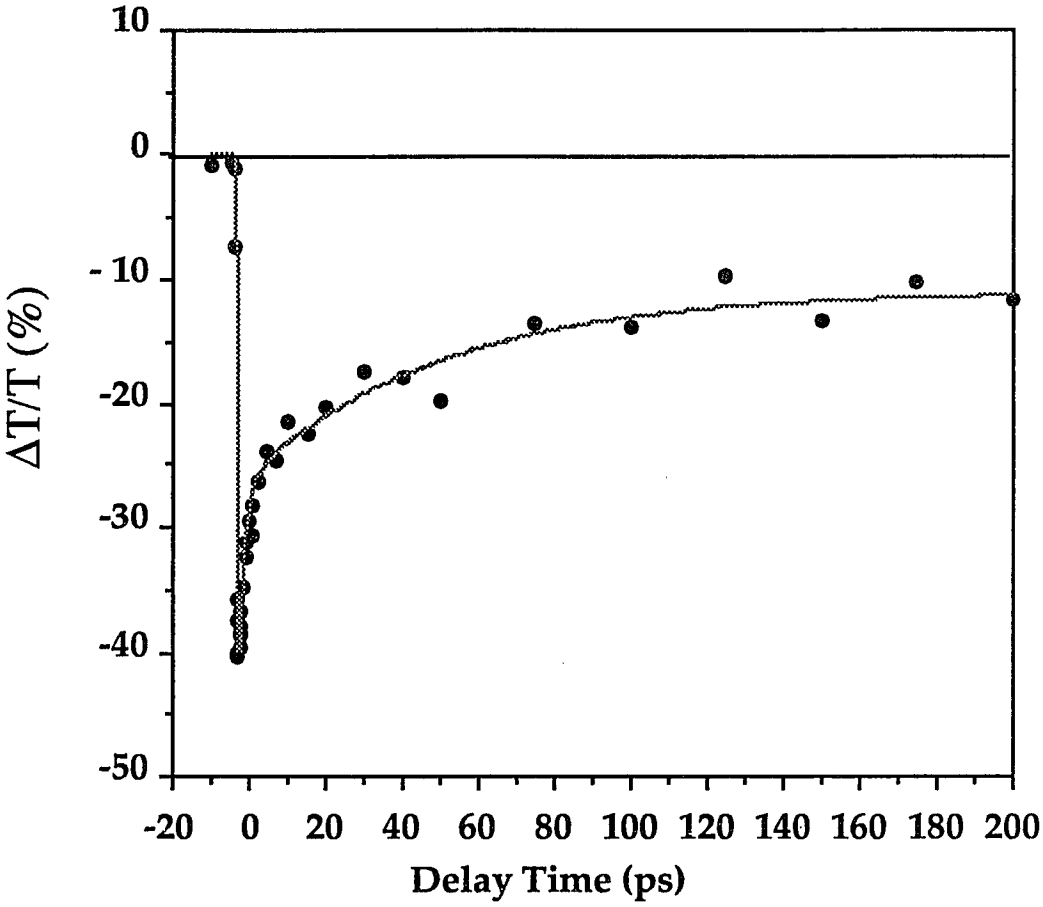

Fig. 8.4 Photoinduced absorption in 900 nm as a function of delay time with excitation at 500nm and polarized perpendicular to the polymer chain

wavelength is assigned to the absorption from the "hot" ground states which non-radiatively decay from the free exciton into the ground state via multiphonon emission. Since this absorption is instantaneously formed within the laser resolution of 200fs with its broad absorption range to the IR, the fast decaying absorption actually accounts for all the absorption from unrelaxed ground state molecules which are spread over the entire ground state vibration ladder after decay from the S_1 state. The slow decay component (~100ps) is assigned to the fast decay rate of polaron pairs. We will discuss these assignments later in the text.

In the blue part of the spectrum (500nm-650nm) the photoinduced transmission change is more complicated than in the red part. A photoinduced transmission increase is observed for perpendicular excitation while photoinduced absorption is still observed for excitation polarized parallel to the chain.(see fig.8.1) Since the wavelength range of the transmission increase (540nm-640nm) is below the π-π^* energy transition gap(500nm), the transmission increase is due to the photoinduced stimulated emission gain for the transition from the populated upper state to a lower state rather than bleaching. It is clear that even for excitation perpendicular to the chain, the gain signal overlaps with the photoinduced absorption. The overlap of the photoinduced absorption with the gain is evident at 530nm where the photoinduced absorption for excitation polarized perpendicular to the chain is shown in figure 8.3 and is slightly smaller than PA for excitation polarized parallel to the chain because of the overlap of the gain and absorption signals.

The stimulated gain spectrum for excitation polarized perpendicular to the chain is plotted as a function of delay time in figure 8.5 with the photoluminescence spectrum within the wavelength range 500nm-620nm. Two peaks are well resolved in the photoinduced gain which correspond to the peaks

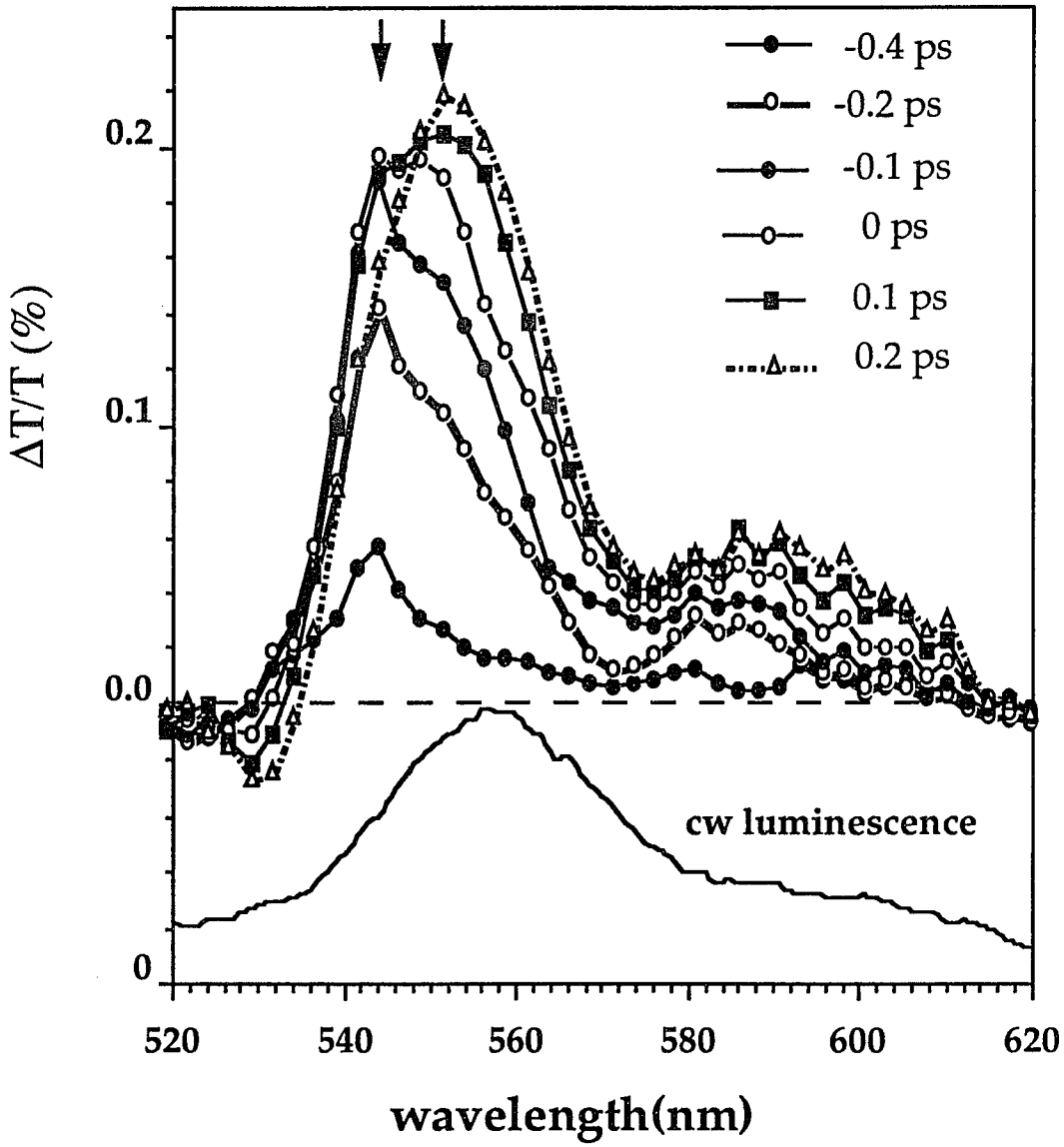

Fig. 8.5 Time resolved photoinduced gain spectrum due to photoexcitation at 500nm and polarized perpendicular to the chain. The bottom is the cw luminescence spectrum. The arrows indicate the spectra shifting.

of luminescence at 550nm and 595nm.. The energy separation of these two peaks, 0.2 eV, agrees with the energy separation of the vibrational structure observed in steady state luminescence which corresponds to the frequency of the C=C vibrations of the polymer backbone at 1550cm^{-1}.

The fact that the gain spectrum agrees with the luminescence spectrum (plotted at the bottom of figure 8.5) implies that the gain is due to stimulated emission from the polaron exciton since the luminescence is from the self-trapped singlet exciton.[7.12-13]. It also suggest that self-trapped singlet excitons are formed 200 fs after photoexcitation which agrees with the formation time of "hot" self-trapped exciton observed in PT and PDA by Kobayashi et al.[6.9,7.18]. The energy peak at 550nm in figure 8.5 is slightly red shifted within the first 200 fs after excitation. This spectrum shift of the gain is due to the overlap of the exciton gain and the Raman gain which I will discuss later.

The gain is not clearly observed in the induced absorption spectrum for excitation polarized parallel to the chain as shown in figure 8.3 due to the induced absorption. This agrees with luminescence measurements by Wong et al. and in this thesis luminescence is found to be more intense for excitation polarized perpendicular to the polymer chain than for excitation parallel to the chain. This result is puzzling since the perpendicular excitation is expected to create some inter-chain electron hole pairs, which have less probability for geminate radiative recombination. This anisotropic effect was also observed in polarization dependent photoinduced absorption in the red part of our spectrum (700nm-1000nm) as mentioned above.

B. Excitation wavelength dependence of absorption

To understand the anisotropic effect of absorption in PPV samples, we tuned the wavelength of the parallel polarized excitation from 500nm to 523nm,

533nm and 543nm to match the absorption coefficient (or photoexcited carrier density) for excitation perpendicular to the chain at 500nm.

One may see that the absorption coefficient is very different for differently polarized excitation light as shown in figure 8.1 where there is no absorption at wavelength of 520-540 nm when the polarization is perpendicular to the chain. The photoinduced transmission changes for photoexcitation parallel to the chain at 523nm and 533nm are shown in figures 8.6 and 8.7, respectively. Photoinduced gain is observed for both excitation wavelength at 523nm and 533nm. Only absorption is observed for the excitation wavelength at 500nm which is polarized along the chain. Therefore, the gain and the induced absorption is observed at same wavelengths. It is evident that the photoinduced gain overlaps with the photoinduced absorption in the wavelength range 530nm-650nm in figure 8.6 and 8.7. Similar results are observed for the excitation wavelength at 500nm polarized perpendicular to the chain(figure 8.3). The photoinduced absorption in the red spectrum range (650nm-900nm) also increases as the excitation is tuned from 500nm to 523nm and 533nm for excitation polarized parallel to the chain. The time resolved spectra and dynamics of photoinduced gain and absorption by photoexcitation at 523-533nm and polarized parallel to the chain are similar to the ones observed by photoexcitation at 500nm with light polarized perpendicular to the chain. So, it seems there is a wavelength dependence for parallel and perpendicular polarized excitation. At certain wavelengths which are different for parallel and perpendicularly polarized excitation (near the absorption gap), the photoinduced gain appears and the intensity of photoinduced absorption in the red is larger. As one will see later in the text this excitation wavelength dependence also agrees with luminescence intensity. The same excitation wavelength dependence for photoinduced gain and absorption (650nm-800nm) suggests that the gain and photoinduced

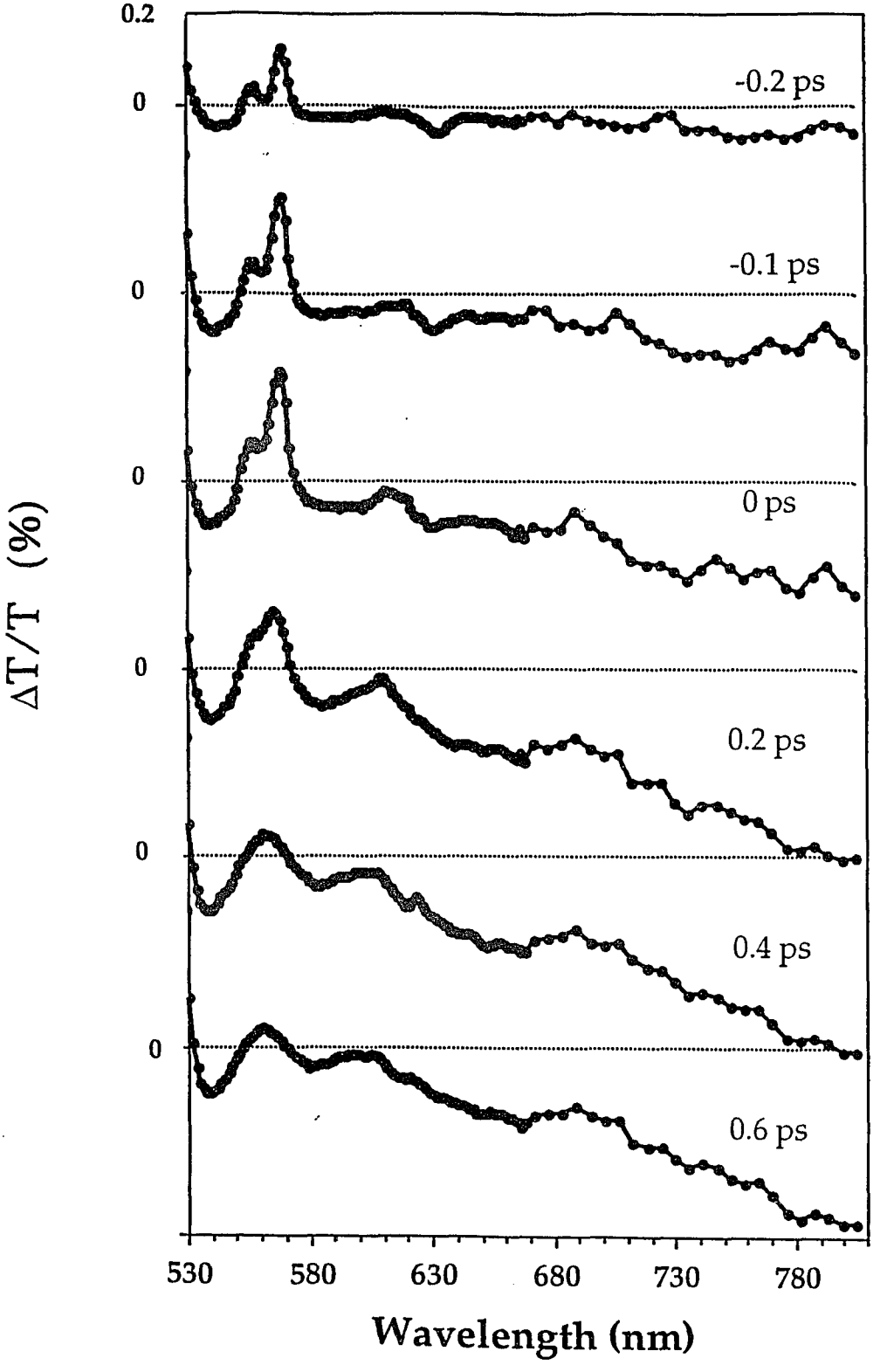

Fig. 8.6(A) Time resolved photoinduced transmission change of oriented PPV film after photoexcitation at 523 nm and polarized parallel to the polymer oriented direction. Delay time is from -0.2 ps to 0.6 ps

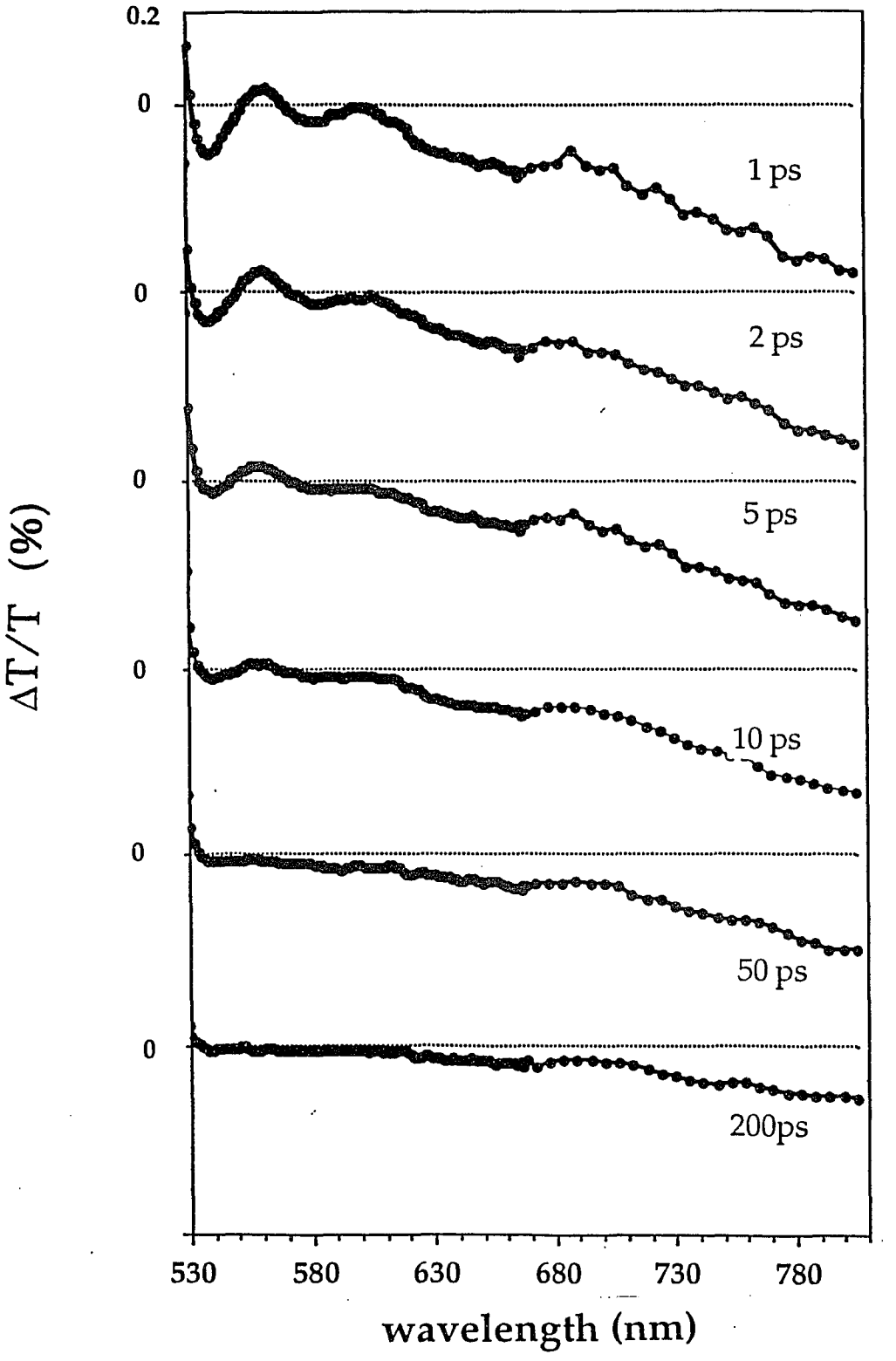

Fig. 8.6(B) Time resolved photoinduced transmission change of oriented PPV film after photoexcitation at 523 nm and polarized parallel to the polymer oriented direction. Delay time is from 1ps to 200 ps

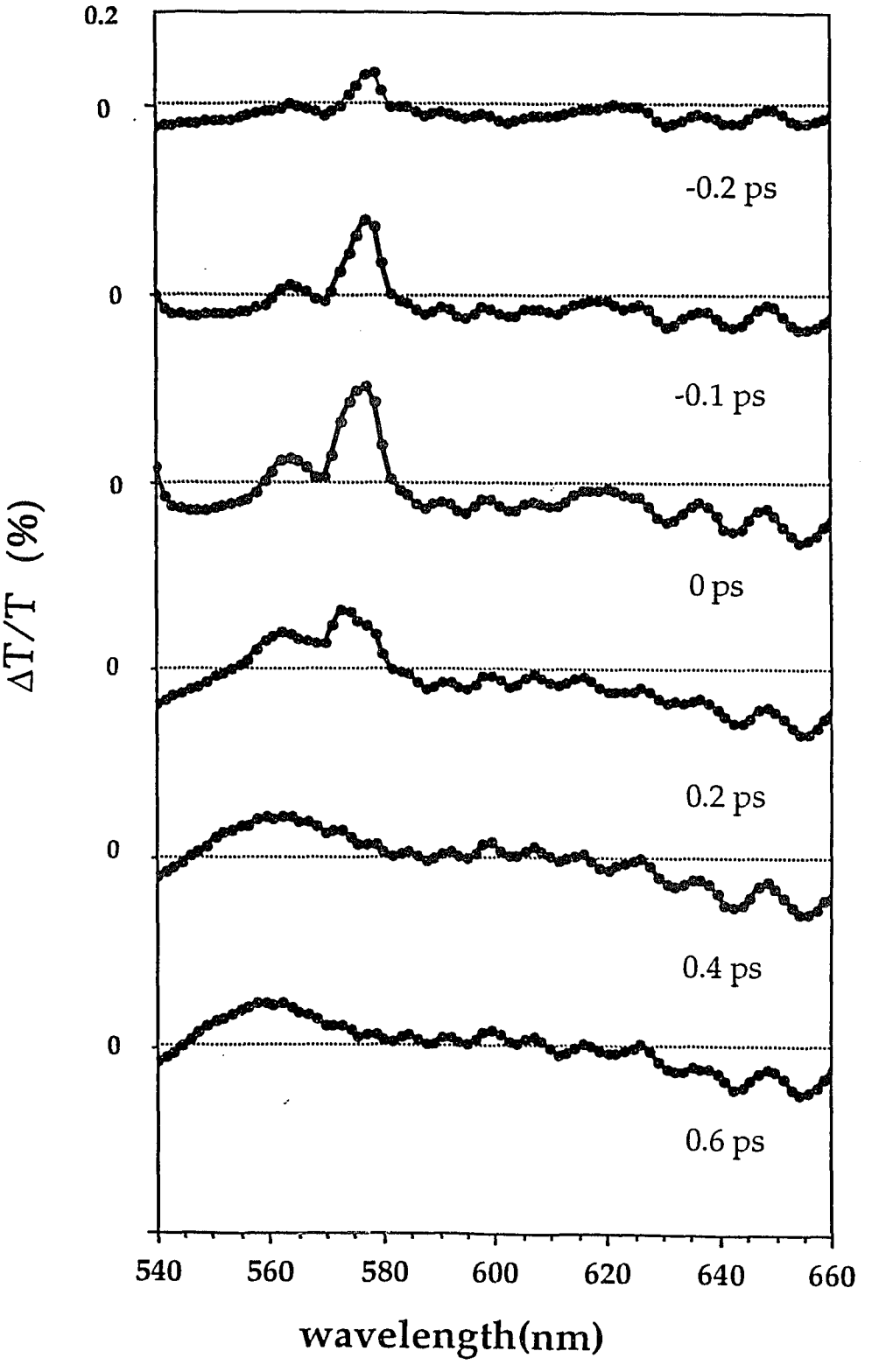

Fig. 8.7(A) Time resolved photoinduced transmission change of oriented PPV film after photoexcitation at 533 nm and polarized perpendicular to the polymer oriented direction. Delay time is from -0.2 ps to 0.6 ps

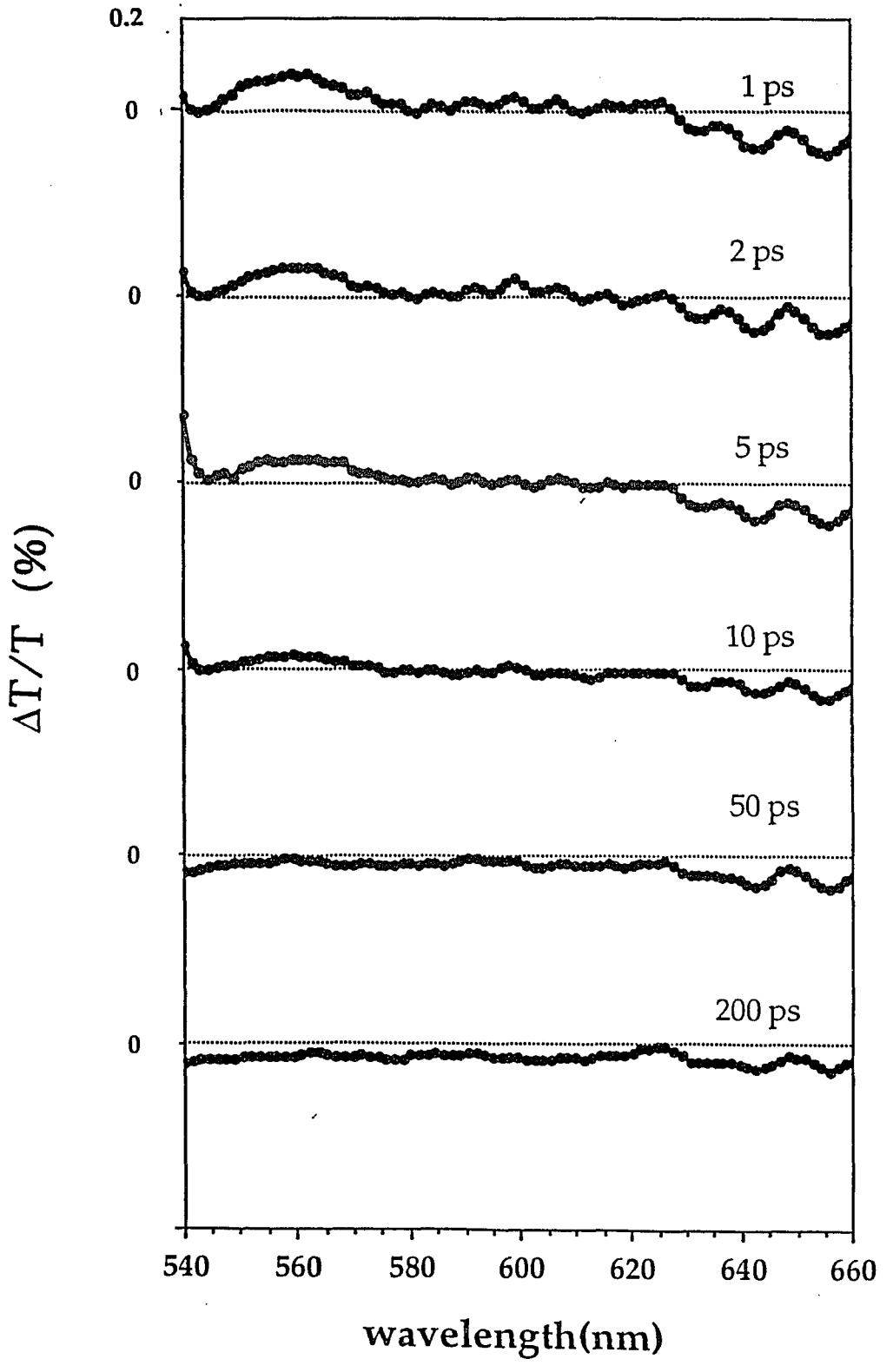

Fig. 8.7(B) Time resolved photoinduced transmission change of oriented PPV film after photoexcitation at 533 nm and polarized perpendicular to the polymer oriented direction. Delay time is from 1 ps to 200 ps

absorption arises from the same species or originally from same species.

The time-resolved absorption change for the wavelengths at 665, 790 and 950 nm due to photoexcitation at 523nm polarized parallel to the chain are plotted in figure 8.8. The double exponential fits described in Eqn.8.1 to the photoinduced absorption yield time constants for the fast component of 800fs and 100 ps for the slow one. Therefore, the photoinduced absorption changes in the red part of the spectrum show the same decay kinetics for photoexcitation at 500, 523 and 533 nm polarization along the chain. This suggests that there is no density dependent kinetics since the excited density changes by a factor of 5 to 10 when the excitation wavelength changes from 500 nm to 530 nm.

When the pump and probe pulses overlap in time, two sharp stimulated gain features are observed at wavelength 540-620nm which is shown in figure 8.9 and assigned to the Raman gain signal. The amplification of the probe pulse (gain) is due to the stimulated Raman gain described by Kobayashi et al.[6.9,8.1] in polythiolene. This Raman gain assignment is verified by tunning the excitation wavelength. The photoinduced gain spectra which is excited by 523 nm and 533nm for the polarization parallel to the chain are shown in figure 8.9.

There are two important observations. First, two sharp gain peaks are observed which shift as the photoexcitation wavelength shifts when the pump and probe pulse overlaps in time, This observation confirms that these two sharp gain peaks are due to the Raman gain since it shifts with excitation wavelength. The frequency shifts of these two Raman gains signals are 1170 cm^{-1} and 1560 cm^{-1} which corresponds to the two most intense Raman modes observed in conventional Raman vibrational spectroscopy in PPV[7.4,7.5] shown in figure 7.1. Second, the photoinduced gain spectra observed after a 0.2 ps delay time do not shifted as the pump wavelength changes and always agree with the luminescence spectrum. This observation confirms that the stimulated gain

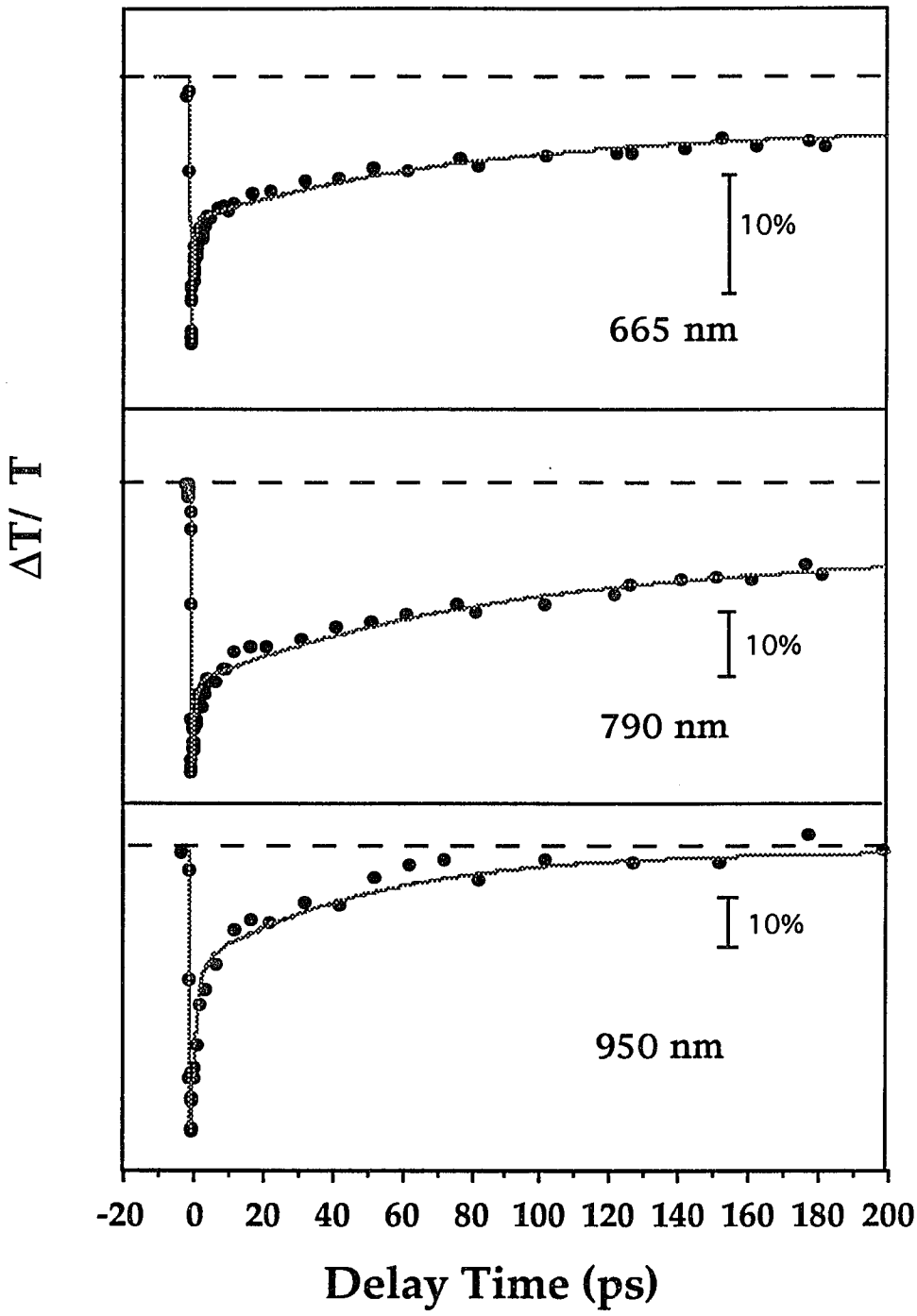

Fig.8.8 Time resolved induced absorption at 665 nm, 790 nm and 950 nm. The excitation wavelength is 523nm and polarization is parallel to the chain. The solid line is the fit of a double exponential decay convoluted with the laser pulse profile as discussed in text.

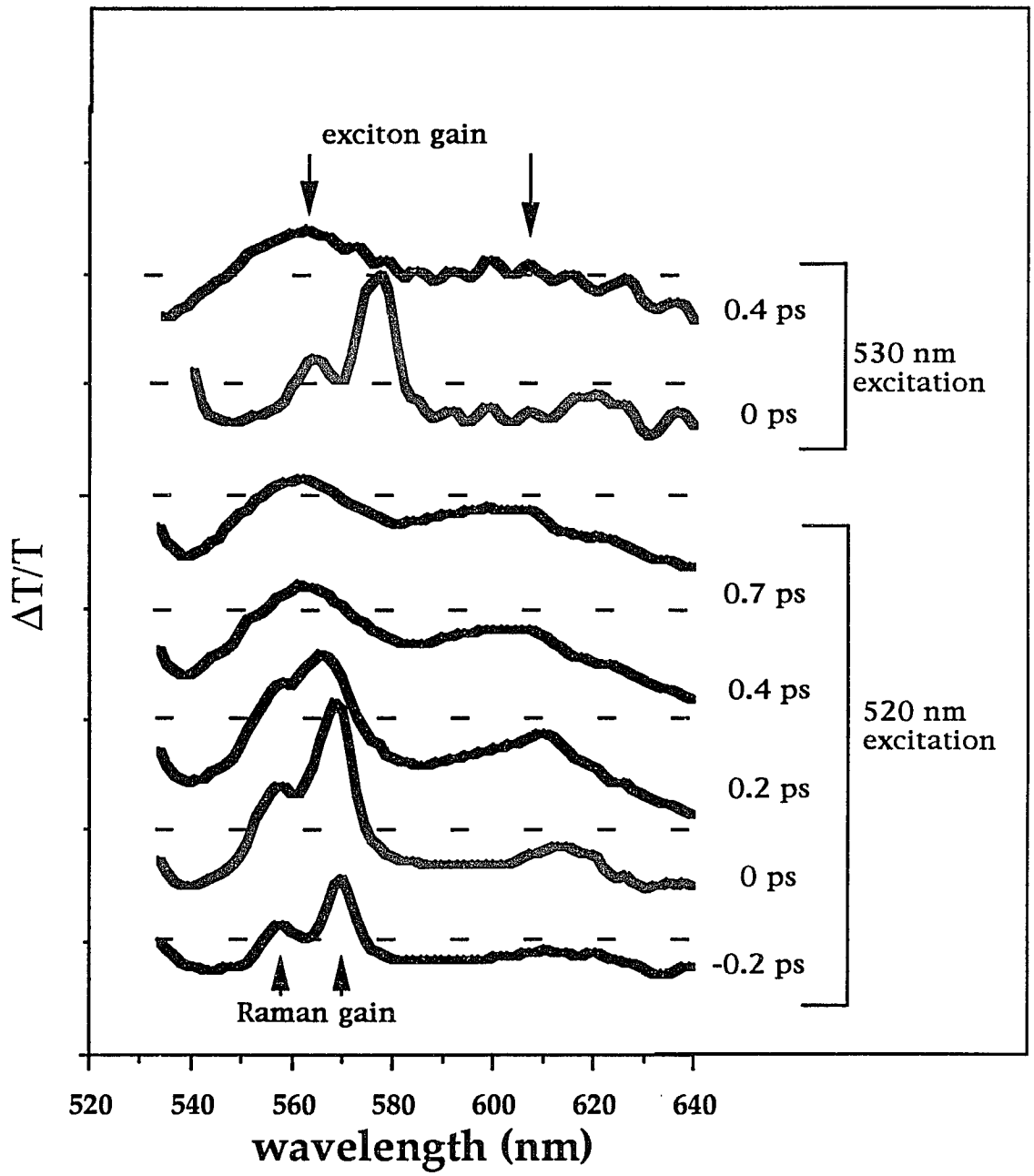

Fig. 8.9 The photoinduced gain near the zero delay time. The bottom set is photoexcited by 523nm and top one is by 533nm, the polarization is set parallel to the oriented sample direction in both sets. Each curve is shifted equally space and the dash line represents the zero of each curve. The Raman and exciton gain are indicated.

observed after 200 fs delay time are the stimulated gain from excitons. The same exciton gain is observed in perpendicularly polarized excitation at 500nm (figure 8.5). The distinction of Raman and exciton gain explains the spectral shift within early 200 fs for perpendicular polarized excitation at 500nm (shown in figure 8.5). This spectral shift is due to the spectral overlapping between the Raman gain and the exciton gain. The observed initial gain signal at 542 nm shown in figure 8.5 is due to the Raman gain peak at frequency of 1560 cm^{-1} rather than the exciton gain. The gain spectra observed 550 nm is due to the exciton gain.

The kinetics of stimulated Raman and exciton gain gain are depicted in figure 8.10 for the photoexcitation at 530nm polarized along the chain. At probe wavelength of 576nm where Raman gain is observed (shown in open circles), the Raman gain is instantaneously formed and quickly decayed in time which consist the assigment of Raman gain since the Raman gain only can be observed when the pump and probe pulse temporally overlaps each other. The slow decayed tail are due to the exciton gain. At 560nm (shown in solid circles) where Raman gain is not observed, only exciton gain is separated from Raman gain. The initial absorption is observed at this wavelength which is due to the excited state absorption. The initial absorption becomes a gain signal within 200 fs. Therefore the exciton is formed within 200 fs after excitation. Furthermore, because this initial absorption is observed in the entire spectrum (520-1000nm), by assuming the absorption in this wavelength have the same kinetics elsewhere (since the induced absorption in our experimental probe wavelength range show same kinetics), we fit the kinetic data at 560 nm by an instantaneously formed exciton gain with an absorption which is instantaneously formed and decayed in 800 fs time constant. Therefore, we conclude that the stimulated exciton gain is formed within 200fs after excitation. The decay of exciton gain is fitted by a 10 ps exponential decay time constant and a much slower one of least at 100 ps.

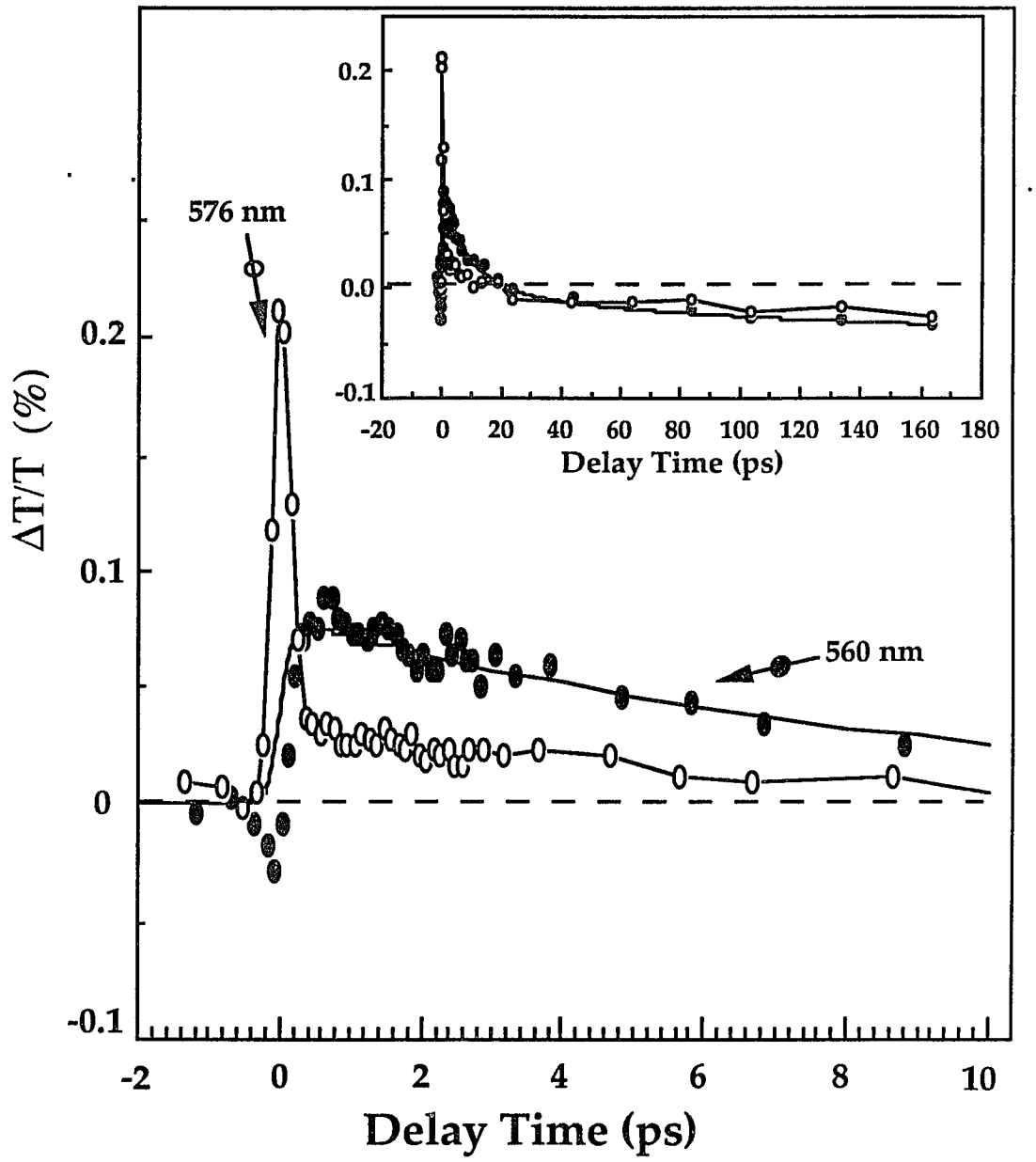

Fig. 8.10 The time resolved photoinduced gain at 560 nm and 576 nm photoexcited by 533nm which is polarized parallel to the oriented sample direction. The decay is fitted by 10 ps and 100 ps biexponential decay time constants as shown by solid lines. The inset is shown for a large time scale.

8.3) Picosecond Photoluminescence Measurements

In this section, I will describe the transient luminescence measurements to study the dynamics of excitons in oriented PPV film because it is believed that luminescence is due to the radiative recombination of exciton.[6.8] The luminescence wavelength dependence, excitation polarization and wavelength dependence are performed to understand the anisotropic effect in absorption and luminescence in PPV.

Figure 8.11 depicts the luminescence spectra of an oriented PPV film due to excitation at 500nm with polarizations parallel and perpendicular to the polymer chain. The luminescence is integrated for both polarizations but nearly all of the luminescence is along the polymer chain regardless of the excitation polarization. The luminescence intensity with polarization along the chain is about 5 times as intense as the luminescence polarized perpendicular to the chain, and luminescence in both polarizations shows the same kinetic behavior. This implies that the exciton geminately recombines along the polymer chain. The luminescence due to perpendicularly polarized excitation is about twice as intense as for parallel excitation when the loss in reflection is taken into account. Again, the consistency between the polarization dependence of the intensity of luminescence and the photoinduced absorption suggests that the luminescence and induced absorption arise from the same or originally from the same species.

Typical time-resolved luminescence is depicted in figure 8.12 which is for photoexcitation at a wavelength of 500nm with 300fs laser pulse polarized perpendicular to the chain at 300K and for luminescence along the chain at 550nm. The luminescence appears within the instrument resolution of 6ps which is determined by the "prepulse" preceding the luminescence. The decay of luminescence is successfully fitted by a two exponential decay convolution with the 6 ps instrument resolution which yields 25 ps and 90 ps exponential decay

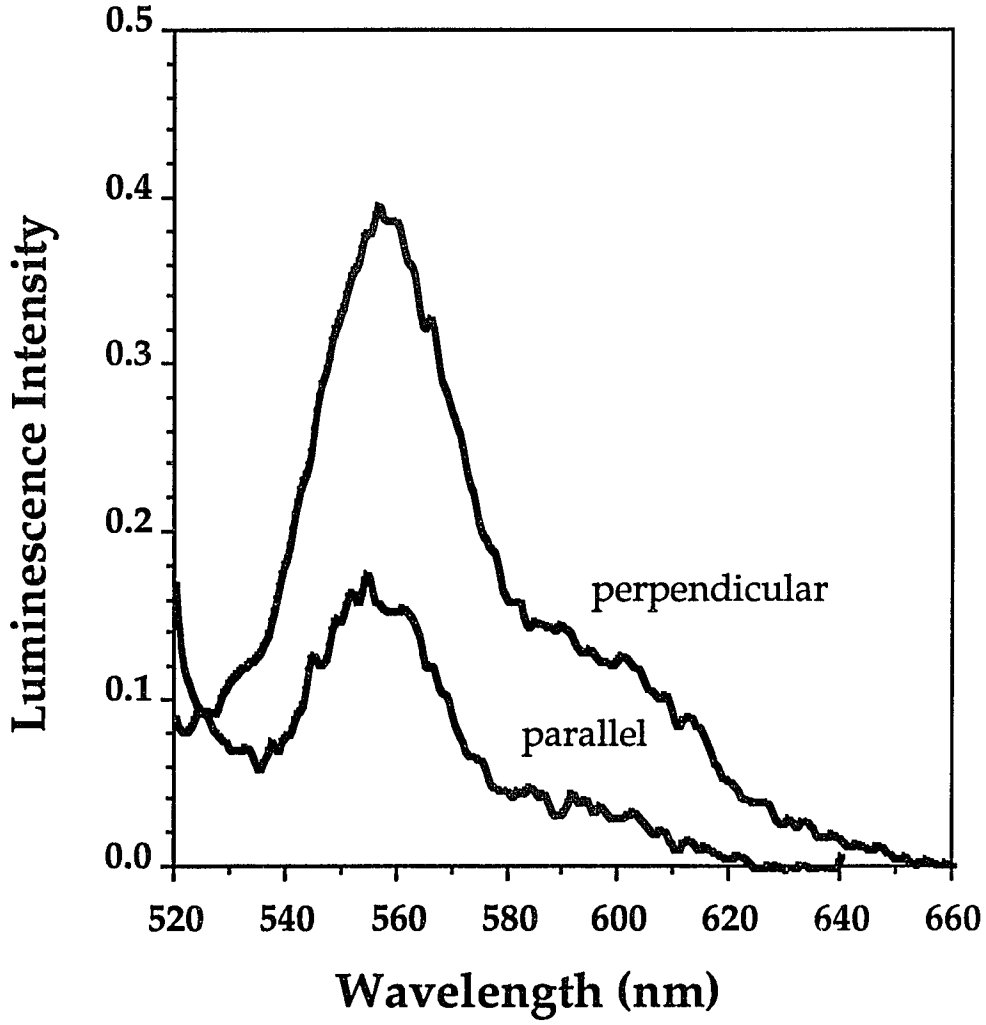

Fig. 8.11 CW luminescence spectra of an oriented PPV film. The excitation polarization is set parallel and perpendicular to the oriented direction.

time constants as depicted in figure 8.12. The luminescence of PPV measurements shows that the luminescence last for nanoseconds[8.2]. The luminescence temporal profile from PPV is non-exponential. This non-exponential decay of luminescence (with initial decay 25 ps and 100 ps) is due to the non-radiative decay of singlet exciton via diffusion into those non-radiative recombination center (defects). The long-lived photoluminescence is probably due to recombination of long-lived polaron pairs which is assigned responsible for the long-lived absorption.

A. photoluminescence wavelength dependence

The time-resolved photoluminescence can be fitted by a double exponential decay kinetics in the luminescence wavelength range 550nm -700nm. In the case of excitation polarized perpendicular to the chain, the kinetics is fitted by 25 ps and 90 ps exponential decay constants which is shown in figure 8.12. The time resolved luminescence spectra are depicted in figure 8.13 together with the cw luminescence spectrum. The time resolved luminescence spectra did not shift with time and essentially agree with the cw luminescence. The decay of luminescence keeps the same vibrational spectral feature suggesting that the luminescence is not from the species such as trapping center after formation of the self-trapped exciton within 200 fs.

The luminescence at different wavelengths has been fitted by a double exponential decay convoluted with a 6 ps Gaussian time profile of instrumental response which is shown in the following:

$$I(\lambda,t) = (a_1(\lambda)e^{-t/\tau_1} + a_2(\lambda)e^{-t/\tau_2}) \otimes G(t) \qquad (8.2)$$

where G(t) is a Gaussian representative of instrumental resolution with FWHM at 6 ps. The τ_1 and τ_2 obtained by fitting is about 25 ps and 90 ps, respectively, for

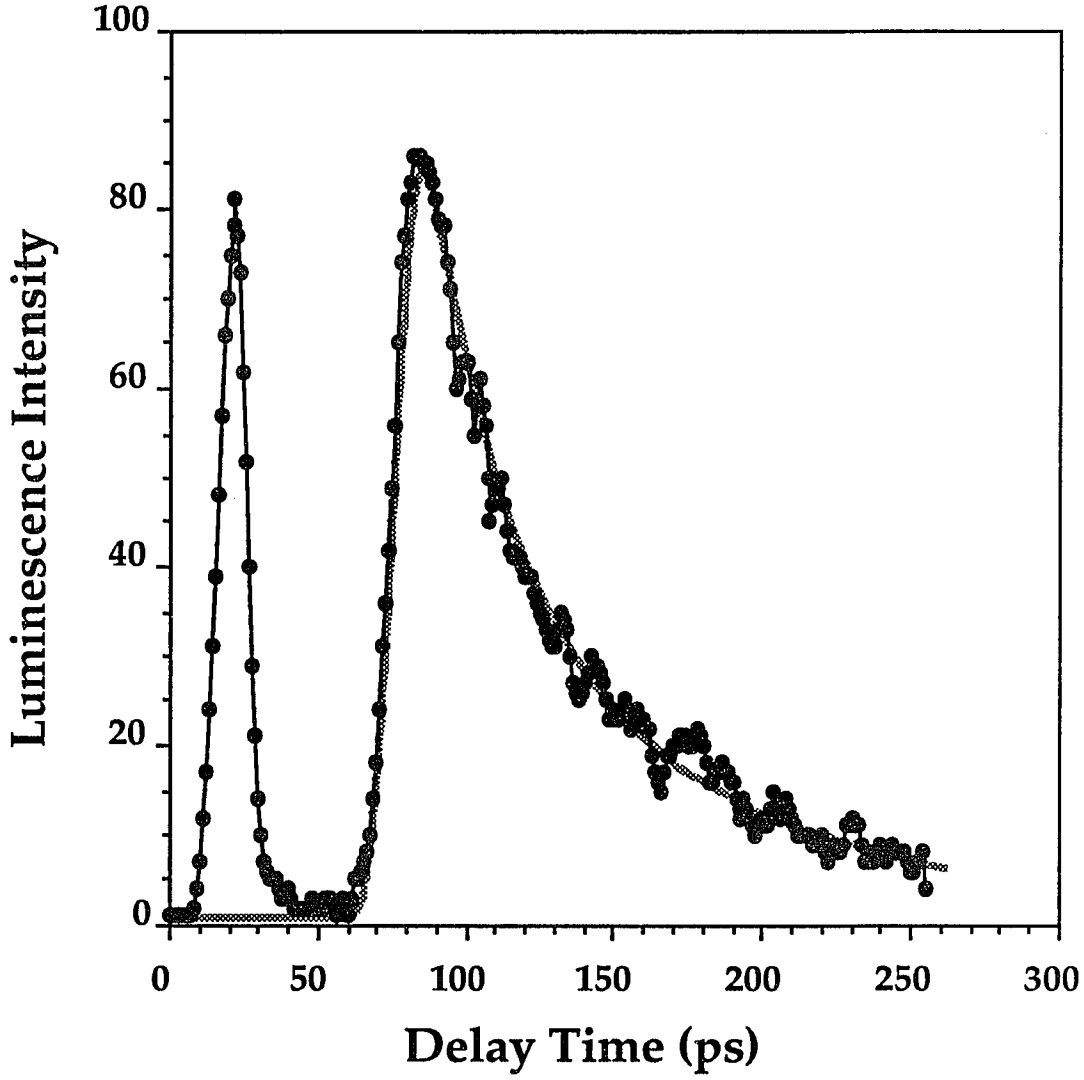

Fig. 8.12 Time-resolved luminescence at a wavelength of 550nm photoexcited by 500nm polarized perpendicular to the chain. The luminescence is measured for the polarization along the chain. The solid line is the fitting of a double exponential decay which yields 25 ps and 100ps time constatnts.

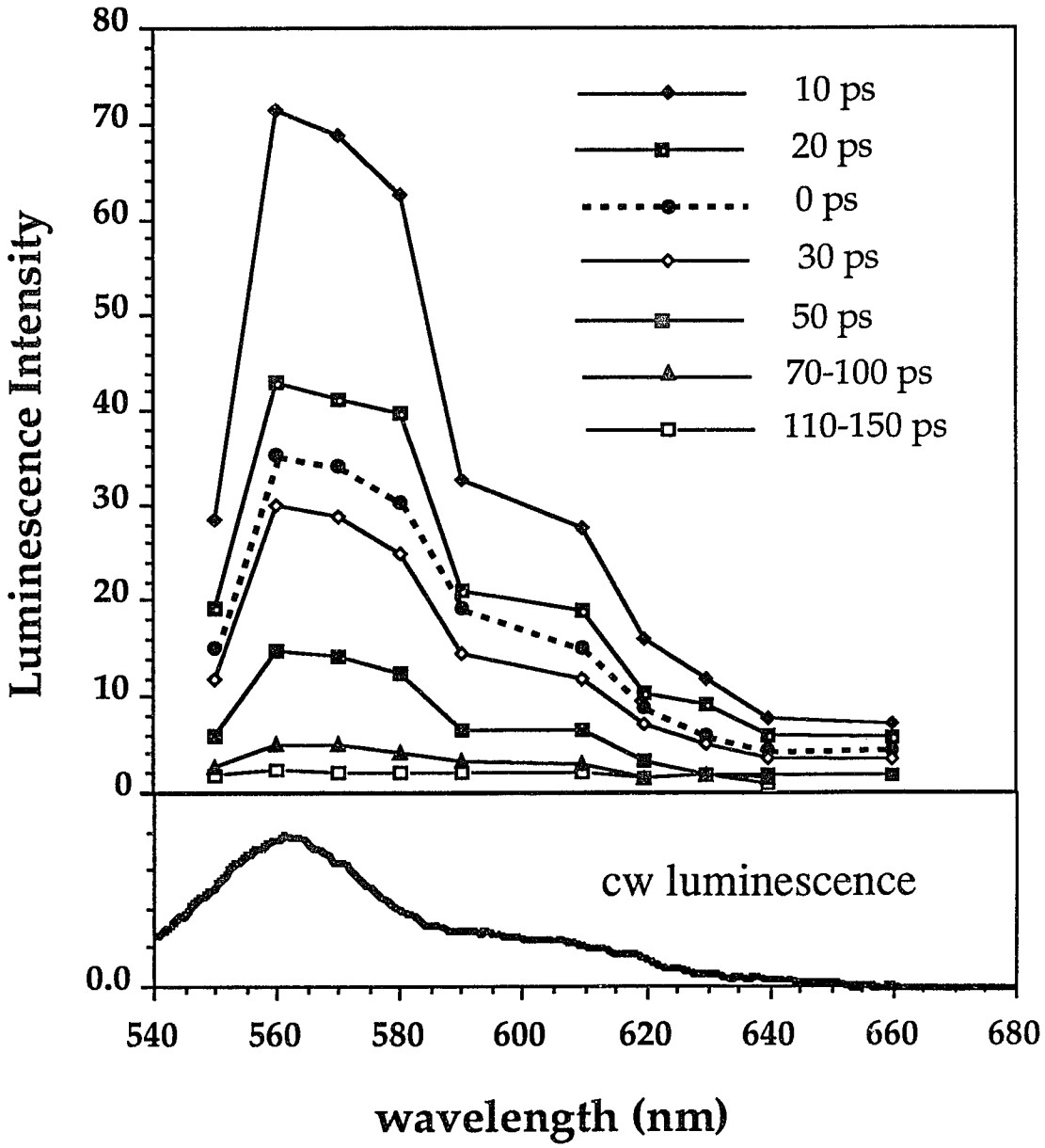

Fig.8.13 Time-resolved luminescence spectrum of an oriented PPV film by photoexcitation at 520nm polarized parallel to the chain. The bottom curve is the cw luminescence spectrum. No spectra shifting is observed between 10 ps and steady state luminescence.

luminescence wavelengths from 550 nm to 700 nm. The amplitude of the fast, $a_1(\lambda)$, and the slow, $a_2(\lambda)$, decay components and their ratios are wavelength dependent and listed in table 4.2.

wavelength (nm)	$a_1(\lambda)$(25ps)	$a_2(\lambda)$(90ps)	ratio a_1/a_2
550	210	114	1.8
560	350	225	1.6
570	325	175	1.8
590	80	50	1.6
610	120	80	1.5
630	40	40	1.0
650	14	14	1.0
700	0	13	0

Table 8.1 The fitting of amplitudes of the fast and slow decay components and their ratio.

Table 8.1 shows that the ratio of fast decay components to slow decay components are relatively larger in the short wavelengths. This implays that the energy redistribution of exciton, i.e. the thermalization of self-trapped exciton in picoseconds time scale. Because the thermalization of the exciton make a greater population at lower vibrational ladders. The long-delayed luminescence are from the radiative recombination of thermally "cooled" self-trapped excitons. Therefore, the long-tail luminescence may have relatively large component in the lower vibrational ladder. This wavelength dependence is similar for excitation with different polarizations and at different excitation wavelengths. The spectral shifting of photoluminescence is not observed which implays that the exciton diffusion is not important since only those longest chain has been photoexcited.

B. Excitation polarization dependence

The luminescence in this oriented sample is found to be twice as intense for excitation polarized perpendicular to the polymer chain as for parallel excitation. A similar polarization effect has been observed in the photoinduced gain and absorption as described above. The decay of luminescence at 300K for excitation polarized parallel and perpendicular to the chain are similar as seen in figure 8.14. The decay of luminescence for excitation polarized parallel to the chain is fitted by 20 ps and 90 ps exponential decay constants while 25 ps and 90 ps fit perpendicularly polarized excitation. The ratio of the amplitudes for the fast decay (25ps or 20 ps) component relative to the slow decay (90ps) is about 3:1 for parallel excitation which is larger than 1.6:1 for perpendicularly polarized excitation. This excitation polarization dependence suggest there is different formation branch or coupling to the initial decayed dself-trapped excitons and long decayed polaron pairs for different polarized photoexcitation.

C. Excitation wavelength dependence

Figure 8.15 depicts the photoluminescence at 570nm by an excitation wavelength of 520nm and 500nm polarized parallel to the chain. The luminescence is instantaneously formed within the instrumental resolution of 6 ps, the decay has been fitted by double exponential time constants, 15ps and 70 ps. The luminescence wavelength dependence is similar to the luminescence excited using wavelength at 500nm. As we described in the earlier text, the absorption cross-section at 520nm is much smaller than at 500nm for parallel polarized excitations. The absorption depth is deeper for 520nm than for 500nm and all the excitation light is absorbed for both 520nm and 500nm. Therefore, the photoexcited density is much higher for excitation at 500nm. As a consequence, this excitation wavelength dependent luminescence measurement is inconsistent

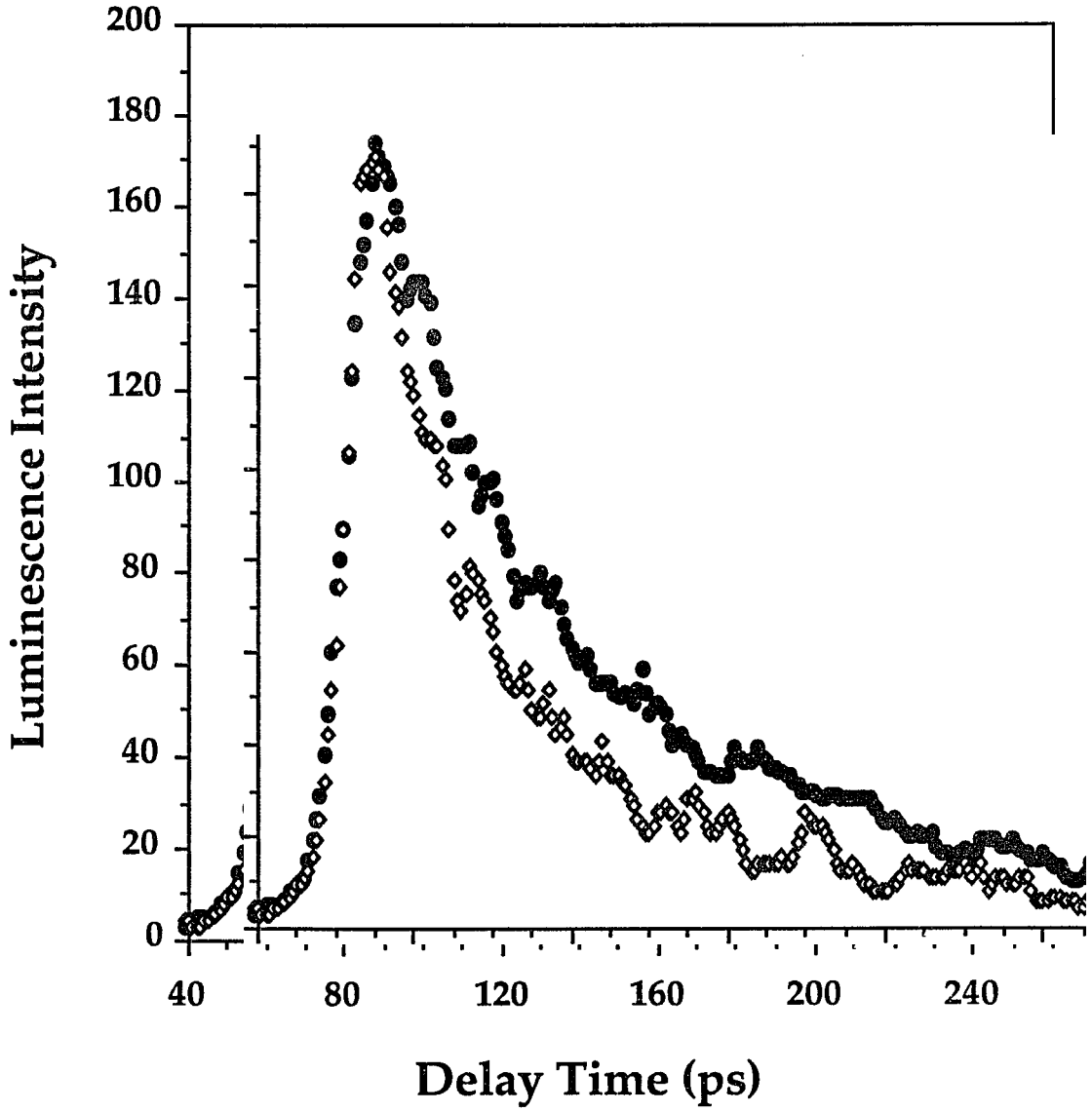

Fig. 8.14 Time resolved luminescence at 570nm by photoexcitation at 500 nm polarized paralle ◇ and perpendicular • to the chain.

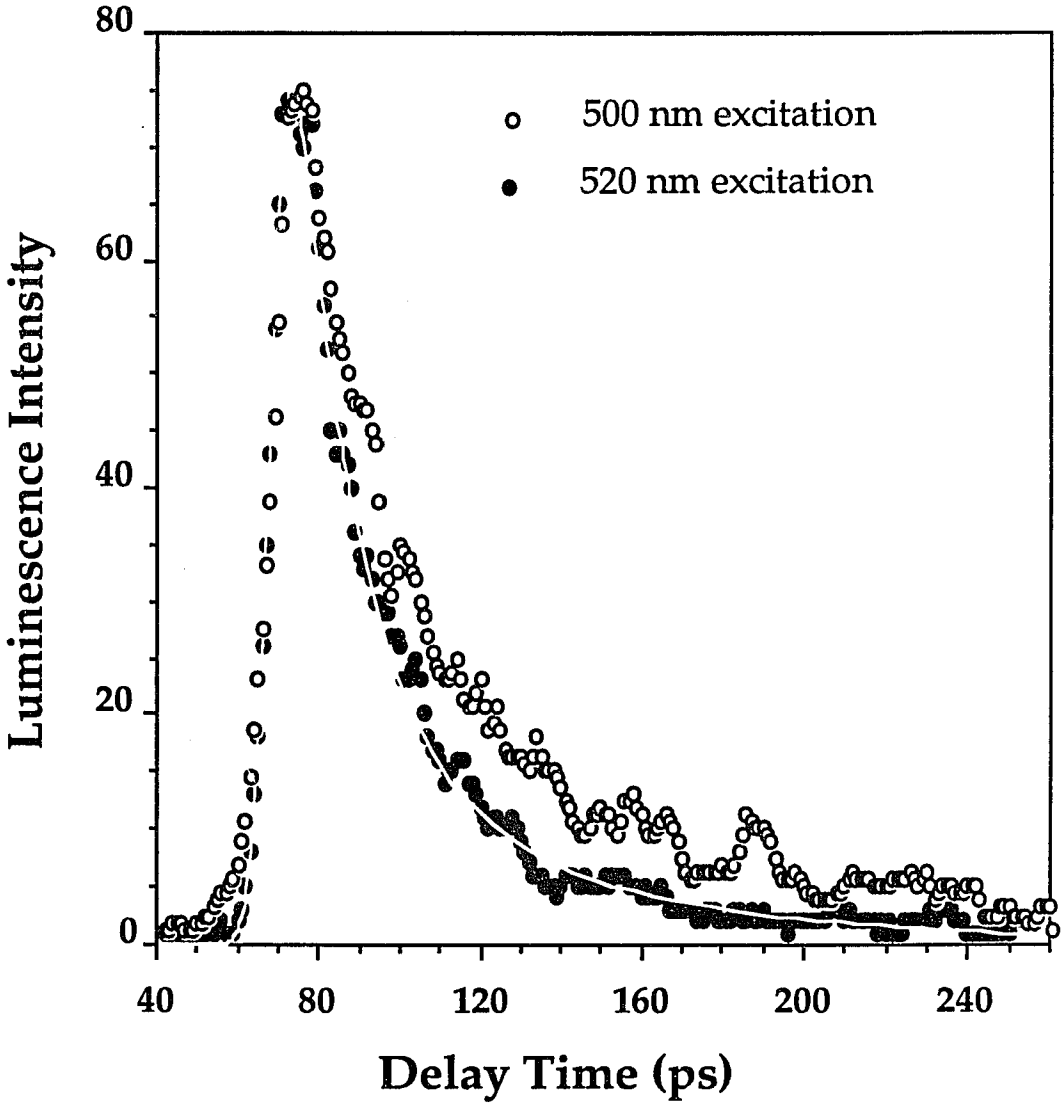

Fig. 8.15 Time resolved luminescence at 570nm by photoexcitation at 520nm ● and 500nm ○ polarized parallel to the chain. The solid fit is for a double exponential decay which are described in the text.

with the bimolecular recombination model[7.13] described above. We will discuss this point later in the text. The 15-ps decay time constant is consistent with the decay time constant of photoinduced gain for 520nm excitation polarized parallel to the chain, this confirms that photoluminescence and photoinduced gain is due to the population of the singlet exciton state. The difference of initial decay luminescence due to the 520nm and 500nm excitaion may be the result of the different thermalization time. Because the excess energy by 500nm excitation is larger than 520nm excitation, it would take longer time for the lattice to thermalize.

8.4) Discussion of experimental results

We have presented the experimental results of time-resolved absorption and luminescence measurements in oriented PPV films. With reference to the experimental results, I will present a model to describe the properties of neutral excitations(singlet excitons and triplet excitons), I will also discuss the possibility of the existence of charged excitations (polarons and bipolarons) in the few hundred picosecond region in oriented PPV films.

A. Singlet Exciton

Photoluminescence is a direct signature for the existence of the singlet exciton which involves the optical transition from the occupied upper gap to the lower gap polaron-exciton state as shown in figure 6.7. Experimentally, photo-luminescence is commonly found to be very weak in conjugated polymers due to the competition of large effective nonradiative decay channels. However, the family of PPV exhibits a high quantum yield for photoluminescence due to sample preparation with very low concentrations of charged and spin defects.

The time resolved stimulated gain at the singlet exciton luminescence

energy suggest that the singlet exciton is formed within 200fs. This formation time of the singlet exciton is consistent with the luminescence observation in which the fitted rise time is much less than the 6 ps streak camera resolution. The stimulated gain decays with two exponential components having a 10 ps and a much slower decay time constants. These decay time constants agree with the exciton luminescence photoexcited at 520nm polarized along the chain which has a double exponential decays with time constants of 15-ps and 70-ps.

The decay of the exciton has been discussed using the bimolecular recombination and intra- and inter-chain excitations [6.8,7.13]. Their model is based on the fact that the luminescence intensity for perpendicular excitation is twice as large as the luminescence in parallel excitation. The decay time is shorter for parallel excitation. In their model the recombination dynamics is described by a non-linear rate equation having the form of

$$\frac{dn(t)}{dt} = -\frac{n(t)}{t} - \beta n^2(t) \qquad (8.4)$$

where n(t) is the concentration of carriers at time t, and ß is associated with a non-radiative bimolecular recombination process. In this model the exciton decay kinetics and intensity is strongly affected by the initial carrier density n(0). As mentioned in early text, the excited carrier density for parallel excitation at 500nm wavelength is much larger (>10 times) than for perpendicularly excitation, thus one may expect that the kinetics changes dramatically in polarization dependent luminescence according to the bimolecular recombination model. The excitation polarization dependence of luminescence (figure 8.14) shows that the fast decay time of 25-ps for perpendicularly photoexcitation is similar to the decay time of 20ps for parallel excitation. Furthermore, when the excitation wavelengthes change from 500nm to 520nm, the concentration of carrier density decreases more than a factor of 5. According to the bimolecular model, the decay rate is

expected to be slower. But the 15-ps decay time of luminescence in excitation at 520nm which is a lower density is slightly faster than the 20-ps for excitation with a wavelength of 500nm(Fig.8.14) This observation contradicts the density dependent bimolecular decay model. Recent intensity dependent time resolved luminescence and absorption measurements [8.2] also show that the decay dynamics is not intensity dependent. Thus, the bimolecular non-radiative recombination model is inadequate to describe this polarization anisotropic effect.

Figure 8.16 depicts the excitation luminescence spectrum for the excitation polarized parallel and perpendicular to the chain. The luminescence is monitored at the luminescence peak wavelength of 560nm. The luminescence increases as the excitation energy approaches the absorption band and followed fairly well the density of states in this energy region. After reaching the luminescence maximum, the luminescence decreases as the excitation energy further increases. Note, the excitation photon is totally absorbed in this region of decreasing luminescence. One may note that the excitation spectrum for perpendicular excitation shifts about 0.15eV to higher energy compared to the parallel excitation spectrum. This excitation luminescence spectrum and shift due to the rotation of excitation polarization is consistent with all the cw and time resolved photoinduced absorption and luminescence results described in the above text.

The photoinduced absorption of 800 nm at 200 ps delay time with different excitation wavelength are plotted as open circles (parallel polarized excitation) and open squares (perpendicular polarized excitation) in figure 8.16. The intensity of photoinduced absorption agree very well with the excitation luminescence spectrum as shown in figure 8.6. Thus, the anisotropic polarized excitation dependence of luminescence and photoinduced absorption is due to the different excitation wavelength dependence for parallel and perpendicularly polarized excitation. It is also shown that the long-lived induced absorption and

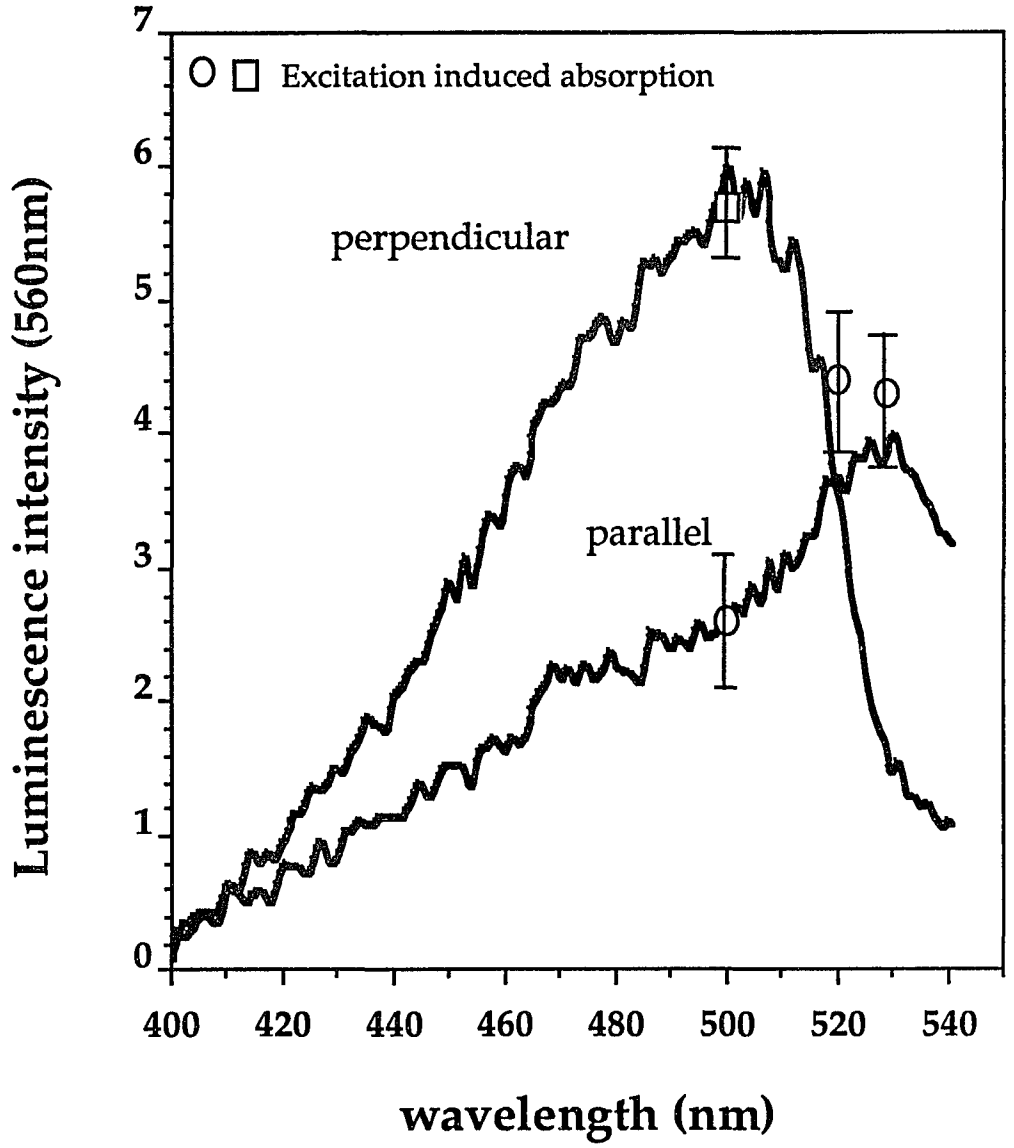

Fig. 8.16 Excitation luminescence spectra at 560 nm of an oriented PPV film for excitation polarization parallel and perpendicular to the chain. The open circles and square indicate the intensity of photoinduced absorption.

long-lived luminescence are correlated. As mentioned in early text, on the similar long decay (100ps) kinetics of induced absorption and luminescence are observed. Therefore, we propose that long-lived polaron pairs are the channel to feed the singlet exciton which give long tail component of luminescence. Those opposite charged polaron pairs re-bound together to form a singlet exciton. We conclude the dynamics scheme of exciton as shown in figure 8.17.

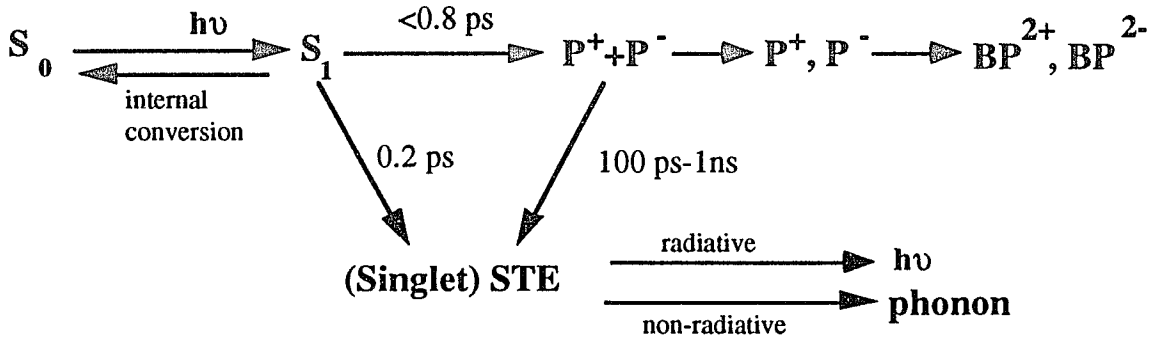

Fig.8.17 Schematic diagram of dynamics scheme of PPV after photoexcitation. where STE is the self-trapped exciton or singlet exciton. P^+ and P^- are positive and negative charged polarons and BP are bipolarons.

After the above band photoexcitation, the electrons have been excited into the excited states (S_1) from ground state (S_0) by Franck-Condon transition within our laser temporal resolution. The Franck-Condon state (S_1) or free exciton (FE) states decay into self-trapped exciton (STE) state by coupling to localized vibrational modes within 200 fs. Also, the S_1 free excitons form polaron pairs by separating the charges within 800 fs. The ST excitons have a lifetime about 20 ps mostly due to the non-radiative recombination into ground state (S_0) due to the defects. Meanwhile, polaron pairs recombine into ST excitons in the time scale from 100 ps to few ns.

The long-lived luminescence has been explained by the diffusion theory of excitons to those recombination center which are probably defects located on the

polymer chains via random walk process. According this theory, all the excitons which radiatively recombined are directly formed from free excitons as proposed by Friend [6.8,7.13] and Kobayashi[6.9,8.1]. The time resolved luminescence measurements utilizing photoaccounting device[8.2] suggest the luminescence could be fitted by diffusion model except the long tail which last to 40 ns. This confirms that the singlet excitons corresponding to the long tail luminescence are not directly formed from free exciton and should from the third party between the free exciton and singlet self-trapped excitons which we proposed as polaron pairs.

We have concluded that the singlet exciton is formed within 200fs and decays with about a 10-20 ps fast exponential decay time constant followed by a 100-ps and even a nanosecond long non-exponential decay tail. The fast decay time constant varies from 15 ps to 25 ps which depends on the excitation wavelength, this suggests the thermalization time is depended on the excess energy and polarization of photoexcitation. The long decay tail of luminescence are from the recombination of self-trapped excitons which are formed from polaron pairs rather than directly from free exciton. The spectral features of photoinduced gain in the early picosecond agree with the spectra of luminescence in the early 10 ps as well as with the cw luminescence spectra. This indicates that the exciton is not further trapped after its formation as a self-trapped exciton within 200fs after photoexcitation.

B. Polarons

The long-lived absorption observed at absorption peak of 1.45 eV is formed within 800 fs and decays in a nonexponential way and last for nanosecond but with an initial decay of about 100 ps time constant. The photoinduced absorption spectra as a function of pump-probe delay time are

depicted in figure 8.18. We assign this to the absorption to the polaron pairs. The polaron pair formation from free excitons could be either by interchain hopping (or diffusion) of charge of free excitons or geometric chain distortions to separate the charge of exciton (e.g. rotation of phenylene ring broke the conjugation of polymer chain). Polaron pairs could disassociate into free polarons which may contribution to the photoconductivity and further trap to form bipolarons. The recombination of polaron pairs are the source to feed the singlet self-trapped exciton which give the long-tail of luminescence. The linear excitaion intensity dependence of long-lived induced absorption and luminescence [8.2] also suggest that absorption from polaron pairs which geminately recombined. The formation time of polarons are measured less than 800 fs because the spectral overlapping with the absorption of "hot" ground state which decay at 800 fs. The polaron pair model also explains the excitation wavelength dependent photoinduced absorption which photoinduced gain only observed at certain excitation wavelength.

The bipolarons have been identified in PPV [7.10] with the absorption peaks at 0.5 and 1.4 eV. Bipolarons are formed by bound two like charged polarons which diffuse away from the originally excited chains. Therefore, one may expect very small quantum yields for bipolaron formation. This may be the reason for the failure to observe bipolarons at 1.4 eV. The higher sensitivity of time resolved IR absorption measurements at 0.5 eV is proposed to study the kinetics of bipolarons, see future experiment in chapter 9.

C. Intra- and Inter- chain Excitation?

Excitation luminescence spectrum (Fig.8.16) clearly shows that the polarization dependent luminescence is excitation wavelength dependent. A fundamental question is raised with regard to these results. Is the commonly

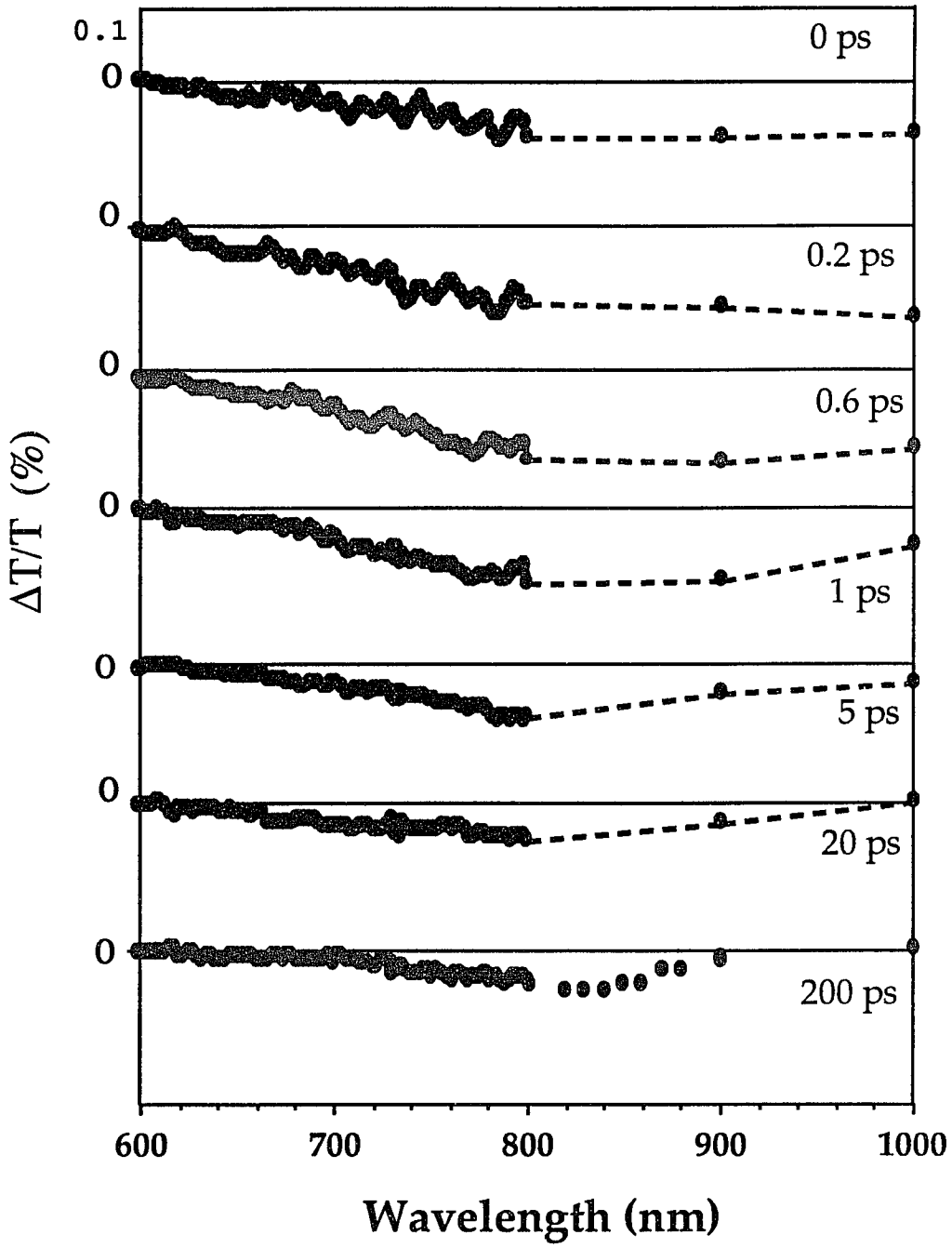

Fig. 8.18 Photoinduced absorption spectrum as a function of delay time by parallel polarized photoexcitation at 500nm.

accepted theory for intra- and inter-chain excitation with different polarizations adequate? According to the intra- and inter- chain excitation model, excitation polarized parallel to the chain generates electron-hole pairs along the same chain; excitation polarized perpendicular to the chain generates some electron and hole located separately on neighboring chains. Therefore, one may expect quite different carrier dynamics and carrier products (i.e. triplet excitons and bipolarons) in polarization dependent measurements. The photoinduced absorption, gain and luminescence measurements show similar carrier dynamics and formation of the same photoproducts (single and triplet exciton) at early few hundred picoseconds. These experimental results are hardly convincing that the intra- and inter- chain excitations exist. The polarization dependent intensity of photoinduced absorption and luminescence, which has been used as evidence for the intra- and inter- chain excitation model, can be explained as the result of different excitation wavelength dependence for different polarizations.

Recently, Hsu et al.[8.2] have suggested that this excitation wavelength dependence for different polarizations results from the different optically allowed transitions for excitation with parallel and perpendicular polarizations. We propose a model to explain the different polarized excitaion as depicted in figure 8.19. In this model, excitation with parallel polarization involves the optical transition to the lowest excited state (S_1); with perpendicularly polarization to the energy transition to a high layer excited state (S'_1) since the transition to the S_1 state is not allowed. The reason why the optical transition for perpendicular excitation to the S_1 state is not allowed may be due to the dipole moment of the S_1 state lies along the polymer backbone, where the dipole moment of S'_1 is perpendicular to the polymer chain. Therefore, the optical transition for perpendicular polarized light to the S'_1 state is dipole-favored. Also, the 0.15-eV energy shift of absorption for different polarized light may involve vibrational

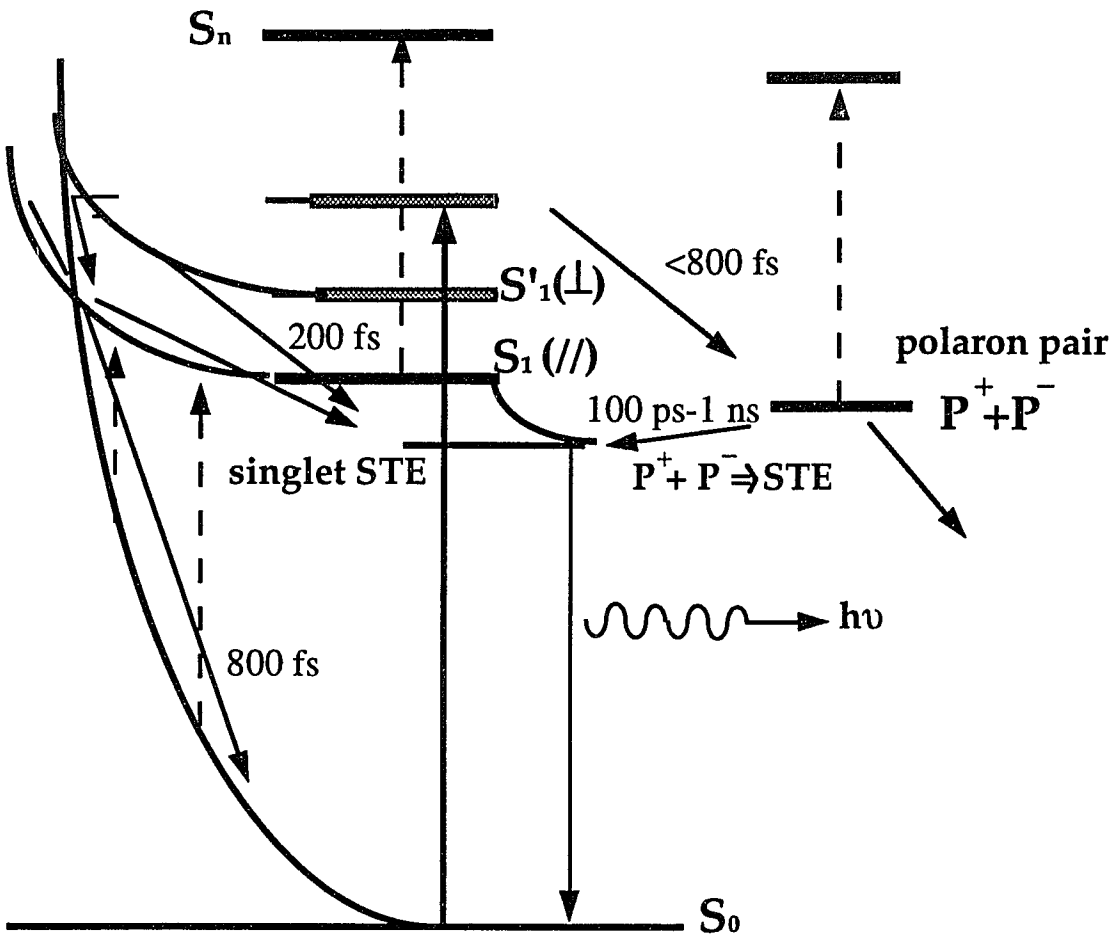

Fig. 8.19 Schematic diagram of the dynamic picture of excitations in oriented PPV films. S_1 represents the lowest singlet excited state which is allowed for parallel polarized excitation, S_1' for perpendicularly polarized excitation and $P^+ + P^-$ is polaron pair. Dashed line represents induced absorption.

coupling for optical transition since the 0.15-eV energy shift is close to the vibrational energy separation observed in luminescence spectrum. This vibrational coupling may result from the strong electron-phonon coupling in conjugated polymers. Therefore, the vibrational lattice wavefunction in the optical transition matrix can no longer be isolated from the electronic eigen wavefunction as treated as a Franck-Condon transition, which results in optical transition being polarization vector k dependent. Thus, the polarized optical transition involving the dipole alignment and vibrational coupling is proposed and need further theoretical studies in oriented conjugated polymers.

Based on this model, we can understand the different yields of excitations responsible for luminescence and induced absorption in the different polarized excitation at 500nm as due to the different coupling of excited state to ground state non-radiative decay channel. At excitation wavelength of 500nm, the perpendicular polarized excitation involves the higher energy transition which has less coupling to the ground state (S_0), therefore, the decay to ground state via multi-phonon emission is less efficient and formation of excitons is larger in perpendicular polarized excitation than parallel polarized excitation. This model also explain the excitation luminescence and excitation photoinduced absorption spectrum depicted in figure 8.16. When the excitation energy becomes larger the non-radiative decay to the ground state is more efficient and less photoproducts (excitons and polaron pairs) are formed contributing photoluminescence and induced absorption. This model also explains the relaxation kinetics are similar in different excitation wavelength.

D. Raman Gain

Raman gain is well resolved in the transient photoinduced gain measurements where the stimulated gain is observed in the vibrational frequency

shift of 1170 cm^{-1} and 1560 cm^{-1} relative to excitation frequency. These two frequency shifts correspond to the two most intense Raman frequencies shown in figure 7.1. The photoinduced Raman vibrational gain shifts as the excitation wavelength shifts while the exciton gain spectrum remains the same as the luminescence spectrum. This vibrational Raman gain is observed when the pump and probe pulse overlap in time. The Raman gain vanishes as the probe pulse is delayed from the pump pulse but the exciton gain remains for few hundred picosecond delay time. This agree with the hypothesis of Raman gain since the stimulated Raman emission gain can be thought of as an inverse Raman process. The probe pulse at Raman frequency ω_R, $\omega_R = \omega_{pump} - \omega_{phonon}$, is amplified when the pump pulse is present.

The distinction of Raman gain and polaron-exciton gain solves the puzzle of the "vibronic fluorescence band" discussed by Rauscher et al [8.3-8.4]. These authors found that photoluminescence shifts to lower energies as the excitation energy shifts when the excitation energy is below the low-energy side of the π-π^* absorption edge (19020 cm^{-1}). This experimental evidence has been used as evidence of further reconfinement of singlet excitons in PPV [7.8]. Our time resolved measurements suggests that the "vibronic fluorescence band" may be due to Raman vibrational scattering from the excitation pulse. The stimulated excitonic gain does not shift its energy peak within the 200 fs laser resolution as the excitation energy changes in our measurements. The exciton is not further reconfined according to our experimental results.

8.5) Summary and Conclusion

The ultrafast optical responses in oriented PPV films have been investigated. The photoinduced absorption and gain below the absorption edge have been observed by femtosecond absorption spectroscopy. When the pump

and probe pulse overlap in time at the sample, nonlinear optical processes, such as Raman gain, have been observed. The photoinduced gain associated with the singlet exciton has been measured and the formation of singlet excitons occurs within the 200fs laser resolution. The luminescence and photoinduced gain in oriented PPV have fast (15-25ps) and slow (70-100ps) components, which is due to the non-radiative decay of singlet excitons. The long tail of luminescence is explained due to the geminate recombination of polaron pairs.

The decay of photoinduced absorption also has fast (800fs) and slow (100ps) components. The fast component is due to the absorption of excited state species, free excitons, which non-radiatively decay into ground state S_0 via internal conversion through the vibrational ladders. The slow one is due to the initial decay of exciton and polaron pairs. The polaron pair is observed and forms within the 800 fs time scale formed from photoexcited free exciton.

The oriented quasi-one-dimensional PPV film enable us to re-exam the hypothesis of intra- and inter- chain excitation. We found that the fundamental statement of this hypothesis, the polarization anisotropic effect, can be explained by polarization dependent optical transitions. This means that the parallel polarized excitation involves transition to the lowest excited state and perpendicularly polarized excitation to the lowest excited state is not dipole allowed. This model explains the wavelength, intensity, and polarization dependent carrier dynamics.

With our experimental evidence, we provide a new dynamic scheme for excitations in oriented PPV films which is depicted in figure 8.19. The photoexcitation excites electrons to excited states, free excitons. The excitation polarized along the chain excite electrons to lowest excited state manifold (S_1) and excitation polarized perpendicular to the chain excite electrons to the S_1' state which has higher energy than the S_1 state. The excited free excitons decay

into singlet self-trapped excitons within 200fs and polaron pairs. Also, some of free excitons nonradiatively decay into the ground state in the time scale of 800 fs. Singlet excitons non-radiatively decayed in about 20 ps into the ground state mostly due the defects. The polaron pairs have long lifetime (up to few ten ns) and re-bound together to form singlet self trapped excitons, the initial decay time is about 100ps. Also, the disassociation of polaron pairs could form further trapped bipolarons.

This new carrier dynamic scheme provides a new thinking of this conjugated polymer system which might help us to understand the formation of these nonlinear excitations. The understanding of these excitations, such as singlet exciton, polarons and bipolarons, involving the mechanism of photoconductivity, photo- and electro- luminescence will be beneficial for developing such photonic and electronic devices using conjugated polymers. As an example of device applications utilizing this understanding of excitons, consider the following example: The positive gain (gain > absorption loss) has only been observed within 10 ps after photoexcitation near the absorption band edge. This selective wavelength excitation is different for parallel and perpendicular polarized excitations. This observation is interested in developing conjugated polymer lasers based on PPV films.

Chapter 9 Remarks and Future Experiments

9.1) Remarks

This thesis has demonstrated the application of ultrafast spectroscopic techniques to study electronic properties of organic and biological materials. Both studied materials exhibit rapid structural changes accomplished with a broad electronic absorption band change in the visible and near ir in the subpicosecond time scale. Therefore, femtosecond laser spectroscopy can be successfully applied in such systems due to its ultrashort pulse duration and broad spectral bandwidth. The experiments in this thesis have shown that the broad wavelength probing (spectroscopy) should be used rather than single wavelength probing because of the overlap of absorption bands in organic and biological systems. In rhodopsin, the absorption band of the excited states is quite similar to the absorption band of ground state bathorhodopsin, therefore, a single wavelength probe may not show its correct kinetics. In the conjugated polymer(PPV), the photoinduced absorption band overlaps with the gain spectrum. It is not easier to separate the kinetics of absorption and gain. As an example, in photoinduced absorption measurements in PPV, the rise time of the increasing in transmission results from the instantaneously formed gain and the decay of the broad excited state absorption. Therefore, spectroscopic studies are important in distinguishing various photoproducts by their wavelength, excitation and intensity dependence study . The ultrashort pulse laser not only provides a fine time resolution to study kinetics but also provides a broad spectral range for spectroscopic study. This combination of temporal and spectral properties makes ultrafast laser spectroscopy an idea tool for material studies.

In both rhodopsin and PPV, the fast structure deformations are observed by measuring the resulting absorption changes. The electronic properties we

observes are related to the lattice (or atomic) structure configuration, which results in a large absorption shift at the subpicosecond time scale. Therefore, these materials exhibit potential for ultrafast optoelectronic device applications, such as light modulators, fast time switches and memory devices.

9.2) Future Experiments

A. Time resolved Raman experiment in rhodopsin

We have studied the electronic absorption of rhodopsin on a subpicosecond time scale which yielded a great deal of structure information about the retinal chromophore. Time resolved Raman experiments can provide direct structural information about the rhodopsin to bathorhodopsin transformation. By studying the "fingerprint" Raman spectral region, time-resolved Raman measurements can monitor the formation of the Raman mode of bathorhodopsin by delaying the excitation pulse with respect to Raman scattering probe pulse. The details of the proposed experiment are as follows. An excitation pulse excites rhodopsin near its absorption peak at 500nm to initiate the photochemical reaction, then a time delayed second pulse is used to probe those excited vibrational modes by measuring their Raman scattering signal. The wavelength of the probe pulse can be in the absorption region of bathorhodopsin (such as 580-620nm) to enhance the bathorhodopsin Raman mode. The Raman mode of bathorhodopsin is well established [4.11]. By measuring those Raman frequencies produced by both the excitation and probe pulses as a function of the delay time between those two pulses, the formation time of bathorhodopsin can be obtained. Similar experimental procedures were used provided in time-resolved Raman measurements in bacteriorhodopsin.[4.8-4.10]

B. Time-resolved infrared absorption in PPV

The bipolaron in PPV exhibits two gap state absorption peaks at 0.5 eV and near 1.45 eV (see figure 7.1), while the triplet exciton only has one absorption peak at 1.45 eV. Therefore, the probe wavelength near 1.45 eV is actually probing the polaron, bipolaron and possiblly triplet exciton. Infrared absorption near 0.5 eV allows us to probe the long-lived bipolaron state because there is no absorption of triplet excitons. This experiment is proposed as follows. An excitation pulse near the absorption edge of PPV at about 500 nm is used to photoexcite the sample, this near band edge excitation may give a large yield for bipolarons (for the same reason which gives a large yield for excitons). The optically delayed infrared pulse at 2-5 μm is used to probe the absorption change. The details of the time resolved infrared absorption laser setup can be found in the literature [9.1-9.2] Since the bipolaron is measured in the millisecond time scale, information on the dynamics of the bipolaron in the picosecond and nanosecond time scale would be beneficial to the understanding of conjugated polymers.

APPENDIX I Solution for Coupled Differential Rate Equations

I.1) Model for excited twisted state

In analysis of bathorhodopsin formation, we use the following rate equation(5.1):

$$\frac{\partial N_r(t)}{\partial t} = (1-\eta)\frac{N_{90}(t)}{\tau_2} - \alpha I_p(t)N_r(t) \qquad (I.1)$$

$$\frac{\partial N_{fc}(t)}{\partial t} = -\frac{N_{fc}(t)}{\tau_1} + \alpha I_p(t)N_r(t) \qquad (I.2)$$

$$\frac{\partial N_{90}(t)}{\partial t} = \frac{N_{fc}(t)}{\tau_1} - \frac{N_{90}(t)}{\tau_2} \qquad (I.3)$$

$$\frac{\partial N_b(t)}{\partial t} = \eta\frac{N_{90}(t)}{\tau_2} \qquad (I.4)$$

and we interest in solving the total absorption as following:

$$\Delta A(\lambda,t)=\sigma_{90}(\lambda)N^*_{90}(t)+\sigma_{batho}(\lambda)N^*_b(t)+\sigma_{fc}(\lambda)N^*_{fc}(t)+\sigma_r(\lambda)(N^*_r(t)-N^*_r(-\infty)) \qquad (I.5)$$

where $N^*(t)$ is the convolution of $N(t)$ with the probe pulse function $I_b(t)$.

$$N^*_i(t) = \int N_i(t')I_b(t-t')dt' \qquad (I.6)$$

First, we calculate the relation between $\frac{\partial N^*_i(t)}{\partial t}$ and $\frac{\partial N_i(t)}{\partial t}$

from (I.6) we have:

$$\frac{\partial N^*_i(t)}{\partial t} = \int_{-\infty}^{\infty} N_i(t')\frac{\partial I_b(t-t')}{\partial t}dt' = -\int_{-\infty}^{\infty} N_i(t')\frac{\partial I_b(t-t')}{\partial t'}dt'$$

$$= N(t')I_b(t-t')|_{-\infty}^{\infty} + \int_{-\infty}^{\infty} I_b(t-t')\frac{\partial N_i(t')}{\partial t'}dt'$$

assuming $I_b(t) = 0$, when $t \to \pm\infty$, we have:

$$\frac{\partial N^*_i(t)}{\partial t} = \int_{-\infty}^{\infty} \frac{\partial N_i(t')}{\partial t'} I_b(t-t')dt' \qquad (I.7)$$

Therefore, we can integral $\int_{-\infty}^{\infty} I_b(t-t')dt'$ at both side of (I.1) to (I.4), and use relation (I.7), we have:

$$(I.3) \text{ --> } \quad \frac{\partial N^*_{90}(t)}{\partial t} = \frac{N^*_{fc}(t)}{\tau_1} - \frac{N^*_{90}(t)}{\tau_2} \qquad (I.8)$$

$$(I.4) \text{ ---> } \quad \frac{\partial N^*_b(t)}{\partial t} = \eta \frac{N^*_{90}(t)}{\tau_2} \qquad (I.9)$$

$$(I.2) \text{ ---> } \quad \frac{\partial N^*_{fc}(t)}{\partial t} = \int_{-\infty}^{\infty} \alpha I_p(t) N_r(t) I_b(t-t')dt' - \frac{N^*_{fc}(t)}{\tau_1} \qquad (I.10)$$

(I.1)+(I.2)+(I.3)+(I.4) ->

$$N^*_{90}(t) + N^*_b(t) + N^*_{fc}(t) + N^*_r(t) = \text{const} = N^*_r(-\infty) \qquad (I.11)$$

we assume the ground polulation change is small, i.e

$|N_r(t)-N_r(-\infty)| << N_r(-\infty)$, we have:

$$\int_{-\infty}^{\infty} \alpha I_p(t) N_r(t) I_b(t-t')dt' = \alpha P(t) N_r(-\infty)$$

where $P(t) = \int_{-\infty}^{\infty} I_p(t) I_b(t-t')dt'$, which is the convolution of pump and probe pulse. We have:

$$(I.10) \text{ ---> } \frac{\partial N^*_{fc}(t)}{\partial t} = \alpha K(t) N_r(-\infty) - \frac{N^*_{fc}(t)}{\tau_1} \qquad (I.12)$$

Let us solve the following differential eqn:

$$\frac{\partial y}{\partial x} + a(x)y = h(x)$$

we have

$$\frac{\partial py}{\partial x} = ph(x)$$

therefore

$$y=\frac{1}{p}\int ph(x)dx + \frac{c}{p} \quad \text{and} \quad p= \exp(\int a(x)dx) \tag{I.13}$$

using (I.13), we can solve (I.12) as follows:

$$N^*_{fc}(t) = \alpha N_r(-\infty) \int_{-\infty}^{t} \exp(\frac{t'-t}{\tau_1})P(t')dt' = M(t,\tau_1) \tag{I.14}$$

insert solution (I.14) into (I.8) to solve $N^*_{90}(t)$

$$\frac{\partial N^*_{90}(t)}{\partial t} + \frac{N^*_{90}(t)}{\tau_2} = \frac{M(t,\tau_1)}{\tau_1}$$

using (I.13) again we have

$$N^*_{90}(t) = \int_{-\infty}^{t} \exp(\frac{t'-t}{\tau_2}) \frac{M(t',\tau_1)}{\tau_1} dt'$$

$$= \frac{1}{\tau_1} \int_{-\infty}^{t} dt' \exp(\frac{t'-t}{\tau_2}) \int_{-\infty}^{t'} dt'' \exp(\frac{t''-t'}{\tau_2})P(t'')$$

by change the integral variable, use the integral diagram in figure I.1

we have:

$$N^*_{90}(t) = \frac{1}{\tau_1} \int_{-\infty}^{t} dt'' \, P(t'')\exp(\frac{t''}{\tau_1} - \frac{t}{\tau_2}) \int_{t''}^{t} dt' \exp[(\frac{1}{\tau_2} - \frac{1}{\tau_1})t']$$

$$= \frac{\tau_2}{\tau_1-\tau_2} \int_{-\infty}^{t} dt'' \, P(t'')\exp(\frac{t''-t}{\tau_1}) - \int_{-\infty}^{t} dt'' \, P(t'')\exp(\frac{t''-t}{\tau_2})$$

$$= \frac{\tau_2}{\tau_1-\tau_2} [M(t,\tau_1) - M(t,\tau_2)] \tag{I.15}$$

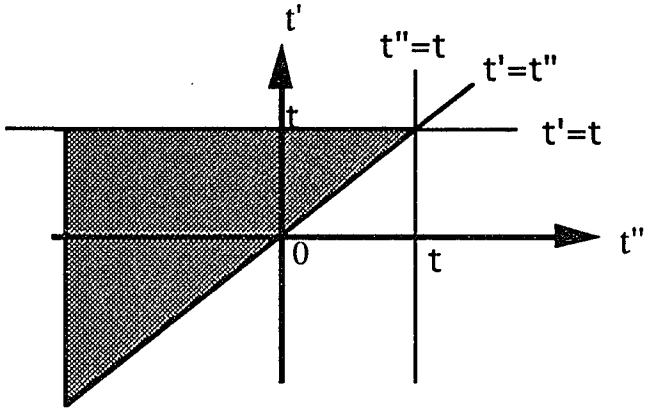

Figure I.1 Integral diagram. t" is integraled from -∞ to t' then t' from -∞ to t. The same area can be integraled by t' from -∞ to t then t" from -∞ to t.

Now, we can use solution (I.15) and solution (I.13) again to solve the differential equation (I.9) to get $N^*_b(t)$. We have:

$$N^*_b(t) = \int_{-\infty}^{t} \exp(\frac{t'-t}{\tau_3})\eta \frac{N^*_{90}(t')}{\tau_2} dt'$$

$$= \frac{\eta}{\tau_1-\tau_2} \int_{-\infty}^{t} \exp(\frac{t'-t}{\tau_3})[M(t',\tau_1) - M(t',\tau_2)] dt'$$

using the same technique for exchange the integral variable, we have:

$$N^*_b(t) = \frac{\eta}{\tau_1-\tau_2} \{\frac{\tau_1\tau_3}{\tau_1-\tau_3} [M(t,\tau_1) - M(t,\tau_3)] - \frac{\tau_2\tau_3}{\tau_2-\tau_3} [M(t,\tau_2) - M(t,\tau_3)] \} \quad (I.16)$$

and from (I.11):

$$N^*_r(t) = N^*_r(-\infty) - M(t,\tau_1) - \frac{\tau_2}{\tau_1-\tau_2} [M(t,\tau_1) - M(t,\tau_2)]$$
$$- \frac{\eta}{\tau_1-\tau_2} \{\frac{\tau_1\tau_3}{\tau_1-\tau_3} [M(t,\tau_1) - M(t,\tau_3)] - \frac{\tau_2\tau_3}{\tau_2-\tau_3} [M(t,\tau_2) - M(t,\tau_3)] \} \quad (I.17)$$

with the condition $\tau_3 >> \tau_2 > \tau_1$, we have simlified solution

$$N^*_{fc}(t) = M(t,\tau_1) \quad (I.18)$$

$$N^*_{90}(t) = \frac{\tau_2}{\tau_1-\tau_2} [M(t,\tau_1) - M(t,\tau_2)] \quad (I.19)$$

$$N^*_b(t) = \frac{\eta}{\tau_2-\tau_1} [\tau_1 M(t,\tau_1) - \tau_2 M(t,\tau_2)] + \eta M(t,\tau_3) \quad (I.20)$$

$$N^*_r(t) = N^*_r(-\infty) - \frac{1-\eta}{\tau_1-\tau_2} M(t,\tau_1) - \frac{(1-\eta)\tau_2}{\tau_2-\tau_1} M(t,\tau_2) - \eta M(t,\tau_3) \qquad (I.21)$$

from (I.5) and (I.11) we have

$$\Delta A(\lambda,t) = \sigma_{90}(\lambda)N^*_{90}(t)+\sigma_b(\lambda)N^*_b(t)+\sigma_{fc}(\lambda)N^*_{fc}(t)+\sigma_r(\lambda)(N^*_r(t)-N^*_r(-\infty))$$
$$= \sigma^*_{90}(\lambda)N^*_{90}(t)+\sigma^*_b(\lambda)N^*_b(t)+\sigma^*_{fc}(\lambda)N^*_{fc}(t)$$

where $\sigma^*_i(\lambda) = \sigma^*_i(\lambda) - \sigma^*_r(\lambda)$, by substitute the solution (I.18)-(I.20), we have:

$$\Delta A(\lambda,t) = a_1(\lambda) M(t,\tau_1) + a_2(\lambda)M(t,\tau_2) + a_3(\lambda)M(t,\tau_3) \qquad (I.22)$$

where:

$$a_1(\lambda) = \sigma^*_{fc}(\lambda) - \frac{\tau_2}{\tau_2-\tau_1} \sigma^*_{90}(\lambda) + \frac{\eta\tau_1}{\tau_2-\tau_1} \sigma^*_b(\lambda)$$

$$a_2(\lambda) = \frac{\tau_2}{\tau_2-\tau_1} \sigma^*_{90}(\lambda) - \frac{\eta\tau_2}{\tau_2-\tau_1} \sigma^*_b(\lambda)$$

$$a_3(\lambda) = \eta\sigma^*_b(\lambda)$$

One may realize $M(t,\tau_i)$ is a convolution of exponential decay $\exp(-\frac{t}{\tau_i})$ and laser pulse correlation function P(t). Therefore we can rewrite (I.22) as:

$$\Delta A(\lambda,t) = (a_1(\lambda)e^{-t/\tau_1} + a_2(\lambda)e^{-t/\tau_2} + a_3(\lambda)) \otimes P(t) \qquad (I.23)$$

If one assume the correlation function, P(t), be Gausian form, $\exp(-t^2/\sigma^2)$, we can calculated (I.23) as:

$$\Delta A(\lambda,t) = a_1(\lambda)\exp[(\frac{\sigma}{2\tau_1})^2] e^{-t/\tau_1} \operatorname{erfc}(-\frac{t}{\sigma} + \frac{\sigma}{2\tau_1})$$
$$+ a_2(\lambda)\exp[(\frac{\sigma}{2\tau_2})^2] e^{-t/\tau_2} \operatorname{erfc}(-\frac{t}{\sigma} + \frac{\sigma}{2\tau_2}) + a_3\int \exp(-y^2)dy \qquad (I.24)$$

where erfc(x) is the error function, $\operatorname{erfc}(x) = \int_x^\infty \exp(-y^2)dy$

I.2) Model for Ground pre-batho State

As discussion in 5.5), if the 90° state is treated as a ground state called b', we can rewrite the equation (I.1)-(I.4) as following:

$$\frac{\partial Nr(t)}{\partial t} = (1-\eta)\frac{N_{fc}(t)}{\tau_2} - \alpha I_p(t)N_r(t) \quad \text{(I.25)}$$

$$\frac{\partial N_{fc}(t)}{\partial t} = -\frac{N_{fc}(t)}{\tau_1} + \alpha I_p(t)N_r(t) \quad \text{(I.26)}$$

$$\frac{\partial N_{b'}(t)}{\partial t} = \eta\frac{N_{fc}(t)}{\tau_1} - \frac{N_{b'}(t)}{\tau_2} \quad \text{(I.27)}$$

$$\frac{\partial N_b(t)}{\partial t} = \frac{N_{b'}(t)}{\tau_2} - \frac{N_b(t)}{\tau_3} \quad \text{(I.28)}$$

If we substitute $N_{b'}(t)$ by $\eta N_{90}(t)$, we can obtain the equation (I.26)-(I.28) as same as (I.2)-(I.4), Therefore follow the same procedure described in I.1), we can have the same solution as (I.23), only thing changing is replace $N_{90}(t)$ by $\frac{N_{b'}(t)}{\eta}$.

Appendix II Dimerization of 1-dimensional lattice structure

In the early 50's, Peierls [II.1] suggested that the equal spaced one dimensional atomic structure is unstable and therefore leading to a dimerization. The physical basic picture can be understood by considering the Fermi surface and Brillouin zone. The Fermi level for a 1-dimensional lattice is:

$$k_f = \frac{n}{4} = \frac{1}{4a} \qquad \text{(II.1)}$$

where the n is the density of electrons and a is the space between the atoms. The boundary for the first Brillouin zone in momentum space for equal space atoms is given:

$$k_b = \frac{1}{2a} \qquad \text{(II.2)}$$

The Fermi surface and first Brilliouin zone are shown in figure II.1(a), in which only half of the first Brillouin zone is filled. By considering basic solid state theory that the energy gap only appears at the edge of the Brillouin zone, the equally spaced atomic chain system would be metallic which is not observed in pure organic polymers. After dimerization the unit cell length changes from a to 2a, the lattice structure as shown in figure II.1(b), Therefore, the first Brillouin zone become k_b=1/4a and overlaps with the Fermi surface. As a consequence, the first Brillouin zone is therefore fully filled and the dimerized lattice structure become stable. This dimerization opens an energy gap at the Fermi surface, thereby lowing the energy of the occupied states and stabilizing the lattice distortion. The competition between the lowering of the electronic energy and the increase of the elastic energy of the polymer leads to an equilibrium for dimerization.

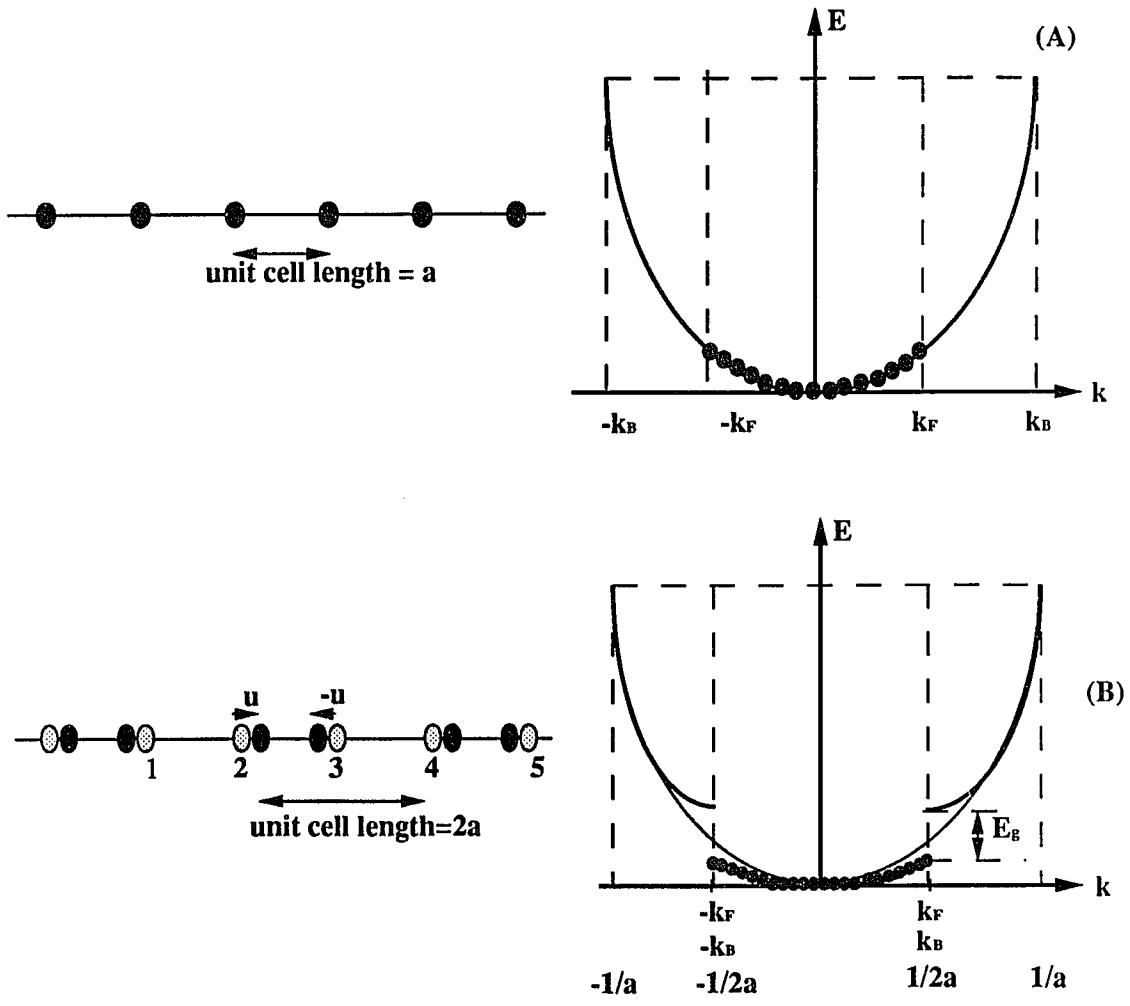

Fig.II.1 The lattice structure and enertgy dispersion relation using free electron model for the lattice before dimerizatiobn (A) and after dimerization (B)

Reference

1.1 G.R. Fleming *Chemical Applications of Ultrafast Spectroscopy* (Oxford University Press, New York, (1986))

1.2 R.R. Birge *Annu. Rev. Phys. Chem.* **41**, 683 (1990)

1.3 T. Miyasaka, K. Koyama, I. Itoh *Science* **255**, 342 (1992)

1.4 P. Pasad *Introduction to Nonlinear Optical Effects in Molecules and Polymers* (John Wiley & Sons, New York, 1991)

1.5 B.R. Weiberger, G.C. Gau, Z. Kiss *Appl. Phys. Lett.* **38**, 555 (1981)

1.6 M. Ozaki, D. Peebles, B.R. Weiberger, A.J. Heeger, A.G. MacDiarmid, *J. Appl. Phys.* **51**, 4245 (1980)

1.7 K.E. Ziemelis, A.T. Hussain, D.D.C. Bardley, R.H. Friend *Phys. Rev. Lett.* **66**, 2231 (1991)

1.8 J.H. Burroughes, D.D.C. Bradley, A.R. Brown, R.N. Markay, R.H. Friend, P.L. Burns, A.B. Holmes *Nature* **347**, 539 (1990)

1.9 D.D.C. Bradley *J. Phys.* **D20**, 1389 (1987)

2.1 M. D. Levenson in *Introduction to Nonlinear Spectroscopy* (Academic Press, San Diego, 1981)

2.2 P.M. Rentzpis *Science* **202**, 174 (1978)

2.3 S.L. Shapiro ed. *Ultrashort Light Pulses* (Springer-Verlag, New York, 1977)

2.4 R.R. Alfano ed. *Biological Events Probed by Ultrafast Laser Spectroscopy* (Academic Press, San Diego, 1982)

2.5 R.L. Fork, C.V. Shank, R. Yen, C.A. Hirlimann *IEEE J. Quantum Electron.* **19**, 500 (1983)

2.6 C.V. Shank in *Ultrafast Laser Pulses and Applications ed. by W. Kaiser* (Topics in Applied Physics **60**, Spinger-Verlag, New York, 1988)

2.7 D.J. Bradley in *Ultrashort Light Pulses ch2* ed. by S.L. Shapiro (Springer-

Verlag, New York, 1977)

2.8 A. Yariv in *Quantum Electronics* 3rd Ed. (Wiley, New York, 1989)

2.9 J.T. Verdeyen *Laser Electronics ch5. ch8-9* (Prentice-Hall, New Jersey, 1981)

2.10 R.L. Fork, B.I. Greene, C.V. Shank *Appl. Phys. Lett* **38**, 671 (1981)

2.11 M. Stix, E.P. Ippen *IEEE J. Quantum Electron.* **19**, 520 (1983)

2.12 G.H.C. New *IEEE J. Quantum Electron.* **10**, 115 (1974)

2.13 R.R. Alfano, S.L. Shapiro *Phys. Rev. Lett* **24**, 584 (1970)

2.14 R.R. Alfano in *Supertinuum Light Source* (Springer-Verlag, New York, 1989)

2.15 R.L. Fork, C.V. Shank, R.T. Yen *Appl. Phys. Lett.* **41**, 223 (1982)

2.16 F. Salin, A. Brun *J. Appl. Phys.* **61**, 4736 (1987)

2.17 R.L. Fork, O.E. Martinez, J.P. Gondon *Optics Lett.* **9**, 150 (1984)

2.18 R.L. Fork *Optics Lett.* **11**, 629 (1986)

2.19 J.D. Kafka, T. Baer *Optics Lett.* **6**, 401 (1987)

2.20 B.I. Greene, J. Orenstein, R.R. Millard, L.R. Williams *Chem. Phys. Lett.* **139**, 381 (1987)

2.21 E.P. Ippen, C.V. Shank in *Ultrashort Light Pulses* ed. by Shapiro (Springer -Verlag, New York, 1977)

2.22 A.G. Doukas, J. Buchert, R.R. Alfano in *Biological Events Probed by Ultrafast Laser Spectroscopy* ch 17, ed. by R.R. Alfano (Academic Press, San Diego, 1982)

3.1 A. Stylere *Biochemistry* 3rd Edition (John Wiley & Sons, 1990)

3.2 A. Lewis, L.V. Del Priore *Phys. Today* **Jan.**, 38 (1988)

3.3 R.R. Birge *Biochimica Biophysica Acta* **1016**, 293 (1990)

3.4 P.S. Zurer *Chem. & Enger. News* Nov. (1983)

3.5 R. Hubbard, G. Wald *J. Gen. Physiol* C, 269 (1952)

3.6 G. Wald *Science* **162**, 230 (1968)

3.7 B. Honig, T. Ebrey, R.H. Callender, U. Dinur, M. Ottolenghi *Proc. Natl. Acad. Sci.(USA)* **76**, 2503 (1979)

3.8 R.R. Birge *Ann. Rev. Phys. Chem.* **41**, 683 (1990)

3.9 R.R. Birge, C.M. Einterz, H.M. Knapp, L.P. Murray *Biophys. J.* **53**, 367 (1988)

3.10 J.R. Tallent, E.W. Hyde, L.A. Findsen, G.L. Fox, R.R. Birge *J. Am. Chem. Soc.* **114**, 1581 (1992)

3.11 R.H. Callender in *Biological Events Probed by Ultrafast Laser Spectroscopy* ch 9, ed. by R.R. Alfano (Academic Press, San Diego, 1982)

3.12 R.M. Hochstrasser, C.K. Johnson in *Ultrafast Laser Pulses and Applications ch 9 ed. by W. Kaiser* (Topics in Applied Physics **60**, Springer-Verlag, 1987)

3.13 D. Oesterhelt, W. Stoeckenius *Nature New Biol.* **223**, 149 (1971)

3.14 R.A. Mathies, S.W. Lin, J.B. Ames, W.T. Pollard *Ann. Rev. Biophys. Biophys. Cham.* **33**, 491 (1991)

4.1 G. Erying, R.A. Mathies *Proc. Natl. Acad. Sci. (USA)* **76**, 33 (1979)

4.2 R.H. Callender, B. Honig *Ann. Rev. Biophys. Bioeng.* **6**, 33 (1977)

4.3 J.D. Spalink, A.H. Reynolds, P.M. Rentzepis, W. Sperling, M.L. Applebury *Proc. Natl. Acad. Sci. (USA)* **80**, 1887 (1983)

4.4 R.H. Callender, A. Doukas, R. Crouch, K. Nakanishi *Biochem.* **15**, 1621 (1976). R. Mathies, A.R. Oseroff, L. Stryer *Proc. Natl. Acad. Sci. (USA)* **73**, 1 (1976)

4.5 B. Aton, A.G. Doukas, D. Narva, R.H. Callender, U. Dinur, B. Honig *Biophys. J.* **29**, 79 (1980)

4.6 G. Eyring, R. Mathies *Proc. Nawl. Acad. Sci. (USA)* **76**, 33 (1979)

4.7 G.R. Loppnow, R.A. Mathies *Biophys. J.* **54**, 35 (1988)

4.8 S.J. Doig, P.J. Reid, R.A. Mathies *J. Phys. Chem.* **95**, 6372 (1991)

4.9 G.H. Atkinson, T.L. Brack, D. Blanchard, G. Rumbles *Chem. Phys.* **131**, 1 (1989)

4.10 R.V.D. Berg, D.J. Jang, H.C. Bitting, M.A. El-Sayed *Biophys. J.* **58**, 135 (1990)

4.11 G. Hayward, W. Carlsen, A. Siegman, L. Stryer *Science* **211**, 942 (1981)

4.12 G.E. Busch, M.L. Applebury, A.A. Lamola, P.M. Rentzepism *Proc. Natl. Acad. Sci. (USA)* **69**, 2802 (1972)

4.13 B.H. Green, T.G. Monger, R.R. Alfano, B. Aton, R.H. Callender *Nature* **269**, 179 (1977)

4.14 T.G. Monger, R.R. Alfano, R.H. Callender *Biophys. J.* **27**, 107 (1979)

4.15 V. Sundstrom, P.M. Rentzepis, K. Peters, M.L. Applebury *Nature* **276**, 645 (1977)

4.16 A.G. Doukas, P.Y. Lu, R.R. Alfano *Biophys. J.* **35**, 547 (1981)

4.17 T. Kobayshi *Photochem. Photobiol.* **32**, 207 (1980)

4.18 Y. Shichida, S. Matuoka, T. Yoshizawa *Biophys. J.* **7**, 221 (1984)

4.19 H. Kandori, S. Matuoka, Y. Shichida, T. Yoshizawa *Photochem. Photobiol.* **49**, 181 (1989) also *Biophys J.* **56**, 453 (1989)

4.20 J. Dobler, W. Zinth, W. Kaiser, D. Oesterhelt *Chem. Phys. Lett.* **144**, 215 (1988)

4.21 M.C. Nuss, W. Zinth, W. Kaiser, E. Kolling, D. Oesterhelt *Chem. Phys. Lett.* **117**, 1 (1985)

4.23 H.-J. Polland, M.A. Franz, W. Zinth, W. Kaiser, E. Kolling, D. Oesterhelt *Biophys. J.* **49**, 651 (1986)

4.24 R.A. Mathies, C.H. Bito Cruz, W.T. Pollard, C.V. Shank *Science.* **240**, 777 (1988)

4.25 A.G. Doukas, R.R. Alfano in *Ultrafast Phenomena IV* ed by D.H. Auston

and K.B. Eisnthal (Springer-Verlag, New York) 1984

4.26 A.G. Doukas, M.R. Jannarkar, R.R. Alfano, R.H. Callender, T. Kakitani, B. Honig *Proc. Ntal. Acad. Sci. (USA)* **81**, 4790 (1984)

4.27 A.G. Doukas, M.R. Jannarkar, R.R. Alfano, R.H. Callender, V. Balogh-Nair *Biophys. J.* **47**, 795 (1985)

4.28 J. Buchert, V. Stefancic, A.G. Doukas, R.R. Alfano, R.H. Callender, J. Pande, H. Akita, V. Balogh-Nair *Biophys. J.* **43**, 279 (1972)

4.29 A.R. Oseroff, R.H. Callender *Biochemistry* **13**, 1621 (1974)

4.30 K. Peters, M.L. Applebury, P.M. Pentzepis *Proc. Ntal. Acad. Sci. (USA)* **74**, 3119 (1977)

4.31 A. Warshel *Nature* **260**, 679 (1976)

4.32 A. Warshel, N. Barboy *J. Am. Chem. Soc.* **101**, 6131 (1982)

4.33 R.W. Schoenlein, C.V. Shank, L.A. Peteanu, R.A. Msthies *Science* **254**, 412 (1991)

5.1 T. Yoshizawa *Handb. Sens. Physiol.* **7**, 146 (1972)

5.2 M. Taiji, K. Bryl, M. Nakagawa, M. Tsuda, T. Kobayashi *Photochem. & Photobiology* **56**, 1003 (1992)

6.1 E. Conwell *Conjugated Polymer Semiconductors: An Introduction* Preprint of review article (1991)

6.2 A.J. Heeger, S. Kivelson, J.R. Schrieffer, W.-P. Su *Rev. Mod. Phys.* **60**, 781 (1988)

6.3 J. Orenstein in *Handbook of Conducting Polymers,* vol.2 ed. by T.A. Skotheim (Dekker, New York, 1986)

6.4 W.-P. Su, J.R. Schrieffer, A.J. Heeger *Phys. Rev. Lett.* **42**, 1698 (1979) and *Phys. Rev. B* **22**, 2099 (1980)

6.5 J. Orenstein, G.L. Baker *Phys. Rev. Lett.* **49**, 1043 (1980)

6.6 J.D. Flood, A.J. Heeger *Phys. Rev. B* **28**, 2356 (1983)

6.7 K. Fesser, A.R. Bishop, D.K. Campbell *Phys. Rev. B* **27**, 4808 (1983)

6.8 R.H. Friend, D.D.C. Bradley, P.D. Townsend *J. Phys. D* **20**, 1367 (1987)

6.9 T. Kobayashi, M. Yoshizawa, U. Stamm, M. Taiji, M. Hasegawa *J. Opt. Soc. Am B* **7**, 1558 (1990)

7.1 T. Ito, H. Shirakawa, S. Ikeda *J. Polym. Sci. Polym. Chem.* **12**, 11 (1974)

7.2 K.F. Voss, C.M. Foster, L. Smilowitz, D. Milailovic, S. Askari, G. Srdanov, Z. Ni, S. Shi, A.J. Heeger, F. Wudl *Phys. Rev. B* **43**, 5109 (1991)

7.3 S. Lefrant, E. Perrin, J.P. Buission, H. Eckhardt, C.C. Hanl, *Synth. Met.* **29**, E91 (1989)

7.4 B. Tian, G. Zerbi, R. Schenk, K. Mullen *J. Chem. Phys.* **95**, 3191 (1991)

7.5 B. Tian, G. Zerbi, K. Mullen *J. Chem. Phys.* **95**, 3198 (1991)

7.6 D.D.C. Bradley, R.H. Friend, H. Lindenberger, S. Roth *Polymer* **27**, 1709 (1986)

7.7 G.E. Harbeke, E. Meier, W. Kobel, M. Egli, H. Kiess, E. Tassatti, *Solid State Commun.* **55**, 419 (1985)

7.8 N. Colaneri, M. Nowak, D. Spiegel, S. Hotta, A.J. Heeger *Phys. Rev. B* **36**, 7964 (1987)

7.9 T.-C. Chung, J.H. Kaufman, A.J. Heeger, F. Wudl *Phys. Rev. B* **30**, 702 (1983)

7.10 X. Wei, B.C. Hess, Z.V. Vardeny, F. Wudl *Phys. Rev. Lett.* **68**, 666 (1992)

7.11 Z.V. Vardeny, E. Ehrenfreund, O. Brafman, B. Horovitz *Phys. Rev. Lett.* **56**, 671 (1986)

7.12 D.D.C. Bradley, R.H. Friend *J. Phys. Condens. Matter* **1**, 3671 (1989)

7.13 K.S. Wong, D.D.C. Bradley, W. Hayes, J.F. Ryan, R.H. Friend, H. Lindenberger, S. Roth, *J. Phys. C* **20**, L187 (1987)

7.14 N.F. Colaneri, D.D.C. Bradley, R.H. Friend, P.L. Burn, A.B. Holmes, C.W. Spangler *Phys. Rev. B* **42**, 11670 (1990)

7.15 L. Rothberg, T.M. Jedju, S. Etemad, G.L. Baker *Phys. Rev. Lett.* **57**, 3227 (1986) and *Phys. Rev. B* **36**, 7529 (1987)

7.16 L. Rothberg, T.M. Jedju, P.D. Townsend, S. Etemad, G.L. Baker *Phys. Rev. Lett.* **65**, 100 (1990)

7.17 G. Kanner, X. Wei, B.C. Hess, L.R. Chen, Z.V. Vardeny, *Phys. Rev. Lett.* **69**, 583 (1992)

7.18 M. Yoshizawa, A. Yasuda, T. Kobayashi *Appl. Phys. B* **53**, 296 (1991)

8.1 T. Kobayashi *J. Luminescence* **53**, 159 (1992)

8.2 L. Rothberg et al. to be published paper.

8.3 U. Rauscher, H. Bassler, D.D.C. Bradley, M. Hennecke *Phys. Rev. B* **42**, 9830 (1990)

8.4 U. Rauscher, L. Schutz, A. Greiner, H. Bassler *J. Phys.: Condens. Matter* **1**, 9751 (1989)

9.1 P.O. Stoutland, R.B. Dyer, W.H. Woodruff *Science* **257**, 1913 (1992)

9.2 T.M. Jedju, L. Rothberg *Appl. Optics* **27**, 615 (1988)

II.1 R.E. Peierls, *Quantum Theory of Solid* (Clarendon, Oxford, 1955)